UNIVERSITÀ DEGLI STUDI DI MILANO

DOTTORATO DI RICERCA IN SCIENZE DELLA TERRA

Ciclo XXXV

DIPARTIMENTO DI SCIENZE DELLA TERRA

TESI DI DOTTORATO DI RICERCA

Lithium enrichment in anatectic pegmatites: new insights from the thermometamorphic aureole of the Adamello batholith

GEO/08

CANDIDATO
Lorenzo Magnani

TUTOR
Federico Farina

COORDINATORE DEL DOTTORATO
Maria Iole Spalla

INDEX

LIST OF FIGURES

CHAPTER 6 ***PAG.***

CHAPTER 7 ***PAG.***

LIST OF TABLES

ABSTRACT

In the contact aureole of the collisional metaluminous Adamello pluton (Italy), pelites reached hornfels facies conditions locally undergoing partial melting, forming Crd-bearing and Crd-absent migmatities. This small-scale migmatitic field is spatially associated with barren and Lithium-Cesium-Tanatalum (LCT) pegmatitic dykes of granitic composition, suggesting a direct link between low-pressure partial melting and generation of Li-enriched felsic melts. Phase equilibria modelling reveals that the Crd-bearing metapelitic migmatites produced around 20 vol.% melt fraction through fluid-assisted melting reactions, while the Crd-absent stromatic metatexites produced ca. 35 vol.% of melt during fluid-rich partial melting. Peak P-T metamorphic conditions were calculated at 690-700°C and 300 MPa for both rock types. Because of the steep contact thermal gradient, the underlying and older conglomerates of the Verrucano Formation, of which the pelitic succession is part of, as well as rock of the Collio Formation experienced comparably lower temperature metamorphism. Their mica-poor mineral compositions prevented them from melting and influencing the local anatectic processes. Crd-bearig migmatites leucosomes are compositionally similar to anatectic melts obtained by phase equilibria modelling, connected to fluid-assisted melting and defined as unfractionated, while the leucosomes dominated by Kfs-Bt cumulus structures and extremely enriched in K_2O, Sr and Ba are connected to fluid-rich melting and Crd-absent migmatites. Major and trace element modelling suggests that part of the melt formed in the latter case was extracted from the source and that the composition of this evolved anatectic magma is compatible with the chemical composition of the migmatites-hosted LCT pegmatites. Whole rock Sr-Nd isotopic data confirm that the Li-rich pegmatites of the Forcel Rosso area are indeed crustally derived, marking them as produced by direct anatexis of metapelites. They also show that they were formed by two melt batches of different trace element composition originated by differential in-source fractionation. Conversely, isotopic data characterizes the pluton-hosted pegmatites as mantle-derived and directly linked to the Adamello batholith, clearly marking the lack of direct relationship existing between this magmatic intrusion and pegmatites featuring Li enrichment in its contact aureole. The data from this study shows that cordierite, or the absence of it, plays a key role in regulating the lithium transfer during partial melting in low pressure migmatites. Zircon U-Pb ages for all pegmatites in the area, point to the same age of the Adamello pluton intrusion, ca. 38 Ma, and trace elements compositions helped to outline the differences in the geochemical signature between pluton-derived and metapelite-derived pegmaties. The Ti-in-zircon geothermometer confirms that anatectic pegmatites crystallized at the peak metamorphic temperature calculated through phase equilibria modelling. Once defined that Li-enriched pegmatites are anatectic, tourmaline was used to study the continous evolution of the metapelitic system from unmetamorphosed up to the conditions of

pegmatite crystallization. This mineral is the main boron carrier among the rock forming minerals and it's obiquitous in the studied rocks. Studying the major element composition and boron isotopic signature several changes and trends are identified highlighting how this mineral evolves through the metamorphic history of metapelites, revealing a seemingly more complex picture compared to what is reported in the published literature data. Also, the data show how this mineral records variations during pegmatites crystallization processes making it valuable in the interpretation of their complex internal evolution processes. This PhD project proved that Li-enriched pegmatites may be anatectic and originate through fluid present melting of metapelites, even in the thermometamorphic aureole of plutons. We identify the mineral cordierite as the main regulator of lithium liberation during low pressure anatexis of suitably Al-rich pelitic rocks. We highlight that in-source and en_route melt fractionation play an extremely important role each time magma is extracted from its source and that this process is the one ultimately responsible for the formation of Li-enriched melts. Pegmatitic zircons, although complex, can be used as tracers in order to help define the origin of pegmatitic dykes, particularly in cases in which these bodies are too old for Sr isotopic determination. The studied area shows that small scale variations in the pre-anatectic abundance and presence of aqueous fluids influences melt production and melt composition of different migmatitic areas. Finally, the metamorphic and magmatic history of the studied tourmaline crystals highlights how this mineral may record almost every boron-involving reaction and help unravel the complex history of migmatites, pegmatites and Tur-bearing plutons.

Chapter 1

Aim of the study and thesis structure

1. Introduction

Lithium is the element with atomic number 3 and the least dense alkali metal, it is electrochemically active featuring the highest redox potential value of all metals and the highest specific heat capacity of any solid element. These characteristics make it one of the most important commodity for modern life and a key element for modern electric vehicle revolution (e.g. Swain et al., 2017). Fig. 1-1 illustrates the different uses of lithium compounds (Kimball et al, 2016).

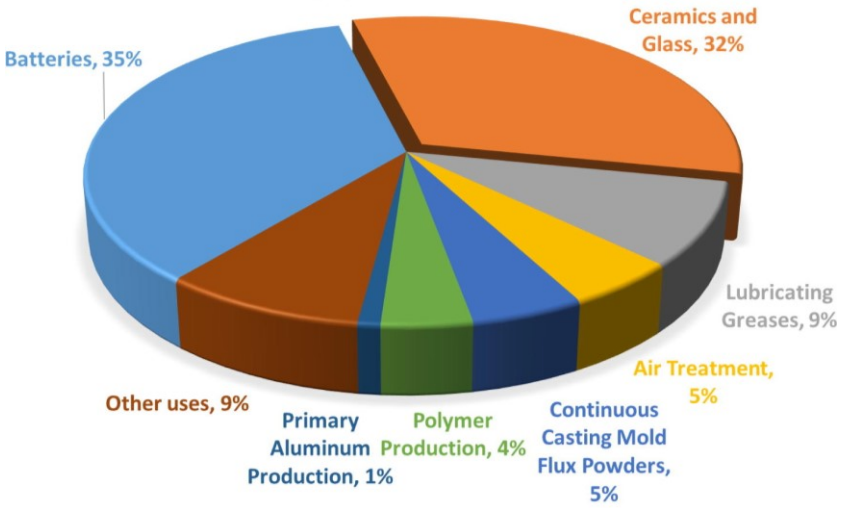

Figure 1-1 Graphic illustrating lithium usage, data from Kimball et al., 2016.

Lithium is industrially produced mainly as lithium carbonate, lithium hydroxide, lithium chloride, lithium bromide, and butyl lithium. Market demands for this element is expected to increase significantly over the next decade, due to its use in batteries for electric vehicles and stationary power storage. Projected demands only for lithium as LIBs (LIB – lithium ion batteries) for the plug-in hybrid electric (PHEV), electric (EV) and hybrid electric (HEV) vehicles in the recent future is huge and estimated to reach $221 billion by 2024 (Swain, 2017). Newly mined lithium to supply the estimated demand will come largely from pegmatite and related magmatic deposits, evaporative brines, and a growing group of unusual deposits including both rocks and brines (Kesler et al., 2012). Very few of these deposits are currently in production and information on geologic factors, such as lithium content and mineralogy, continuity and size, relation to enclosing rocks, and location, all of which might affect their economic development, is relatively sparse and scattered. Global supplies of lithium are currently dominated by salt-lake brines (salars) and hard rock-hosted deposits such as Li-

pegmatites. Pegmatites, in which Li is mainly present in spodumene ($LiAlSi_2O_6$), petalite ($LiAlSi_4O_{10}$) and lepidolite ($KLi_2Al(Si_4O_{10})(F,OH)_2$-$K(Li,Al)_3(AlSi_3O_{10})(F,OH)_2$), characterize several orogenic belts in the world while Li-rich brines are mainly diffused in desertic areas of the planet. The global geographical distribution of lithium deposit types is quite diffuse (Fig. 2-2) with brine reservoirs holding a much larger total lithium resource (21.6 Million Tones – Mt - Li) than pegmatites (3.9 Mt) (e.g. Kesler et al., 2012). Brine resources can be found in the "Lithium Triangle" of Bolivia (21 Mt, salar de Uyuni, unexplored), Argentina (17 Mt, salar del Hombre Muerto), and Chile (9 Mt, salar de Atacama; Chaves et al., 2021). This area, submitted to geostrategic and geo-economic bottlenecks (Grosjean et al., 2012), represents about 30% of global production of lithium, and approximately 60% and 70% of total world reserves and resources respectively. Other important brine deposits are located in the U.S.A and China.

Compared with brines, pegmatites, are of interest due to their wider geographic distribution, lesser susceptibility to supply disruptions and environmental impact. For all these reasons pegmatites are the types of Li deposits on which the research effort has mostly focused on in the last years. The most important deposits are found in Australia (Greenbushes pegmatite, Partington et al., 1995), Brazil, China, some African countries such as South Africa, Namibia and Zimbabwe.

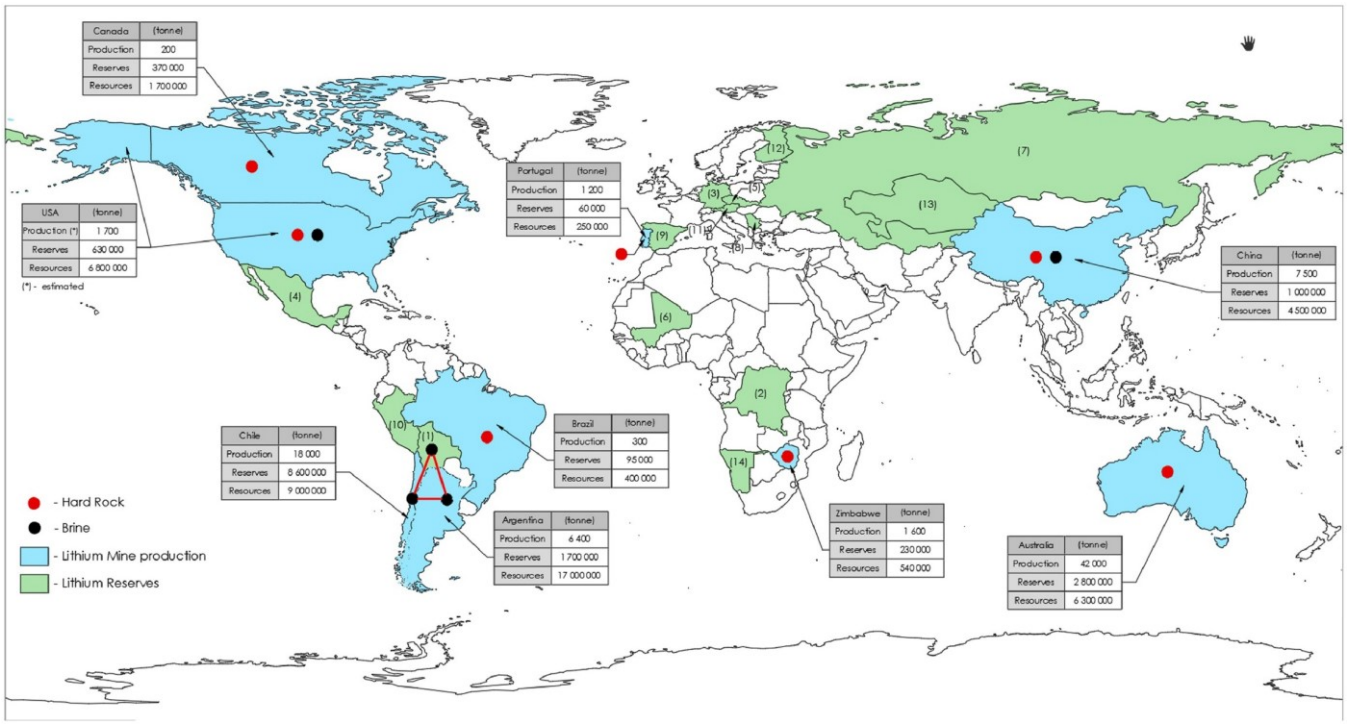

Figure 1-2 World map highlighting the most important Li producers, from Chaves et al., 2021.

In Europe, hard rock mine projects exist in Austria, Portugal, Serbia and Finland, with a collective planned capacity of 11000 tonnes of Lithium Carbonate Equivalent (LCE), corresponding to about 8% of the estimated 2027 world demand (ETIP 2020). In Italy, Li-enriched pegmatites are rare and small,

comprising the gem-bearing LCT pegmatites of the Elba Island, the Permo–Triassic spodumene pegmatites in the Austroalpine units of the Central Alps and the Adamello pegmatites focus of this study. Li-rich magmatic rocks, associated to granites and vulcanites, occur extensively in Sardinia and Calabria and in the Tertiary–Quaternary Tuscan and Roman magmatic provinces and have systematically higher Li contents than those recorded in normal arc igneous rocks worldwide (Dini et al., 2022) but their potential for Li extraction is unknown.Although several works addressing the genesis of Li-enriched pegmatites have been published (e.g. Černý, 1991; Černý&Ercit, 2005, Simmons et al., 1995, 1996, 2008, 2016, 2018), the processes that lead to the formation of these rocks are still not well understood.

New research on these economically strategic resources are needed to expand our knowledge on the geological constraints that determine their formation and produce the metal endowment of pegmatites-hosted Li resources. The presented PhD project, in particular, tries to provide tighter constraints on the evolution of Li-pegmatites by studying small Li-enriched bodies emplaced in the thermometamorphic aureole of the Adamello pluton (Northern Italy).

1.1 Pegmatites

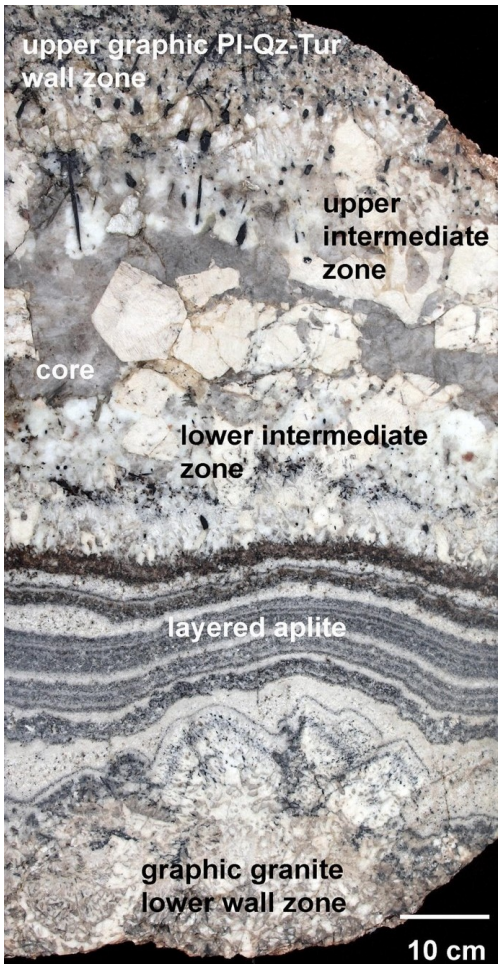

Pegmatites are intrusive igneous rocks expressing the greatest range of grain sizes known in any rock type, with crystals going from sub-millimeter to tens of meters. Pegmatitic textures can develop in any intrusive igneous rock type from ultramafic, to granitic and syenitic in composition but the term is most commonly used for granitic pegmatites. In fact, whenever the term “pegmatite” is used without a qualifying adjective it refers to rocks with granitic composition (e.g. Simmons et al., 2008). Granitic pegmatites are predominantly composed of quartz, K-feldspar, Na-plagioclase and micas. The graphic granite texture, produced by the simultaneous growth of quartz and feldspar in non-equilibrium conditions (e.g. Fenn, 1986), is a typical feature of these pegmatitic bodies and differentiate pegmatites from other magmatic rocks.

Figure 1-3 Barren pegmatite cross-section From London (2005)

These magmatic bodies are texturally, mineralogically and, in most cases chemically, heterogeneous. Common internal zonation patterns (Fig. 1-3) involve graphic granite external zones and several repetitions of blocky pegmatitic (characterized by large, sometimes skeletal crystals) and aplitic (equant small crystals dominated) textures. Zonations characterized by the accumulation of a particular mineral, called line rock areas, are also common.

Rare elements enrichment is usually concentrated in the innermost zones, sometimes alongside gem-bearing miarolitic cavities. Černý (1991) proposed that the trace-element signatures of pegmatites fall into two distinct categories, which he referred to as pegmatite families: LCT (Li-Cs-Ta) and NYF (Nb-Y-F which will not be discussed in this work). According to Černý (1991) the signature of the family appears only in the most fractionated members of a group in the form of exotic minerals such as spodumene, tantalite, pyrochlore, pollucite, etc.

1.1.1 LCT pegmatites

In Černý's (1991) classification, LCT pegmatites are always affiliated with S-type granites (Chappell and White, 2001), with these granitoids originating from partial melting of previously unmelted Al-rich clastic sedimentary material. According to the main genetic model proposed for LCT pegmatites, their characteristic chemical signature is the result of a two steps process that involves partial melting of aluminous metasediments and fractional crystallization of the anatectic melt. Therefore, the high Li, Ta, Cs Be, Rb, Ga, Nb, Sn, B, P, and F which is characteristic of these rocks is derived both by the metapelitic source and the magma fractionation process following the liquid line of descent followed by S-type magmas. Pegmatites of the LCT family are generally undeformed (London, 2018) suggesting that they tend to be generated and emplaced in the waning stages of tectonism, after crustal thickening (Bea, 2012). Černý and Ercit (2005) noted that I-type granites, do not produce pegmatitic bodies belonging to the LCT lineage. Černý et al. (2012) make the further point that I-type granites generally do not spawn pegmatites at all, unless they contain manifestly elevated amounts of B or of F. In that case, the sources of the granites are mixed: they contain a component derived ultimately from seawater in the form of marine sediment, water expelled from marine sediment (e.g., Bebout et al., 2007; Mallik et al., 2016), or hydrothermally altered oceanic crust (e.g. Palmer and Swihart, 1996). Insofar as the I-type granites arise as direct melts from the mantle, by remelting of ponded basalts and volcanic sequeces or immature sedimets they are not sources of B that ca culminates in tourmaline-rich pegmatites (Ottolini et al., 2004).

1.1.1.1 Geochemical and isotopic characteristics

The main characteristic of LCT pegmatites is their enrichment in lithium is. The predominant lithium minerals include the silicates spodumene, petalite, lepidolite, and elbaite (i.e. Li-tourmaline), and the phosphate series amblygonite–montebrasite [$LiAlPO_4(F,OH)$] and lithiophilite–triphylite [$Li(Mn,Fe)PO_4$]. Cesium can be highly concentrated in micas (up to ca. 22% Cs_2O, Černý et al. 2003), but can also achieve concentrations sufficient to crystallize pollucite, $CsAlSi_2O_6$. Although columbite (a Nb-dominant oxide) appears early in the evolutionary sequence of the LCT pegmatites, Ta-rich oxides usually predominate towards the end of it (e.g. Linnen et al., 2012) but the factors that fractionate Ta from Nb in pegmatites and granites are not yet fully known. The important fluxing components B, P, and F are elevated but variably enriched (London and Morgan 2012). Boron is found in black tourmaline in the margins of pegmatites, but also in gem-forming elbaite in the central zones (Simmons et al., 2012). Many of the LCT pegmatites contain a plethora of primary and secondary phosphates in addition to apatite, and phosphorus is also a significant component of the feldspars (London et al. 1999). REE abundances in the LCT pegmatites are negligible, largely owing to their high-silica and peraluminous liquid compositions in which REE are highly insoluble (< 500 ppm total REE: Duc-Tin and Keppler, 2015). White mica (muscovite–paragonite–phengite solid solutions) and dark mica (biotite-group solid solutions) carry most of the trace elements that define the signature of the LCT pegmatites (e.g. Dahl et al. 1993).

Initial $^{87}Sr/^{86}Sr$ data that might elucidate the source characteristics of pegmatites or the relations of pegmatites with their host rocks are sparse. Peraluminous, beryl- and tourmaline-bearing pegmatites of the Middletown district, Connecticut, gave initial $^{87}Sr/^{86}Sr$ values of 0.743 for mineral separates (Brookins, 1986) and 0.7300–0.790 for whole rock samples from the Hale quarry, Portland (Methot, 1973). Whole-rock $^{87}Sr/^{86}Sr$ values for the Tanco pegmatite, Manitoba are ∼0.81 (Camacho et al., 2012). If nothing else, this smattering of data reflects extremely Rb-rich sources for pegmatites, which would be consistent with their derivation from the same parental materials as are S-type granites.

1.1.1.2 Pegmatites genetic mechanisms

There are two competing models explaining the origin and evolution of pegmatites:

- The *fractional crystallization* model is the most widespread and it considers the extremely differentiated composition of pegmatites as the result of fractional crystallization processes. This interpretation was first proposed during the ‘80s and even if it was refined during the years with new classifications and ideas (e.g. Černý et al. 2005) its core did not change. It is well accepted and is supported by many studies and several examples all over the world (e.g. Elba Island, Tonarini et al., 1998; Pezzotta, 2000 and many others in Černý et al. 2005 and

references therein). This interpretation explains the fact that pegmatites may emplace inside or outside the parent pluton, where, if internally hosted, could have intrusive or gradational contacts with their surroundings. Although well-defined and in some cases exhaustive, this model shows some weaknesses such as:

(i) the lack of field evidence of direct connections between pegmatites and spatially related plutons;

(ii) the "viscosity problem" concerning the ability of extremely evolved felsic melts to travel long distances while remaining mobile and fluid enough to form dikes and masses up to several hundreds of meters from their plutonic source (e.g. Simmons&Webber, 2008);

(iii) the existence of "plutonless" pegmatitic fields that are isotopically incompatible with nearby magmatic masses (Tomascak et al., 1998).

- In the *anatectic* model (e.g. Simmons et al.,1995, 1996; Tomascak et al., 1998; Nabelek et al.,1992a, b; Roda-Robles et al. 1999; Schuster 2017; Ballouard 2020) pegmatitic melts are thought to be formed by low degrees of partial melting of fertile crustal lithotypes (i.e. metapelites) during high temperature metamorphism. Internal fractionation following melt segregation from the source can contribute to produce rare elements-enriched pegmatities. Although this alternative model contributes to explain the formation of pegmatites in geological context where there is no apparent link with larger magmatic masses, the conditions that lead to the generation of anatectic pegmatites are still largely unexplored. This model also shows some weaknesses such as:

  (i) the presence of pegmatites in unmelted host rocks, which needs to be addressed with thorough studies on Li-rich melt mobility;

  (ii) the difficulty of explaining the origin of the Li (and other rare elements) enrichment without extensive fractionation, a question mainly concerning the biggest lithium enriched pegmatites and granites;

  (iii) our incomplete comprehension of which physical and chemical properties concur in determining the expression of pegmatitic textures instead of granitic ones.

1.2 Anatectic rare elements-enriched pegmatites

While the anatectic model is increasingly more accepted for barren pegmatites (i.e. not concentrating rare elements), the case of rare metals-enriched pegmatites is more complex. Although many authors in recent years pointed to an anatectic origin for these mineralized pegmatites, they did not propose a

comprehensive genetic model explaining why and under which conditions (temperature, pressure, fluid regime, geodynamic context) they may have formed.

The fact that Li-enriched pegmatites could also be anatectic has been explored in three main cases: the Mt Mica pegmatite (Simmons, 1995-1996, 2018), the Laxfordian pegmatites (Shaw et al., 2016) and the Austrian Alps pegmatites (Schuster et al., 2017, 2019). The Mt. Mica pegmatite occurs near Paris, Maine, USA in rocks of the Central Maine Belt (CMB) in the northern Appalachians. These bodies intrude stromatic migmatites (Solar & Brown 2001, Solar & Tomascak 2009) consisting of felsic leucosomes of quartz and feldspar and melanosomes of biotite-quartz-feldspar schist with sharp contacts between the pegmatite and melanosomes that become completely gradational between the leucosomes and the pegmatite (Simmons et al., 2018). Nearly the same geological setting is observed in the Australian fold belt by Shaw and co-authors that suggest that all the observed pegmatites in the area may be anatectic in origin. Finally, Schuster et al. suggest that the LCT pegmatites found in the Austrian Alps formed through partial melting of staurolite-bearing metapelites. As highlighted by the most advanced studies in this field, the biggest challenge in this field resides in pinpointing the exact source of the anatectic pegmatitic melt and in explaining their Li and rare elements endowment (e.g. Villaros&Pichavat, 2019), which are not discussed in detail in these works. Our usual inability to identify the source of the anatectic melt hampers our understanding of the range of P-T-H_2O conditions required for the production of Li-rich melt as well as impeding the determination of the chemical characteristics that a potential source must have. Hence, a systematic work defining lithium enrichment from partial melting of crustal rocks is still lacking. In this area we still do not understand if there is a “fertility threshold” for a migmatite in order to produce Li (or other rare elements)-enriched melts and what are the general kinetics,, mineralogical and physical characteristics needed for this enrichment.

1.3 Aim of the PhD project and thesis structure

Rare metal pegmatites are among the most difficult magmatic rocks to study due to their extreme zonation, which can be difficult to sample due to the complexity, coarse-grained texture and size of the magmatic body. Therefore, many studies are focussed on the mineral chemistry of rock-forming and accessory phases. Many studies have investigated the composition of mica and tourmaline as these phases have complex structures that can accommodate many different elements, while in general less attention has been focused on feldspar and quartz.

Whole rock Sr and Nd isotopes are usually useless in old pegmatites since they are enriched in Rb and depleted in Sr, with this feature resulting in large errors on the calculated initial isotopic Sr ratios.

Moreover, in situ isotopic determination on minerals (e.g. boron on tourmaline, lithium on mica), which has been used several times for their less variable behavior compared to whole rock chemistry, was never applied to defining the pegmatites genetic model because the geological context was usually too complex to define. This results in the fact that among the many studies performed on these bodies only few recognize the origin of their pegmatites on the basis of chemical data and not only circumstantial conditions (i.e. the presence of a nearby pluton). In order to create a genetic model for anatectic (rare elements-enriched) pegmatites we therefore need to be able to directly connect a migmatitic terrane to a specific population of pegmatites and the best opportuity to do this may arise where a suitably small-scale pegmatitic field is found in the high-grade thermal aureole of a felsic intrusion. In this case, it would be possible to effectively discriminate the the contribution from the fractionating pluton to the pegmatitic field from the anatectic component of the system. Such of occurrences are rare and in many cases these pegmatites would have been typically attributed to the plutonic intrusion and linked to the internal evolution of the magmatic system.

The choice fell on a geologically complex part of the Adamello massif, situated in Northern Italy, between the Forcel Rosso pass and Mount Ignaga, an area of 20 km^2 (Fig. 1-4, 4-2). Here, a small LCT pegmatitic field is hosted in the thermometamorphosed metapelitic migmatites of the Verrucano Lombardo formation. In addition to this situation, the Adamello pluton hosts a wide set of barren pegmatites having orientations similar to the LCT pegmatites.

The Forcel Rosso - Mount Ignaga pegmatitic field, and particularly the lithium enrichment, which is rare in Italy, was first discovered in 2010 and so far no field and chemical data are available, making this the perfect place for a new study. With the aim of proposing a broad genetic model for these pegmatites, this PhD thesis combines field-based observations, petrography, whole rock geochemistry, conventional geothermobarometry, phase equilibrium simulations (Rcrust, Mayne et al., 2016) as well as U-Pb data and both in-situ and whole rock isotopic analyses. This thesis is structured as a collection of manuscripts that were either published, or are in preparation. These are:

(i) The first paper (chapter 4), which was published in November 2022 in Lithos (*Magnani et al., 2022*) and is focused on the evaluation of the metamorphic conditions experienced by the thermometamorphic aureole of the Adamello pluton.

(ii) The second manuscript (chapter 5), which will be submitted to Earth and Planetary Science Letters during January 2023, is focused on defining the connection between migmatites and LCT pegmatites in order to propose a genetic model for anatectic Li-enriched pegmatites.

(iii) A third manuscript in preparation (in chapter 7), is focused on the chemical and isotopic evolution of tourmaline in the complete Forcel Rosso metamorphic system, from unmetamorphosed rocks to the terminal stages of their anatectic products crystallization.

Finally, chapter 6, delves into the study of Forcel Rosso pegmatitic zircons. The main focus of this chapter is to combine in-situ zircon U-Pb ages to trace element data to further support our interpretations of chapter 5.

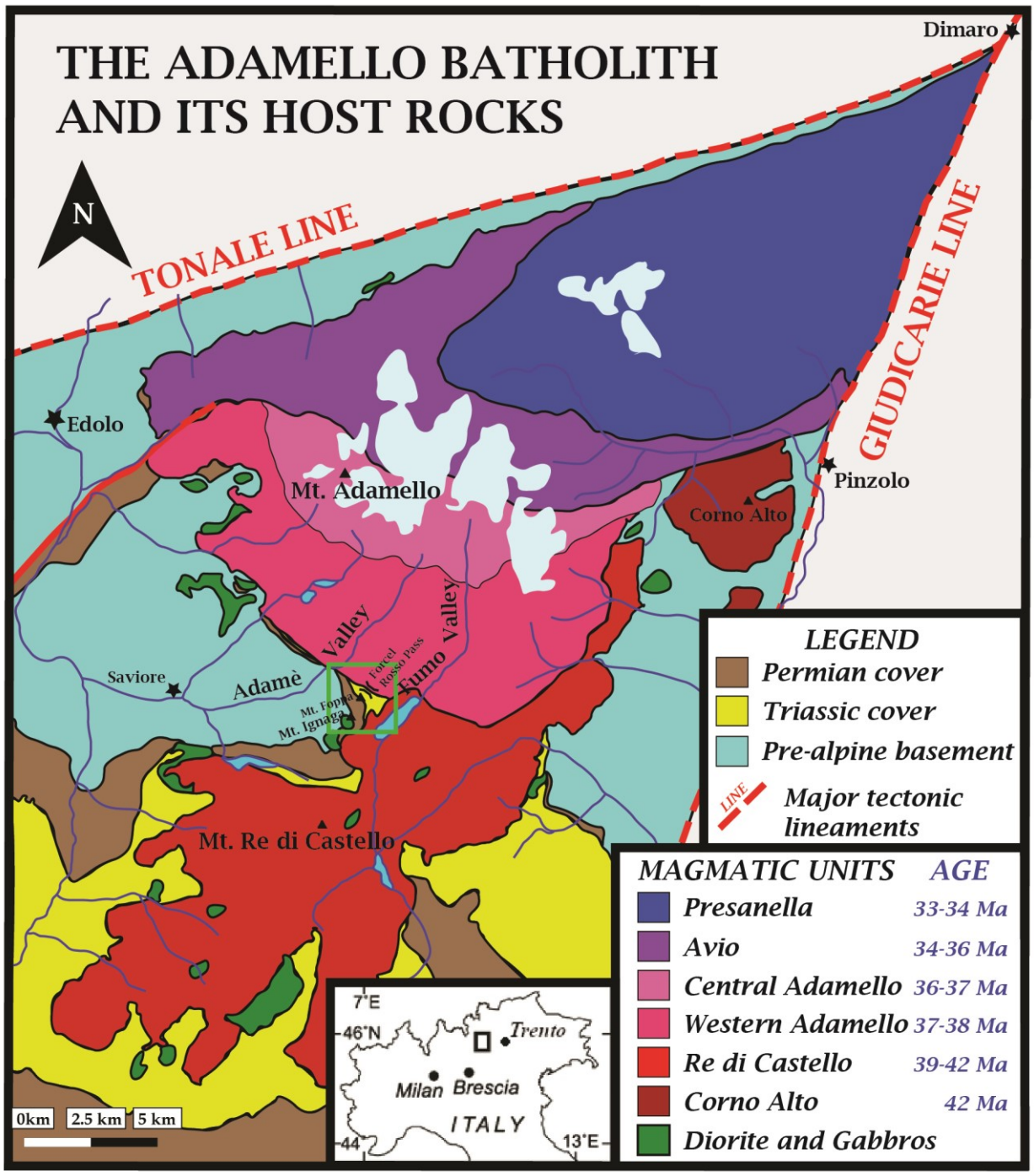

Figure 1-4 Adamello batholith map and area of interest, from Magnani et al., 2022.

References

Ballouard, C., Elburg, M. A., Tappe, S., Reinke, C., Ueckermann, H., & Doggart, S. (2020). Magmatic-hydrothermal evolution of rare metal pegmatites from the Mesoproterozoic Orange River pegmatite belt (Namaqualand, South Africa). Ore Geology Reviews, 116, 103252.

Bea, F., 2012. The sources of energy for crustal melting and the geochemistry of heat-producing elements. Lithos 153, 278–291.

Bebout, G.E., Bebout, A.E., Graham, C.M., 2007. Cycling of B, Li, and LILE (K, Cs, Rb, Ba, Sr) into subduction zones: SIMS evidence from micas in high-P/T metasedimentary rocks. Chem. Geol. 239, 284–304.

Brookins, D. G. (1986). Rubidium-strontium geochronologic studies of large granitic pegmatites. Neues Jahrbuch für Mineralogie. Abhandlungen, 156(1), 81-97.

Camacho, A., Baadsgaard, H., Davis, D. W., & Černý, P. (2012). Radiogenic isotope systematics of the Tanco and Silverleaf granitic pegmatites, Winnipeg River pegmatite district, Manitoba. The Canadian Mineralogist, 50(6), 1775-1792.

Černý, P. (1991). Rare-element granitic pegmatites. Part I: Anatomy and internal evolution of pegmatite deposits. Geoscience Canada, 18(2), 49-67.

Cerný, P. & Ercit, T.S. (2005): Classification of granitic pegmatites revisited. Can. Mineral., 43, 2005-2026.

Černý, P., London, D., & Novák, M. (2012). Granitic pegmatites as reflections of their sources. Elements, 8(4), 289-294.

Černý, P., Chapman, R., Teertstra, D. K., & Novák, M. (2003). Rubidium-and cesium-dominant micas in granitic pegmatites. American Mineralogist, 88(11-12), 1832-1835.

Chappell, B. W., & White, A. J. (2001). Two contrasting granite types: 25 years later. Australian journal of earth sciences, 48(4), 489-499.

Chaves, C., Pereira, E., Ferreira, P., & Dias, A. G. (2021). Concerns about lithium extraction: A review and application for Portugal. The Extractive Industries and Society, 8(3), 100928.

Dahl, P.S., Wehn, D.C., and Feldmann, S.G., 1993, The systematics of trace-element partitioning between coexisting muscovite and biotite in metamorphic rocks from the Black Hills, South Dakota,

USA: Geochimica et Cosmochimica Acta, v. 57, p. 2487–2505, https://doi .org /10 .1016 /0016-7037(93)90412-P.

Dini, A., Lattanzi, P., Ruggieri, G., & Trumpy, E. (2022). Lithium Occurrence in Italy—An Overview. Minerals, 12(8), 945.

Duc-Tin, Q., & Keppler, H. (2015). Monazite and xenotime solubility in granitic melts and the origin of the lanthanide tetrad effect. Contributions to Mineralogy and Petrology, 169(1), 1-26.

ETIP (European Technology and Innovation Platform) on Batteries. Batteries Europe Strategic Research Agenda For Batteries 2020, Supported by the European Commission (2020) https://ec.europa.eu/energy/sites/ener/files/documents/batteries_europe_strategic_research_agenda_december_2020__1.pdf

Fenn, P. M. (1986). On the origin of graphic granite. American Mineralogist, 71(3-4), 325-330.

Grosjean, C., Miranda, P. H., Perrin, M., & Poggi, P. (2012). Assessment of world lithium resources and consequences of their geographic distribution on the expected development of the electric vehicle industry. Renewable and Sustainable Energy Reviews, 16(3), 1735-1744.

Kesler, S. E., Gruber, P. W., Medina, P. A., Keoleian, G. A., Everson, M. P., & Wallington, T. J. (2012). Global lithium resources: Relative importance of pegmatite, brine and other deposits. Ore geology reviews, 48, 55-69.

Kimball, S.J.S.M, U.S. Geological Survey, 2016, Mineral Commodity Summaries 2016, U.S. Geological Survey, Reston, Virginia, January 2016

Linnen, R. L., Van Lichtervelde, M., & Černý, P. (2012). Granitic pegmatites as sources of strategic metals. Elements, 8(4), 275-280.

London, D., 1999. Melt boundary layers and the growth of pegmatitic textures. (abstr.). Can. Mineral. 37, 826–827.

London, D. (2005). Granitic pegmatites: an assessment of current concepts and directions for the future. Lithos, 80(1-4), 281-303.

London, D. (2018). Ore-forming processes within granitic pegmatites. Ore Geology Reviews, 101, 349-383.

Magnani, L., Farina, F., Pezzotta, F., Dini, A., Mayne, M. J., & Bartoli, O. (2022). Role of aqueous fluids during low pressure partial melting of pelites in the Adamello pluton contact aureole (Italy). Lithos, 430, 106853.

Mallik, A., Dasgupta, R., Tsuno, K., Nelson, J., 2016. Effects of water, depth and D. London Ore Geology Reviews 101 (2018) 349–383 381 temperature on partial melting of mantle wedge fluxed by hydrous sediment-melt in subduction zones. Geochim. Cosmochim. Acta 195, 226–243.

Mayne, M. J., Moyen, J. F., Stevens, G., & Kaislaniemi, L. (2016). Rcrust: A tool for calculating path-dependent open system processes and application to melt loss. Journal of Metamorphic Geology, 34(7), 663-682.

Methot, R. L. (1973). Internal geochronologic study of two large granitic pegmatites, Connecticut. Kansas State University.

Nabelek, P. I., Russ-Nabelek, C., & Denison, J. R. (1992a). The generation and crystallization conditions of the Proterozoic Harney Peak leucogranite, Black Hills, South Dakota, USA: petrologic and geochemical constraints. Contributions to Mineralogy and Petrology, 110(2), 173-191.

Nabelek, P. I., Russ-Nabelek, C., & Haeussler, G. T. (1992b). Stable isotope evidence for the petrogenesis and fluid evolution in the Proterozoic Harney Peak leucogranite, Black Hills, South Dakota. Geochimica et Cosmochimica Acta, 56(1), 403-417.

Ottolini, L., Le Fever, B., Vannucci, R., 2004. Direct assessment of mantle boron and lithium contents and distribution by SIMS analyses of peridotite minerals. Earth Planet. Sci. Lett. 228, 19–36.

Palmer, M.R., Swihart, G.H., 1996. Boron Isotope Geochemistry: An Overview. In: Grew, E.S., Anovitz, L.A. (Eds.), Boron; Mineralogy, Petrology and Geochemistry. Mineralogical Society of America Reviews in Mineralogy, 33, pp. 709–744.

Partington, G. A., McNaughton, N. J., & Williams, I. S. (1995). A review of the geology, mineralization, and geochronology of the Greenbushes pegmatite, Western Australia. Economic Geology, 90(3), 616-635.

Robles, E. R., Perez, A. P., Roldan, F. V., & Fontan, F. (1999). The granitic pegmatites of the Fregeneda area (Salamanca, Spain): characteristics and petrogenesis. Mineralogical Magazine, 63(4), 535-558

Schuster, R., Ilickovic, T., Mali, H., Huet, B., & Schedl, A. (2017). Permian pegmatites and spodumene pegmatites in the Alps: Formation during regional scale high temperature/low pressure metamorphism. NGF Abstr. Proc, 2, 122-125.

Schuster, R., Huet, B., Knoll, T., & Paulick, H. (2019). Anatectic origin of albite-spodumene pegmatites: a geochemical model. In Geophysical Research Abstracts (Vol. 21).

Shaw, R. A., Goodenough, K. M., Roberts, N. M. W., Horstwood, M. S. A., Chenery, S. R., & Gunn, A. G. (2016). Petrogenesis of rare-metal pegmatites in high-grade metamorphic terranes: A case study from the Lewisian Gneiss Complex of north-west Scotland. Precambrian Research, 281, 338-362.

Simmons, Wm.B., Foord, E.E., Falster, A.U., King, V.T. (1995): Evidence for an anatectic origin of granitic pegmatites, western Maine, USA. Geol. Soc. Amer. Ann. Mtng., New Orleans, LA, Abstr. Prog., 27, A411.

Simmons, Wm.B., Foord, E.E., Falster, A.U. (1996): Anatectic origin of granitic pegmatites, western Maine, USA. GAC-MAC Ann. Mtng., Winnipeg, Abstr. Prog., A87.

Simmons, W. B. S., & Webber, K. L. (2008). Pegmatite genesis: state of the art. European Journal of Mineralogy, 20(4), 421-438.

Simmons, W. B., Pezzotta, F., Shigley, J. E., & Beurlen, H. (2012). Granitic pegmatites as sources of colored gemstones. Elements, 8(4), 281-287.

Simmons, W., Falster, A., Webber, K., Roda-Robles, E., Boudreaux, A. P., Grassi, L. R., & Freeman, G. (2016). Bulk composition of Mt. Mica pegmatite, Maine, USA: Implications for the origin of an LCT type pegmatite by anatexis. The Canadian Mineralogist, 54(4), 1053-1070.

Simmons, W. B., Webber, K. L., Falster, A. U., & Roda-Robles, E. (2018). Post-orogenic, prerifting anatectic origin of the Oxford Co., Maine, USA pegmatite field. In XXII International Mineralogical Association meeting at: Melbourne, Australia. Book of Abstracts (Vol. 288).

Solar, G. S., & Brown, M. (2001). Petrogenesis of migmatites in Maine, USA: possible source of peraluminous leucogranite in plutons?. Journal of Petrology, 42(4), 789-823.

Solar, G. S., & Tomascak, P. B. (2009). The Sebago pluton and the Sebago Migmatite Domain, Southern Maine: results from new studies. In 2009 Annual Meeting of Northeastern Section, Geological Society of America, Field Trip (Vol. 2, pp. 1-24).

Swain, B. (2017). Recovery and recycling of lithium: A review. Separation and Purification Technology, 172, 388-403.

Tomascak, P. B., Krogstad, E. J., & Walker, R. J. (1998). Sm-Nd isotope systematics and the derivation of granitic pegmatites in southwestern Maine. The Canadian Mineralogist, 36(2), 327-337.

Villaros, A., & Pichavant, M. (2019). Mica-liquid trace elements partitioning and the granite-pegmatite connection: The St-Sylvestre complex (Western French Massif Central). Chemical Geology, 528, 119265.

Chapter 2

Geological setting and mapping

The geological setting described in this paragraph is common to the presented manuscripts. I intend this paragraph as a recollection of all the geological background information for the Forcel Rosso area needed to understand this complex zone of the Adamello Massif (Southern Alps in central northern Italy).

2.1 Tectonic evolution of the Central Southern Alps

The Alpine chain is divided in three main domains by regional lineaments: i) the Pennidic domain in the north, ii) the Austroalpine domain in the axial region of the chain and iii) the South Alpine domain (or Southern Alps) in the south. The Southern Alps represent the south-verging retro-belt of the Alps (Montrasio et al., 1994; Carminati et al., 1997; Schmid et al., 2000) and this domain is sharply separated from the Austroalpine domain by the E-W trending Periadriatic Lineament (Schmid et al.1989). This fault branches out in several roughly N-S trending smaller faults that crosscut the Paleozoic successions, reactivating Lower Permian faults, which were exploited by the emplacement of intermediate to felsic magmatic masses in the Paleogene, among which the Adamello batholith is the largest (Fig. 2-1; e.g Stipp et al., 2004). The presence of the Adamello batholith and other periadriatic intermediate to felsic granitoids in Northern Italy (e.g. the Bergell pluton) is a direct consequence of the collision between the European and African tectonic plates during the Alpine orogeny in the Eocene-Oligocene.

2.2 The Paleozoic succession and pre-intrusion metamorphic conditions

During the Early Permian, the central southern Alpine area was characterized by the development of fault-controlled extensional basins where thick successions of calc-alkaline pyroclastics products, lava flows and vulcanosedimentary deposits alternated with continental clastics deposits (Berra and Felletti, 2011). These basins, which are largely unmetamorphosed in the Southern Alps, continued their subsidence during the rest of the Paleozoic and Mesozoic and were filled up by marine sediments (Cassinis et al. 2012), reaching a maximum thickness of up to 4000 m (Athesian basin; Marocchi et al. 2008) and more than 1000m in the study area (Berra and Felletti, 2011). The sedimentary succession found in the Forcel Rosso was originally part of a fault-controlled system of extensional basins that developed during the Early Permian in the central Southern Alps and it corresponded to a structural

high characterized by very limited deposition of volcanic rocks and by slightly reduced sedimentary input (Sciunnach et al. 1996).

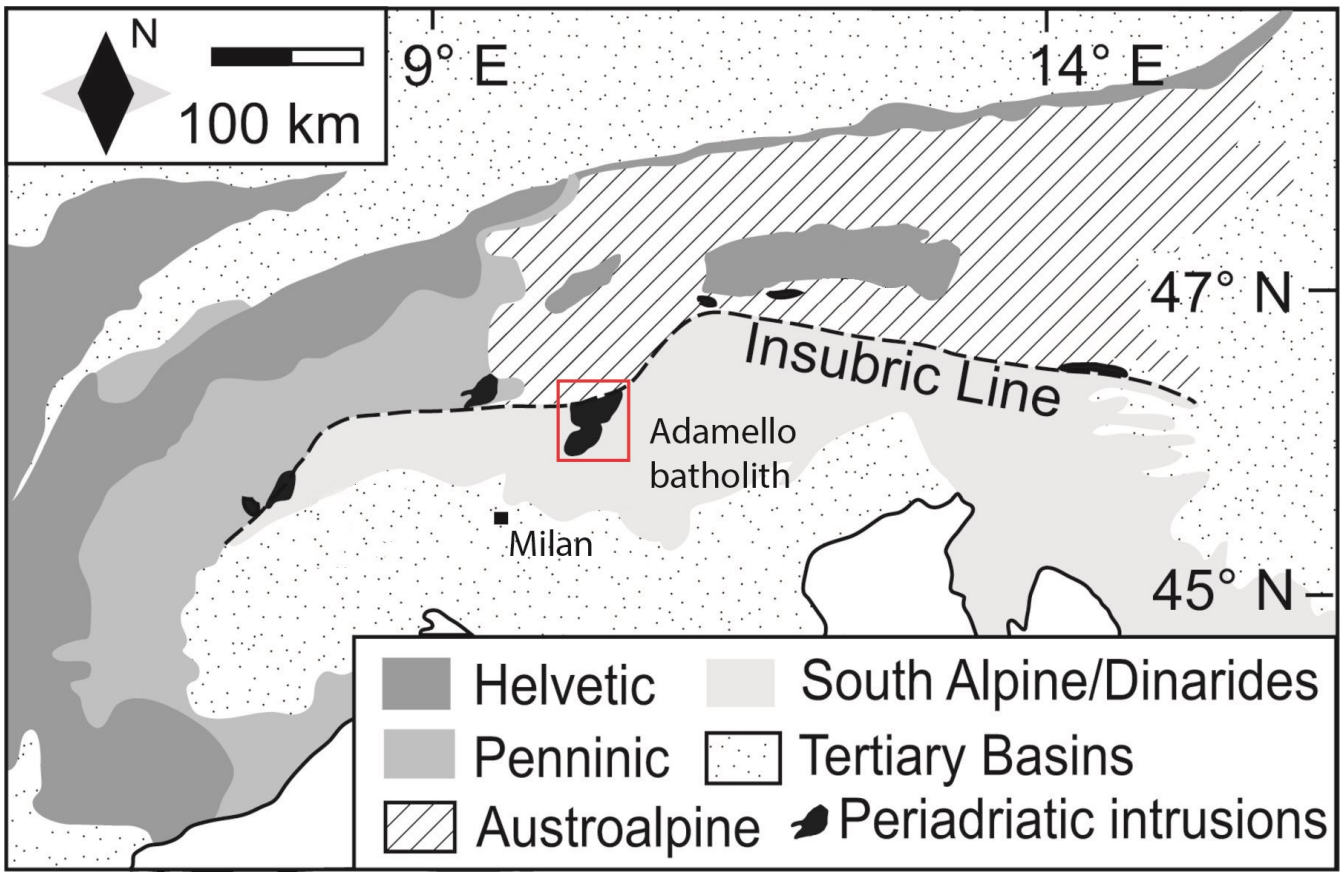

Figure 2-1 Map of the Periadriatic intusions, Adamello batholith highlighted in red, modified from Tiepolo et al., 2014

In the area, ten stratigraphically distinct sedimentary formations can be identified above the Variscan basement, which was also intruded by the Adamello batolith. The oldest sedimentary unit is represented by the clastic continental fluvial fan deposits of the Verrucano Lombardo formation (VER) that reach up to 400m in thickness and is mainly composed of Variscan basement-derived arenaceous, pelitic and conglomeratic material. The Verrucano Lombardo sedimentation was abruptly halted by a late Permian marine transgression that submerged the continental fan and promoted the deposition of a sequence of alternating carbonatic and low energy pelitic layers constituting the Servino fm. (SRV, e.g. Assereto et al., 1973, Sciunnach et al., 1996). The oscillating sea level caused the subsequent deposition of a thick evaporitic layer (Carniola di Bovegno fm., BOV), and then, when the transgression stabilized, the sedimentation of neritic limestones (Calcare di Angolo fm., ANG, and Calcare di Prezzo fm., PRZ) in largely anoxic marine environments and late pelagic limestones and cherts (Wengen fm. and Buchenstein fm.). On the top of these units stand the products of a period of marine regression marked by the Pratotondo limestone and subsequent Lozio shale and Breno formation. This sedimentary succession (Fig. 2-2) was not involved in the Alpine regional

metamorphism, as it is part of the South-Alpine tectonic block south of the Giudicarie Line (e.g. Zanchetta et al., 2015) but was intruded during the Tertiary by the Adamello batholith that metamorphosed the sedimentary sequence to hornfels.

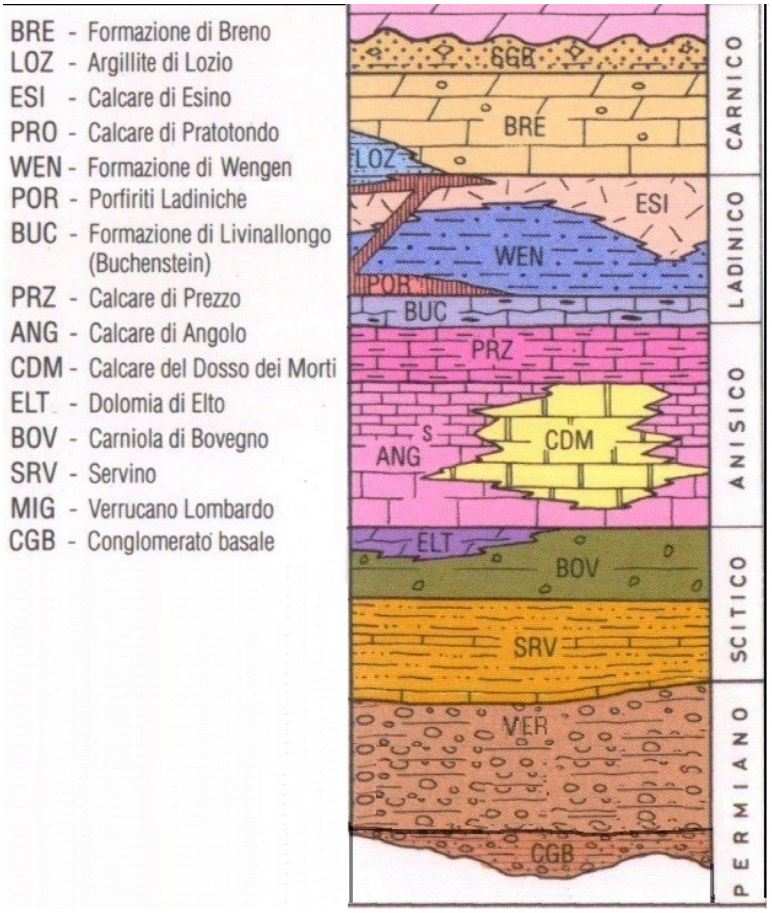

Figure 2-2 Collio basin sedimentary succession, modified from Callegari et al., 1998.

The unmetamorphosed Verrucano Lombardo Formation (VER) in the Forcel Rosso area is mainly composed of unfossiliferous conglomeratic to arenaceous red beds that continuously grade into each other containing rounded quartz clasts and basement rocks fragments of metamorphic origin. The basal fluvial conglomerates are covered by sandstones and poorly selected siltstones that constitute one-third of the total Verrucano Lombardo formation thickness (Massari&Cadel, 1977). The pelitic rocks, which are central to this work, are badly classed silts made of ca. 55 vol% qtz, 30 vol% clay minerals and muscovite, 12 vol% feldspars, 3 vol% Fe-oxides (Riklin, 1983).

The main Al-rich phases are represented by sedimentary and diagenetic clay minerals, occupying the interstices between grains or overgrowing them as well as by detrital muscovite. Accessory minerals are tourmaline, hematite, detrital zircon, monazite, apatite and rutile. The area experienced severe shortening events during the Alpine orogeny that determined its fold-and-thrust belt structure but was not affected by regional metamorphism (Schönborn, 1992; Jadoul and Forcella, 2000; Carminati, 2009). Because of this, the plutons forming the Adamello Massif intruded a widely folded, thick-skinned sedimentary block that was locally deformed by the batholith's emplacement. The ambient conditions of the Paleozoic succession prior to the emplacement of the batholith were 2-4 kbar (Blundy&Sparks, 1992) and 250 °C (Pennacchioni et al. 2006). The temperature was constrained by

zircon fission-track data obtained from basement rocks (Viola et al. 2001) and is consistent with estimates of illite crystallinity from Permian sandstones (Riklin 1983). Pressure estimates, which are relatively poorly constrained, were obtained through Al-in-hornblende geobarometry applied to different units of the Adamello batholith (Blundy&Sparks, 1992).

2.3 The Adamello batholith

The Adamello batholith is the largest of the Tertiary Periadriatic plutons and was emplaced at 6-10 km depth (Broderick et al., 2015) in the central Southern Alps during the Eocene-Oligocene. The pluton was originally divided into 5 units, but recently Schaltegger et al. (2019) proposed a new subdivision of the batholith recognizing seven main units based on chemical, geochronological and structural observations (Fig. 1-3): the Presanella, Avio, Central and Western Adamello, Re di Castello (north and south) and Corno Alto units. This pre- to syn-collisional batholith is composed of an association of tonalites, granodiorites and quartz-diorites with minor mafic units in the southernmost part of the batholith (Brack 1983; Callegari and Brack 2002) bearing textural and chemical similarities with plutonic rocks formed in a continental magmatic arc setting (McCarthy et al., 2018). The rocks of the Adamello massif show a distinct compositional similarity to volcanic rocks of equivalent SiO_2 content from calc-alkaline suites of continental margins (Dupuy et al., 1982). Variation trends of major and trace elements generally resemble trends generated by fractional crystallization dominated by plagioclase and to a smaller degree by amphibole and pyroxene. Overall, the Adamello plutons show a sequential emplacement from the oldest units in the south (Re di Castello pluton, RdC, ~43 Ma) to the youngest in the north (Avio pluton, ~30 Ma; Del Moro et al., 1985, Schaltegger et al., 2019). Strontium isotope ratios ($^{87}Sr/^{86}Sr$) increase from 0.7036 in the south to 0.7120 in the north (Del Moro et al, 1983a; Blundy, 1989) indicating that contamination by radiogenic upper-crustal strontium increased with time, becoming most significant in the youngest, northernmost plutons. A smaller body of Nd isotope data (Kagami et al., 1991) shows a complementary northwards decrease in $^{143}Nd/^{144}Nd$. These isotopic and major element compositional data are consistent with a model in which the Adamello granitoid rocks formed from mantle-derived hydrous magmas through a combination of fractional crystallization and assimilation of crustal material (Kagami et al, 1991). Brack (1983) argued that the RdC intruded by a combination of ‘‘passive’’ processes involving stoping and block rotation to more ‘‘forceful’’ intrusive processes that deformed the surrounding host rocks. Blundy (1989) observed that the RdC pluton evolved as a series of concentric diapiric pulses of quartz-gabbro to tonalite in composition, each pulse deforming its partially consolidated envelope and that strain analysis are compatible with a model of ballooning emplacement. While there has been syn-

emplacement deformation of the northernmost intrusive Adamello units along the dextral Tonale line (Bianchi et al. 1970, Werling 1992), there is no clear evidence for Eocene to Oligocene movement along the sinistral Giudicare Line (Brack, 1983, Castellarin&Sartori 1983, Laubscher 1990) showing that the intrusion was mostly undisturbed by Alpine deformation.

2.4 The Adamello batholith contact metamorphic aureole

Most of the country rocks (ca. 90%) surrounding the Adamello batholith exhibit evidence of contact metamorphism within the ca. 1 km to 4 km thick thermal aureole (Callegari and Brack, 2002). The first works focused on contact metamorphosed rocks surrounding the batholith were carried out at the end of the 20th century by Salomon (e.g. Salomon, 1894) and since then other works have been published (e.g. Lorenzoni, 1955; Zanettin, 1956; Riklin, 1983; Floess and Baumgartner, 2013, 2015). The first two papers focused on the Corno di Bos area, on the opposite flank of the valley of the studied Forcel Rosso area, where they found evidences of high temperature metamorphism and formation of sillimanite, corundum and cordierite at the contact between the host metapelites and pluton. The larger scale contact metamorphism in the Forcel Rosso-Mount Ignaga area was studied by Riklin (1983) in the siliciclastic sequences of the Permian Verrucano Lombardo formation, while more recently, Floess&Baumgartner (2013, 2015) described the metamorphic thermal overprint in the pre-Alpine Variscan metapelitic basement as well as cryptic evidence of partial melting in the Triassic metacarbonates and metaevaporites. In the Verrucano Lombardo formation, according to the research of Riklin (1983), the first effect of contact metamorphism is observed in the values of illite crystallinity, particularly in pelitic lithotypes. Because of this process, the typically reddish clastics lithologies of the Verrucano Lombardo formation become dark violet in the outermost contact area, and then grey upon the first appearance of biotite in the inner parts of the aureole. Temperatures at the magmatic contact between the Adamello pluton and the Permo-Mesozoic sedimentary succession, in the Lozio Shales (LOZ), reached up to 815°C (Floess & Baumgartner, 2015) while in the mid-sequence Bovegno Carniole the temperature is inferred to have reached over 670°C (Floess & Baumgartner, 2015). Because of the steep contact thermal gradient, the underlying and older conglomerates of the Verrucano Formation, of which the pelitic succession is part of, and of the Collio Formation experienced comparably lower temperature metamorphism. Their mica-poor mineral composition prevented them from melting and influencing the local anatectic processes.

2.5 Geological mapping and survey results

2.5.1 Field campaigns

Since the Forcel Rosso area is part of the Adamello-Brenta National Geopark, a collaboration between the University of Milan and the Adamello National Geopark was established giving us permission to conduct sampling and surveying.

The fieldwork was articulated in four stages:

- Survey trip (duration 3 days), September 2019, during which the co-supervisor of this PhD project Dr. Federico Pezzotta, curator of the Museo di Scienze Naturali di Milano, showed us the main features of the Forcel Rosso area as well as excellent samples of LCT pegmatites containing elbaite, lepidolite and pyroclore collected in previous field trips. Limited sampling was subsequently carried out aiming to collect a small number of samples that encompassed the great variability of rocks found between the Forcel Rosso pass and Mount Ignaga.

Figure 2-3 Panoramics of the Forcel Rosso area from the Rifugio Lissone.

This first survey was important to start the project because due to the high elevation of the site (altitude comprised between 2000 and 2700m above sea level, Fig. 2-3) the area is only accessible for a short period each year (July-end of September). One day was spent collecting unmetamorphosed Verrucano Lombardo and Servino formations rock samples from pelites. These samples were collected in the same stratigraphic positions of the metamorphosed samples to observe and quantify the effects of metamorphism on the pelitic rocks.

- Field campaign 1 (duration 8 days), July 2020, in which the most part of the sampling and surveying was carried out. This campaign produced all the base data needed for drawing the 1:5000 scale geological map including GPS points, orientation measures of geological structures and geological relations and correlations between rocks. We also obtained a near complete sampling of the contact metamorphosed Verrucano Lombardo and Servino formations (the pegmatites host rocks) and of the LCT and barren pegmatites in every different geological context they were emplaced. The LCT pegmatites were studied in detail and their internal zonation was understood and documented with in situ sampling and photos details.
- Field campaign 2 (duration 6 days), August-September 2020, focused on completing the sampling, surveying complex areas of the map and defining the lithological heterogeneity of the Verrucano Lombardo formation.

2.5.2 New Findings

The geological survey produced a complete geological map of the Forcel Rosso-Mount Ignaga area of the Adamello massif which has been used for all manuscripts produced in this PhD thesis (Fig. 4-2, chapter 4). During the survey, a much wider set of pegmatites than it was previously known (and mapped in the 1:50000 scale geological maps) was discovered in the area showing that these magmatic bodies are here hosted in the Verrucano Lombardo formation, the Adamello pluton and the Variscan basement. The ones hosted in the Verrucano metapelites are the most evolved and Li-enriched: they will be the main focus of this thesis and will be described in detail in the next chapters.

During geological mapping we observed that the progression of the metamorphic facies is oblique to the Verrucano Lombardo formation's dip and, as expected, radiates directly away from the Adamello pluton. The metasedimentary succession is N-E trending and nearly verticalized, with inclination ranging from 65 to 80°, in the study area. The Adamello Tonalite cuts the bedding at a low angle, obliterating all the formations overlying the Verrucano Lombardo at the bottom of the Adamè Valley while leaving a seemingly undisturbed metasedimentary sequence forming the mountain ridge between the Adamè and Fumo valleys. The juxtaposition of the sedimentary sequence and the Western

Adamello Tonalite is generated at the Forcel Rosso pass by exploiting an E-W trending subvertical normal fault. This was reported in the Callegari and Brack (2002) geological map and was confirmed and better defined during the geological survey activity of this study which links it to the emplacement of the Adamello pluton. This fault is well expressed between the Forcel Rosso Pass and the "Forcellino" Pass dislocating the upper part of the Paleozoic succession generating a tectonic contact between the Angolo limestone (ANG) and the Pratotondo Limestone (PRT), eliding from the Adamè Valley eastern flank the Prezzo Limestone (PRZ), the Buchenstein formation (BUC) and the Wengen formation (WEN). The fault remains covered by landslide products on the slope and reappears on the valley bottom putting in direct contact the Western Adamello Tonalite and the Bovegno Carniole (BOV) and ultimately the WAT with the Verrucano Lombardo formation. The strain field present during the metamorphic and magma intrusion event was near vertically oriented, with compression toward the south caused by the intrusion.

References

Assereto, R., Sestini, N. F., Bosellini, A., & Sweet, W. C. (1973). The Permian-Triassic boundary in the Southern Alps (Italy).

Berra, F., & Felletti, F. (2011). Syndepositional tectonics recorded by soft-sediment deformation and liquefaction structures (continental Lower Permian sediments, Southern Alps, Northern Italy): stratigraphic significance. Sedimentary Geology, 235(3-4), 249-263.

Bianchi, A., Callegari, E., Jobstraibizer, P. G., & Consiglio nazionale delle ricerche (Italia). Centro di studio per la geologia e la petrografia delle formazioni cristalline. (1970). I tipi petrografici fondamentali del plutone dell'Adamello: tonaliti, quarzodioriti, granodioriti e loro varietà leucocrate. Società cooperativa tipografica.

Blundy, J. D. (1989). The geology of the southern Adamello Massif, Italy (Doctoral dissertation, University of Cambridge).

Blundy, J. D., & Sparks, R. S. J. (1992). Petrogenesis of mafic inclusions in granitoids of the Adamello Massif, Italy. Journal of Petrology, 33(5), 1039-1104.

Brack, P. (1983). Multiple intrusions-examples from the Adamello batholith (Italy) and their significance on the mechanisms of intrusion. Memorie della Societa Geologica Italiana, 26(1), 145-157.

Broderick, C., Wotzlaw, J. F., Frick, D. A., Gerdes, A., Ulianov, A., Günther, D., & Schaltegger, U. (2015). Linking the thermal evolution and emplacement history of an upper-crustal pluton to its lower-crustal roots using zircon geochronology and geochemistry (southern Adamello batholith, N. Italy). Contributions to Mineralogy and Petrology, 170(3), 1-17.

Callegari, E., Dal Piaz, G., & Trommsdorff, V. (Eds.). (1998). Carta geologica del gruppo Adamello-Presanella. Consiglio nazionale delle ricerche.

Callegari, E., & Brack, P. (2002). Geological map of the tertiary Adamello batholith (northern Italy). Explanatory notes and legend. Mem Sci Geol, 54, 19-49.

Carminati, E. (2009). Neglected basement ductile deformation in balanced-section restoration: An example from the Central Southern Alps (Northern Italy). Tectonophysics, 463(1-4), 161-166.

Carminati, E., Siletto, G. B., & Battaglia, D. (1997). Thrust kinematics and internal deformation in basement-involved fold and thrust belts: The eastern Orobic Alps case (Central Southern Alps, northern Italy). Tectonics, 16(2), 259-271.

Cassinis, G., Perotti, C. R., & Ronchi, A. (2012). Permian continental basins in the Southern Alps (Italy) and peri-mediterranean correlations. International Journal of Earth Sciences, 101(1), 129-157.

Castellarin, A., & Sartori, R. (1983). Il sistema tettonico delle Giudicarie, della Val Trompia e del sottosuolo dell'alta pianura lombarda. Memorie della Societa Geologica Italiana, 26(1), 31-37.

Del Moro, A., Pardini, G. C., Quercioli, C., Villa, I. M., & Callegari, E. (1983). Rb/Sr and K/Ar chronology of Adamello granitoids, southern Alps. Memorie della Società Geologica Italiana, 26(1), 285-299.

Del Moro A., Ferrara G., Pescia A., Callegari E. (1985) A geochemical study on the acid and basic rocks of the Adamello batholith. Mem. Soc. Geol. It., 1985.

Dupuy, C., Dostal, J., Marcelot, G., Bougault, H., Joron, J. L., & Treuil, M. (1982). Geochemistry of basalts from central and southern New Hebrides arc: implication for their source rock composition. Earth and Planetary Science Letters, 60(2), 207-225.

Floess D., Baumgartner L.P., Vonlanthen P. (2015) An observational and thermodynamic investigation of carbonate partial melting. Earth and Palentary Science Letters 409, 147-156.

Floess, D., & Baumgartner, L. (2013). Formation of garnet clusters during polyphase metamorphism. Terra Nova, 25(2), 144-150.

Floess D., Baumgartner L.P. (2015) Constraining magmatic fluxes through thermal modelling of contact metamorphism. From: Caricchi L., Blundy J.D. (eds) Chemical, Physical and Temporal Evolution of Magmatic Systems. Geological Society, London, Special Publications 422.

Forcella, F., & Jadoul, F. (2000). Carta Geologica della Provincia di Bergamo a scala 1: 50.000 (Geological Map of the Bergamo Province, scale 1: 50.000). Bergamo: Grafica Monti.

Kagami, H., Ulmer, P., Hansmann, W., Dietrich, V., & Steiger, R. H. (1991). Nd-Sr isotopic and geochemical characteristics of the southern Adamello (northern Italy) intrusives: Implications for crustal versus mantle origin. Journal of Geophysical Research: Solid Earth, 96(B9), 14331-14346.

Laubscher, H. (1990). Material balance in Alpine orogeny.

Lorenzoni S. (1955). Studio geologico-petrografico dell'Alpe di Bos (Adamello occidentale). Società Cooperativa Tipografica.

Marocchi, M., Morelli, C., Mair, V., Klötzli, U., & Bargossi, G. M. (2008). Evolution of large silicic magma systems: new U-Pb zircon data on the NW Permian Athesian Volcanic Group (Southern Alps, Italy). The Journal of Geology, 116(5), 480-498.

Massari, F., Cadel G. (1977). La successione continentale permiana del Monte Ignaga nel massiccio dell'Adamello.

McCarthy, A., Chelle-Michou, C., Müntener, O., Arculus, R., & Blundy, J. (2018). Subduction initiation without magmatism: The case of the missing Alpine magmatic arc. Geology, 46(12), 1059-1062.

Montrasio, A., Bersezio, R., Forcella, F., Jadoul, F., Sciesa, E., & Motrasio, A. (1994). Geological interpretation of the profile crop-central alps (passo spluga-bergamo). In Proc. Symp. CROP-Alpi Centrali, Sondrio 20–22 Oct. 1993, Quad. Geodinam. Alpina e Quat. (Vol. 2, pp. 171-186).

Pennacchioni, G., Di Toro, G., Brack, P., Menegon, L., & Villa, I. M. (2006). Brittle–ductile–brittle deformation during cooling of tonalite (Adamello, Southern Italian Alps). Tectonophysics, 427(1-4), 171-197.

Riklin, K. (1983). Contact metamorphism of the permian «Red Sandstone» in the Adamello area. Memorie della Società Geologica Italiana, 26(1), 159-169.

Salomon W. (1894) Sul metamorfismo di contatto, subito dalle arenarie permiane della Val Daone. Giorn. Mineral., Cristallogr., Petrogr., 5, Tipogr. Fusi, Pavia, 97-147.

Schaltegger, U., Nowak, A., Ulianov, A., Fisher, C. M., Gerdes, A., Spikings, R., ... & Müntener, O. (2019). Zircon petrochronology and 40Ar/39Ar thermochronology of the Adamello Intrusive Suite, N. Italy: monitoring the growth and decay of an incrementally assembled magmatic system. Journal of Petrology, 60(4), 701-722.

Schmid, S. M., Aebli, H. R., Heller, F., & Zingg, A. (1989). The role of the Periadriatic Line in the tectonic evolution of the Alps. Geological Society, London, Special Publications, 45(1), 153-171.

Schmid, S. M., & Kissling, E. (2000). The arc of the western Alps in the light of geophysical data on deep crustal structure. Tectonics, 19(1), 62-85.

Schönborn, G. (1992). Kinematics of a transverse zone in the Southern Alps, Italy. In Thrust tectonics (pp. 299-310). Springer, Dordrecht.

Sciunnach, D., Garzanti, E., & Confalonieri, M. P. (1996). Stratigraphy and petrography of Upper Permian to Anisian terrigenous wedges (Verrucano Lombardo, Servino and Bellano formations; western southern Alps). Rivista Italiana di Paleontologia e Stratigrafia, 102(1).

Stipp, M., Fügenschuh, B., Gromet, L. P., Stünitz, H., & Schmid, S. M. (2004). Contemporaneous plutonism and strike-slip faulting: A case study from the Tonale fault zone north of the Adamello pluton (Italian Alps). Tectonics, 23(3).

Tiepolo, M., Tribuzio, R., Ji, W. Q., Wu, F. Y., & Lustrino, M. (2014). Alpine Tethys closure as revealed by amphibole-rich mafic and ultramafic rocks from the Adamello and the Bergell intrusions (Central Alps). Journal of the Geological Society, 171(6), 793-799.

Viola, G., Mancktelow, N. S., & Seward, D. (2001). Late Oligocene-Neogene evolution of Europe-Adria collision: New structural and geochronological evidence from the Giudicarie fault system (Italian Eastern Alps). Tectonics, 20(6), 999-1020.

Werling, E. (1992). Tonale-, Pejo-und Judicarien-Linie: Kinematik, Mikrostrukturen und Metamorphose von Tektoniten aus räumlich interferierenden aber verschiedenaltrigen Verwerfungszonen (Doctoral dissertation, ETH Zurich).

Zanchetta, S., Malusà, M. G., & Zanchi, A. (2015). Precollisional development and Cenozoic evolution of the Southalpine retrobelt (European Alps). Lithosphere, 7(6), 662-681.

Zanettin B. (1956). Il gruppo del Marsèr, Adamello occidentale: studio geologico-petrografico. Centro Studi di Petrografia e Geologia del Consiglio Nazionale delle Ricerche presso l'Università di Padova.

Chapter 3

Analytical methods

I have collected 50 samples subdivided between pegmatites (25 samples), metasedimentary rocks (20 samples) and magmatic rocks (5 samples) from which were produced powders and mineral separates. In order to analyze these samples I developed and applied two new techniques that are now standardized at the Geochemistry, Geochronology and Isotope Geology laboratory of the Earth Science Department, Università degli Studi di Milano (Italy), the PPP technique (3.1) and the In-situ boron isotopes on tourmaline (3.3). I also participated in the analytical preparation of my samples at the IGG-CNR of Pisa for Sr-Nd isotopic analyses (3.2).

3.1 Development of PPP LA-ICP-MS whole rock analysis technique

The whole rock major and trace element composition, comprising Li and B, was determined on Pressed Powder Pellets adapting the method recently proposed by Peters and Pettke (2017) to our needs and to the instruments available in the department of Earth Sciences of the University of Milano. The advantage of this method consists in the possibility to determine major and trace elements at the same time as well as in the possibility to determine also the content of Li and B. During my thesis I spent a few months setting up this method.

The original method is based on the wet pulverization of samples under 1µm particle size in a RETSCH PM100 planetary mill allowing for rotation sense inversion and subsequent hand-mixing of microcellulose binder to the micronized powder in order to form resistant and homogeneous pellets that can be analyzed using LA-ICP-MS techniques. The method used in the analyses presented in this thesis were developed between December 2020 and March 2021 had to deal with several concerns, among which the major one was the lack of a modern Retsch PM100 planetary mill which can routinely pulverize rock samples to uniform powders under 1µm. This threshold is very important for the outcome of the LA-ICP-MS major and trace elements determinations as it ensures the laser spot volume is representative of the pellets, and therefore sample, composition. The problem was overcome by using 3mm agate spheres in the 50ml jars avalaible in the department instead of the 7mm ones used by the Retsch PM100. This ensured the production of a suitable submicrometric powder for analyses without significant added contamination. The original method was further modified to make it faster and more user-friendly by intruducing wet milling of the samples with cellulose already in the agate

jars, eliminating the time-consuming step of mixing sample and cellulose, which often caused problems of pellet dishomogeneity in case it was not carried out to perfection.

Major and trace element concentrations were determined by LA-ICP-MS on the pressed powder pellets (PPP) at the Geochemistry, Geochronology and Isotope Geology laboratory of the Earth Science Department, Università degli Studi di Milano (Italy). The instrument couples an Analyte Excite 193 nm ArF excimer laser microprobe system equipped with a double volume chamber cell HelEx II (Teledyne Cetac Technologies) to a single-quadrupole ICP-MS (iCAP-RQ, Thermo Fisher Scientific). Wet milling was performed in a planetary mill without the possibility of inverting the sense of rotation so, keeping the same milling proportions, the 36g of 7mm agate spheres used by Peters&Pettke (2017) were substituted with 36g of 3mm agate spheres, which gave better results in terms of particle size while not causing additional contamination. 0.8g of sample powder were directly placed in 50-ml size agate jars together with 0.2g of Merck microcrystalline cellulose as binder. Cellulose was, in this procedure, mixed directly with the sample during wet milling as to eliminate the need of homogeneization during pelletization, thus producing more homogeneous pellets in less time. About 5.6g of ultra-pure water (MilliQ Pore) were added to the mixture together the agate spheres. The mixture was milled in 4 repetitions of 10 minutes with a step pause of 5 minutes between each run to avoid excessive heating. This setup ensures a final homogenized powder with ultrafine particle (close to 1µm) ready for pressing. After drying overnight at T ~ 100 °C, ca. 200 mg of powder mixture were pressed using a half-inch die at 10 ton for 10 minutes. The resulting PPP were ~13 mm in diameter and 1.0mm thick with very good cohesiveness allowing for easy handling in the LA-ICP-MS system. Laser beam size was set at 85µm diameter on PPP in order to avoid overloading of the plasma with aerosol particle that may decrease ionization efficiency and amplify potential fractionation effects (e.g. Kroslakova and Gunther, 2007; Peters and Pettke, 2017), whereas spot size of 50µm was chosen on GSD-2G and ARM-3 glasses. Six spots of 85µm were measured on each pellet at 10 Hz repetition rate, using fluence values from 3 to 4 J/cm^2. The data were treated using SILLS (Guillong et al., 2008) and normalized to the international glass standard GSD-2G. The USGS GSD-2G, a synthetic basaltic reference glass was used as external standard to minimize matrix effects between glass and pellets (Peters and Pettke, 2017). The internal standardization was done by summing the measured mass fractions of major and minor element oxides to 100% minus loss of ignition (LOI) determined ca. 1000°C. Final concentrations were obtained by averaging the six analyses performed on each sample. The RSD% values for major element data are all under 2% while trace elements data are always under 10%. Reported final data are the mean of 6 spot analyses and the error is expressed as their standard deviation (1σ). Accuracy was checked by repeated analysis of international reference materials SDC-1,

BHVO-1, UB-N and MA-N that were prepared and analyzed in the same way as the unknowns. At least two international standards were characterized on every run to constrain accuracy. Accuracy error rates are under 5% for all major elements and under 10% for all trace elements except Vanadium, which is under 20%.

3.2 Sr-Nd whole rock isotopic determination

Radiogenic Sr and Nd isotopic analyses of 10 selected samples were performed using a Thermo Fisher Neptune Plus MC-ICP-MS at the Istituto di Geoscienze e Georisorse - CNR in Pisa (Italy) in 2% HNO3 solution containing 20-200ng*g-1 of analyte. The instrument was equipped with a combined cyclonic and Scott-type quartz spray chamber, Ni-cones and a MicroFlow PFA 100µl/min self-aspiring nebuliser. Rock powders were leached with strong HCl (6.6 N for half an hour at ≈ 80 °C) to cut off any effect of secondary minerals, and then rinsed 5 times with ultrapure water. Subsequently, samples were digested in a concentrated Ultrapur HF+HNO3, dried and brought again into solution, then subdivided into two aliquots, one in diluted HNO3 and one in diluted HBr. Sr was then separated from HNO3 solution using Sr-Spec resin, Nd was separated from the same aliquot trough a two-step procedure with TRU-spec and Ln-Spec resins, whereas Pb was collected starting from the portion diluted in HBr after separation with AG50W-X8 resin. (Agostini et al., 2022)

Sr analyses were corrected for mass bias fractionation using the $^{88}Sr/^{86}Sr$ ratio (8.375209) and for Kr and Rb mass interferences using the ratios $^{83}Kr/^{84}Kr$ (0.201750), $^{83}Kr/^{86}Kr$ (0.664740) and $^{85}Rb/^{87}Rb$ (2.592310). Eight repeated analyses of standard NIST SRM 987 gave a result of 0.710348 ± 16. Results were adjusted to a ratio of 0.710248.

Instrumental mass fractionation during Nd analyses was corrected using the $^{146}Nd/^{144}Nd$ ratio (0.7219). Mass interference of ^{147}Sm was corrected using the ratios $^{147}Sm/^{144}Sm$ (4.838710), and $^{147}Sm/^{148}Sm$ (1.327400). Three analyses of $^{143}Nd/^{144}Nd$ ratio of reference material J-Ndi-1 gave an average of 0.512085 ± 5.

Sr total blank was better than 2 ng while Nd total blank was less than 1 ng during the period of measurement. Measured $^{87}Sr/^{86}Sr$ ratios have been normalized to $^{86}Sr/^{88}Sr$= 0.1194; $^{143}Nd/^{144}Nd$ ratios to $^{146}Nd/^{144}Nd$ = 0.7219. During collection of the isotopic data, 15 replicate analyses of SRM 987 ($SrCO_3$) standard gave an average value of 0.710200 ± 8 (2σ mean) and 14 measurements of La Jolla standard gave an average $^{143}Nd/^{144}Nd$ of 0.511851 ±3 (2σ mean). All $^{87}Sr/^{86}Sr$ data were normalized to a value of 0.71025 for the SRM 987 standard.

3.3 Boron isotopes in-situ determination on tourmaline

The in-situ B isotope composition of tourmaline crystals was measured by LA-MC-ICP-MS technique at the Geochemistry, Geochronology and Isotope Geology Laboratory at the Earth Science Department "A. Desio", University of Milan (Italy) by coupling the laser system used for the trace element determination to a Neptune XT MC-ICP-MS (Thermo Fisher Scientific). All measurements (i.e., standards and samples) were performed at a repetition rate of 5 Hz, fluence of 3.0 J/cm2 and in single spot mode with a diameter of 40 μm. Helium flux in the sample chamber and the cup were set to 0.500 l/min and to 0.240l/min, respectively, to maximize the signal without compromising its stability. Boron isotopes were simultaneously collected on two Faraday cups (^{10}B on L2 and ^{11}B on H4) both connected to 10^{11} Ω resistors. The instrument is equipped with 0.8 X-skimmer (Ni) + 1.2 Jet sample (Ni) cones and a large dry interface pump (Jet pump). Each analyses consisted of 78 cycles of ~1s each subdivided in 30 cycles of background acquisition, 40 cycles of signal acquisition and 8 cycles of washing time (Cannaò et al., 2022). The addiction of ~25s between each analyses ensures the complete wash out of the gas line. Data reduction was carried out offline with an in-house spreadsheet; ^{11}B/^{10}B ratios exceeding 2σ have been discharged. No downhole isotope ratio fractionation was observed. The results are reported in the common delta (δ)-notation as permil (‰) and expressed relative to the isotopic ratio of the NIST SRM 951 boric acid (^{11}B/^{10}B = 4.04362 ± 0.00137 2σ; (Catanzaro et al., 1970). Instrumental and laser-induced isotope fractionation were evaluated adopting the standard-sample bracketing protocol and using the as calibrating standard the B4 tourmaline (Tonarini et al., 2003), with schorlite composition. Accuracy was constrained by analyzing the dravitic tourmalines SY309 and SY441 from Syros (Marschall et al., 2006; Fig. 7-1). Boron isotope composition of these two tourmalines were mostly within the analytical error (2SD) of their reference values (respectively 21.6±0.8‰ and 18.8-19.3±0.9‰) indicating no matrix-effect during the different analytical runs and a properly correction of the instrumental fractionation and drift over time. Moreover, being able to correctly reproduce dravitic tourmaline B isotopic values through schorlitic standardization suggest that we correctly compensate for the different isotopic fractionation of these two species (Mikova et al., 2014). Spot precisions (SE‰) originally were between ca. 0.7 to 1.8‰ but the method was further developed by bracketing with three B4 standard analyses and shortening the integration time from 1 sec to 0.5 sec, definitely increasing the precision on single spots between 0.2 to 0.7‰. Hereafter, errors of each single spot analyses is expressed as 2 standard error (2SE).

References

Agostini, S., Di Giuseppe, P., Manetti, P., Savaşçın, M. Y., & Conticelli, S. (2022). Geochemical and isotopic (Sr-Nd-Pb) signature of crustal contamination in Na-alkali basaltic magmas of South-East Turkey. Italian Journal of Geosciences, 141(3), 363-384.

Cannaò, E., Tiepolo, M., Fumagalli, P., Grieco, G., & Agostini, S. (2022). Metasomatism in the Finero Phlogopite Peridotite: New insights from C and N concentrations and δ13C-δ11B signatures. Chemical Geology, 614, 121181.

Catanzaro, E. J. (1970). Boric acid: isotopic and assay standard reference materials (Vol. 260, No. 17). National Bureau of Standards, Institute for Materials Research.

Guillong, M., Meier, D. L., Allan, M. M., Heinrich, C. A., & Yardley, B. W. (2008). Appendix A6: SILLS: A MATLAB-based program for the reduction of laser ablation ICP-MS data of homogeneous materials and inclusions. Mineralogical Association of Canada Short Course, 40, 328-333.

Kroslakova, I., & Günther, D. (2007). Elemental fractionation in laser ablation-inductively coupled plasma-mass spectrometry: evidence for mass load induced matrix effects in the ICP during ablation of a silicate glass. Journal of Analytical Atomic Spectrometry, 22(1), 51-62.

Marschall, H. R., Ludwig, T., Altherr, R., Kalt, A., & Tonarini, S. (2006). Syros metasomatic tourmaline: evidence for very high-δ11B fluids in subduction zones. Journal of Petrology, 47(10), 1915-1942.

Míková, J., Košler, J., & Wiedenbeck, M. (2014). Matrix effects during laser ablation MC ICP-MS analysis of boron isotopes in tourmaline. Journal of Analytical Atomic Spectrometry, 29(5), 903-914.

Peters, D., & Pettke, T. (2017). Evaluation of major to ultra trace element bulk rock chemical analysis of nanoparticulate pressed powder pellets by LA-ICP-MS. Geostandards and Geoanalytical Research, 41(1), 5-28.

Tonarini, S., Pennisi, M., Adorni-Braccesi, A., Dini, A., Ferrara, G., Gonfiantini, R., ... & Gröning, M. (2003). Intercomparison of boron isotope and concentration measurements. Part I: Selection, preparation and homogeneity tests of the intercomparison materials. Geostandards Newsletter, 27(1), 21-39.

Chapter 4

Role of aqueous fluids during low pressure partial melting of pelites in a contact aureole (Adamello pluton, Italy)

Paper published in Lithos in 2022.

Reference: Magnani, L., Farina, F., Pezzotta, F., Dini, A., Mayne, M. J., & Bartoli, O. (2022). Role of aqueous fluids during low pressure partial melting of pelites in the Adamello pluton contact aureole (Italy). *Lithos*, *430*, 106853.

4.1 Introduction

Thermal aureoles around large middle crustal and shallow-level intrusions are valuable natural laboratories for studying in detail various aspects of metamorphism (Droop and Moazzen, 2007). One of their most useful characteristics is the presence of large variations in metamorphic grade within relatively small distances, allowing for small-scale studies of the metamorphic variability of single stratigraphic units from unmetamorphosed to high temperature metamorphic facies. Moreover, their metamorphic evolution is essentially isobaric and commonly the initial small-scale lithological variability of the protolith can be derived by studying unmetamorphosed rocks preserved close by. In particular, thermal aureoles allow investigating natural low pressure melting, a process that has received limited attention both in natural occurrences (e.g. Bea et al., 1994) and in experiments (e.g. Spicer et al., 2004) compared to medium to high pressure anatexis, which has been extensively studied in high-grade metamorphic terranes (e.g. Harley, 1989; Vielzeuf et al., 1990) and in many experimental works (e.g. Patiño Douce and Johnston, 1991; Patiño Douce and Harris, 1998; Pickering and Johnston, 1998; Vielzeuf and Holloway, 1988).

One of the main opportunities provided by thermal aureoles is the possibility to investigate the role exerted by fluids during partial melting, a topic that is highly debated because it has profound implications on crustal evolution (e.g. Weinberg and Hasalova, 2015). There are two main contrasting views about the fluid regime during crustal melting processes, mainly focused on the lower crust. Several authors advocate for fluid absent conditions during partial melting in the continental crust (e.g. Spicer et al., 2004; Stevens et al., 1992; Stevens and Clemens, 1993; Vielzeuf and Holloway, 1988), as fluids would exceed the low porosity of the rock and be efficiently extracted. In some cases (e.g. Clemens and Watkins, 2001) it has been suggested that fluid absent conditions at granulite facies

temperatures are the only way to produce large volumes of granitic magma in the continental crust. On the other hand, recent studies (Jung et al., 2000; Genier et al., 2008; Ward et al., 2008) of migmatites argued that large volumes of granitic melt have been produced at relatively low temperatures (ca. 700 °C) by fluid-fluxed partial melting.

This study focuses on the Forcel Rosso Pass zone in the core of the Adamello Massif (Northern Italy Central Alps, Fig. 4-1). This area is characterized by anatexis of metapelitic rocks in the thermal aureole of this shallow metaluminous batholith connected to the formation of leucosomes, aplites and small pegmatitic bodies. The pelites were unmetamorphosed before the intrusion and thus allow the evaluation of the effects of high temperature metamorphism and partial melting on previously undisturbed clay minerals-rich pelites. We studied the metamorphic history of the metapelites combining field-based observations, petrography, whole rock geochemistry and conventional geothermobarometry with a series of calculated phase equilibrium diagrams using Rcrust (Mayne et al., 2016) which used Meemum function of Perple_X (Connolly, 2009). This study constrains the peak P-T field of the migmatites, delineates the fluid conditions during metamorphism of these rocks and links the different metamorphic reactions with the production of different melts observed in the field.

4.2 Regional setting

4.2.1 The Paleo-Mesozoic succession

In the central part of the Southern Alps, the Paleo-Mesozoic succession intruded by the Adamello batholith is composed of rocks documenting continental deposition followed by marine transgression. This sequence starts with Permian continental clastic conglomerates grading upward to psammitic and pelitic red beds (i.e. Verrucano Lombardo formation) and ends with limestones and Triassic dolomitic limestones. The study area is located between the Fumo and Adamé valleys between the Forcel Rosso Pass and Mount Ignaga (Fig. 1). This area, which was part of a structural high in an Early Permian extensional basin, is characterized by very limited deposition of volcanic products (Schunnach et al. 1996). The complete sedimentary succession is ca. 500m thick in the Adamè Valley (Perotti and Siletto, 1996) and up to 1000m in the adjacent Fumo Valley which is mainly composed of conglomerates and sandstones in its lower and middle portion and becomes dominated by pelites and limestones in its uppermost part. Prior to the emplacement of the batholith, the sedimentary succession was at a temperature of ca. 250 °C (Pennacchioni et al. 2006) at pressures of 3-5 kbar (e.g. Schaltegger et al., 2019). The temperature was constrained by zircon fission-track data obtained from basement rocks (Viola et al. 2001) and is consistent with estimates of illite crystallinity from Permian sandstones (Riklin 1983). Pressure estimates where obtained indirectly through Al-in-hornblende geobarometry

applied to the different units of the Adamello batholith (e.g. Brack et al., 1983). In the study area, the unmetamorphosed Verrucano Lombardo Formation (VER) is composed of alternating unfossiliferous

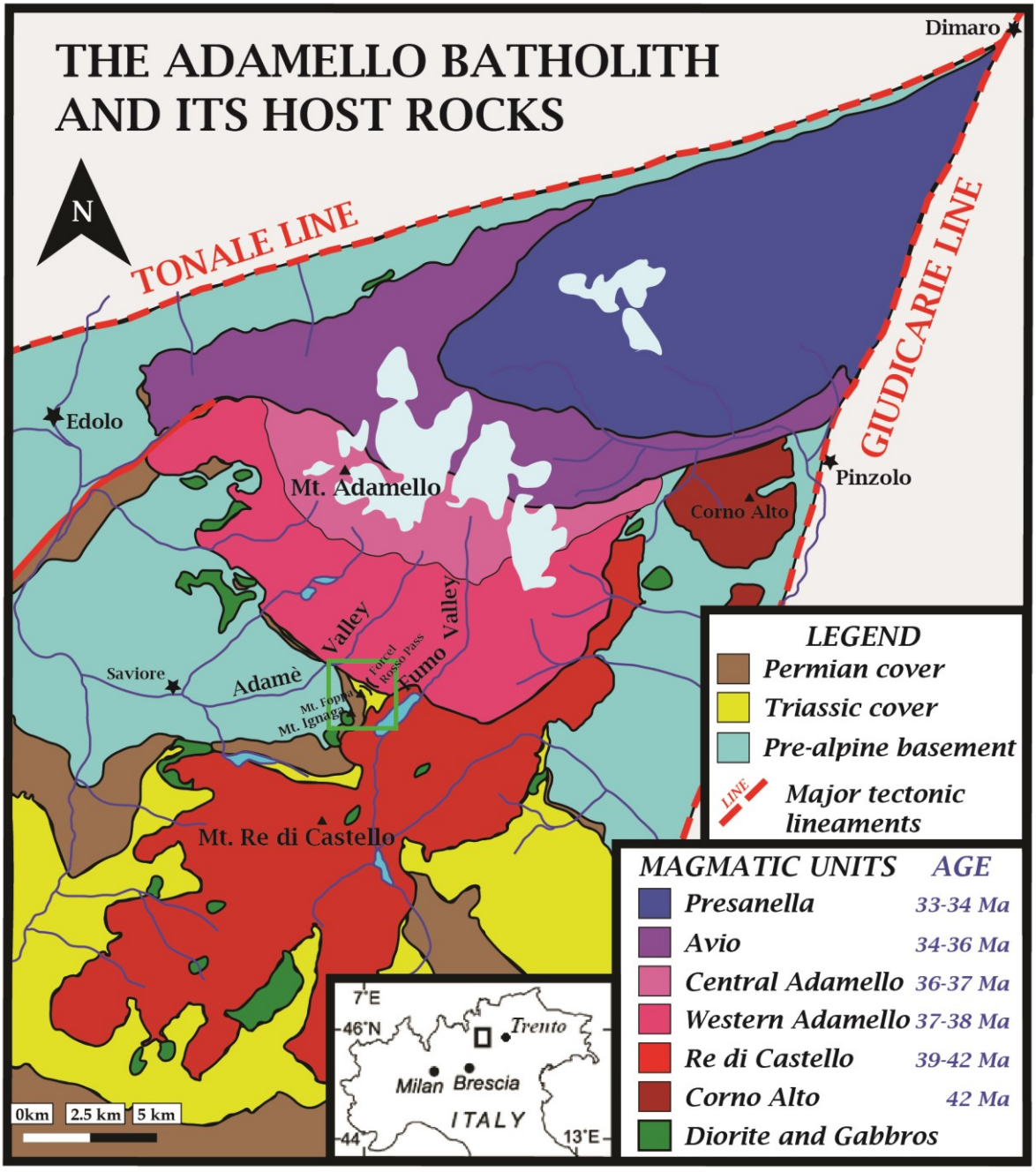

Figure 4-1 Adamello batholith architecture and principal types of host rocks in which it was intruded. Study area is highlighted by the green square. Re-drawn from Schaltegger et al., 2019.

conglomeratic and pelitic-arenaceous red beds that grade into each other and contain rounded quartz clasts and basement rock fragments of metamorphic origin. In the upper part of the sequence, the pelitic protolith is a badly classed silt made of ca. 55 vol% quartz, 30 vol% clay minerals and muscovite, 12 vol% feldspars and 3 vol% Fe-oxides (Riklin, 1983). Accessory minerals are tourmaline, hematite and rare zircon, monazite, apatite and rutile.

4.2.2 The Adamello batholith

The Adamello batholith is the largest of the Tertiary Periadriatic plutons and was emplaced at 6-10 km depth (Broderick et al., 2015) in the central Southern Alps during the Eocene-Oligocene. Schaltegger et al. (2019) subdivided the batholith into seven main units based on chemical, geochronological and structural observations (Fig. 4-1): the Presanella, Avio, Adamello (Central and Western), Re di Castello (Northern and Southern) and Corno Alto units. This pre- to syn-collisional batholith is composed of an association of tonalite, granodiorite and quartz-diorite with minor mafic units in the southernmost part of the batholith (e.g. Callegari and Brack 2002) bearing textural and chemical similarities with plutonic rocks formed in a continental magmatic arc setting (McCarthy et al., 2018). The Adamello plutons show a sequential emplacement from the oldest units in the south (~43 Ma) to the youngest in the north (~30 Ma; Schaltegger et al., 2019).

4.2.3 The Adamello batholith contact metamorphic aureole

Most of the country rocks (ca. 90%) surrounding the Adamello batholith exhibit evidence of contact metamorphism, with thermal aureoles of variable sizes extending from ca. 1 km to up to 4 km from the intrusion (Callegari and Brack, 2002). The Adamello pluton intruded the unmetamorphosed sequence at low regional temperature (Pennacchioni et al., 2006) and no further metamorphic events were recorded in the area after its intrusion. The first works focused on contact metamorphosed rocks surrounding the batholith are Salomon (1894), Lorenzoni (1955), Zanettin (1956), Riklin (1983) and recently Floess and Baumgartner, (2013) and (2015). In the Forcel Rosso area, the metamorphic thermal imprint was recently investigated by Floess et al., (2015) who described cryptic evidence of partial melting in the Triassic metacarbonates and meta-evaporites. In the Verrucano Lombardo formation the first effect of contact metamorphism is the increase in illite crystallinity (Riklin, 1983). Due to the metamorphism, the typically reddish clastics lithologies of the Verrucano Lombardo become grey upon the first appearance of biotite in the inner parts of the aureole. Temperatures at the magmatic contact between the Adamello pluton and the Permo-Mesozoic sedimentary succession reached up to 815°C in the Lozio Shales (LOZ) while in the mid-sequence Bovegno Carniole the temperature reached 670°C (Floess et al., 2015).

In the study area, barren pegmatites are widespread intruding different metamorphic rocks as well as the Adamello pluton, while Lithium-Cesium-Tantalum (LCT, Černý et al., 2005) mineralized pegmatitites (Diella et al., 2018) are exclusive to the Verrucano Lombardo formation. The barren bodies are characterized by Kfs, Qz, Pl, Ms, schorlitic Tur ± And (minerals abbreviations follow Whitney and Evans, 2010) mineral assemblages while the LCT-mineralized contain Kfs, Qz, Pl, Ms,

Schorlitic to Li-rich Tur, lepidolite, fluorite, pyroclore series minerals, pollucite, columbite-tantalite, apatite, monazite, xenotime, zircon and host rare miarolitic cavities.

4.3 Methods

This study is based on a set of forty samples from low-grade metamorphosed to migmatitic rocks of the Verrucano Lombardo formation as well as barren and Li-rich pegmatites collected in the Forcel Rosso area. In addition, five unmetamorphosed samples of Verrucano Lombardo pelites were also collected. Extensive and detailed field mapping was carried out to identify small-scale lithological variations and map the distribution of pegmatitic dykes (Fig. 4-2). The mineralogy and texture of the collected samples were characterized in fifty-five thin sections by optical microscopy while mineral chemical data were obtained by electron microprobe.

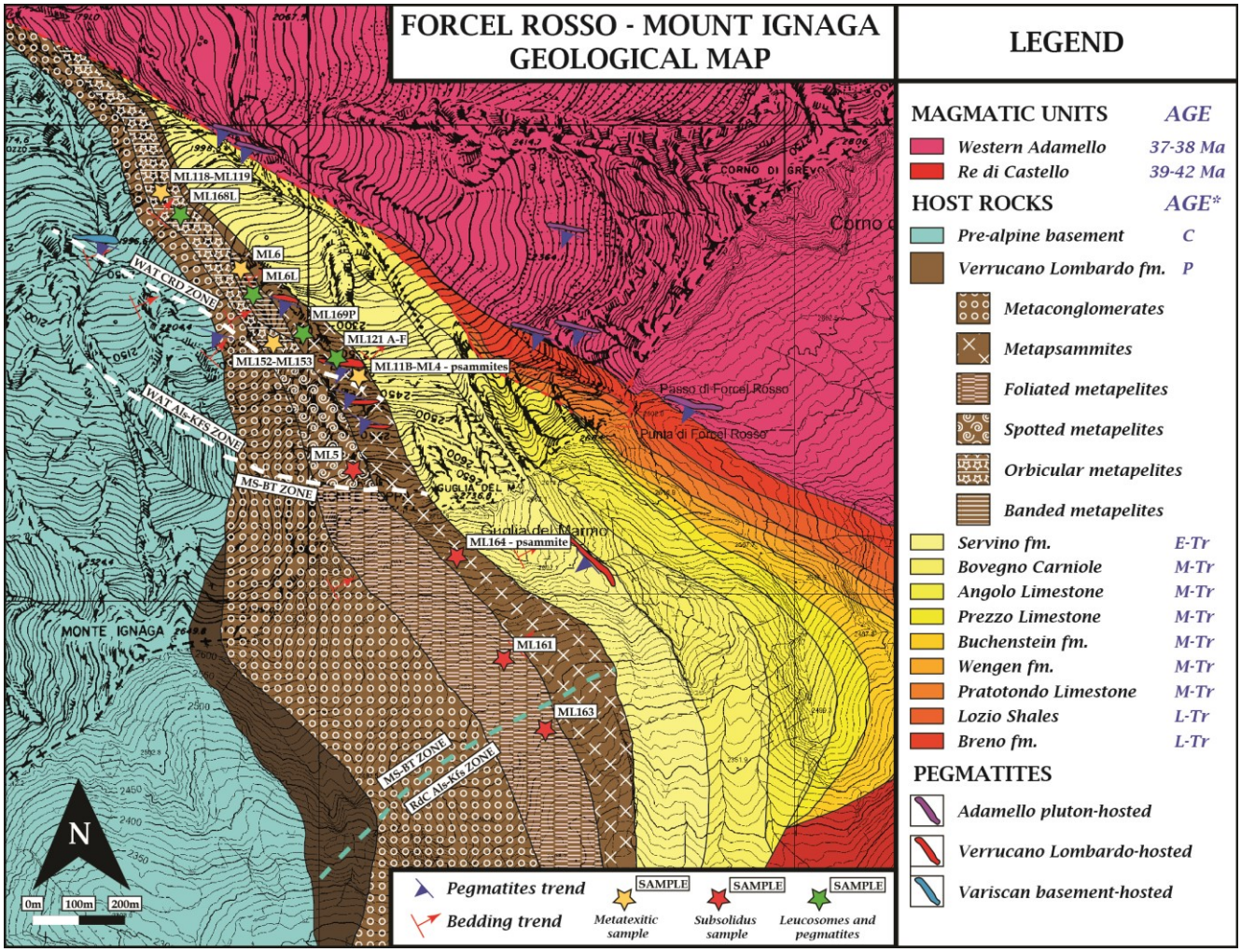

Figure 4-2 Geology of the Forcel Rosso mapped for the present study. White and cyan dashed lines represent the transition between the different metamorphic zones.

The whole rock major elements composition of the samples was determined at the department of Earth Sciences of the University of Milan (Italy) using an iCAP ICP-MS quadrupole coupled with a 193 nm

Ar-F excimer laser on pressed powder pellets following the procedure of Peters and Pettke (2016). Data treatment was performed on SILLS (Guillong et al., 2008). Details on sample preparations and data treatment are available in the supplementary material. All analyses are shown in Table A3. The major elements composition of the unmetamorphosed samples were obtained at the University of Stellenbosch, South Africa. Analyses were performed on fused discs through XRF equipped with a Rh tube at 3kW operating power.

The whole rock composition of the zoned LCT pegmatites has not been determined directly due to its extreme textural heterogeneity and large crystal dimensions which have hindered the collection of a single representative sample. To overcome this limitation, we sampled the six textural zones that characterize these pegmatites and for each of these zones we determined the major elements composition on pressed powder pellets as described in the supplemetary material. The average composition of the pegmatite was calculated as the weighted average of the composition of each zone multiplied for their volumetric abundance. The overall precision was estimated by taking into consideration both the analytical precision and the uncertainty on the determination of the volumes of the individual internal zones of the pegmatitic body. Electron microprobe analyses were performed at the Earth Sciences department of the University of Milan on a JEOL JXA-8200 using wavelength-dispersive spectrometry. Operating conditions were 15 kV accelerating voltage and beam current of 5 nA, with a beam diameter of 1 μm.

Image analysis was used to estimate mineral modal abundances on thin sections and on field photographs using the ImageJ software. During these analyses, multiple images of entire thin sections were processed through cleaning and sharpening, converted to 32-bit images and analyzed applying different thresholds. This technique was also implemented to control the field estimates of the volume abundance of felsic melts (i.e. leucosomes and pegmatites) in the migmatitc zones.

4.3.2 Thermodynamic modeling

Phase equilibria modeling was performed using the Rcrust software (Mayne et al. 2016), which allows path dependent phase equilibria modelling by changing bulk composition in the investigated P-T field on selected whole rock compositions of metamorphosed and unmetamorphosed lithotypes of the Verrucano Lombardo formation. The complete dataset and the calculated models used in this study are available in the supplementary materials. Calculations were performed in Rcrust version 2017-10-26 using a compiled form of the meemum function (version 6.8.6) from the Perple_X suite of programs (Connolly 2009) in the MnNCKFMASHTO chemical system using the 2011 revised hp11ver.dat thermodynamic data file from the internally consistent dataset of Holland and Powell (2011). The

Rcrust modeling methodology implemented involved water and melt extraction and was operated through the internal routine based on 'path dependence', that allows bulk compositional changes to be passed on from point to point (Mayne et al., 2020). The following solution models were used from solution_model_686.dat: Bi(W) for biotite, Crd(W) for cordierite, Gt(W) for garnet, melt(W) for melt, Mica(W) for white micas, Mt(W) for magnetite, Opx(W) for orthopyroxene, St(W) for staurolite (White et al. 2014), Sp(WPC) for spinel (White et al 2002), Ilm(WPH) for ilmenite (White et al 2000), Ep(HP11) for epidote (Holland and Powell 2011), Fsp(C1) for plagioclase and alkali-feldspar (Holland and Powell 2003), Cpx(HP) for clinopyroxene (Holland and Powell 1996). Additional phases with no solid solution include andalusite, sillimanite, kyanite, quartz, rutile, corundum and H_2O while microcline, albite and ilmenite were excluded from consideration as pure phases. At present, there is no tourmaline solution model and thus this phase is not considered in the modelling. The P-T phase diagrams that we obtained are calculated between 550 and 850°C on the x-axis and between 2 and 5 kbar on the y-axis. The choice of the temperature range is based on two main factors: it allowed for sufficient detail in the visualization of the compositional fields while comprising all the relevant metamorphic reactions which products we observed in our samples. Since no solution models are presently available for clay minerals, lower temperature assemblages were not correctly calculated. Because the amount of Fe_2O_3 in the bulk rocks was not constrained, the initial redox state of the system was estimated to be near the Fayalite-Magnetite-Quartz buffer based on the Ti-oxides compositions and biotite modal content of the rocks. This value was chosen after comparing the results of several models run at different oxygen fugacities.

T-X pseudosections were also calculated with Perplex (version 6.8.9) using the same solution models and initial compositions at pressures between 1 and 5 kbar at 1 kbar increments (in supplementary material).

4.4 Field geology

The contact metamorphic imprint on the pelitic sequence generated a great variety of rock textures and mineral assemblages in response to the increasing metamorphic grade. On the other hand, the metamorphosed conglomerates do not show any significant textural and mineralogical variations and remain largely similar to their unmetamorphosed counterpart.

4.4.1 Field charateristics of metapelites

In the field, four main metapelitic lithotypes can be identified:

i) Foliated metapelites (Fig. 4-3a) are low-grade, greyish rocks with pervasive to spaced foliation characterized by equant Qz, Pl and Kfs crystals showing annealed triple points. Bt and Ms are grown from the original illite-hematite aggregates and ilmenite is present.

ii) *Spotted metapelites* (Fig. 4-3b) are characterized by millimetric to centimetric, rounded to dendritic biotite-rich dark domains commonly surrounded by white halos made of Kfs, Pl and Qz. There is a positive correlation between the size of the halos and that of the bt-rich cores and field mapping suggests that the spots become larger with increasing metamorphic grade. The spots cut across the original foliation of the rock and where these white halos connect the original structure of the rock is locally obliterated (Fig. 4-3b). The appearance of this rock is similar to the "mottled gneisses" described by Vernon (1978) and to the crd-bearing Velay migmatites described by Barbey et al. (1999) where biotite in the dark domains is interpreted as replacing former cordierite crystals. Contrarily to the foliated metapelites, Qz segregation is observed in these samples.

iii) *Orbicular metapelites* (Fig. 4-3c,d) are characterized by orbicular leucocratic domains and an anastomosing melanocratic foliation. The leucocratic areas are mainly composed of unaltered cordierite poikiloblasts hosting biotite, andalusite and quartz inclusions and surrounded by Kfs+Qz+Pl aureoles. The melanocratic portion of the rock is composed of Bt-Pl-rich iso-oriented domains where the foliation observed in the low-grade metapelites is partially preserved but evolves into recrystallized biotite-rich schlieren around the orbicules (Fig. 4-4b). Patches reaching up to a few centimeters and composed of aggregates of Qz, Kfs, Ms and euhedral schorlitic Tur are disseminated throughout the rock. They appear as whitish iso-oriented veinlets cutting the metamorphic foliation at a 30° angle (Fig. 4-4a and c), rarely these leucosomes fill tension gashes (Fig. 4-4d). In the areas of more intense deformation, the orbicules are flattened and the rock lost its orbicular appearance becoming more pervasively foliated with the tourmaline-bearing patches showing pegmatitic textures. We interpret this rock as a metatexite where the orbicular portion represents the neosome and the biotite schlieren represent the residuum. Biotite-rich paleosome areas are also preserved while low grade partial melting was achieved as shown by the occurrence of in-situ Qz+Kfs+Ms+Tur leucosomes.

iv) *Banded metapelites* (Fig. 4-3e) show a stromatic structure with strongly iso-oriented fabric formed by biotite-sillimanite layers alternated to K-feldspar-rich leucocratic domains of

homogenous thickness. This lithotype hosts Kfs+Qz+Bt leucosomes (red arrows Fig. 4-3e) collected in extensional shear bands and asymmetrical foliation boudins around which the leucocratic domains tend to become thinner and the layered structure is locally deformed. The leucosomes are characterized by large blocky Kfs crystals, euhedral Bt and almost no quartz. The almost undisturbed stromatic structure implies that melt was efficiently extracted and collected in the leucosomes. Several leucosomes are connected to pervasive 190-200° N striking suture structures that connect deformed ends of the stromatic layers but do not host any melt (black arrows in Fig. 4-3e). We interpret these channels to be melt extraction structures that drained the local magmatic system. The banded metapelites are interpreted to be stromatic metatexite migmatites with high melt productivity. Occasionally, barren pegmatitic dykes with Kfs+Qz+Ms+Tur composition cut the rock forming an angle of ca. 30° with the stromatic foliation.

A synthesis of the main pelitic and metapelitic rocks described above is available in Table A1.

4.4.2 Leucosomes, pegmatites and aplites

The Verrucano Lombardo formation in the Forcel Rosso area hosts leucosomes, pegmatites and aplites formed during a single anatectic-magmatic event.

The leucosomes are observed in the metapelites of the innermost part of the thermal aureole and exhibit variable mineral composition and distribution, forming small veins, dykelets and patches. In the orbicular metapelites, leucosomes with assemblage Kfs+Qz+Ms+Tur±And occupy ca. 10 to 20 vol.% of the outcrop (e.g. Fig. 4-4c) without apparent extraction structures. In the banded metapelites, leucosomes composed of Kfs+Qz+Bt are less widespread and amount to 10-15 vol.%.

Figure 4-3 a) Low grade foliated metapelite; b) Spotted metapelite with coalesced bleached aureolas; c,d) Orbicular metapelites with leucosomes (red arrows) and spaced cleavage (black arrows); e) Banded metapelites with stromatic texture, the red arrows indicate the leucosomes cutting the foliation, suture structures indicating extraction are highlighted in black.

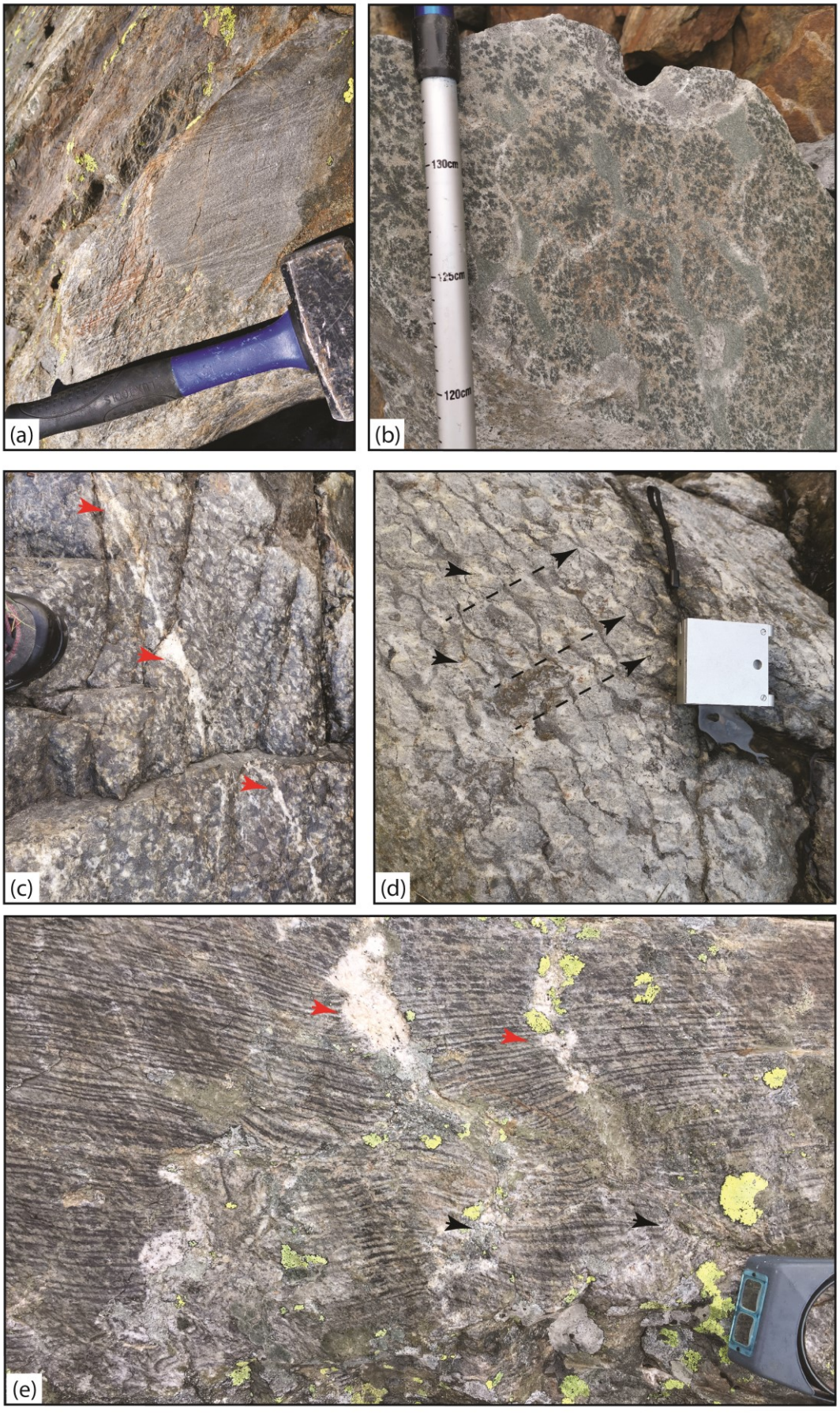
(a)
(b)
130cm
120cm
(c)
(d)
(e)

In the studied area, the Verrucano Lombardo formation hosts several ca. E-W trending, 190-220°N striking pegmatitic LCT-mineralized bodies as well as an interconnected net of small-scale barren pegmatites collected in centimetric fractures in the metapelites and in the metapsammites. The barren pegmatites are centimetric and show no internal differentiation (e.g. Fig. 4-4d), while the Li-rich pegmatites (Fig. 4-4e) are metric and exhibit a clear internal zonation. The latter are not homogeneously enriched in lithium, as is common for LCT pegmatites, in fact several barren zones occur alongside the mineralized zones, with Li-bearing minerals concentrated in the internal parts of the dykes. Large pegmatitic dykes are usually confined within the metapsammitic layers, while the leucosomes are relegated to the orbicular and banded metapelites. The barren dykelets are particularly abundant in the area between the leucosomes-hosting banded metapelites and the metapsammite-hosted LCT pegmatites. All the pegmatitic dykes and dykelets show sharp contacts with the host and are particularly abundant within the metapsammitic and metaconglomeratic lenses in the metapelitic succession. The pegmatites are limited to the Verrucano Lombardo formation and they stop abruptly against the carbonate layers at the base of the pelitic-carbonatic Servino formation, which is positioned vertically between the study area and the Adamello pluton as shown in Fig. 4-2.

4.5 Petrography

Based on field and petrographic observations, three zones are identified within the metapelitic sequence investigated in this study. The petrographic features of each zone are here detailed from lowest to highest metamorphic grade, together with the retrograde evolution. In Table A2 we report the modal abundances of every rock type described. Figure A1 (Appendix A) shows back-scattered electron images of the two types of metatexites that were not included in the published article.

4.5.1 Ms-Bt zone

The muscovite-biotite zone is observed on the Fumo Valley slope of Mount Foppa in the foliated metapelites. This metamorphic facies is characterized by fine-grained Ms+Bt+Qz+Kfs+Pl+And+Tur+Ilm phyllites. Muscovite (Fig. 4-5a) that appears as both large detrital grains and micro- to nanometric crystals derived from recrystallization of diagenetic clay minerals, accounts for 25 to 30 vol.% of the samples. Plagioclase forms up to 10 vol.% of the rock but its distribution is not homogeneous and its modal proportion varies in different rock domains. K-feldspar is generally rare and never exceeds 15 vol.%. Biotite forms up to 17% of the rock and is present in micrometric to millimetric crystals growing from original clay minerals in the interstices between Qz

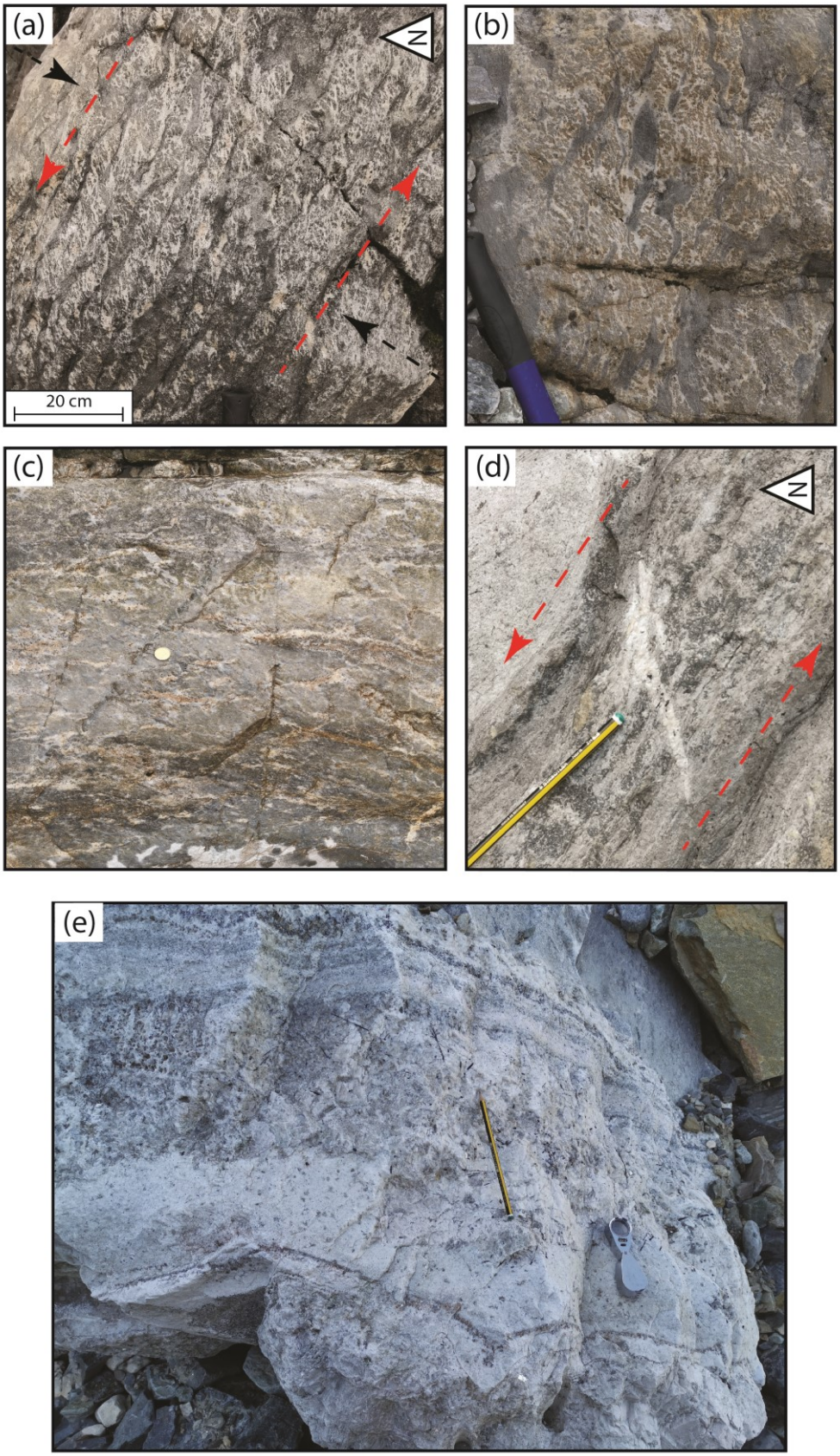

Figure 4-4 a,b) Deformed orbicular metapelites with dendritic cordierite, the red arrows indicate the shear sense; c) Isooriented leucosomes of Qz+Kfs+Ms+Tur composition in orbicular metatexites; d) melt filled tension gash, the red arrows indicate the shear sense; e) Li-rich pegmatite cross section showing two repetitions of aplite and pegmatitic zones. At the top, metapsammitic country rock, at the bottom, lithium enriched core with lepidolite and elbaite.

and Kfs grains. Andalusite is rare but present in the assemblage as small subhedral prisms in the foliation. Magnetite is the most common accessory mineral appearing as micrometric rounded crystals particularly in sample ML161 in which it composes up to 3 vol.% of the mineral assemblage. Magnetite is interpreted to be of metamorphic origin as it is absent in the unmetamorphosed pelites. High magnetite contents in the studied samples are always coupled with high muscovite contents (up to 30%) and, as suggested by Sola et al. (2017), this is a characteristic of partially oxidized pelites. Tourmaline is the second most common accessory mineral and it is present as zoned anhedral crystals between quartz clasts or as subehedral prisms at 0.1 vol% abundance. The upper limit of this zone is marked by the complete disappearance of muscovite during prograde metamorphism and the appearance of andalusite and sillimanite in the mineral assemblage.

4.5.2 And-Sil-Kfs zone

This zone is characterized by the appearance of the andalusite-sillimanite foliation (Fig. 4-5b), the absence of muscovite and by a marked increase in the modal abundance of Kfs. This metamorphic zone defines the transition between the foliated metapelites and the spotted metapelites lithotypes. The two aluminosilicates are always found together constituting up to 15 vol.% of the rock. Andalusite is less abundant and it is usually partially replaced by fibrolitic sillimanite, with this substitution starting from the crystal rims (Fig. 4-5c). This process is often incomplete and occasionally andalusite can be found even in the higher temperature melt zone. Aluminosilicates enter in the mineral assemblage through the reaction Ms+Qz+Pl→Kfs+Als+Bt+H_2O (Dyck et al., 2020) that completely consumed muscovite. Andalusite, where preserved, is usually subhedral to euhedral showing pink cores and transparent rims with intergrowths of K-feldspar. Microcline crystals with their characteristic twinning are common in the leucocratic parts of the samples. Passing from the Ms-Bt to the And-Sil-Kfs zone, the grain sizes of all minerals tend to increase and the tourmaline content increases from 0.1 vol% to 0.5 vol.%.

4.5.3 Melt producing zone

This zone extends from the intrusion to the Verrucano Lombardo for ca. 350m and contains the orbicular and banded metapelites. The orbicular metapelites are characterized by abundant cordierite and K-feldspar and by the almost complete disappearance of aluminosilicates. Cordierite in these rocks occurs as skeletal and poikilitic crystals of millimetric to centimetric size with ubiquitous inclusions of Qz, Kfs and Bt (Fig. 4-5d). The amount of cordierite observed varies with the distance from the contact. Those samples located near the intrusion (100 m), have the highest Crd modal abundance (up

to 20 vol%) and millimetric to centimetric crystals (average 0.8 mm) while samples that were collected further from the magmatic contact (300 m), have the lowest Crd content (5 vol%) and micrometric to millimetric crystals (avg. 500 μm). The changes in mineralogy from the And-Sil metamorphic zone are most likely produced through the reaction Als+Bt+Qz+Pl→Kfs+Crd+melt (e.g. Clarke, 1995). The identification of quartz pseudomorphing melt-filled pores (Fig. 5e; e.g. Holness and Sawyer, 2008) in orbicular metapelites reveals that partial melting was involved in the evolution of these rocks confirming our field-based interpretation. In the orbicular metapelites, sillimanite is scarce and located only in anhedral Kfs patches that likely shielded it from reacting (Fig. 4-5e). Quartz is present (15 to 20 vol.%), mainly occurring in cordierite coronas and as inclusion in poikilitic cordierite crystals. Leucosomes with Qz+Kfs+Ms+Tur mineral composition start appearing and are collected in shear zones. The modal proportions of mineral phases in these leucosomes are ca. 12% Ms, 30% Kfs, 22% Pl, 32% Qz and 4% Tur.

In the banded metapelites, cordierite is absent. The petrography of this lithotype is dominated by Bt, Sil and Kfs, which form alternating leucocratic and melanocratic layers. In the leucocratic bands, composed by Kfs and minor euhedral to subhedral Pl, quartz pseudomorphs on former melt films are widespread (Fig. 4-5f; e.g. Holness et al., 2018) suggesting limited but pervasive partial melting. The melanocratic layers are Bt+Sil+And+Ms schlieren where Bt is ca. 30 vol% more abundant than Sil. Biotite is present both as small, rounded crystals indicating that it participated in the partial melting reactions (e.g. Sawyer, 2010) and in euhedral grains with straight crystal boundaries that show no sign of reaction. The reacted biotites are usually hosted in Sil rich nodules, which were produced during prograde muscovite dehydration (FIg. 4-5g). And and Ms are interpreted as retrograde. The banded metapelites-hosted leucosomes are composed of Bt+Kfs+Qz+Pl assemblages, with euhedral Bt crystals growing from the borders towards the center surrounded by subhedral to euhedral Kfs crystals with interstitial Qz and Pl. The modal proportions of minerals in these leucosomes are ca. 5% Bt, 83% Kfs and 12% Qz.

In both orbicular and banded metapelites, tourmaline composes up to 1 vol% of the samples and is mainly concentrated in Als and Bt rich zones. The crystals are usually large, euhedral to subhedral and show no zonation, in contrast to the zoned and rare crystals observed at lower metamorphic grades. Common accessory minerals are zircon, monazite, apatite, ilmenite and Ti-rich magnetite.

Figure 4-5 Photomicrographs of a) deformed detrital Ms (in red) and fine-grained Ms+Bt aggregates in the Ms-Bt zone; b,c) Bt+Sil foliation in the Sil-Kfs zone, with andalusite being replaced by fibrolitic Sil during And-Sil inversion process (in red); d) Poikilitic Crd from orbicular metapelites including rounded Qz and Bt, on the right side blocky Kfs on Sil ghosts (red arrow); e) Anhedral peritectic Kfs crystal growing on Sil; f) Qz pseudomorphs after melt in the banded metapelites; g) Bt+Ms+Qz+Sil aggregates in banded metapelites melanosome; h) polarized image of partially rehydrated Sil+And+Qz in the banded metapelites.

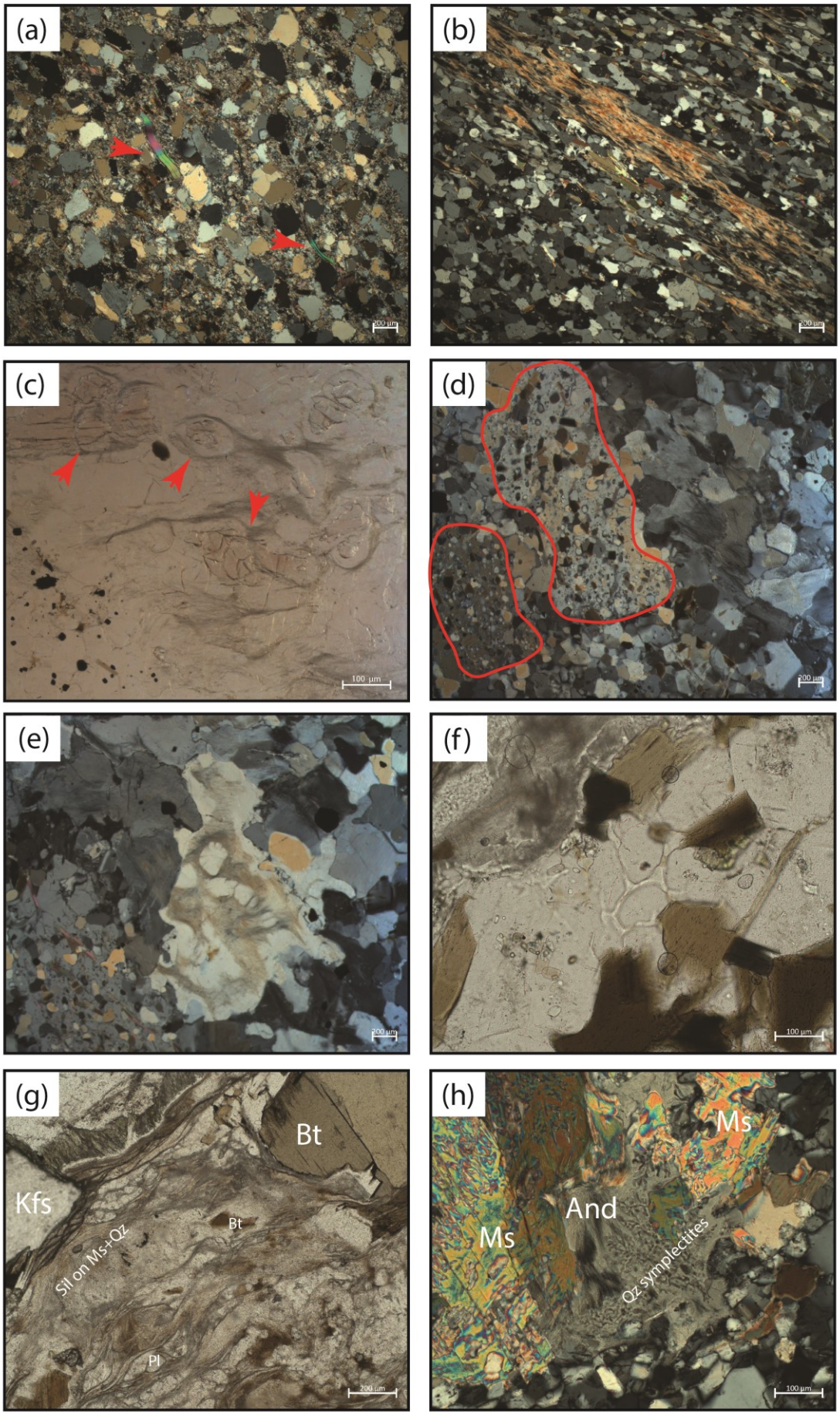
(a)
(b)
(c)
(d)
(e)
(f)
(g)
Bt
Kfs
Bt
Sil on Ms+Qz
Pl
(h)
Ms
And
Ms
Qz symplectites

4.5.4 Retrograde metamorphic reactions

Retrograde metamorphism in the banded metapelites is highlighted by Ms monocrystals pseudomorphing Sil nodules, in association with Qz (Fig. 5h; e.g. Clarke et al., 2005), and by Bt chloritization and Ep formation. Almost no metamorphic retrogression reactions are observed in the orbicular metapelites. In the lithotypes where no melt was produced, the pinnitization process is complete and the Crd poikiloblasts are completely transformed by low temperature rehydration into fine grained Bt+Ms+Qz aggregates.

4.6 Mineral chemistry and geothermobarometry

Cordierite shows very little chemical variations and is characterized by Mg# (Mg/(Mg+Fe)) between 52 and 63 forming a solid solution between cordierite and sekaninaite. Na content of cordierite is between 0.45 and 0.64 apfu. No clear compositional Mg-Fe trends can be identified based on the distance from the pluton.

Other mineral phases were analyzed but their composition is not discussed in the present work, the completedataset can be found in the supplementary material. The recently proposed Na in cordierite geothermometer (Tropper et al., 2018) was used to determine the temperature of the Crd zone. This geothermometer was recently calibrated between 0.1 and 0.6 GPa, and was applied using the following equation: T(°C) = (Na[apfu]-0.4052)/(-0.000487) with an R^2 value of 0.96 for initial compositions that are muscovite rich and have plagioclase as an accessory phase. The temperature calculated for the cordierite zone are between 672 and 709°C with a mean temperature estimate of 687°C in the samples that produced melt while the temperature estimates are as low as 616°C for subsolidus cordierite at the edge of the Crd-zone.

In the Verrucano Lombardo metapelites, the occurrence of andalusite and the lack of staurolite in equilibrium with a Crd+Sil+Kfs assemblage, suggest a pressure below 3.1 kbar as proposed by Pattison and Tracy (1992) and Pattison and Vogl (2005). Bt and Crd chemical data are shown respectively in Table 4 and 5.

4.7 Phase equilibria modelling

The role exerted by fluid on the partial melting of the Verrucano Lombardo metapelites has been investigated studying three main cases: fluid-limited, fluid assisted and fluid rich. In the fluid-limited scenario free water is assumed to be present at any given time only as a pore fluid filling a nominal porosity of 0.1 vol.% (i.e. porosity limited condition, Mayne et al., 2019). The software was initially set to

start with 2 wt.% H_2O in order to form all the hydrous phases observed in the natural samples, but from 550°C onward all excess water higher than 0.1 vol.% was systematically removed from the simulation. This allows simulating a system that progressively loses water. This defined a nearly fluid absent system where the H_2O produced by dehydration reactions was continuously extracted from the P-T field. In the fluid assisted scenario the software was again initially set to 2 wt.% H_2O and, like in the fluid-limited case, the excess fluid was extracted to reach 0.1 vol.% at 550°C. However, in this simulation no further phase extraction was performed and thus all the H_2O liberated at temperature above 550°C during dehydration of hydrous minerals remains in the system, contributing to the partial melting reactions. Finally, in the fluid rich scenario the initial conditions were set at 5 wt.% H_2O as this allowed us to model a non-infinite external water phase influx on the system.

For the fluid rich scenario, an additional simulation was performed in which the melt produced was efficiently extracted from the system whenever it reaches a 7 vol.% threshold, leaving behind 1 vol.% melt fraction (as described by Mayne et al., 2020). This model is run to investigate the behavior of an anatectic system undergoing melt loss and to determine the impact of melt extraction on the rock. Results of this last scenario were checked against an excess fluids model using 7 wt.% water (available in the supplementary material), which ensured that a free H_2O phase was present in the entire investigated P-T conditions (2-5 kbar and 550-850°C), in order to observe if the fluid rich model produced consistent results at the inferred peak P-T conditions. For the fluid limited, assisted and rich scenarios, the variations of mineral modal abundances with temperature at 3 kbar is highlighted in Fig. 8. The whole-rock composition of sample ML161 (foliated metapelites, modal abundance in Table A2) was used as starting composition for phase equilibria modeling. This sample was chosen over its unmetamorphosed counterparts because it was sampled in the same stratigraphic position as the metatexitic samples, therefore reducing the effect of compositional variability introduced by sampling different strata in the pelitic succession. Moreover, we selected ML161 as starting composition because its CaO content result in a better match between the observed and modelled plagioclase modal abundance. The relatively constant K_2O values within the layer likely imply a constant mica abundance and hence a fixed water content to be produced by dehydration reactions.

4.7.1 Subsolidus Phase Equilibria

The phase equilibria diagrams for the three fluid scenarios at subsolidus conditions are similar (Fig. 4-6, 4-7), with a maximum temperature difference between individual reactions of around 10°C. The metamorphic history of the Verrucano Lombardo metapelites evolved at low pressure and nearly isobaric conditions in a thermometamorphic contact aureole. At low pressures, rutile is stable up to

570°C, while at higher temperature ilmenite is the only Ti-bearing phase. Due to the low Mg content of the starting material (MgO = 1.3 wt.%) chlorite and low temperature Mg-cordierite are not stable. At pressures below 4.5 kbar the muscovite-out reaction is crossed between 600 and 650°C producing andalusite below 3.2 kbar and sillimanite between 3 and 4.5 kbar. At pressure above 4.5 kbar, the muscovite-out curve is in the suprasolidus field.

At the pressure estimated for the Verrucano Lombardo at the time of intrusion of the Adamello pluton (3-5 kbar; e.g. Schaltegger et al., 2019) muscovite dehydration is expected to occur at sub-solidus conditions at 635°C. Andalusite is predicted to be stable between 620 and 650°C in a narrow stability

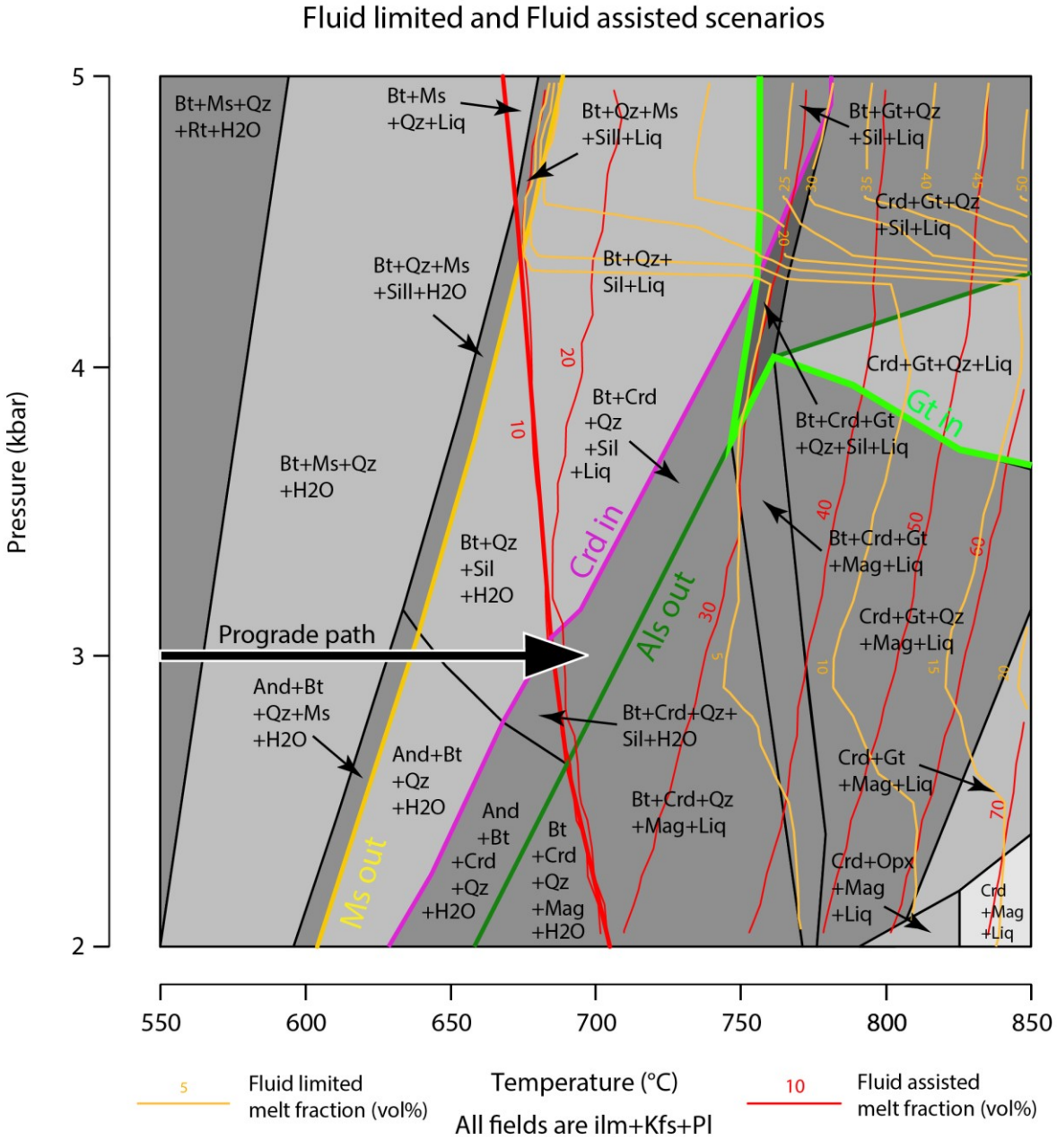

Figure 4-6 Fluid limited and fluid assisted scenarios phase diagrams.

field above which the stable aluminosilicate is sillimanite. Petrographic observations show that andalusite is widespread in the thermometamorphosed rocks of the Adamello pluton thermal aureole, thus confirming general low pressure conditions of emplacement.

Thermodynamic modelling predicts biotite to destabilize above 660°C forming cordierite in a subsolidus reaction limited to a small stability field. Cordierite starts forming between 660 and 700°C through the reaction Bt+Pl+Qz+Al_2SiO_5 → Kfs+Crd while melting starts only above 680°C. The existence of subsolidus cordierite is in agreement with textural, petrographic and field observations. Plagioclase and quartz are never the limiting factors for dehydration metamorphic reactions as they are present at all pressure and temperature conditions in the phase diagrams. K-feldspar modal abundance increases with increasing temperature as it is part of the dehydration reactions products.

4.7.2 Supersolidus Phase Equilibria

The supersolidus topology for the fluid limited and fluid assisted scenarios remains very similar, with the two models that can be only distinguished on the base of melt productivity (Fig. 4-6). On the other hand, the fluid rich scenario features a more complex stability field arrangement (Fig. 4-7). Garnet was never observed in the Verrucano Lombardo metapelites and its stability is predicted only above 750°C and 4.5 kbar. Above the solidus, the assemblage evolves into the peak assemblage close to the sillimanite-out and magnetite-in curve and, depending on the fluid scenario, crossing the Crd-in curve.

In the fluid limited scenario (Fig. 4-6), partial melting starts at ca. 680°C but melt productivity remains very low until 800°C, with less than 7 vol.% of melt predicted below 740°C and only 20 vol.% formed at 900°C (Fig. 4-8a). The melt productivity observed in this phase diagram does not match the amount of melt estimated in the cordierite zone of the Verrucano Lombardo metapelites, which was estimated to be around 20 vol.%.

In the fluid assisted scenario (Fig. 4-6) partial melting starts at around 680°C and fluid addition due to muscovite and biotite dehydration, cause melt productivity to rapidly increase, producing a melt fraction of up to 22 vol.% at 710°C (Fig. 4-8b) where sillimanite reacts out and all fluids are consumed following the reaction:

$$8Bt + 4Kfs + 3Pl + 6Sil + 11Qz + 1H_2O \text{ --> } 13Crd + 20melt$$

After H_2O is exhausted, melt production increases with temperature at a less steep rate, as highlighted by the larger spacing between melt isopleths in the pseudosection, reaching ca. 50 vol.% at 800°C. In this reaction, the amount of water and sillimanite in the rock are the limiting reactants. This scenario is

applicable to the orbicular metatexites where the incomplete sillimanite-out reaction confines the maximum temperature to be under 710°C (Sil 1-4 vol.%). At this temperature Pl is predicted to be around 5 vol.% and Qz at ca. 26 vol.% in agreement with the modal abundances of these phases in the orbicular metapelites (Fig. 4-8b). Cordierite is always a product of partial melting in this scenario and the Crd-absent banded metapelites cannot therefore be produced under these P-T-H_2O conditions.

In the fluid rich scenario (Fig. 4-7 for topology, 8c for phase volumes) above 680°C the melt productivity increases dramatically reaching up to 80 vol.% of melt at 700°C (Fig. 4-8c). Total Pl exhaustion is predicted above 740°C while Qz persists up to 710°C at 3 kbar (Fig. 4-8c). In this scenario,

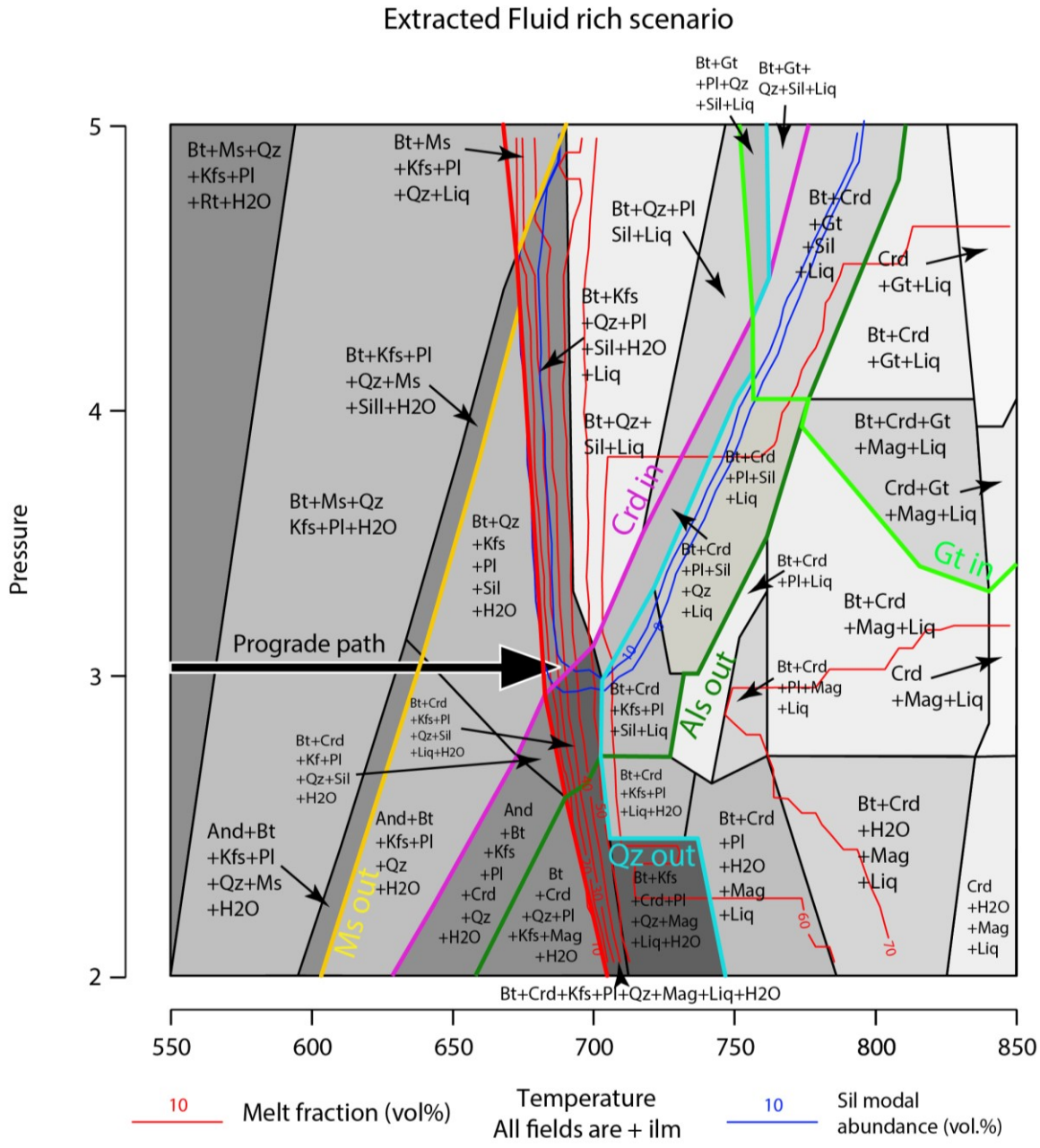

Figure 4-7 Extracted Fluid rich scenario phase diagram, extraction performed at 7 vol.% melt intervals.

Qz and Pl are the limiting reactants while sillimanite and biotite remain in the assemblage in higher proportions than in the fluids assisted case, following the reaction:

$$1Bt + 15Kfs + 3Pl + 2Sil + 9Qz + 4.5H_2O \text{ --> } 35melt + 2.5H_2O$$

Above 700°C, all free water is accommodated in melt while at lower temperatures water remains as exsolved free water in the system. The cordierite-in reaction is subsolidus below 3 kbar while above 3 kbar it crosses the solidus defining, with increasing pressure, a Crd-absent area in which no peritectic phases are formed during partial melting reactions. While this scenario may produce Crd-absent assemblages through congruent partial melting, it is not applicable to the Verrucano Lombardo metapelites as it produces an extremely high melt fraction, which would have destroyed the stromatic texture observed in the banded metapelites, creating a diatexite migmatite. Moreover, the accumulation of ca. 80 vol.% of melt (at 700°C) without extraction does not fit with the volume of leucosomes observed in the rock (Fig. 4-8c).

In this fluid rich scenario, we performed a simulation of melt extraction. Every time a hypothetical 7 vol.% liquid fraction threshold is reached, all melt except 1 vol.% is extracted from the residual system (Mayne et al., 2020) in order to simulate the persistence of intergranular melt (e.g. Farina et al., 2020). The phase diagram we obtain (Fig. 4-7) features the same topology of the unextracted fluid rich scenario apart from the amount of melt produced. In this case, the amount of liquid produced is ca. 35 vol.% at 690-700°C constrained on the Sil modal fraction at the observed Sil modal proportions (Fig. 4-7). This scenario may be applicable to the banded metapelites of the Verrucano Lombardo formation based on the mineral modal abundances, and on the absence of cordierite in the residuum. The changes in mineral phases volume proportions with temperature for the three main scenarios (fluid limited, assisted and rich) are reported in Fig. 8, at the pressure of 3 kbar.

In the excess fluid control model (7 wt.% initial water, melt extracted), H_2O is present as free phase in all the investigated P-T field while producing a phase diagram very similar to the fluid rich scenario. This supports the hypothesis that the 5 wt.% initial water value used in the fluid rich scenario correctly models the reactions in the P-T range of interest while realistically modelling a finite external fluid influx on the system.

The modal results of all phase equilibria models are synthetized in Table A6.

The predicted melt compositions for the fluid assisted and fluid rich scenarios are shown in Table A7.

Figure 4-8 Mineral phases vol.% variations in the fluid limited, assisted and rich scenarios. The red lines highlight the calculated T field for our metatexites.

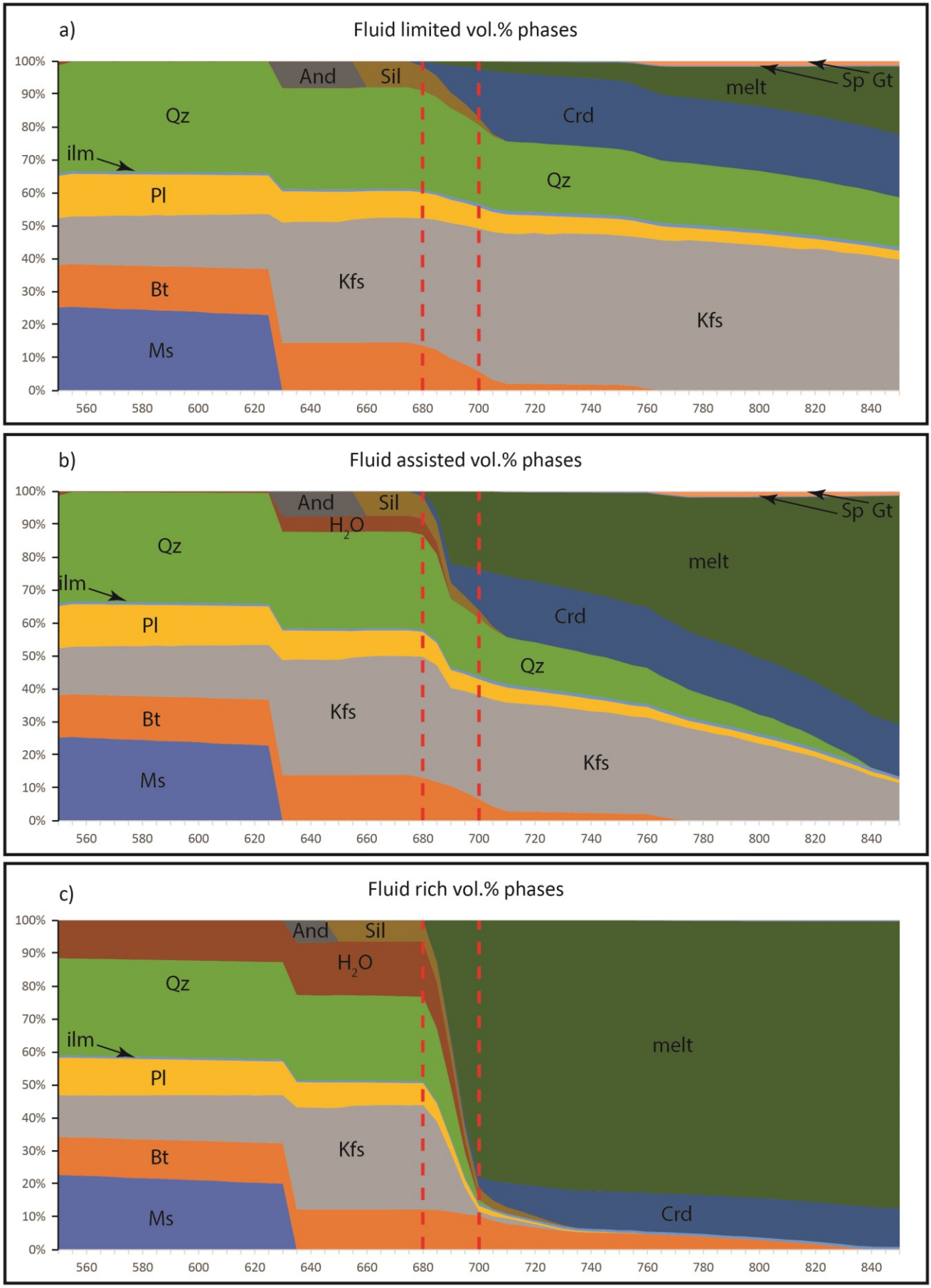
a)
Fluid limited vol.% phases
And
Sil
melt
Sp
Gt
Qz
Crd
ilm
Pl
Qz
Kfs
Bt
Kfs
Ms
b)
Fluid assisted vol.% phases
And
Sil
H_2O
Sp
Gt
Qz
melt
ilm
Pl
Crd
Qz
Kfs
Bt
Kfs
Ms
c)
Fluid rich vol.% phases
And
Sil
H_2O
Qz
melt
ilm
Pl
Kfs
Bt
Crd
Ms
100%
90%
80%
70%
60%
50%
40%
30%
20%
10%
0%
560
580
600
620
640
660
680
700
720
740
760
780
800
820
840

4.8 Whole rock chemistry

The whole rock composition of pelites, metapelite, leucosomes and pegmatites generates a linear trend in the Al_2O_3 vs. SiO_2 diagram (Fig. 4-9). The pelite and low-grade metapelitic samples plot in the middle of the trend, in an area that is located halfway between the composition of the metatexites (orbicular and banded metapelites), which are higher in Al_2O_3 and lower in SiO_2, and the compositions of the felsic magmatic rocks, both leucosomes and pegmatites. The mean Al_2O_3 content of low grade metapelites is 16.4 wt.% while orbicular and banded metapelites are characterized by mean Al_2O_3 of, respectively, 20.2 wt.% and 25.7 wt.%.

All the magmatic rocks in the Forcel Rosso area are high in silica (SiO_2 > 65 wt.%) and low in FeO_t (Fig. 4-10a) and MgO. The leucosomes hosted in the banded metapelites are extremely K_2O-rich (12.7 wt.%) while those in the orbicular metapelites have K_2O of 5.8 wt% (Fig. 4-10b). The latter plotting in the field of fluid present and absent experimental melts (Gao et al., 2016 and references therein) and natural leucosomes in metapelites (Bea et al.,1994; Sawyer et al., 1987). Moreover, the Na_2O and K_2O content of the leucosomes in the orbicular metapelites are similar to the values calculated for the melts in the phase equilibria simulations in both fluid assisted and fluid rich scenarios (Fig. 4-10b).

Barren and LCT-pegmatites have different K_2O contents and Na_2O/K_2O ratios that greatly differ from those of the predicted primary melts (Fig. 4-10a-b). Barren pegmatites are relatively K_2O-rich (8 wt%) and have Na_2O/K_2O <1, intermediate between the values characterizing the two leucosomes types. On the other hand, despite their significant internal variability the Li-mineralized pegmatites are enriched in Na_2O and characterized by Na_2O/K_2O ratio of 2. The different zones inside the composite Li-enriched pegmatites range from medium-high K_2O and low Na_2O in the external zones to extremely Na_2O-enriched cores. It is worth noting that the K_2O content in the external zone is similar to that calculated for the melts extracted from the banded metapelites.

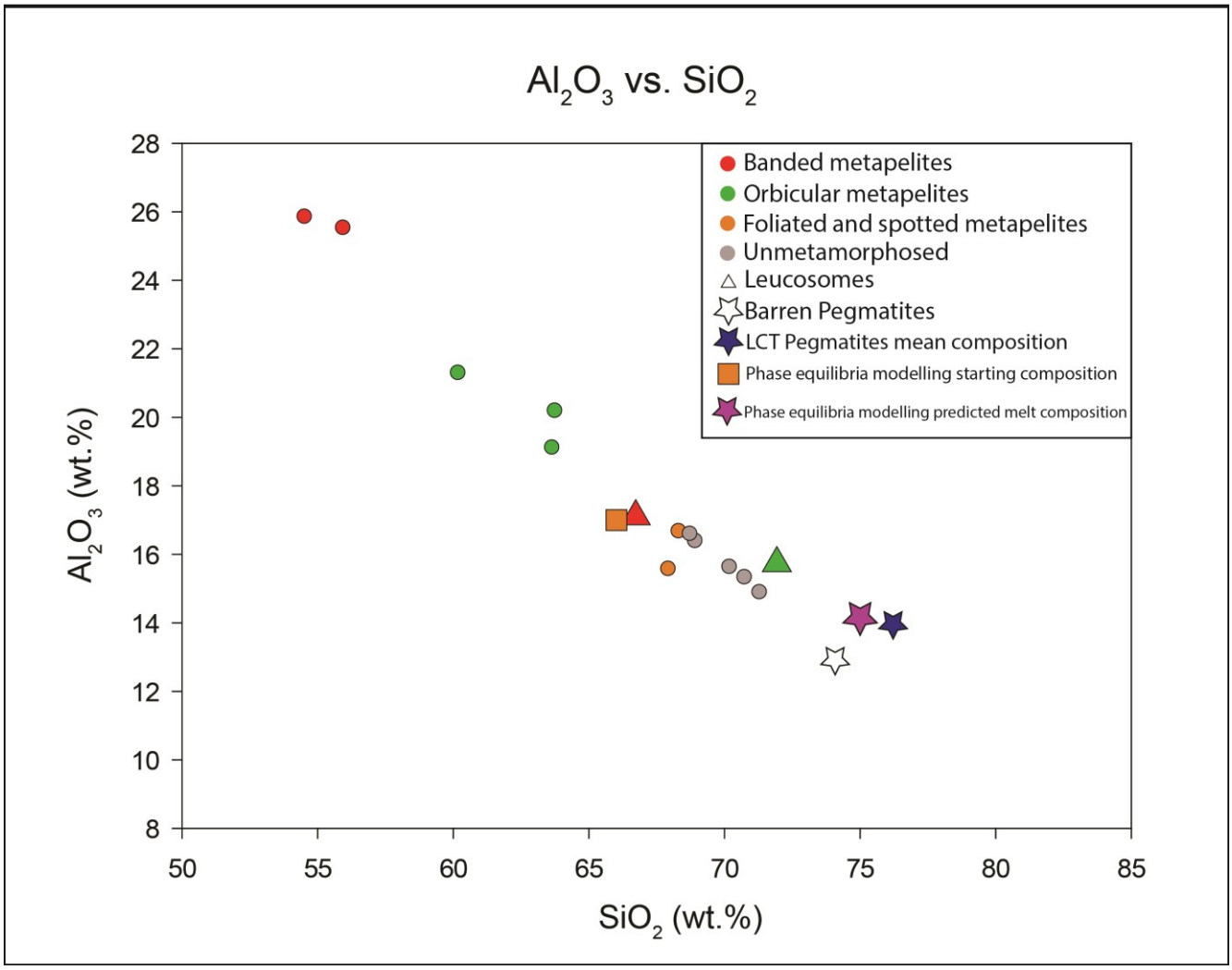

Figure 4-9 Al_2O_3 vs. SiO_2 whole rock data of low grade samples, migmatites, leucosomes and pegmatites.

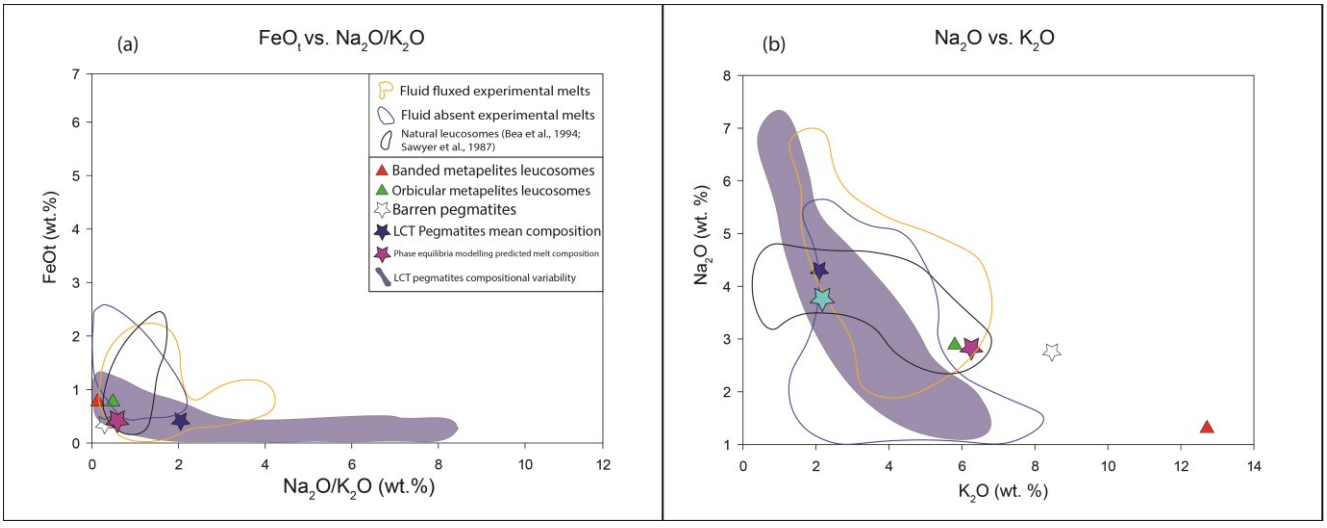

Figure 4-10 a) FeOt vs. Na2O/K2O diagram comparing the Forcel Rosso leucosomes and pegmatites to natural and experimental data. b) Na2O vs. K2O plot of all melt types in the Forcel Rosso; literature leucosomes and experimental melts compositions for reference.

4.9 Discussion

4.9.1 Metamorphic conditions in the thermal aureole

The peak P-T conditions that produced the metatexites were constrained by comparing the mineral assemblage observed in the high-grade rocks with the results of the thermodynamic models (Fig. 4-11). The co-occurrence of andalusite and sillimanite in the studied samples constrains the peak pressure to be in the range between 2.8 and 3.2 kbar. In several thin sections of orbicular metatexites, andalusite is partially replaced by sillimanite, with these textural features suggesting that Sil represents the stable aluminosilicate. This is documented in other metamorphic terranes (e.g. White et al. 2003) and advocates for the metastable nature of andalusite at higher temperatures beyond its stability field. The absence of cordierite in the banded metapelites allows a further refinement of this pressure range, suggesting 3 kbar. This result, which is consistent with both the fluid rich and the excess fluids scenarios, is also in agreement with the mineral paragenesis geobarometer of Pattison and Tracy (1992), and Pattison and Vogl, (2005). Thesedefined pressures <3.5 kbar for andalusite bearing metapelites lacking staurolite and, in particular, confines the ambient conditions to pressures under 3.1 kbar for rocks with Crd+Sil+Kfs assemblages. These pressure estimates are also consistent with field constraints on the maximum thickness reached by the Permo-Triassic sedimentary sequence, which was estimated by Berra and Felletti (2011) in ca. 10km. Moreover, the area experienced severe shortening during the Alpine orogeny without being affected by regional metamorphism, which determined the shortening and thickening of the crustal section successively intruded by the Adamello batholith (e.g. Schönborn, 1992), increasing the maximum thickness of the Permo-Mesozoic succession in the studied area. Finally, it is worth noting that pressures ranging between 3-5 kbar were calculated for the emplacement of the Adamello batholith using the Al-in-horneblende geobarometer (Brack et al., 1983; Schaltegger et al., 2019) and 2-4 kbar were reported by Müntener et al. (2021). Therefore, our data bring tighter constraints on the intrusion conditions for the Adamello pluton in the central part of the Adamello massif.

Concerning temperature, the peak assemblage indicates 680 and 720°C for both fluid assisted and fluid rich scenarios (Fig. 4-11). By comparing the phase abundance of the modelled scenarios we were able to further narrow the peak P-T fields defined by the two lithotypes. For the orbicular metatexites the best fit for temperature is around 690-700°C while for the banded metatexites this is ca. 690°C. These values match with the temperatures calculated using the Na-in-cordierite thermometer (Tropper et al., 2018, Fig. 4-12). In fact, the temperature estimates for the Crd-bearing rocks in the melt zone are between 672 and 709°C with a mean temperature estimate of 687°C.

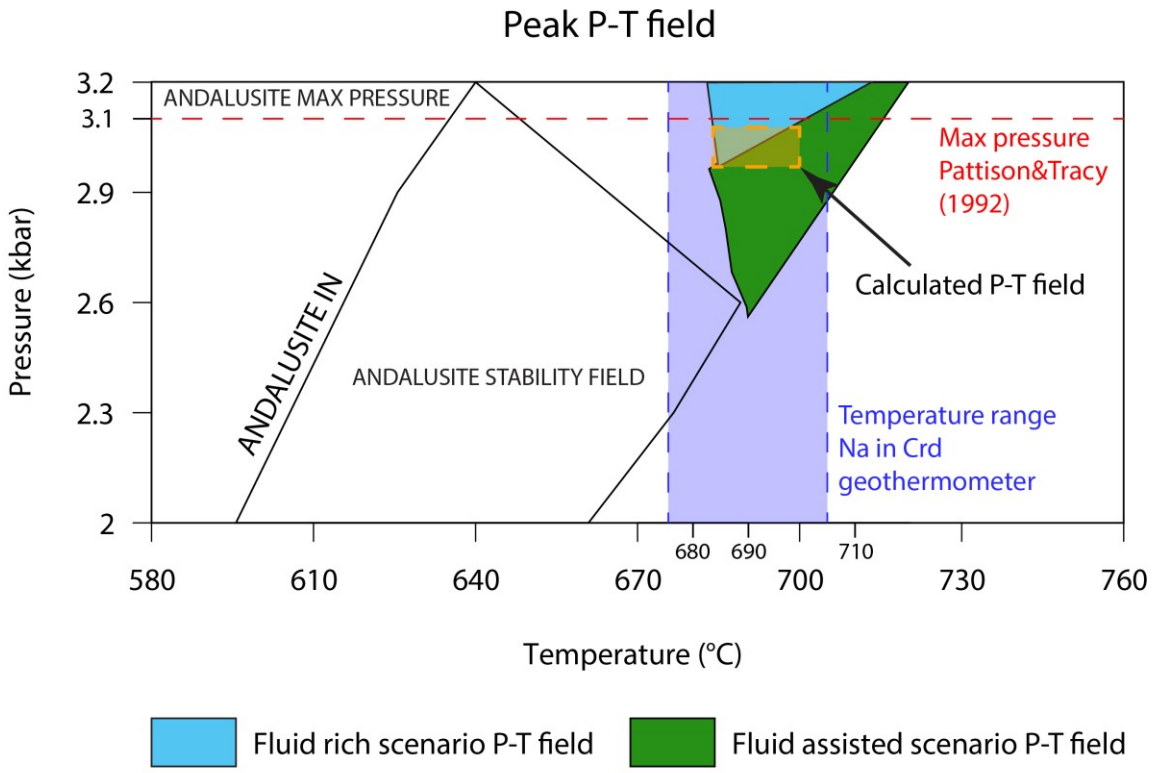

Figure 4-11 T (°C) vs. Na (apfu) in cordierite at different distances from the pluton. The temperatures were calculated using the Na in Crd geothermometer of Tropper et al. (2018);

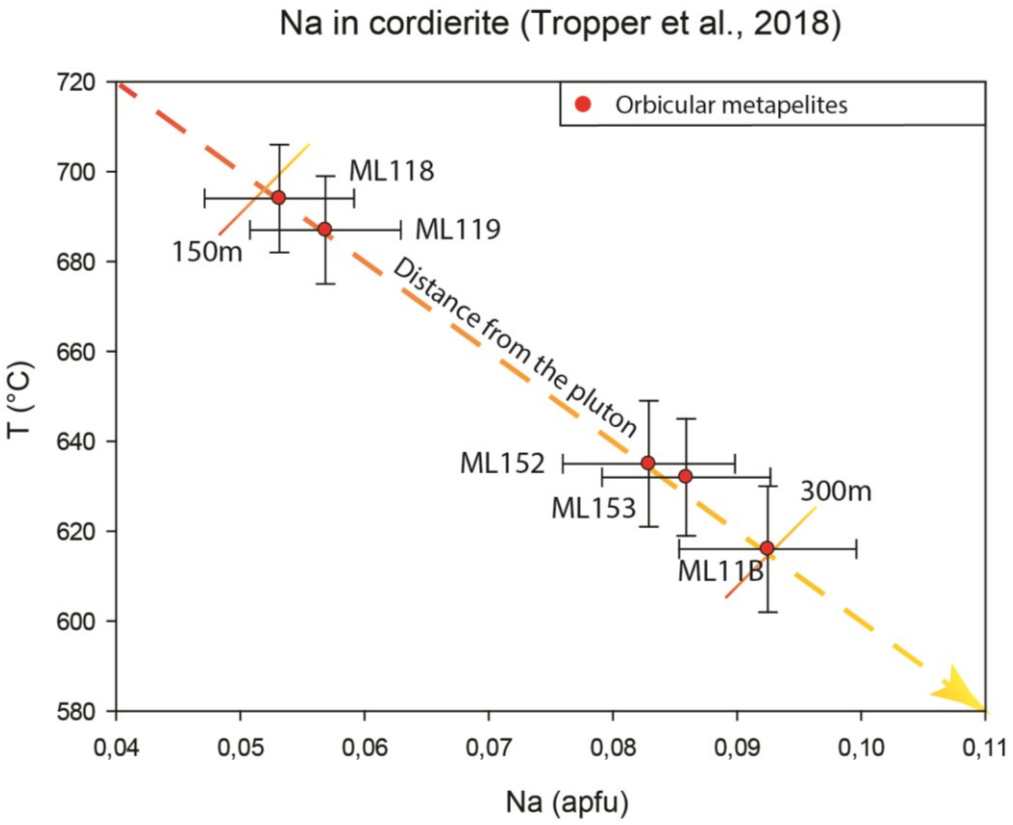

Figure 4-12 Mineral isopleths intersection highlighting the peak P-T field reached by the Verrucano Lombardo metapelites.

In addition, temperature data obtained using the Na-in-Crd geothermometer for the Crd-bearing orbicular metapelites, sampled at ca. 160m from the intrusion are in agreement with the temperatures estimated by Floess and Baumgartner (2015) through thermal modelling in the Adamè Valley thermal aureole. These temperatures vary from 815°C at 25m from the intrusion and 670-680°C at 100-200m, with this latter range obtained for rocks of the Variscan basement located a few meters apart from where we have sampled the orbicular metatexites.

Several authors have pointed out that trace elements such as B, Li, F and P, which are not included in the phase equilibria modeling calculations, may shift the position of the solidus by a few tens of degrees. In particular, the influence of boron in metapelites remains highly debated with some authors suggesting that the lack of a tourmaline solution model could lead to an overestimation of the peak temperature of the system as boron is thought to play a significant role in lowering the solidus temperature (e.g. Cesare et al., 2008). In contrast, in an experimental study on the low-pressure partial melting behavior of natural boron-bearing metapelites, Spicer, et al. (2004) found that even when tourmaline is a reactant phase in the partial melting process, it does not shift the position of the solidus. These authors concluded that the infiltration of boron-rich fluids into high-grade metasedimentary rocks, at near solidus conditions would likely result in tourmaline precipitation, rather than triggering substantial partial melting. Finally, high concentrations of lithium and fluorine, (i.e. 1 to 2 wt.% Li_2O and 4 to 5 wt.% F) were also suggested to lower the solidus by a few tens of degrees and significantly lower melts viscosity (Bartels et al., 2011; 2015). Despite the fact that boron, lithium and fluorine are likely to be liberated during micas dehydration in the Forcel Rosso area, the almost perfect agreement between the phase equilibria modeling and the Na in Crd geothermometer indicates that these elements did not impact significantly on the position of the solidus in the Adamello thermal aureole at Forcel Rosso.

4.9.2 Chemical Evolution of Metapelites and Melts

The field and petrographic observations, united with the stratigraphic positions of the collected samples, concur in defining the described metapelitic lithotypes as part of a continuous evolution from low to high metamorphic grade up to anatexis. The evolution of the Forcel Rosso metamorphic-magmatic system can be disclosed by looking at the chemical diagrams reporting the content in alkali and Al_2O_3 for the metapelites, leucosomes and pegmatites. The metapelites in the melt-zone have produced significant amounts of melt resulting in the accumulation of restitic and peritectic mafic minerals in the residuum, which are mainly represented by biotite, sillimanite and cordierite. The effect of this process can be observed in the Al_2O_3 vs. SiO_2 (Fig. 9) diagram, where Al is concentrated

in the melt-depleted metatexites while SiO_2 is mostly incorporated in the melts. We therefore argue that the process of melt loss accounts for most of the chemical difference existing between unmetamorphosed, foliated/spotted and orbicular metapelites as shown in the K_2O vs. Na_2O+CaO diagram (Fig. 4-13a). The banded metapelites are enriched in K_2O compared to the orbicular metapelites. This feature can be explained by invoking melting of the same lithotype under different fluid conditions. In fact, the high counsumption of Pl and Qz in banded metapelites (fluid rich scenario) could have concentrated Kfs and Bt in the rock, therefore increasing its K_2O content after efficient melt extraction. Alternatively, it is also possible that this minor difference in K_2O between the two partially molten rocks is due to the fluid mediated retrograde rehydration of the banded metapelites. This is supported by textural and petrographic evidence as this lithotype shows high concentrations of retrograde Ms overgrowing Sil aggregates. These reactions were extensively described by Clarke et al. (2005) and particularly the large individual crystals observed in our samples are interpreted as caused by medium temperature retrogression of aluminosilicates in the presence of aqueous fluids. Textural observations suggest that in our samples Kfs is not involved in this reaction, so the fluids had to be K-bearing in order to be able to pervasively rehydrate Sil aggregates.

The major elements composition of leucosomes in the orbicular metapelites, (Fig. 4-10a-b, 4-13a-b), is similar to the composition obtained by the thermodynamic modeling, thus suggesting that these melts represent primary anatectic melts. The compositions of these leucosomes is also compatible with those of other metapelite-derived leucosomes (Sawyer et al., 1987; Bea et al., 1994) and to fluid present experimental melts (Gao et al., 2016 and references therein; Michaud et al., 2021) (Fig. 4-10a-b). The lack of medium scale extraction structures in the orbicular metapelites supports the idea that the majority of the produced melt in this rock remained in-situ.

On the other hand, the leucosomes hosted in the banded metapelites show a different composition departing from the composition of the calculated primary melts. These leucosomes in fact, have extremely high K_2O and Al_2O_3 contents and very low Na/K ratio. The petrographic study and their peculiar chemical features suggest that they do not represent primary melts but cumulates dominated by K-feldspar formed from a granitic melt composition similar to the leucogranitic dykes observed by Morfin et al. (2014) in the Opinaca subprovince in Canada. The cumulitic nature of these leucosomes (modal composition ca. 83% Kfs, 4% Bt and 10% Qz), their connections to pervasive collapse structures andthe lack of sizeable dikes in the banded metapelites led us to infer that most of the produced melt was efficiently extracted and migrated away. The banded metapelites contain 12-15 vol.% of residual Kfs-rich leucosome while our calculations suggest that this rock produced ca. 30 to 40 vol.% of melt. Importantly, the metapsammites outcropping nearby do not show any evidence of

partial melting but host pegmatitic dikes and aplitic veins that are likely to originate from the metapelites. These lines of evidence led us to conclude that ca. 60% of the anatectic melt produced in the banded metapelites left its source and accumulated in the more competent psammitic layer at the stratigraphic contact with the Servino formation. Starting from the composition of the anatectic melt derived from the phase equilibria modelling at 3 kbar and 690°C, we calculated the chemical composition of the extracted melt by subtracting the composition of the leucosomes in the banded metapelites, corresponding to nearly exclusive Kfs fractionation (Fig. 4-13b). This extracted melt composition, while considering the uncertainties related to phase equilibria modelling and mass balance, closely fits the major element mean composition of the LCT pegmatites hosted in the nearby metapsammites at 200m distance from the melt source, marking these structures as the likely final accumulation of the melts, where they ultimately internally differentiated (Fig. 4-13b).

Barren pegmatites are found between the VER melt zone and the LCT pegmatites, they show definite and linear contacts with the host rock and they are diffused both into the metapsammitic and metapelitic rocks. Their chemical composition does not fit with the composition of primary melts (Fig. 4-10a-b). Their K_2O-rich composition (Fig. 4-13a-b) indicates that, as in the case of the leucosome in the banded metapelites, fractional crystallization was important in their genesis. They may represent portions of the LCT pegmatites system enriched in Kfs, Qz, Ms and Tur formed during the fractionation of the migrating magma from the metapelitic source to the metapsammitic emplacement area.

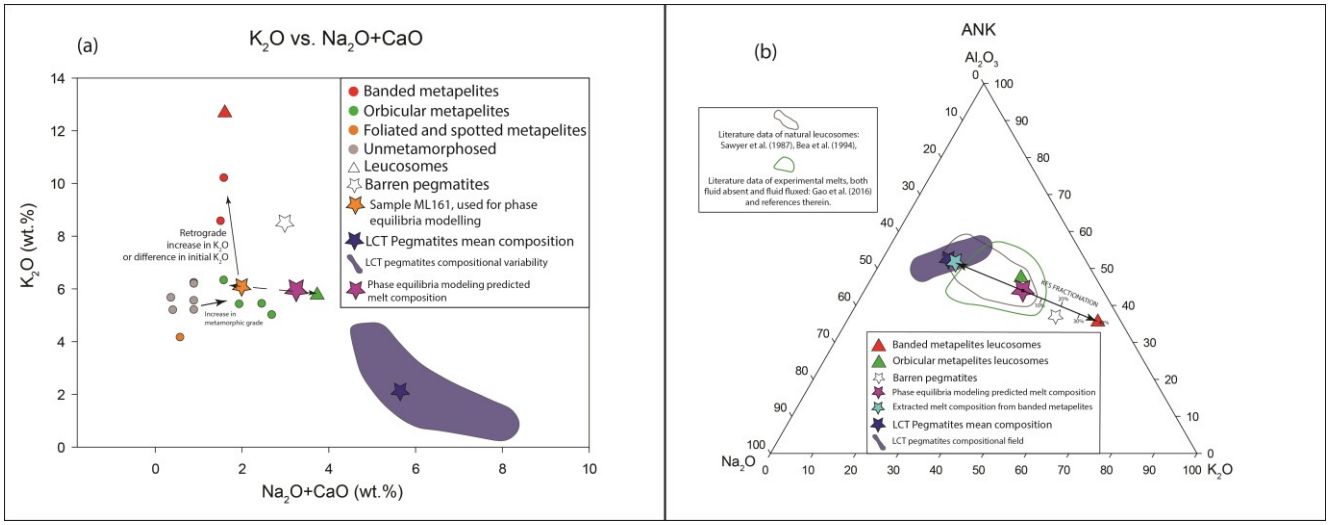

Figure 4-13 a) Whole-rock Na2O+CaO vs. K2O diagram. The dashed lines indicate melt segregation from migmatites to leucosomes, arrows indicate the evolution history of the metamorphic system; b) Al2O3-Na2O-K2O ternary diagram describing the variability of melts in the Forcel Rosso area. The black trend line highlights the Kfs fractionation process that produced barren pegmatites finally forming the LCT parent melt.

4.9.3 Role of fluids during partial melting

The different distribution of fluids at the small scale caused the formation of two different metatexites starting from the same protolith in the same P-T field. In this low pressure, contact metamorphic environment partial melting progressed under fluid present conditions with some areas experiencing limited aqueous fluids circulation whereas some areas experienced more pronounced percolation, which triggered the production of higher melt fractions. Phase equilibria modelling indicates that the fluid limited scenario, cannot produce the amount of melt observed in the Forcel Rosso area at 680-700°C and that fluid present melting was required in order to form both the orbicular and banded metatexites as well as their leucosomes. We highlight that a system consuming the equivalent of its available dehydration fluids (fluid assisted case, Fig. 4-6) can produce the melt fraction observed in the orbicular metatexites (ca. 20%). The occurrence of unaltered cordierite in the orbicular metapelites suggests that the fluids were completely consumed during the melting reactions and incorporated into the melt. In fact, if fluids were present during the retrograde metamorphic path, this would have caused the complete pinitization of the cordierite.

The origin of the banded metapelites can only be explained by partial melting in a fluid rich environment resulting in the production of ca. 35 wt% of leucocratic melt. In this context, the nearly undisturbed schlieric texture that characterize this rock is the result of an efficient mechanism of melt segregation as also supported by field and chemical lines of evidence. Fluid-present congruent melting of metapelites has a stoichiometry that consumes lower amounts of Bt and Sil and higher volumes of Qz and Kfs with respect to the reaction producing the orbicular metapelites (Fig. 4-8), with this feature resulting in the formation of the sillimanite-rich residuum observed in the banded metapelites.
At 3 kbar, muscovite dehydration occurred subsolidus producing ca. 1.5 wt.% of free H_2O during contact metamorphism of the Verrucano Lombardo metapelites. This amount of fluids cannot be hosted within the metapelites (ca. 0.1 vol.% of porosity, e.g. Thompson and Connelly, 1990) and was thus likely extracted through a net of widespread microcracks likely linked to pore overpressure (e.g. Connolly, 1997). In our model, these fluids were heterogeneously distributed and concentrated in the thermal aureole triggering different melting reactions. Fluid distribution is probably linked to small-scale differences in permeability between the rock types as well as controlled by structural parameters. Although no major fluid were recognized in the field, the banded metapelites were significantly richer in chlorite-filled fractures than their orbicular counterpart, advocating for a more efficient fluid transfer in the rock mass during metamorphism. We infer that above the solidus, the microcracks that were originally developed at subsolidus conditions were used by the aqueous fluids to move through

the rock mass and subsequently facilitated the transfer of the melt phase, particularly in the banded metapelites which experienced efficient melt extraction. Volume decrease is an intrinsic characteristic of fluid present melting (e.g. Weinberg and Hasalova, 2015) which although accounting for the occurrence of orbicular metapelites where melt remained trapped in-situ, poses a problem with our hypothesis of melt extraction from the banded metapelites. In the Forcel Rosso area, the syn-metamorphic deformation, reported in Fig. 4-3 and 4-4, and compressive stress linked to the plutonic intrusion induced flattening, folding and formation of a foliation sub-parallel to the magmatic contact, particularly in the banded metatexites, which may have counteracted the volume loss and caused the water-saturated anatectic melt to escape its source. The compatibility in the structural trends of the banded metapelites suture structures (Fig. 4-3e) and the metapelites-hosted pegmatites suggests that melt escape was then tectonically controlled by the opening of fractures perpendicular to the rock foliation connected to the pegmatitic system.

By looking at the phase diagram in Fig. 4-6, we observe that the commonly inferred amount of pore water contained in a metapelite is not sufficient to trigger partial melting below 4.5 kbar and 800°C. Therefore, we conclude that partial melting of metapelites in the upper crust should always be linked to fluids circulation. in the Forcel Rosso area, there are two main possible fluid sources: i) magmatic hydrothermal fluids derived from the Adamello pluton, which is thought to originate from volatile-rich melts (e.g. Müntener et al., 2021) or ii) metamorphic fluids formed by dehydration reactions during contact metamorphism. The Adamello batholith emplacement involved intense magmatic fluids metasomatism as shown by several portions of the skarn-hosting carbonatic country rocks in the southern part of the Re di Castello pluton (e.g. Gerdes et al., 1999, Marger&Mueller, 2014) and other zones of the thermal aureole. Furthermore, multiple pegmatoid and aplitic dykes are present in the Forcel Rosso-Mount Ignaga area inside the Western Adamello Tonalite advocating for the magmatic mass being fluid rich at least in its terminal stages of evolution. However, Floess and Baumgartner (2015) and Floess et al. (2015) argued that oxygen and carbon isotopes analyses performed on carbonates at 100-200m from the intrusion show no evidence of significant meteoric or magmatic fluid flow. This is in accordance with our field observations in which metasomatized carbonate country rocks are limited to the innermost thermal aureole (first 30m from the magmatic contact). Although, we do not have decisive isotopic data to shed lights into the origin of fluids in the thermal aureole, our field observations suggest that circulation of magmatic hydrothermal fluids was limited to the innermost portion of the aureole and that the fluids accumulated in the metapelites were likely of metamorphic origin. We argue that the aqueous fluids were derived from other portions of the same metamorphic system, in a similar fashion as White et al., (2005) describe the partial melting event at Broken Hill where the fluids produced in one area fluxed another part of the system. Within the same

source the subsolidus dehydration of micas give rise to internally-produced aqueous fluids that due to the low porosity of the rock tend to escape from the system increasing the permeability of the rock and opening the metamorphic system to fluids circulation. This implies that fluid circulation during prograde metamorphism may influence partial melting reactions even at the small scale, therefore creating local fluid present anatectic conditions in metamorphic terranes, which control melt and restite formation. Our conclusions are also concordant with the hypothesis put forth by Weinberg and Hasalova (2015) that water fluxes lead to heterogeneous melt production at the meter scale. As shown in the models, fluid present melting is a transient phase in the history of migmatites, particularly if the amount of available fluid is limited: this leads to partial melting being initially fluid fluxed to become fluid absent with increasing temperature. This mechanism could explain the difficulties encountered by several authors in rigidly defining fluid absent versus fluid present partial melting sources for plutons and magmatic suites as even small-scale variations of the fluid component could influence melt productivity and restite mineral modal abundances.

4.10 Conclusions

The pelitic layers of the Verrucano Lombardo formation underwent thermal metamorphism in the Adamello pluton aureole and show evidence of partial melting. Calculated peak P-T conditions for the metamorphic event are constrained to be between 680-700°C at 3 kbar. Phase equilibria modeling using low-grade metamorphosed samples collected from the same stratigraphic position in the Permian succession show that fluids played a major role in the partial melting process. Small-scale heterogeneities in fluid presence during partial melting is well documented in the rock record and generated two lithotypes. The anatectic magma derived from the metapelites was granitic and strongly peraluminous. This was preserved as in-situ leucosomes in the orbicular metapelites while in the banded metapelites they migrated away from the source. These extracted melts underwent Kfs fractional crystallization and led to the formation of small Na_2O-enriched pegmatitic bodies, which subsequently internally evolved and produced complex LCT-pegmatitic dikes.

4.11 Acknowledgements

This publication is part of the PhD project of Lorenzo Magnani. The Co-Editor, Nadia Malaspina, and the two reviewers, Etienne Skrzypek and Kai Zhao are gratefully thanked for their valuable comments and suggestions, which improved the manuscript quality. Andrea Risplendente is thanked for the EPMA–WDS analyses. The authors acknowledge the Italian Ministry of Education and University (MIUR) for the support through the project “Dipartimenti di Eccellenza 2018–2022 – Le Geoscienze

per la società: Risorse e loro evoluzione". The Stellenbosch University (SA) Center for Analytical Facilities (CAF) is thanked for their contribution in the XRF analyses.

4.12 References

Barbey, P., Marignac, C., Montel, J.M., Macaudiere, J., Gasquet, D., Jabbori, J., 1999. Cordierite growth textures and the conditions of genesis and emplacement of crustal granitic magmas: the Velay granite complex (Massif Central, France). Journal of Petrology, 40(9), 1425-1441.

Bartels, A., Vetere, F., Holtz, F., Behrens, H., Linnen, R.L., 2011. Viscosity of flux-rich pegmatitic melts. Contributions to Mineralogy and Petrology, 162(1), 51-60.

Bartels, A., Behrens, H., Holtz, F., Schmidt, B.C., 2015. The effect of lithium on the viscosity of pegmatite forming liquids. Chemical Geology, 410, 1-11.

Bea, F., Pereira, M.D., Stroh, A., 1994. Mineral/leucosome trace-element partitioning in a peraluminous migmatite (a laser ablation-ICP-MS study). Chemical Geology, 117(1-4), 291-312.

Berra, F., Felletti, F., 2011. Syndepositional tectonics recorded by soft-sediment deformation and liquefaction structures (continental Lower Permian sediments, Southern Alps, Northern Italy): stratigraphic significance. Sedimentary Geology, 235(3-4), 249-263.

Brack, P., 1983. Multiple intrusions-examples from the Adamello batholith (Italy) and their significance on the mechanisms of intrusion. Memorie della Societa Geologica Italiana, 26(1), 145-157.

Broderick, C., Wotzlaw, J.F., Frick, D.A., Gerdes, A., Ulianov, A., Günther, D., Schaltegger, U., 2015. Linking the thermal evolution and emplacement history of an upper-crustal pluton to its lower-crustal roots using zircon geochronology and geochemistry (southern Adamello batholith, N. Italy). Contributions to Mineralogy and Petrology, 170(3), 1-17.

Callegari, E., Brack, P., 2002. Geological map of the Tertiary Adamello batholith (northern Italy): Explanatory notes and legend. Memorie di Scienze Geologiche, 54, 19-49.

Černý, P., Ercit, T.S. 2005. The classification of granitic pegmatites revisited. The Canadian Mineralogist, 43(6), 2005-2026.

Cesare, B., Satish-Kumar, M., Cruciani, G., Pocker, S., Nodari, L., 2008. Mineral chemistry of Ti-rich biotite from pegmatite and metapelitic granulites of the Kerala Khondalite Belt (southeast India): Petrology and further insight into titanium substitutions. American Mineralogist 93, 327-338.

Clarke, D.B., 1995. Cordierite in felsic igneous rocks: a synthesis. Mineralogical Magazine, 59(395), 311-325.

Clarke, D.B., Dorais, M., Barbarin, B., Barker, D., Cesare, B., Clarke, G., El Baghdadi, M., Erdmann, S., Förster, H.-J., Gaeta, M., Gottesmann, B., Jamieson, R.A., Kontak, D.J., Koller, F., Gomes, G.L., London, D., Morgan, G.B. VI, Neves, L.J.P.F, Pattison, D.R.M., Pereira, A.J.S.C., Pinchavant, M., Rapela, C.W., Renno, A.D., Richards, S., Roberts, M., Woodard, H.H., 2005. Occurrence and origin of andalusite in peraluminous felsic igneous rocks. Journal of Petrology, 46(3), 441-472.

Clemens, J., Watkins, J.M., 2001. The fluid regime of high-temperature metamorphism during granitoid magma genesis. Contributions to Mineralogy and Petrology, 140(5), 600-606.

Connolly, J.A.D., 1997. Devolatilization-generated fluid pressure and deformation-propagated fluid flow during prograde regional metamorphism. Journal of Geophysical Research: Solid Earth, 102(B8), 18149-18173.

Connolly, J.A.D., 2009. The geodynamic equation of state: what and how. Geochemistry, Geophysics, Geosystems, 10(10).

Droop, G.T., Moazzen, M., 2007. Contact metamorphism and partial melting of Dalradian pelites and semipelites in the southern sector of the Etive aureole. Scottish Journal of Geology, 43(2), 155-179.

Dyck, B., Waters, D.J., St-Onge, M.R., Searle, M.P., 2020. Muscovite dehydration melting: Reaction mechanisms, microstructures, and implications for anatexis. Journal of Metamorphic Geology, 38(1), 29-52.

Farina, F., Mayne, M.J., Stevens, G., Soorajlal, R., Frei, D., Gerdes, A. 2020. Phase equilibria constraints on crystallization differentiation: insights into the petrogenesis of the normally zoned Buddusò Pluton in north-central Sardinia. Geological Society, London, Special Publications, 491(1), 243-265.

Floess, D., Baumgartner, L., 2013. Formation of garnet clusters during polyphase metamorphism. Terra Nova, 25(2), 144-150.

Floess, D., Baumgartner, L.P., 2015. Constraining magmatic fluxes through thermal modelling of contact metamorphism. From: Caricchi L., Blundy J.D. (eds) Chemical, Physical and Temporal Evolution of Magmatic Systems. Geological Society, London, Special Publications 422.

Floess, D., Baumgartner, L.P., Vonlanthen, P., 2015. An observational and thermodynamic investigation of carbonate partial melting. Earth and Palentary Science Letters 409, 147-156.

Gao, P., Zheng, Y.F., Zhao, Z.F., 2016. Experimental melts from crustal rocks: a lithochemical constraint on granite petrogenesis. Lithos, 266, 133-157.

Gavrilenko, P., & Gueguen, Y., 1993. Fluid overpressures and pressure solution in the crust. Tectonophysics, 217(1-2), 91-110.

Genier, F., Bussy, F., Epard, J.L., Baumgartner, L., 2008. Water-assisted migmatization of metagraywackes in a Variscan shear zone, Aiguilles-Rouges massif, western Alps. Lithos, 102(3-4), 575-597.

Gerdes, M.L., Baumgartner, L.P., Valley, J.W., 1999. Stable isotopic evidence for limited fluid flow through dolomitic marble in the Adamello contact aureole, Cima Uzza, Italy. Journal of Petrology 40, n. 6, 853-872.

Guillong, M., Meier, D.L., Allan, M.M., Heinrich, C.A., Yardley, B.W., 2008. Appendix A6: SILLS: A MATLAB-based program for the reduction of laser ablation ICP-MS data of homogeneous materials and inclusions. Mineralogical Association of Canada Short Course, 40, 328-333.

Harley, S.L., 1989. The origins of granulites: a metamorphic perspective. Geological Magazine, 126(3), 215-247.

Holland, T., Powell R., 1996. Thermodynamics of order-disorder in minerals: II. Symmetric formalism applied to solid solutions. American Mineralogist, 81(11-12), 1425-1437.

Holland, T., Powell, R., 2003. Activity–composition relations for phases in petrological calculations: an asymmetric multicomponent formulation. Contributions to Mineralogy and Petrology, 145(4), 492-501.

Holland, T.J.B., Powell, R., 2011. An improved and extended internally consistent thermodynamic dataset for phases of petrological interest, involving a new equation of state for solids. Journal of Metamorphic Geology, 29, 333-383.

Holness, M.B., Sawyer, E.W., 2008. On the pseudomorphing of melt-filled pores during the crystallization of migmatites. Journal of Petrology, 49(7), 1343-1363.

Holness, M.B., Clemens, J.D., Vernon, R.H., 2018. How deceptive are microstructures in granitic rocks? Answers from integrated physical theory, phase equilibrium, and direct observations. Contributions to Mineralogy and Petrology, 173(8), 1-18.

Jung, S., Hoernes, S., Mezger, K., 2000. Geochronology and petrogenesis of Pan-African, syn-tectonic, S-type and post-tectonic A-type granite (Namibia): products of melting of crustal sources, fractional crystallization and wall rock entrainment. Lithos, 50(4), 259-287.

Lorenzoni, S., 1955. Studio geologico-petrografico dell'Alpe di Bos (Adamello occidentale). Società Cooperativa Tipografica.

Marger, K., Mueller, T., 2014. Formation of contact metamorphic reaction rims in the Southern Adamello Massif, N-Italy: A natural study on transport controlled growth mechanisms. EGU General Assembly 2014.

Mayne, M.J., Moyen, J.-F., Stevens, G., Kaislaniemi, L., 2016. Rcrust: a tool for calculating path-dependent open system processes and application to melt loss. J. Metamorph. Geol. 34, 663–682.

Mayne, M.J., Stevens, G., Moyen, J.-F., 2019. A phase equilibrium investigation of selected source controls on the composition of melt batches generated by sequential melting of an average metapelite. Geological Society, Londo, Special Publications, 491, 223-241.

Mayne, M.J., Stevens, G., Moyen, J.-F., Johnson, T., 2020. Performing process-oriented investigations involving mass transfer using Rcrust: a new phase equilibrium modelling tool. From: Janusek V., Bonin B., Collins W.J., Farina F., Bowden P., (eds) 2020. Post-Archean granitic rocks: petrogenetic processes and tectonic environments. Geological Society, London, Special Publications, 491, 209-221.

McCarthy, A., Chelle-Michou, C., Müntener, O., Arculus, R., Blundy, J., 2018. Subduction initiation without magmatism: The case of the missing Alpine magmatic arc. Geology, 46(12), 1059-1062.

Michaud, J.A.S., Pichavant, M., Villaros, A., 2021. Rare elements enrichment in crustal peraluminous magmas: insights from partial melting experiments. Contributions to Mineralogy and Petrology, 176(11), 1-33.

Morfin, S., Sawyer, E.W., Bandyayera, D., 2014. The geochemical signature of a felsic injection complex in the continental crust: Opinaca Subprovince, Quebec. Lithos, 196, 339-355.

Müntener, O., Ulmer, P., Blundy, J. D., 2021. Superhydrous arc magmas in the Alpine context. Elements: An International Magazine of Mineralogy, Geochemistry, and Petrology, 17(1), 35-40.

Patiño Douce, A.E., Harris, N., 1998. Experimental constraints on Himalayan anatexis. Journal of petrology, 39(4), 689-710.

Patiño Douce, A.E., Johnston, A.D., 1991. Phase equilibria and melt productivity in the pelitic system: implications for the origin of peraluminous granitoids and aluminous granulites. Contributions to Mineralogy and Petrology, 107(2), 202-218.

Pattison, D.R.M., Tracy, R.J., 1992. Phase equilibria and themobarometry of metapelites. In: Contact Metamorphism (Kerrick M.D., ed) Rev. Mineral. 26, 105-206.

Pattison, D.R.M., Vogl, J.J., 2005. Contrasting sequences of metapelitic mineral-assemblages in the aureole of the tilted Nelson Batholith, British Columbia: Implications for phase equilibria and pressure determination in andalusite-sillimanite-type settings. The Canadian Mineralogist 43, 51-88.

Pennacchioni, G., Di Toro, G., Brack, P., Menegon, L., Villa, I.M., 2006. Brittle–ductile–brittle deformation during cooling of tonalite (Adamello, Southern Italian Alps). Tectonophysics, 427(1-4), 171-197.

Perotti, C.R., Siletto, G.B., 1996. Le caratteristiche geometriche dei bacini permiani tra la ValCamonica e la Val Giudicarie (Sudalpino Centrale). Atti Tic. Sc. Terra, 1996 (Ser. Spec.), 4: 77-86, 6 figg., Pavia.

Peters, D., Pettke, T., 2016. Evaluation of major to ultra trace element bulk rock chemical analysis of nanoparticulate pressed powder pellets by LA-ICP-MS. Geostandards and Geoanalytical Research, vol. 41, n. 1, pp. 5-28.

Pickering, J.M., Johnston, D.A., 1998. Fluid-absent melting behavior of a two-mica metapelite: experimental constraints on the origin of Black Hills granite. Journal of Petrology, 39(10), 1787-1804.

Riklin, K., 1983. Contact metamorphism of the permian «Red Sandstone» in the Adamello area. Memorie della Società Geologica Italiana, 26(1), 159-169.

Salomon, W., 1894. Sul metamorfismo di contatto, subito dalle arenarie permiane della Val Daone. Giorn. Mineral., Cristallogr., Petrogr., 5, Tipogr. Fusi, Pavia, 97-147.

Sawyer, E.W., 1987. The role of partial melting and fractional crystallization in determining discordant migmatite leucosome compositions. Journal of Petrology, 28(3), 445-473.

Sawyer, E.W., 2008. Atlas of Migmatites. The Canadian Mineralogist, Special Publication 9.

Sawyer, E.W., 2010. Migmatites formed by water-fluxed partial melting of a leucogranodiorite protolith: Microstructures in the residual rocks and source of the fluid. Lithos, 116(3-4), 273-286.

Schaltegger, U., Nowak, A., Ulianov, A., Fisher, C.M., Gerdes, A., Spikings, R., Whitehouse, M.J., Bindeman, I., Hanchar, J.M., Duff, J., Vervoort, J.D., Sheldrak,e T., Caricchi, L., Brack, P., Müntener,

O., 2019. Zircon Petrochronology and $^{40}Ar/^{39}Ar$ Thermochronology of the Adamello Intrusive Suite, N. Italy: Monitoring the Growth and Decay of an Incrementally Assembled Magmatic System. Journal of Petrology 60, vol. 4, 701-722.

Schönborn, G., 1992. Kinematics of a transverse zone in the Southern Alps, Italy. In Thrust tectonics (pp. 299-310). Springer, Dordrecht.

Schunnach, D., Garzanti, E., Confalonieri, M.P., 1996. Stratigraphy and petrography of Upper Permian to Anisian terrigenous wedges (Verrucano Lombardo, Servino and Bellano Formations; western Southern Alps). Riv. Ital. Pal. Strat., 102 (1): 27-48, 12 figg., 2 tabb., Milano.

Sola, A.M., Hasalová, P., Weinberg, R.F., Suzaño, N.O., Becchio, R.A., Hongn, F.D., Botelho, N., 2017. Low-P melting of metapelitic rocks and the role of H2O: Insights from phase equilibria modelling. Journal of Metamorphic Geology, 35(9), 1131-1159.

Spicer, E.M., Stevens, G., Buick, I.S., 2004. The low-pressure partial-melting behaviour of natural boron-bearing metapelites from the Mt. Stafford area, central Australia. Contributions to Mineralogy and Petrology, 148(2), 160-179.

Stevens, G., Van Reenen, D., 1992. Partial melting and the origin of metapelitic granulites in the Southern Marginal Zone of the Limpopo Belt, South Africa. Precambrian research, 55(1-4), 303-319.

Stevens, G., Clemens, J.D., 1993. Fluid-absent melting and the roles of fluids in the lithosphere: a slanted summary?. Chemical Geology, Volume 108, Issues 1–4, 5 August 1993, Pages 1-17.

Thompson, A. B., & Connolly, J. A. D., 1990. Metamorphic fluids and anomalous porosities in the lower crust. Tectonophysics, 182(1-2), 47-55.

Tropper, P., Wyhlidal, S., Haefeker, U.A., Mirwald, P.W., 2018. An experimental investigation of Na incorporation in cordierite in low P/high T metapelites. Miner. Petrol. 112, 199-217.

Vernon, R.H., 1978. Pseudomorphous replacement of cordierite by symplectic intergrowths of andalusite, biotite and quartz. Lithos, 11(4), 283-289.

Vielzeuf, D., Clemens, J.D., Pin, C., Moinet, E., 1990. Granites, granulites, and crustal differentiation. In Granulites and crustal evolution (pp. 59-85). Springer, Dordrecht.

Vielzeuf, D., Holloway, J.R., 1988. Experimental determination of the fluid-absent melting relations in the pelitic system. Contributions to Mineralogy and Petrology, 98(3), 257-276.

Viola, G., Mancktelow, N.S., Seward, D., 2001. Late Oligocene-Neogene evolution of Europe-Adria collision: New structural and geochronological evidence from the Giudicarie fault system (Italian Eastern Alps). Tectonics, 20(6), 999-1020.

Ward, R., Stevens, G., Kisters, A., 2008. Fluid and deformation induced partial melting and melt volumes in low-temperature granulite-facies metasediments, Damara Belt, Namibia. Lithos, 105(3-4), 253-271.

Weinberg, R.F., Hasalová, P., 2015. Water-fluxed melting of the continental crust: A review. Lithos, 212, 158-188.

White, R. W., Pomroy, N. E., & Powell, R. (2005). An in situ metatexite–diatexite transition in upper amphibolite facies rocks from Broken Hill, Australia. Journal of Metamorphic Geology, 23(7), 579-602.

White, R.W., Powell, R., Holland, T.J.B., Worley, B., 2000. The effect of TiO2 and Fe2O3 on metapelitic assemblages at greenschist and amphibolite facies conditions: mineral equilibria calculations in the system K2O–FeO–MgO–Al2O3–SiO2–H2O–TiO2–Fe2O3.Journal of Metamorphic Geology, 18, 497–511.

White, R.W., Powell, R., Clarke, G.L., 2002. The interpretation of reaction textures in Fe-rich metapelitic granulites of the Musgrave Block, Central Australia: constraints from mineral equilibria calculations in the system. Journal of Metamorphic Geology, 20,41–55.

White, R.W., Powell, R., Clarke, G.L., 2003. Prograde metamorphic assemblage evolution during partial melting of metasedimentary rocks at low pressures: migmatites from Mt Stafford, Central Australia. Journal of Petrology, 44(11), 1937-1960.

White, J.T., Doherty, J.E., Hughes, J.D., 2014. Quantifying the predictive consequences of model error with linear subspace analysis. Water Resources Research, 50(2), 1152-1173.

Whitney, D.L., Evans, B.W., 2010. Abbreviations for names of rock-forming minerals. American mineralogist, 95(1), 185-187.

Zanettin, B., 1956. Il gruppo del Marsèr, Adamello occidentale: studio geologico-petrografico. Centro Studi di Petrografia e Geologia del Consiglio Nazionale delle Ricerche presso l'Università di Padova.

Chapter 5

Unraveling lithium-rich anatectic pegmatites: insights from the Adamello Massif (Italy).

5.1 Introduction

Lithium is the lightest alkali metal, characterized by high electrochemical activity and redox potential value (Wiśniewska et al., 2018). Numerous industries employ it as a presently irreplaceable element, such as in Li-ion batteries (LIBs), ceramic glass production, nuclear fusion processes, pharmaceutical industry, adhesives, lubricant greases, cements, and electrode welding (e.g. Christmann et al., 2015). The green transition in particular, spearheaded by several countries, is driven by the revolution happening in the automotive sector and to the ever-expanding electronic products market which call for huge and increasing demand for LIBs. Lithium extraction is (and will increasingly be) crucial to satisfy the strong market demand for this metal, whose primary resources are represented by lithium-rich brines and Li-bearing ores such as spodumene and lepidolite pegmatites (e.g Kavanagh et al., 2018). Although brine reservoirs hold a much larger portion of the lithium global resources, these deposits are extremely localized while pegmatites are now of broad interest due to their wider geographic distribution and consequently lesser susceptibility to supply disruptions. Also, their higher lithium concentration and their relatively low costs of exploitation might allow for more flexible responses to market changes (e.g. Kesler et al., 2012).

The renewed interest in Li-enriched magmatic bodies expresses the need for new resources to be discovered which in turn imposes to understand the geological processes responsible for Li concentrations in the continental crust and for pegmatites formation. Pegmatites are shallow-level intrusive rocks characterized by strongly disequigranular textures and exhibit the greatest range of grain sizes known in any rock type, with crystals spanning from sub-millimetric to tens of meters. They typically form small to medium-sized bodies showing extreme zoning and characterized by graphic textures (i.e. Simmons&Webber, 2008), aplites and coarse-grained zones. Among granitic pegmatities, Lithium-Cesium-Tantalum (LCT) pegmatites (Černý&Ercit, 2005) are uncommon shallow-level intrusives representing important source of rare and strategic elements such as Li, Nb and Ta. The process of formation of these lithium-enriched pegmatites is presently not well understood even though several works have been published on this topic (e.g., Černý, 1991; Černý&Ercit, 2005 and references therein; Müller et al., 2022; Wise et al., 2022). These rocks are customarily considered as the product of extreme differentiation through fractional crystallization from a peraluminous

granitic parental magma of S-type affinity (Černý, 1991, Simmons&Webber, 2008). This model has been recently challenged based on field and chemical observations as it implies the occurrence of a close temporal and spatial association between the granite and the pegmatites as well as a simple geometric relationship between these rocks (Villaros and Pichavant, 2019).

In fact, if the genesis of LCT pegmatites is controlled by the physical separation of melt from crystals, the most fractionated and rare element enriched bodies are expected to be located farther from the granitic parental magma. In the last decade, numerous pegmatitic fields have been described having features that are at odds with this simple genetic mechanism, leading different authors to consider alternative models (e.g. Tomascak et al., 1998, Knoll et al., 2018, Schuster et al., 2019). In several cases, the LCT pegmatites are closely associated to migmatites or intruded in high-grade migmatitic terrains while lacking a direct connection to any nearby granitic mass. This evidence has recently brought authors to suggest a possible derivation of pegmatites from small degrees of partial melting of continental lithologies (e.g. Villaros and Pinchavant, 2019, Chakraborty et al., 2020). Even if the so-called anatectic pegmatites have been recognized (e.g. Simmons et al., 1995, 1996, 2016; Schuster et al., 2019) in many high-grade metamorphic terrains, the processes that lead to the formation of mineralized anatectic pegmatites have never been studied in detail and the economic relevance of these rocks is still unclear. Following the anatectic model for the origin of pegmatites, low grade partial melting of metapelites produces highly peraluminous, incompatible elements-rich melts that are chemically similar to the highly evolved terminal products of magmatic differentiation of S-type granites (Moyen et al., 2021). These melts are potentially enriched in water and fluxing elements such as Li, B, P and F which contribute to lower the solidus temperature and viscosity of the melt triggering the development of pegmatitic textures once collected in dykes (Morgan&London, 1999; London, 2005). In a previous recent publication, we have documented LCT pegmatites formed through anatexis of metapelites at low pressure and in the presence of fluid in the thermal aureole of the Eocene-Oligocene Adamello pluton in the Italian Alps (Magnani et al., 2022; Fig. 1). In this work, which represents a follow up from Magnani et al. (2022), we focus our attention on the processes that led to the enrichment in lithium, cesium and tantalum and thus to the formation of small bodies of mineralized pegmatites. The goal of this paper is to shed lights into the behavior of lithium and other critical metals during partial melting, melt segregation and formation of pegmatitic dikes to get a better understanding on the mechanism of enrichment of these elements in felsic crustally-derived magmas. With this work we aim at pinpointing the set of conditions that are required for formation of mineralized pegmatites in anatectic terranes.

5.2 Geological setting of the Forcel Rosso area

5.2.1 Contact metamorphic migmatites

The Forcel Rosso area of the Adamello Massif (Fig. 1), described in detail by Magnani et al. (2022) and Floess and Baumgartner (2015) is characterized by a vertical sequence of Permo-Mesozoic metasediments that were thermometamorphosed by the intrusion of the Adamello pluton in the Eocene-Oligocene. The pre-metamorphic, sedimentary succession was composed of a series of psammitic-pelitic to carbonatic formations starting with Permian continental clastic conglomeratic to pelitic redbeds up to Triassic dolomitic limestones (e.g. Floess and Baugartner 2013 and 2015).
The succession is presently composed of metapelites and marbles that underwent partial melting up to 350m from the magmatic contact (Floess et al., 2015; Magnani et al., 2022). Temperatures at the magmatic contact reached up to 815°C in the Lozio Shales (LOZ), (Floess&Baumgartner, 2015) and decreased to 690-700°C in the metatexites formed from the metapelites of the Verrucano Lombardo formation. Pressure was constrained at around 3 kbar on the base of paragenesis-based geobarometry and phase equilibria modelling (Magnani et al., 2022). Two main types of migmatites are distinguished: a Crd-bearing metatexite, that experienced partial melting through the incongruent reaction Bt+Kfs+Pl+Sil+Qz+H_2O → Crd+melt at relatively low water activity and a Crd-absent metatexite that melted following the congruent reaction Bt+ Kfs+Pl+Sil+Qz+H_2O → melt+H_2O at higher water activity. Field, petrographic and chemical lines of evidence argue for a genetic connection existing between the Crd-absent metatexites and the Li enriched metapelites-hosted pegmatites (Magnani et al., 2022).

In the Forcel Rosso area (Fig. 5-1), two types of leucosomes are hosted in the two types of migmatitic metapelites:

1) in the Crd-bearing migmatites (defined as orbicular metapelites in Magnani et al., 2022), the leucosomes are characterized by Kfs+Qz+Ms+Tur±And assemblages and occupy ca. 10 to 20 vol.% of the outcrops, collecting melt from patches and zones around cordierite poikiloblasts. The chemical composition of the unfractionated leucosomes is similar to the major elements composition of the primary anatectic melt as calculated by thermodynamic modelling.
2) in the Crd-absent migmatites (defined as banded metapelites of Magnani et al., 2022), Kfs+Qz+Bt leucosomes are extremely enriched in K_2O and are cumulates formed through fractional crystallization of the anatectic melt produced from these stromatic metatexites. These leucosomes constitute ca. 10-15 vol.% of the outcrops. Their mineralogical composition and

their connections to pervasive collapse structures indicate that part of the anatectic melt was efficiently extracted from this system.

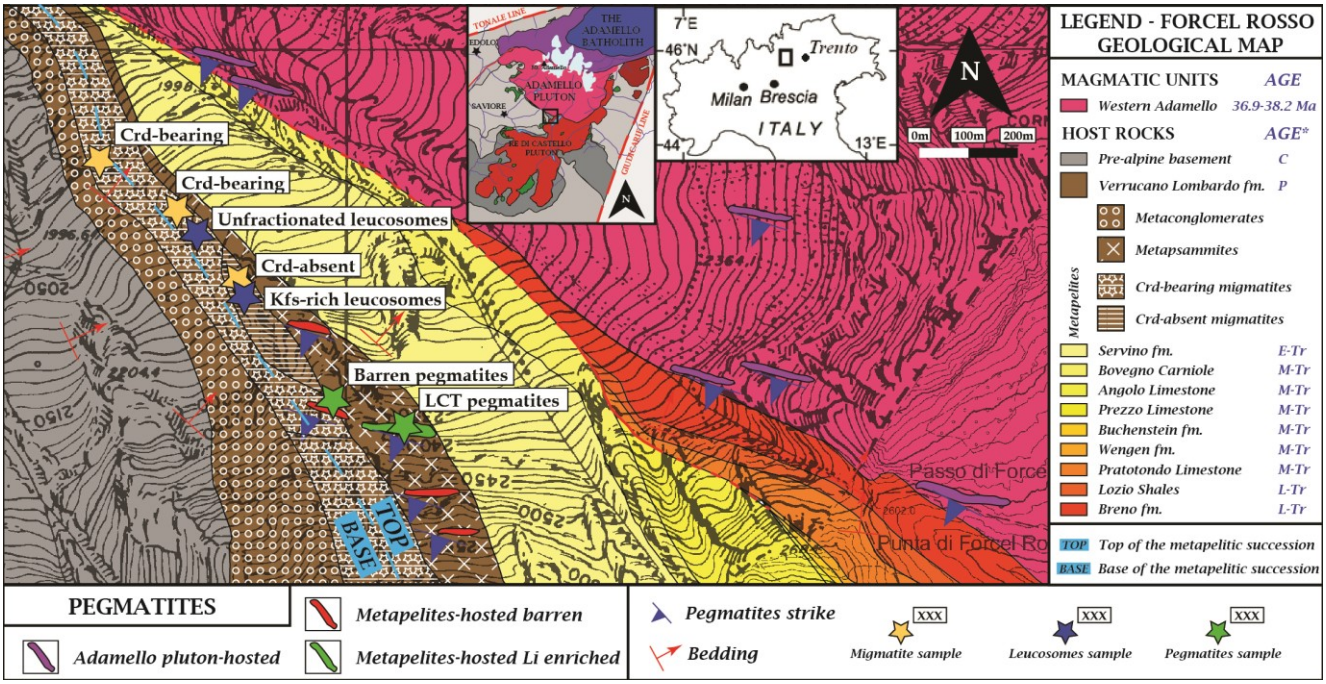

Figure 5-1 Geology of the Forcel Rosso area highlighting the newly mapped pegmatites and the sampling areas.

5.2.2. Migmatites-hosted pegmatites

The metapelites-hosted pegmatites range from evolved but barren to LCT-mineralized with miarolitic cavities. The lithium-enriched pegmatites are limited to the Verrucano Lombardo formation and, at the stratigraphic limit with the verticalized metacarbonates of the lower Servino Formation, they abruptly stop against the carbonatic lithology (Magnani et al., 2022). The metapelites-hosted barren pegmatites are usually centimetric to decimetric thick bodies showing no internal differentiation while the Li-rich pegmatites are metric and exhibit a clear internal zonation. Magnani et al. (2022) suggest the existence of a genetic relationship between the metapelites-hosted leucosomes and the pegmatites, arguing that ca. 60% of the anatectic melt that was produced in the banded metapelites may have left its source (i.e. the Crd-absent migmatites) and accumulated in the more competent psammitic layer forming lithium-enriched pegmatites.

5.3 Methods

Major and trace element concentrations were determined on 17 samples of metamorphic and magmatic rocks from the Forcel Rosso area. The analyses were performed by laser-induced inductively coupled mass spectrometry (LA-ICP-MS) on pressed powder pellets (PPP) at the Geochemistry, Geochronology and Isotope Geology laboratory of the Department of Earth Sciences, Università degli

Studi di Milano (Italy). The instrument couples an Analyte Excite 193nm ArF excimer laser system equipped with a double volume chamber cell HelEx II (Teledyne Cetac Technologies) to a single-quadrupole ICP-MS (iCAP-RQ, Thermo Fisher Scientific). The PPP preparation follows the protocol developed by Peters and Pettke (2016) with the modifications described in Magnani et al. (2022). A complete description of the technique is available in the supplementary material. The RSD% values for major element data are all under 2% while trace elements data are always under 10%. Reported final data are the mean of 6 spot analyses and the precision is expressed as their standard deviation (1σ). Accuracy was checked by repeated analysis of international reference materials SDC-1, BHVO-1 and MA-N that were prepared and analyzed in the same way as the unknowns. At least two international standards were characterized on every run to constrain accuracy. Accuracy error rates are below 5% for all major elements and under 10% for all trace elements except for Vanadium, which is below 20%.

Sixteen thin sections of metapelites were analyzed by electron microprobe. Electronic microprobe analyses were conducted at the Earth Sciences department of University of Milan on a JEOL JXA-8200 using wavelength-dispersive spectrometry. Operating conditions were 15kV accelerating voltage and beam current of 5nA, with a beam diameter of 1 μm. The trace element composition on minerals previously analyzed by EMPA were obtained at the the Geochemistry, Geochronology and Isotope Geology laboratory of the Department of Earth Sciences, Università degli Studi di Milano (Italy). using an iCAP ICP-MS quadrupole coupled with a 193nm Ar-F excimer laser. Analyses on biotite and cordierite were obtained using a spot size of 40μm spot size at 10Hz and 2 J/cm^2 fluence. The runs were standardized using the international glass standard NIST612 (Pearce et al., 1997) analyzed using a 40μm spot size at 10Hz and 4J/cm^2 and calculated using the software suite Glitter. The complete electron microprobe and laser ablation mineral chemistry dataset is provided in supplementary material.

Radiogenic Sr and Nd isotopic analyses of 10 selected samples were performed using a Thermo Fisher Neptune Plus MC-ICP-MS at the Istituto di Geoscienze e Georisorse - CNR in Pisa (Italy) in 2% HNO3 solution containing 20-200 ng*g-1 of analyte. The instrument was equipped with a combined cyclonic and Scott-type quartz spray chamber, Ni-cones and a MicroFlow PFA 100 μl/min self-aspiring nebuliser. Rock powders were leached with strong HCl (6.6 N for half an hour at ≈ 80 °C) to cut off any effect of secondary minerals, and then rinsed 5 times with ultrapure water. Subsequently, samples were digested in a concentrated Ultrapur HF+HNO3, dried and brought again into solution, then subdivided into two aliquots, one in diluted HNO3 and one in diluted HBr. Sr was then separated from HNO3 solution using Sr-Spec resin, Nd was separated from the same aliquot trough a two-step

procedure with TRU-spec and Ln-Spec resins, whereas Pb was collected starting from the portion diluted in HBr after separation with AG50W-X8 resin.

Sr analyses were corrected for mass bias fractionation using the $^{88}Sr/^{86}Sr$ ratio (8.375209) and for Kr and Rb mass interferences using the ratios $^{83}Kr/^{84}Kr$ (0.201750), $^{83}Kr/^{86}Kr$ (0.664740) and $^{85}Rb/^{87}Rb$ (2.592310). Eight repeated analyses of standard NIST SRM 987 gave a result of 0.710348 ± 16. Results were adjusted to a ratio of 0.710248.

Instrumental mass fractionation during Nd analyses was corrected using the $^{146}Nd/^{144}Nd$ ratio (0.7219). Mass interference of ^{147}Sm was corrected using the ratios $^{147}Sm/^{144}Sm$ (4.838710), and $^{147}Sm/^{148}Sm$ (1.327400). Three analyses of $^{143}Nd/^{144}Nd$ ratio of reference material J-Ndi-1 gave an average of 0.512085 ± 5.

Sr total blank was better than 2 ng while Nd total blank was less than 1 ng during the period of measurement. Measured $^{87}Sr/^{86}Sr$ ratios have been normalized to $^{86}Sr/^{88}Sr = 0.1194$; $^{143}Nd/^{144}Nd$ ratios to $^{146}Nd/^{144}Nd = 0.7219$. During collection of the isotopic data, 15 replicate analyses of SRM 987 ($SrCO_3$) standard gave an average value of 0.710200 ± 8 (2σ mean) and 14 measurements of La Jolla standard gave an average $^{143}Nd/^{144}Nd$ of 0.511851 ±3 (2σ mean). All $^{87}Sr/^{86}Sr$ data were normalized to a value of 0.71025 for the SRM 987 standard.

5.4 Pegmatites field geology and petrography

The pegmatites of the Forcel Rosso area can be subdivided in two main groups, one metapelites-hosted and one hosted in the adiacent Adamello pluton. They all share ca. 190-220° N striking and 40 to 60° dip with local deformation impacting only the Adamello pluton-hosted bodies. The metapelites-hosted pegmatites are widespread in the migmatitic zone but are even more concentrated in the metapsammitic interlayers characterizing the local metasedimentary succession. Where they reach the top of the Verrucano Lombardo formation, they abruptly stop against the verticalized basal metacarbonate layer of the overlying Servino formation. The pegmatites hosted in the Adamello pluton are invariably contained only in the magmatic mass and abruptly stop ath contact between the pluton and the verticalized metadolomites of the Breno formation. On the field, no sign of direct connection between the two different pegmatitic groups were identified are identifiable.

5.4.1 Metapelites-hosted pegmatites

The LCT pegmatitic dykes are zoned (Fig. 5-2), alternating graphic granite areas, pegmatoid and aplitic zones, featuring miarolitic pockets in their most internal zones. The different parts of the

pegmatites were sampled individually and can be described from the lowermost part of the dykes to the top as:

- Zone A) Qz+Kfs+Pl+Ms+Schorl Tur graphic granite border zone. Apatite, monazite, rutile and zircon are the main accessory minerals. It features a sharp contact with the host metapsammitic rock of the Verrucano Lombardo formation and has an overall thickness of ca. 10 cm;
- Zone B) line rock characterized by several bands enriched in black tourmaline with Qz+Kfs+Pl+Ms+Schorl Tur assemblage. Apatite, monazite, rutile, zircon, ilmenite, magnetite and xenotime are present as accessory phases. Rare pollucite crystals have been identified. Overall thickness ca. 3 cm.
- Zone C) external layered aplite featuring Qz+Kfs+Pl+Ms+Schorl Tur mineral composition. Mean crystals diameter ca. 1-2 mm. Overall thickness of the zonation ca. 15 cm;
- Zone D) pegmatoid zone defined by Qz+Kfs+Pl+Ms+Schorl Tur composition. Apatite, xenotime, fluorite and micrometric zircons are the main accessory minerals. Tourmaline crystals reach up to 10 cm in length and mean length of Kfs crystals is ca. 5 cm. Overall zonation thickness ca. 30 cm;
- Zone E) internal layered aplite with Qz+Kfs+Pl+Ms+Schorl to Elbaite Tur featuring a spessatine-rich line rock. Spessartine garnet, Mn-columbite, fluorite, antimonite, apatite and micrometric zircons are present as accessory phases. Mean diameter of crystals ca. 1-3 mm. The presence of Mn-rich garnet and elbaitic tourmaline denote a sharp evolution from the mineral and chemical compositions of zones C and D. Overall thickness ca. 20 cm;
- Zone F) internal pegmatoid zone showing the most important lithium enrichment, with Qz+Kfs+Pl+Znw+Lpd+Elbaitic Tur composition and Mn-columbite, fluorite, antimonite, apatite and micrometric zircons accessory minerals. Overall thickness ca. 50 cm. Inside the miarolitic cavities, pollucite and pyroclore have been found and calcite is common as late stage mineral filling.
- Zone G) a Qz+Schorl Tur+Ms palisade zone that developed starting from the roof of the magmatic body. In this widely variable zone, black tourmaline crystals reach up to 8cm in length the sampled areas.

As the mineralogy implies, the LCT pegmatites are dishomogeneously enriched in lithium as it is common in these magmatic bodies. Barren mineral assemblages (Kfs, Qz, Pl, Ms, dravitic to schorlitic Tur) characterize the external zones while the lithium mineralization is widespread in the internal zones of the dykes.

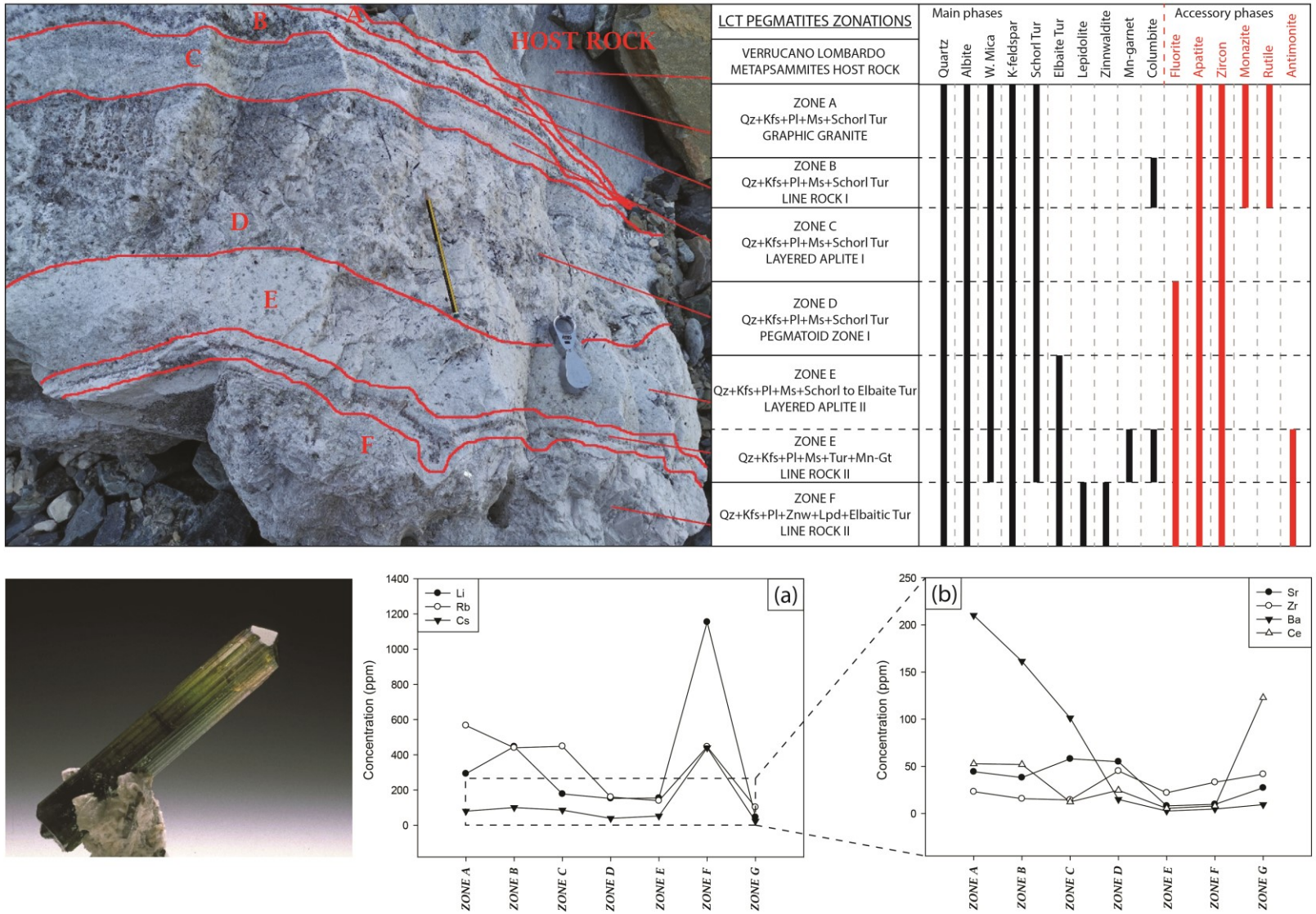

Figure 5-2 Zonations of the studied LCT pegmatites with visual mineralogical composition. Bottom left: elbaite crystal from a miarolitic cavity (Collection: Natural History Museum of Milano, Italy. Photo Roberto Appiani); bottom right: variations of - a) Li, Rb, Cs and – b) Sr, Zr, Ba, Ce among the pegmatitic zones.

Both in the aplitic zone E and pegmatoid zone F, several miarolitic cavities were discovered where the terminal melts and fluids deposited the most incompatible elements forming Li-rich tourmaline species as Fluor-Elbaite, Foitite, Fluor-Liddicoatite and Rossmannite (Diella et al., 2018).

5.4.2 Adamello pluton-hosted pegmatites-aplites

Several pegmatitic dykes of white to reddish colour intrude the Adamello pluton magmatic mass. Their contact with the tonalite is sharp, suggesting a brittle behaviour of the pluton during emplacement. In some areas, their orientation is disturbed by limited plastic deformation. The centimetric to metric-wide pegmatitic dykes close to the border of the magmatic intrusion exhibit coarse-grained pegmatitic textures while those occurring in the internal zones of the pluton have a similar external zone but are characterize by thick aplites in the center of the dyke. Their mineralogy consists of Kfs+Pl+Qz+Bt assemblages completed by apatite, thorite, titanite and zircon accessory minerals in both pegmatitic and aplitic zones.

5.5 Whole rock chemistry

In the spider diagram of Fig. 5-3a all samples are normalized to the composition of the Adamello tonalite sampled in the area (ML12C). The complete dataset is reported in the Supplementary material. The two types of anatectic leucosomes and the Li-enriched pegmatites show an enrichment in Li, B and Cs compared to the Adamello pluton-hosted pegmatites, which are in turn enriched in Th and U. The Kfs-rich leucosomes feature a positive Eu anomaly and are depleted in Zr and Hf but otherwise all other elements are compatible with the other anatectic melts. Fig. 5-3b identifies a positive correlation between Sr and Ba. Metapelites-hosted pegmatites, both barren and lithium-rich are clustered at low values of both Sr and Ba, opposite to the Kfs -rich cumulates, which are extremely enriched in both these elements. The unfractionated leucosomes, genetically related to the Crd-bearing migmatites, plot almost exactly between the two groups. Pluton-hosted pegmatites are slightly richer in Sr and Ba compared to the metapelites-hosted pegmatitic dykes. Finally, Fig. 5-3c shows the positive correlation existing between Li and Cs, which identifies three main groups: an extremely depleted cluster composed of pluton-hosted pegmatites, a low-Li and low-Cs group composed of leucosomes and barren pegmatites and a Li-Cs-rich group formed by metapelites-hosted LCT pegmatites. Fig. 5-2 highlights the widely variable trace elements compositions characterizing the different zonations of the Forcel Rosso LCT pegmatites. The diagram in Fig 5-2a shows that Li, Rb and Cs are correlated and tend to decrease from the external towards the internal zones where they suddenly become extremely

enriched in zone F. Sr, Zr, Ba and Ce (Fig. 5-2b) also tend to decrease from the external to the internal zones of the LCT dykes but do not concentrate in them like the other elements. Interestingly, they all show the lowest concentrations in zone E and not in zone F, the most evolved zonation.

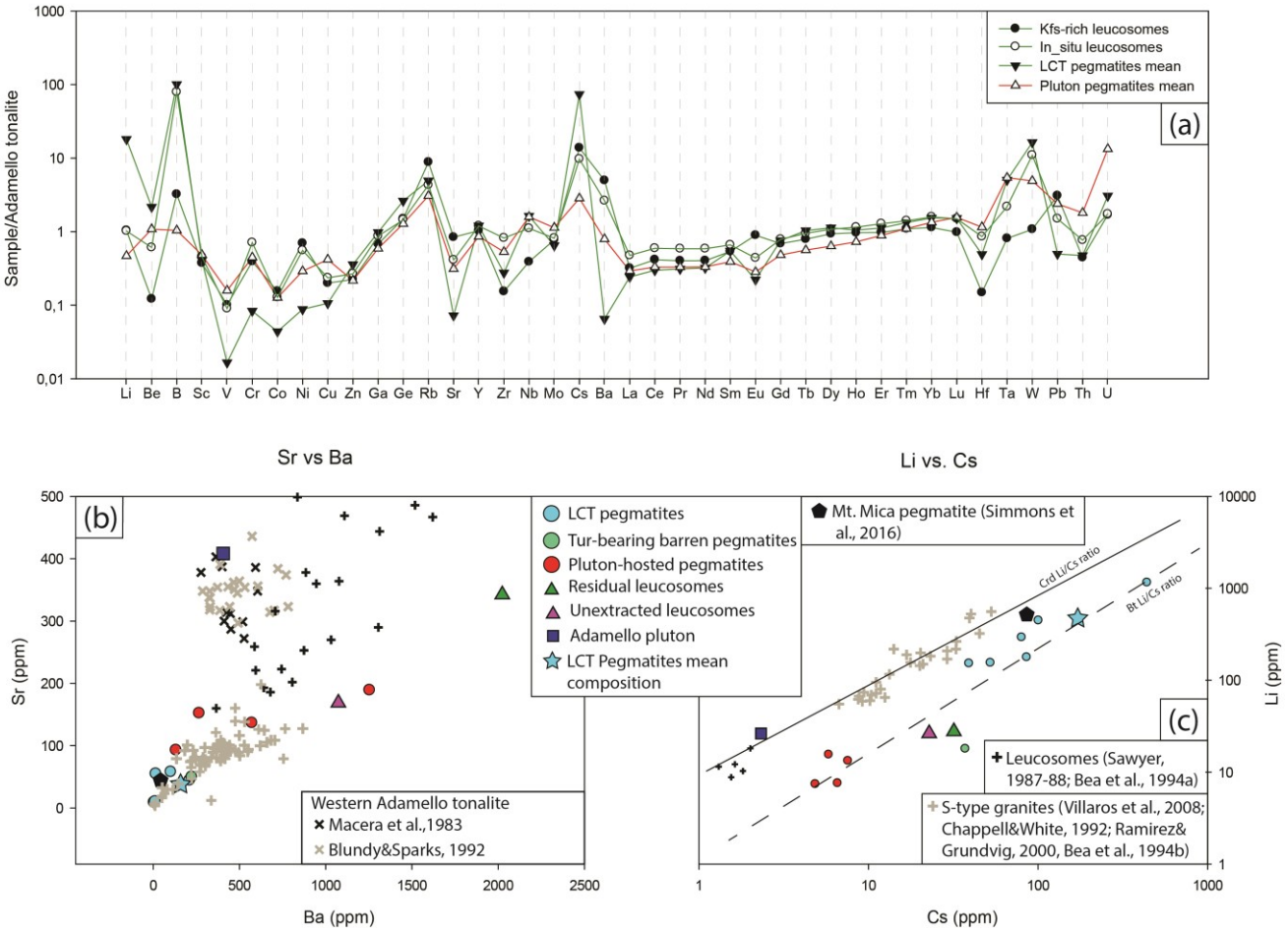

Figure 5-3 Whole rock data - a) Trace elements composition of leucosomes and pegmatites of the Forcel Rosso area normalized to the Adamello pluton compositon in the area; b) Sr vs. Ba graph and c) Li vs. Cs diagram, references reported in grey and black crosses. The single reference of mean LCT pegmatites composition avalaible in literature is reported in the black pentagon. All data is reported in Table B1. Crosses for S-type granites are common to b) and c).

5.6 Sr and Nd isotopes whole rock data

Strontium and neodymium whole rock isotopic data for a selected range of samples are reported in Table 1 and Fig. 5-4. All isotopic values are calculated at 38.23 Ma, the age of the Adamello pluton intrusion determined at the Forcel Rosso pass (Schaltegger et al., 2019). The Verrucano Lombardo pelites and metapelites from all amphibolite facies feature initial $^{87}Sr/^{86}Sr$ values ranging between 0.721 (migmatites) and 0.737 (unmetamorphosed) and Nd signature ranging from -1.05 to -8.85 εNd units, highlighting great differences in both Sr and Nd between different metapelites samples. All magmatic rocks hosted inside the migmatites (leucosomes and LCT pegmatites) are characterized by initial $^{87}Sr/^{86}Sr$ values ranging from 0.719 to 0.726 and εNd values between -10.7 and -6.8 indicating a

crustal origin and mirroring the great variability observed in the connected metapelites. Pluton-hosted pegmatites yielded initial $^{87}Sr/^{86}Sr$ values between 0.706 and 0.7075 and εNd between -3.2 and -3.4.
The two types of leucosomesw we analysed, unfractionated and Kfs-rich, feature different Sr and Nd isotopic compositions. Unfractionated leucosomes Sr-Nd signature is extremely similar to that of their reference migmatite while Kfs-rich leucosomes are characterized by markedly lower $^{87}Sr/^{86}Sr_i$ (ca. 0.721) and εNd (-10.7) values, highlighting their connection with the internal portion of the LCT pegmatitic dyke and the barren pegmatites network.
Inside the LCT pegmatites we analyzed two samples, one from the internal Li-enriched part and the other from the external zone, which are characterized by different Sr-Nd isotopic compositions. The internal zone features lower initial $^{87}Sr/^{86}Sr$ (ca. 0.720) and lower εNd value (-9.77) compared to the external zone, respectively characterized by 0.726 $^{87}Sr/^{86}Sr_i$ and -6.88 εNd. Even though the sample representing the internal zone of the Li-rich pegmatites is characterized by a very high Rb/Sr ratio resulting in a large uncertainty on the initial $^{87}Sr/^{86}Sr$ values due to error propagation, the analyses do not overlap and cannot be considered as one. It was not possible to analyze the Nd isotopic composition of the barren pegmatites sample due to the very low Sm and Nd concentration, although its $^{87}Sr/^{86}Sr_i$ value is compatible with that of the internal LCT zone.

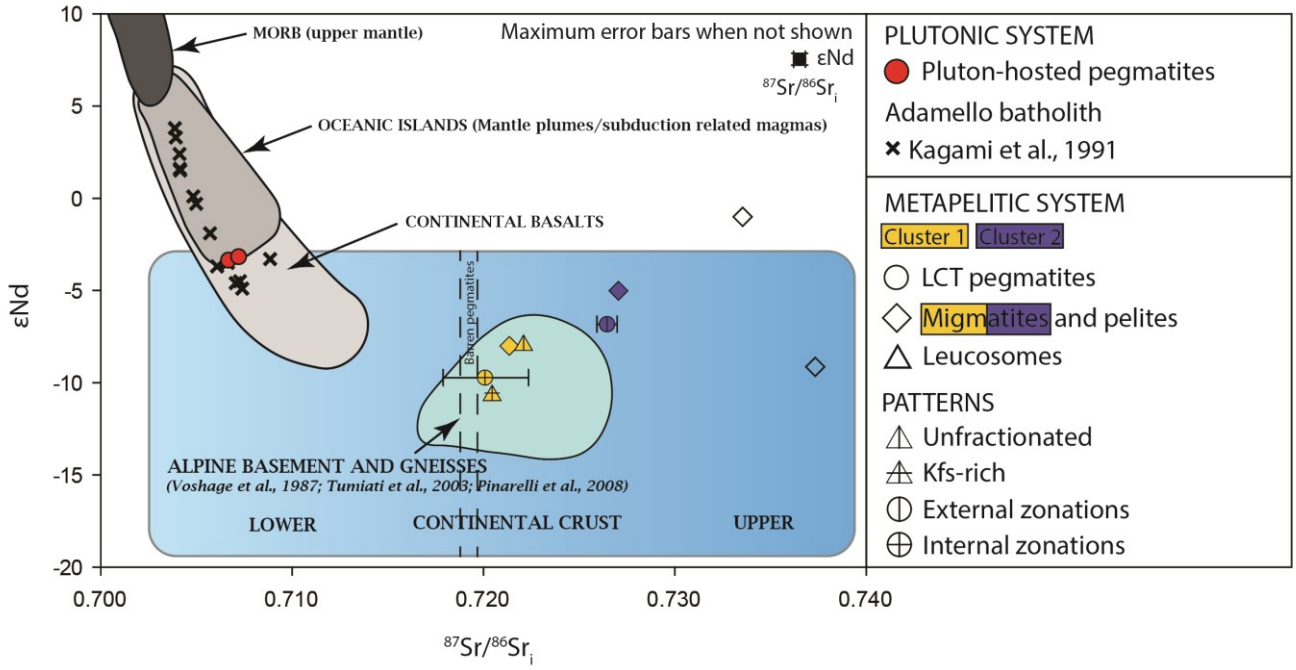

Figure 5-4 Isotopic Sr-Nd data for selected rock samples of the Foercel Rosso area. See text for explanation of the Cluster division. All data is reported in Table B2.

5.7 Chemistry of the main Li host minerals

In this section, we focus on the behavior of biotite and cordierite, the main minerals hosting Li and Cs in the metapelites during partial melting reactions (Fig. 5-5, 5-5b). Biotite is an important mineral

throughout the metamorphic history of the studied pelites and its major elements composition was reported by Magnani et al. (2022). The main trace elements hosted by this mineral are Li, Sc, V, Cr, Mn, Co, Ni, Zn, Rb, Nb, Cs, Ba, Ta and W. Biotite crystals hosted in metapelites at different metamorphic grades show distinctive trace elements compositions, as shown in Fig. 5a. Lithium and cesium contents are similarly high in biotite crystals from low grade metapelites and Crd-absent migmatites while they are depleted in the biotite crystals of Crd-bearing migmatites (Fig. 5-5a-c). Also, elements such as Cr, Mn, Co and Ni tend to decrease, while Ba tends to increase with increasing metamorphic grade. Finally, biotites in Crd-absent migmatites are enriched in both Nb (Fig. 5-5a-b) and Ta compared to the other Bt types.

Cordierite, found only in the Crd-bearing migmatites in the Forcel Rosso area, is produced as a peritectic product during partial melting reactions (Magnani et al., 2022). This mineral is enriched in few elements, which are Li, Be, Mn, Co, Ni, Zn and Cs. Lithium is extremely concentrated in the studied cordierite crystals, ranging from 390 to 500 ppm and averaging ca. 480 ppm Li (Fig. 5-5c). Beryllium and cesium are moderately concentrated, both with 25 ppm median values. Manganese enrichement is comparable with the previously described Bt crystals while Zn is slightly less concentrated than in Bt. Crd does not host any Rb, Ba, Nb or Ta. All data is reported in SM.

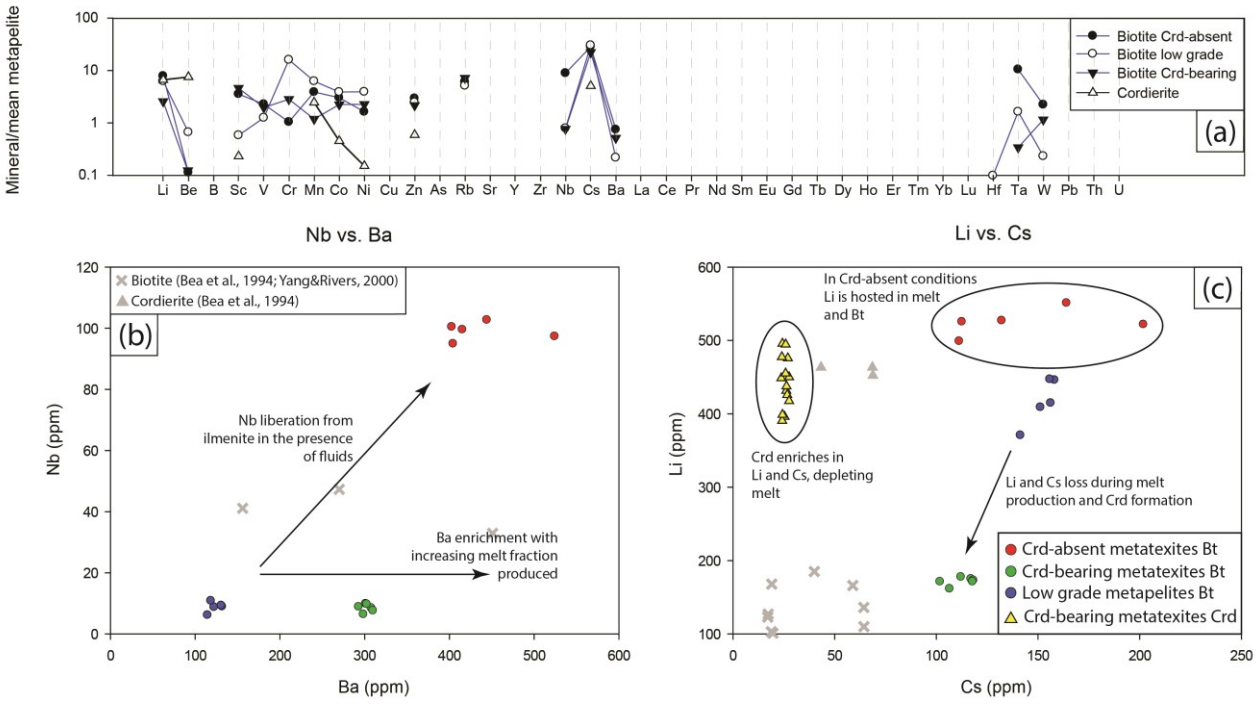

Figure 5-5 Biotite and cordierite trace elements compositions – a) spider diagram featuring Bt and Crd compositions normalized to the mean pelite composition (Wedepohl, 1995), unreported data is under the detection limit; b) Nb vs. Ba diagram for Bt compositions; c) Li vs Cs diagram for Bt and Crd. References in grey. Bt data is reported in Table B3.1, Crd data is reported in Table B3.2.

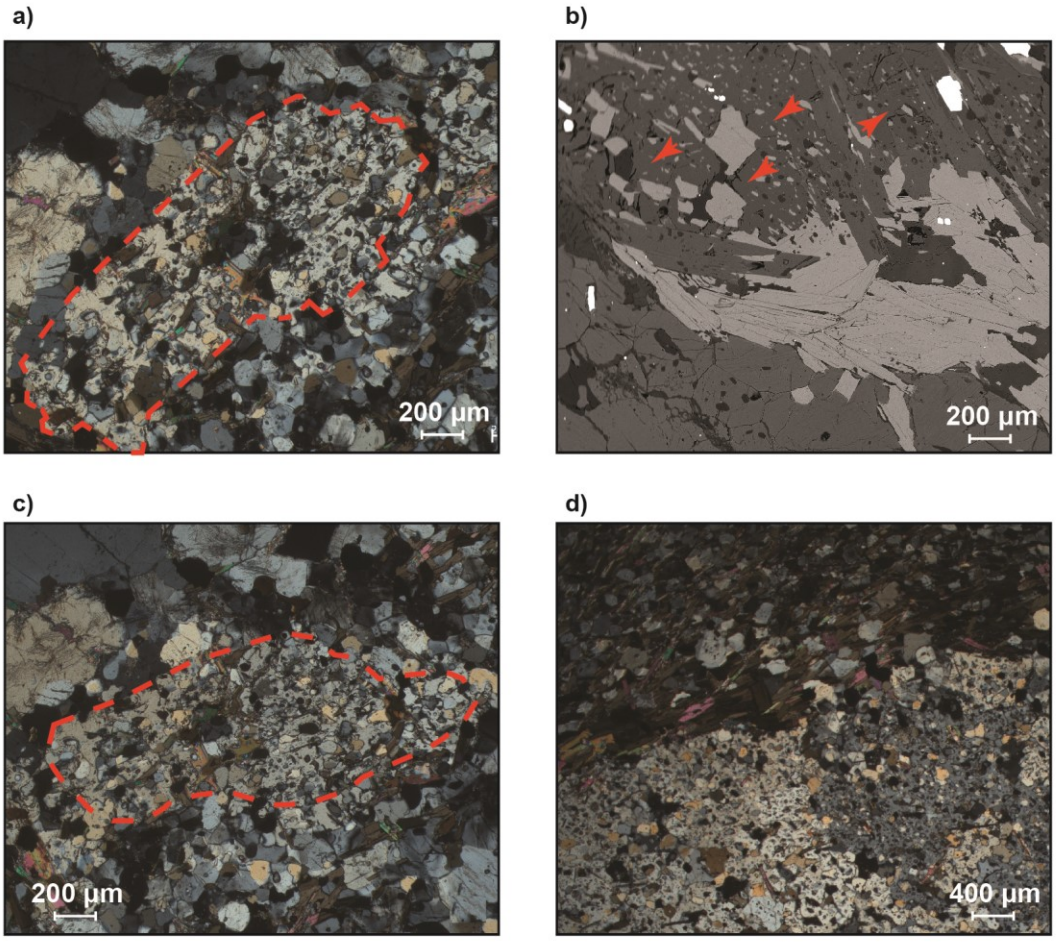

Figure 5-5b Biotite and Cordierite micrographs highlighting how Crd grew on Bt pseudomorphosing its former crystals. Image b) shows how inside some Crd poikiloblasts it is still possible to observe the remnants of the former biotite.

5.8 Discussion

5.8.1 The Forcel Rosso contact anatectic system

The Forcel Rosso migmatitic terrane, related to the shallow level emplacement of the Adamello batholith, hosts two different types of metatexites with related leucosomes and a network of pegmatites with composition ranging from barren to lithium and cesium enriched. Crd-bearing and Crd-absent migmatites formed here through fluid present partial melting of the same metapelitic source at different water activities, which determined if peritectic cordierite was produced during biotite destabilization and defined the melt fraction produced (ca. 20 vol.% for Crd-bearing and ca. 30-35% for Crd-absent; Magnani et al. 2022). Biotite trace elements composition evolved according to its host rock geological history and melting conditions, becoming a tracer of anatectic processes. This mineral enriched in Ba with increasing melt fraction produced (Fig. 5-5b), suggesting that this element preferentially partitioned in the melanosome residuum during melting, and recorded a dramatic

increase in Nb and Ta concentration in the Crd-absent migmatites fluid-rich system, possibly following ilmenite, the main Nb and Ta carrier in metapelitic rocks (e.g. Ewart&Griffin, 1994; Stimac&Hickmott, 1994), destabilization in the presence of fluids. Biotite also recorded Li and Cs variations during metamorphism, as Fig. 5-5c shows that the concentration of biotite-hosted lithium and cesium sharply declined in Crd-bearing migmatites compared to the other metapelites of the area, similarly to what have been observed in other Crd-bearing terranes (e.g. Bea et al., 1994a). The high Li and Cs contents of cordierite and its genetically related Li and Cs-poor unfractionated leucosomes show that these elements strongly partition in the peritectic mineral rather than in the melt phase ($D_{Li}^{Crd/melt}$ ca. 18; $D_{Cs}^{Crd/melt}$ ca. 1.2), in agreement with the calculations of Bea et al. (1994a) based on the analysis of cordierite and leucosomes from the Pena Negra complex. The Li partition coefficient obtained in this work is very different from the low ones proposed by the experimental work of Evensen&London (2003). This may be linked to the fact that they studied magmatic cordierite, while metamorphic crystals, developing on biotite during peritectic reactions, could trap and incorporate Li. Crd also concentrates Be ($D_{Be}^{Crd/melt}$ ca. 20), as previously reported by Evensen&London (2002) and Bea et al. (1994). The presented data show that trace elements behaviour in migmatitic terranes is regulated by the metamorphic P-T conditions and water activity characterizing the system, ultimately influencing the partial melting kinetics and formation of peritectic minerals. This helps us explain the compositional features observed in the Forcel Rosso migmatites-related leucosomes, either unfractionated, considered representative of the Crd-bearing migmatites primary melt, or formed by accumulation of Kfs and Bt from the anatectic melt related to Crd-absent migmatites (Magnani et al., 2022). Fig. 5-3 shows that the primary melt formed from Crd-bearing migmatites is boron and cesium enriched, with Ba values similar to other unfractionated leucosomes from literature but with lower Sr content (e.g. Bea et al., 1994a; Sawyer et al., 1987, 1988). Interestingly, Cs and Li are more enriched compared to the Crd-migmatites-related leucosomes from the Pena Negra complex (Bea et al., 1994a). The low Sr and high Li-Cs concentrations may be controlled by the fertility of the specific pelitic source and by its initial feldspar content, which in the case of the Verrucano Lombardo pelites is very low (e.g. Riklin, 1983). The barium concentrations we report for unfractionated leucosomes, like the others leucosomes from literature, are invariably higher than those observed in the data compilation of S-type granites (Villaros et al., 2008; Chappell&White, 1992; Ramirez&Grundvig, 2000; Bea et al., 1994b) suggesting that, between formation and emplacement, these magmas may experience Kfs fractionation events (e.g. Morfin&Sawyer, 2014) or are originated through the production of high melt fractions. Based on the trace elements evolution during metamorphism pictured by biotite compositions, the expected unfractionated leucosomes in Crd-absent migmatites should have been Li, B and Cs-rich but, instead, only Kfs cumulates have been found connected to this rock-type.

Compared to this expected primary melt composition, they are enriched in Kfs-compatible elements such as Sr, Ba and Rb but depleted in all the mentioned elements and also in Zr and Hf, usually hosted in zircon. The disappearance of incompatible elements like Li, B and Cs suggest that a portion of the primary melt was extracted from here, while the complete lack of zircon suggests that this either happened before zircon saturation or that at the low temperature inferred for these melts (ca. 680-690°C, Magnani et al., 2022) zircon remained stable in the melanosome. Fractionated leucosomes found in migmatitic terrains are common but usually ignored although they may represent the inequivocable signs that melt extraction and "in-source" evolution occurred there as they may play an important role in the evolution of the crustal magmas in their earliest stages. In the light of the presented data, it is worth considering that, during anatexis of metapelites, lithium may either be not released from the melanocratic portion of the anatectic metapelitic migmatites (e.g. Bea et al., 1994a) or incorporated into mobile melts that migrate away from the source, leaving behing only a Kfs-cumulate that is unrepresentative of their primary compositions, de facto explaining why the majority of migmatitic metapelites-hosted leucosomes are Li-poor (e.g. Bea et al., 1994a; Sawyer et al., 1987, 1988). Finally, Fig. 5-3c highlights how the mica-related evolved melts found in the Forcel Rosso area similar in their Li/Cs ratio to the most of the S-type granites compositions from literature. Interestingly, by compiling biotite (Yang&Rivers, 2000; Neiva et al., 2022; Breiter et al., 2017, Kunz et al., 2022), cordierite (Bea et al., 1994a; Erdmann et al., 2009, Evensen&London, 2002) and muscovite (Kunz et al., 2022) trace elements data from this work and literature sources we obtain three distinct power law linear trends for each of the studied minerals that well describe the data distribution featured in Fig. 5-3c. The lowest corresponds to the Li/Cs ratio of Ms, that models well all the leucosomes in the Forcel Rosso area and the barren pegmatites, while the middle trend line corresponds to the biotite Li/Cs ratio (ca. 1.5 to 5), correctly modelling all the LCT pegmatites data and the most S-type granites from literature. The uppermost trend corresponds to the cordierite Li/Cs ratio (ca. 15 to 20), which does not model any plotted data but helps explain the mixed signature of some S-type granites characterized by mixed Crd-Bt signature. This suggests that both the LCT pegmatites of the Forcel Rosso area and the S-type granites for which data is available were produced during Bt destabilization, supporting the arguments of Magnani et al., 2022 on biotite involvement in the process. The Forcel Rosso primary leucosomes are well described by the Ms Li/Cs ratio that suggest this mineral was the main source of Li and Cs and that the Bt contribution was locked in place by subsolidus or near solidus Crd formation. The Ms signature of the cumulates (barren pegmatites and Kfs-leucosomes) is related to the extraction of the most of the related magma and the fractional crystallization of mica with that Li/Cs signature.

5.8.2 The anatectic LCT pegmatites of the Adamello pluton thermal aureole

5.8.2.1 Sr-Nd isotopic affinity

All the metapelites, leucosomes, barren and lithium-rich pegmatites hosted in the metasediments exhibit crustal $^{87}Sr/^{86}Sr_i$ values > 0.719 and εNd < -5., with the only exception of one metapelite with higher εNd of ca. -1 (Fig. 4). The Adamello pluton-hosted pegmatites yield lower and less variable initial $^{87}Sr/^{86}Sr$ values between 0.706 and 0.7075 associated to εNd of ca. -3.2, that perfectly match the Sr-Nd isotopic signature of the Adamello batholith available in the literature (e.g. Bigazzi et al., 1986; Kagami et al., 1991). The extreme differences in $^{87}Sr/^{86}Sr$ values existing between the LCT pegmatites (0.7237 to 0.7269) and the Adamello pluton and pluton-hosted pegmatites clearly indicates that the two are not directly correlated, while the compatibility with the migmatites isotopic signatures at typically crustal values point to an anatectic origin for the studied Li-enriched pegmatites. The compatibility between the Sr-Nd isotopic signatures of pluton-hosted pegmatites and Adamello batholith units, defines them as structures that collected the most evolved melts produced through fractional crystallization of the Adamello central units.

Pelites and metapelites from the Verrucano Lombardo formation sampled at different metamorphic grades feature a great range of both Sr and Nd isotopic signatures at 38.23 Ma, the inferred date of partial melting, suggesting that the Verrucano Lombardo pelitic strata were diversified in their original source composition and that they sedimented during a long period of time. Several authors report this feature arguing that towards the late Permian in the Southern Alps, several sedimentation hiatus are present, sometimes with the formation of paleosols (e.g. Schunnach et al., 1996). Among the presented data we could identify two main clusters (Fig. 5-4), defined by source derived Sr-Nd isotopic differences and connected to well defined positions in the metapelitic stratigraphic succession. Cluster 1 includes migmatites sampled near the top of the formation (Fig. 5-1), unfractionated and Kfs-rich leucosomes and the internal portion of the Li-enriched pegmatitic dykes. Cluster 2 includes migmatites sampled near the bottom of the formation and the external zonations of the LCT pegmatites. Although migmatites in this area are characterized by Crd-bearing and Crd-absent rocks, which are the result of different amphibolitic-facies metamorphic reactions on starting metapelites with the same mineral and chemical compositions (Magnani et al., 2022), we infer that their different partial melting kinetics did not greatly influence their isotopic signature. In fact, the impact of isotopic non-equilibrium during partial melting (e.g. Farina et al., 2011; Wolf et al., 2019) would have had a negligible impact compared to their Sr and Nd evolution between their deposition (late Permian) and the age of 38.23 Ma we focused on. Other, more studied, metapelitic successions in Northern Italy (e.g. Voshage et al., 1987 Ivrea zone; Pinarelli et al., 2008 Serie dei Laghi) feature much smaller whole rock Sr-Nd

variabilities even being many times thicker than the Verrucano Lombardo metapelites, highlighting the extreme stratigraphic complexity of the studied area.

Sr and Nd whole rock isotopic data show that unfractionated leucosomes are characterized by $^{87}Sr/^{86}Sr_i$ and εNd values extremely similar to their source metapelites, with slight differences in the Sr signature, while Kfs-rich leucosomes differ from them both in $^{87}Sr/^{86}Sr_i$ and εNd. The highlighted divergence between anatectic leucosomes and sources in the Forcel Rosso metapelites can only be explained through isotopic non-equilibrium melting processes, which is fundamentally controlled by biotite and plagioclase-feldspar participation to the melting reactions (Farina et al., 2011). The $^{87}Sr/^{86}Sr_i$ values characterizing unfractionated leucosomes suggest that the partial melting kinetic that produced them mainly consumed Rb-rich biotite, an interpretation that agrees with the kinetic for fluid-assisted melting of Crd-bearing migmatites proposed by Magnani et al. (2022). The low $^{87}Sr/^{86}Sr_i$ values characterizing Kfs-rich leucosomes suggest that Sr-rich plagioclase and feldspar dissolution played the most important role during partial melting. This observation is in agreement with the melting reaction for fluid-rich partial melting kinetics proposed by thes same authors, characterizing the Crd-absent migmatites in this area. Defining the impact of isotopic disequilibrium melting on the leucosomes εNd signature proves to be more difficult as Sm and Nd main contributors in the metapelites are the accessory phases apatite and monazite (e.g. Ayres&Harris, 1997 and references therein). We observe a difference of -2.7 εNd units between Kfs-leucosomes and their related melanosome while Ayres&Harris (1997) report an increase in εNd for himalayan granitic melts of ca. +1.1 from their source whole rock isotopic composition. They explain their findings through the much higher contribution of apatite compared to monazite during vapour absent muscovite disequilibrium melting of the Himalayan Crystalline Series (Harris and Inger, 1993; Harris et al., 1995). More data would be needed in order to rigorously model apatite and monazite contribution to the melt in our case but we can infer that, since the Forcel Rosso metapelites essentially evolved through fluid-present partial melting at low pressure (Magnani et al., 2022), fluid fluxed partial melting conditions may have had an impact on accessory phases stability in the anatectic system. This may have caused monazite, extremely susceptible to fluid circulation (e.g. Seydoux-Guillaume et al., 2012 and references therein), to contribute more to the melt compared to apatite. Monazite is poorer in Sm than apatite, developing though time a lower $^{143}Nd/^{144}Nd$ ratio (e.g. Ayres&Harris, 1997), and subsequently more negative εNd values, which could have been then passed on to the forming melts.

Although we proved that the Forcel Rosso Li-rich pegmatites are anatectic, defining their source metapelites in the area on an isotopic basis is complicated by the fact that the two analyses we have are different both in $^{87}Sr/^{86}Sr_i$ and εNd. Our data suggest that the external portion of the dykes (LCT zone B), weakly enriched in Li and Cs, is isotopically extremely similar to the migmatites of Cluster 2,

sampled at the bottom of the metapelitic succession. Conversely, the internal part of the dykes (LCT zone F), strongly enriched in Li and Cs, is, within error, very similar to Kfs-rich leucosomes and migmatites of Cluster 1, from the top of the formation. The Sr and Nd isotopic composition of these samples highlights processes of isotopic disequilibrium during melting similar to those identified for Kfs-rich leucosomes, suggesting that the same fluid rich partial melting kinetic was involved in the genesis of both the internal and external parts of the Li-rich dyke. In this situation, the great differences existing in Sr-Nd isotopic signature between the strata in the Verrucano Lombardo metapelites help us infer that the studied LCT pegmatites formed by the multi batch coalescence of anatectic melt from two different sources that underwent different evolution processes and that did not completely mix inside the pegmatites. Since the isotopic difference is so well defined, we argue that the Li, Cs-enriched melt, linked to Kfs-rich cumulates, was injected towards the terminal crystallization stages of the first, relatively Li, Cs-poor batch. More in-situ $^{87}Sr/^{86}Sr$ data on apatite crystals will be needed in order to assess the internal Sr isotopic variability characterizing the complex Forcel Rosso LCT pegmatitic dykes.

5.8.2.2 Forming anatectic Li-enriched melts

Isotopic data reveal that the Li-rich pegmatites of the Forcel Rosso migmatites have a crustal geochemical affinity different from that of pluton-hosted pegmatites and that they are formed by two different Li-Cs-rich melt components. The pegmatites whole rock trace elements compositions support this interpretation as the migmatites-hosted group is enriched in lithium, boron and cesium, elements usually concentrated in tourmaline and micas, which are abundant in metapelites, while the pluton-hosted pegmatites are depleted in these elements and are, in turn, enriched in Th and U (Fig. 5-3a), which tend to concentrate in the terminal stages of fractional crystallization of I-type granitoids (Chappell&White, 1992). The extreme differences existing between these two families of pegmatites can be seen so clearly thanks to the verticalized metacarbonate secta separating the magmatic system fromits host rocks, as they acted as impermeable and plastic separators that did ot allow for the mixig of metamorphic and pluton-related material (fluids and magma). Without these structures rigidly defining the two domains it would have been probably impossible to constrain and compare them so precisely. The large initial $^{87}Sr/^{86}Sr$ variation observed inside the LCT dykes may have several possible explainations:

I) it may be linked to the coalescence of magma batches from different stratigraphical levels of the formation, reflecting the extreme Sr isotopical heterogeneity of their sources;

II) it may be due to the interaction of the external zonations of the pegmatites with the host rocks, either through magmatic assimilation (unlikely), diffusion or through fluid migration;

III) multiple injections of isotopically different pegmatitic magma batches.

More data will be needed to define the origin of this feature, but it is possible to model the third possibility in order to ascertain if it is plausible or not.

In order to do this we need to define the limits of the two portions composing the studied LCT pegmatites with the aim of calculating their chemical compositions. For this we have to rely on the mineralogy of the dykes and on the chemical composition characterizing each zonation (Fig. 5-2). The external portion of the dykes, formed by zones A, B and G, is characterized by the presence of monazite while this mineral is not present in the internal part, represented by zones C-D-E and F. As a result, the external zonations are characterized much higher REEs and Th contents compared to the internal zones (Fig. 5-2a). These characteristics suggests that the two melts are represented by these zonations and that they either originated from two source metapelites featuring slightly different monazite content or that the differentiation process of the internal melt determined the fractionation monazite. The boundaries between the two portions of the LCT pegmatititc dykes are well preserved in the tourmaline rich lines forming up zone B and between zone F and G where the largest miarolitic cavities formed. If this hypothesis is true, it may indicate that pegmatitic gem bearing cavities may form when new melt batches are injected into an already partially cooled pegmatitic dyke where fluids cannot escape through the host rock, remaining sealed inside the structure. Following this line of inquiry, we calculated the mean composition of the "external melt" through a weighted mean of zones A-B and G and the "internal melt" as a weighted mean of zoens C-D-E and F, using as weight the specific volume occupancy of each zonation on the totality of the respective melt. The composition of the former is moderately enriched in Li (ca. 175 ppm), Cs (ca. 50 ppm) and depleted in Sr, Ba while the latter is charaterized by much higher Li and Cs contents (respectively ca. 484 ppm Li and 178 ppm Cs) but Rb Sr, Ba contents comparable the "external melt". We infer that these two Li,Cs and (relatively to Crd-bearing related leucosomes) Be-rich anatectic melts should have been produced in fluid rich conditions, since we previously argued that Crd formation during biotite destabilization causes Li,Cs and Be to remain in the melanosome. This is also supported by the fact that both feature Sr-Nd isotopic disequilibrium-related shifts from their inferred source comparable to those existing between Kfs-rich leucosomes and their connected migmatite. The geochemical signature similarities between the "external melt" and the experimental results of fluid fluxed partial melting, without peritectic cordierite, in the experimental work of Garcia-Arias et al. (2011) suggest that it may be representative of the Crd-absent migmatites primary melt composition and that further investigations through trace elements modelling are needed in order to determine it. On the other hand, the internal zone of the LCT pegmatites is too enriched to be primary, suggesting that "in-source" fractionation played an important role in its formation. In fact, isotopic data suggest the "internal melt" is directly

related to Kfs-rich leucosomes and barren pegmatites which could represent its fractionated counterparts therefore determining its evolved geochemical signature.

5.8.2.3 Trace elements partitioning in the anatectic system

Isotopic and chemical data suggest that the moderately Li-enriched "external LCT melt" may represent the primary melt deriving from fluid-rich partial melting of metapelites. In order to determine if this is plausible, we apply a Monte Carlo simulation-based trace elements model focusing on the elements Li, Rb, Sr, Cs and Ba, which are the most interesting and best studied trace elements in the investigated system. Statitstical validity was insured by computing a large number of melt compositions (N= 10,000) using randomly chosen sets of partition coefficients inside the given ranges. The partition coefficients (Kd) we used (Table B4), sourced from different authors, are reported in Table 3: for Rb, Sr and Ba we used the Kds reported by Laurent et al. (2013) for SiO_2>63%, for lithium we used the ones proposed by Icenhower&London (1995) and, finally, for Cs we used Kds proposed by Evensen&London (2002).

The absence of unreacted domains in these metapelites suggests that equilibrium at the scale of the outcrop was attained during partial melting, therefore we decided to model the trace elements partitioning in the anatectic melts using the batch melting equation expressed as $C_L=C_0/[D_0+F(1-D_0)]$ where D_0 represents the mineral proportions weighted sum of the Kds and F the melt fraction. Lithium, Rb and Cs are typically incompatible elements in crustal anatectic systems while Sr and Ba behave as compatible elements, mainly in Kfs and Pl. The starting material trace elements composition used (ML161, Table B1) is the same low grade metapelite used by Magnani et al (2022) for phase equilibria modelling purposes.

The results of the Monte Carlo simulation at ca. 32% melt fraction highlight that the modelled primary melt composition expected from the Verrucano metapelites is characterized by 140±6 ppm Li, 280±47 ppm Rb, 70±14 ppm Sr, 53.7±0.6 ppm Cs and 178±51 ppm Ba. While these values are perfectly in range with the S-type granites in Fig. 3b and c, they are different from the ulk pegmatite, the "external melt" and the "internal melt", suggesting that neither of them is a primary melt and that "in-source" fractionation played a importat role. Isotopic and geochemical data suggest that Kfs-rich leucosomes are cumulates related to a more evolved melt that was extracted from its source so we used their modal compostion (Magnani et al., 2022) in order to quantify the fractionation process using a new Monte Carlo simulation. This new model predicts that 75% of Kfs-rich cumulates fractionation was needed in order to obtain the trace element concentrations observed in the bulk pegmatite from the primary melt (Fig. 5-7). The external melt gained its chemical composition through fractionation of ca. 20% of Kfs-rich leucosomes (Fig. 5-6a) while the "internal melt" required ca. 75% of "in-source" Kfs fractionation

(Fig. 5-6b). Cs is the least well modelled element, as in the case of the "external melt" it differs from any result of the fractionation Monte Carlo simulation: we argue that

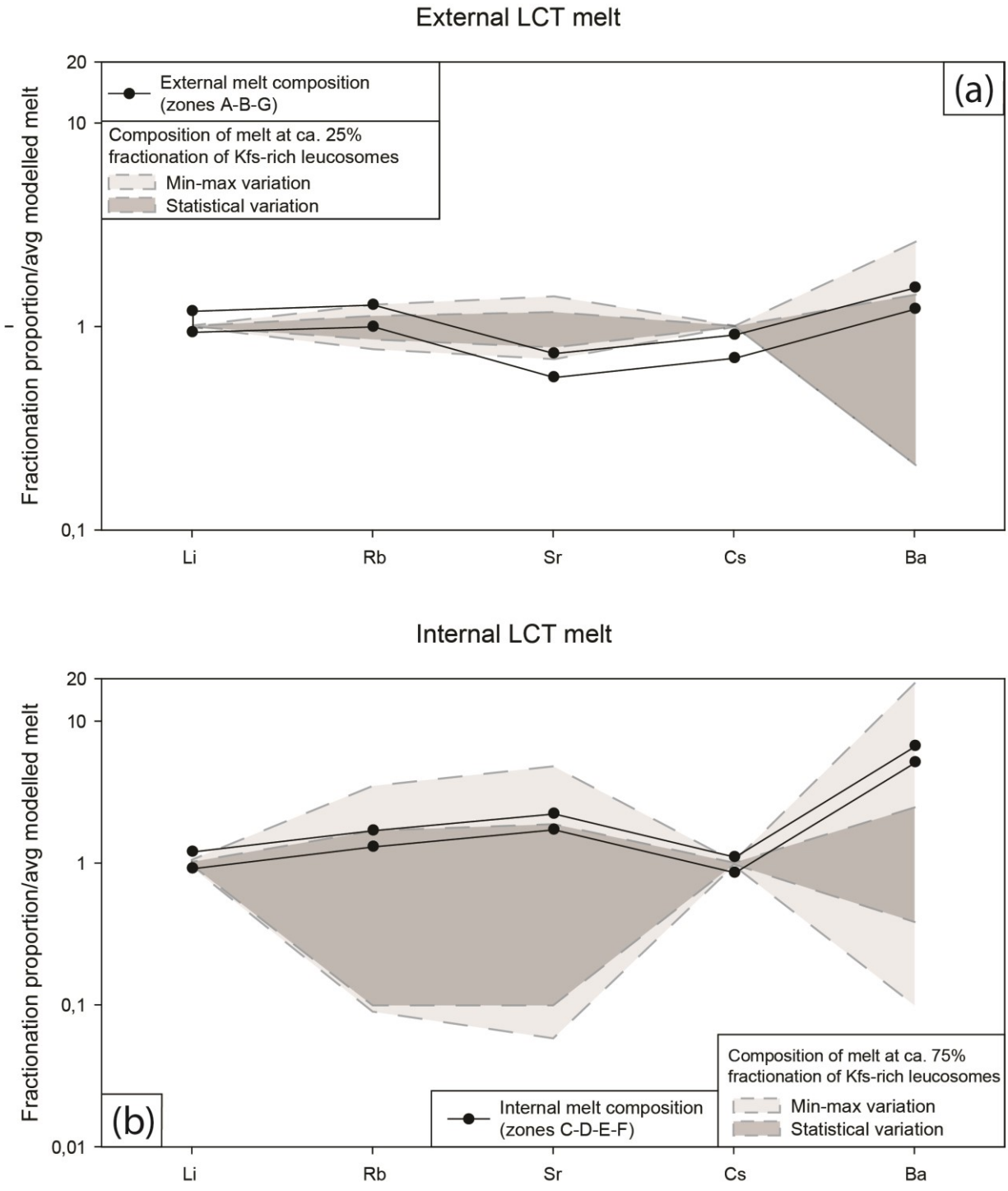

Figure 5-6 Results of the Monte Carlo simulations for the fractionation of the predicted primary melt. a) comparison with the "external melt" composition; b) comparison with the "internal melt" composition

this may be the result of the extremely restrict range of partition coefficients available for Cs in Bt, its main carrier in the metapelites, which basically derive only from one experimental work. The possibility that the efficient extraction of ca. 25 vol.% of an extremely fractionated melt could actually

happen is debatable since its viscosity, linked to the silica content, should have been extremely. Recent studies suggest that the high concentrations of Li, P, B, F and H_2O characterizing these evolved magmas may cause a dramatic decrease in viscosity and ensure they remain fluid (or gel-like) even at low temperatures (e.g. Bartels et al. 2011-2015), supporting our calculations. The presented data shows how important ”in-source” Kfs fractionation (represented by Kfs-cumulates) processes are in the formation of anatectic evolved melts capable of concentrating rare elements like lithium. The preseted calculations show that both scenarios are indeed possible and that more isotopic data will be needed to better constrain this occurrence.

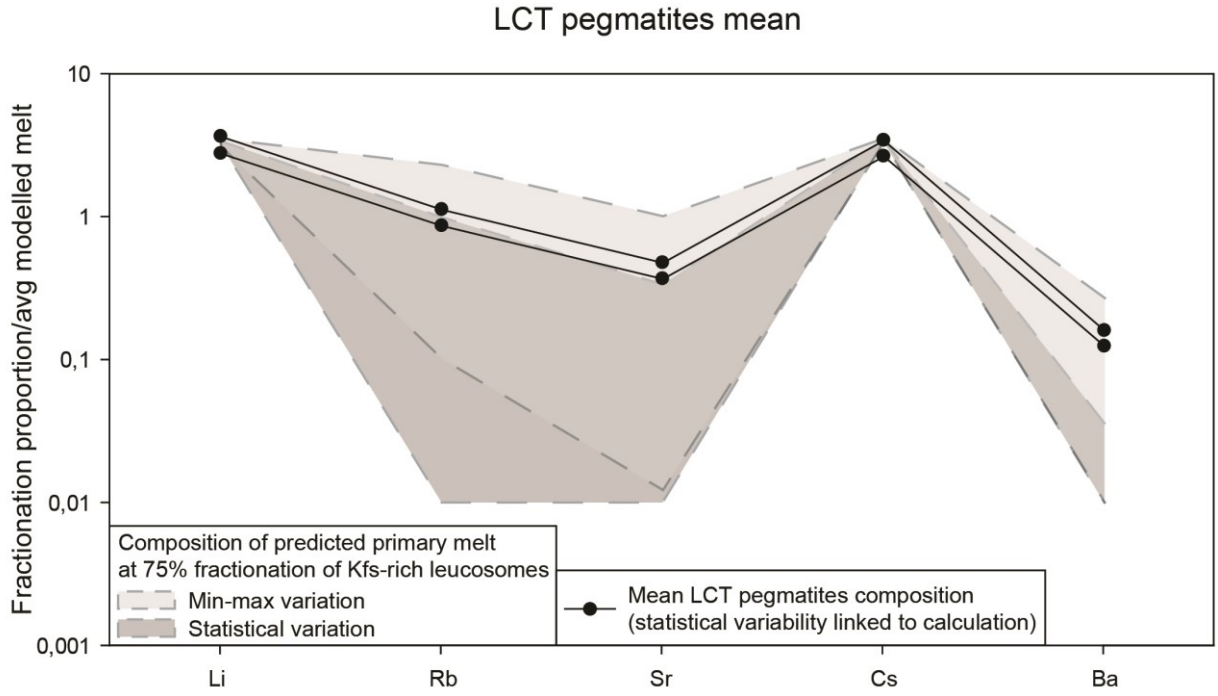

Figure 5-7 Results of the Monte Carlo simulations for the fractionation of the predicted primary melt in comparison with the bulk pegmatite composition.

5.9 Conclusions and critical resources targeting implications

Although the existence of anatectic LCT pegmatites has already been established by some authors in recent years (Simmons et al., 2016; Ilickovic et al., 2017; Schuster et al., 2019) and several other authors pointed to anatexis as source of lithium enriched pegmatites because of the lack of connected nearby plutons (e.g. Ballouard et al., 2020; Tomascak et al., 1998; Chackraborty et al., 2020), we believe that the presented evidence may help clarify a strongly debated process and shed new lights on their genetic mechanisms. In this paper, we highlight how, even in the thermal aureole of granitoid plutons, anatectic pegmatites could form and evolve until reaching interesting lithium enrichment grade without necessarily being directly linked to the plutonic magma. The calculations also define

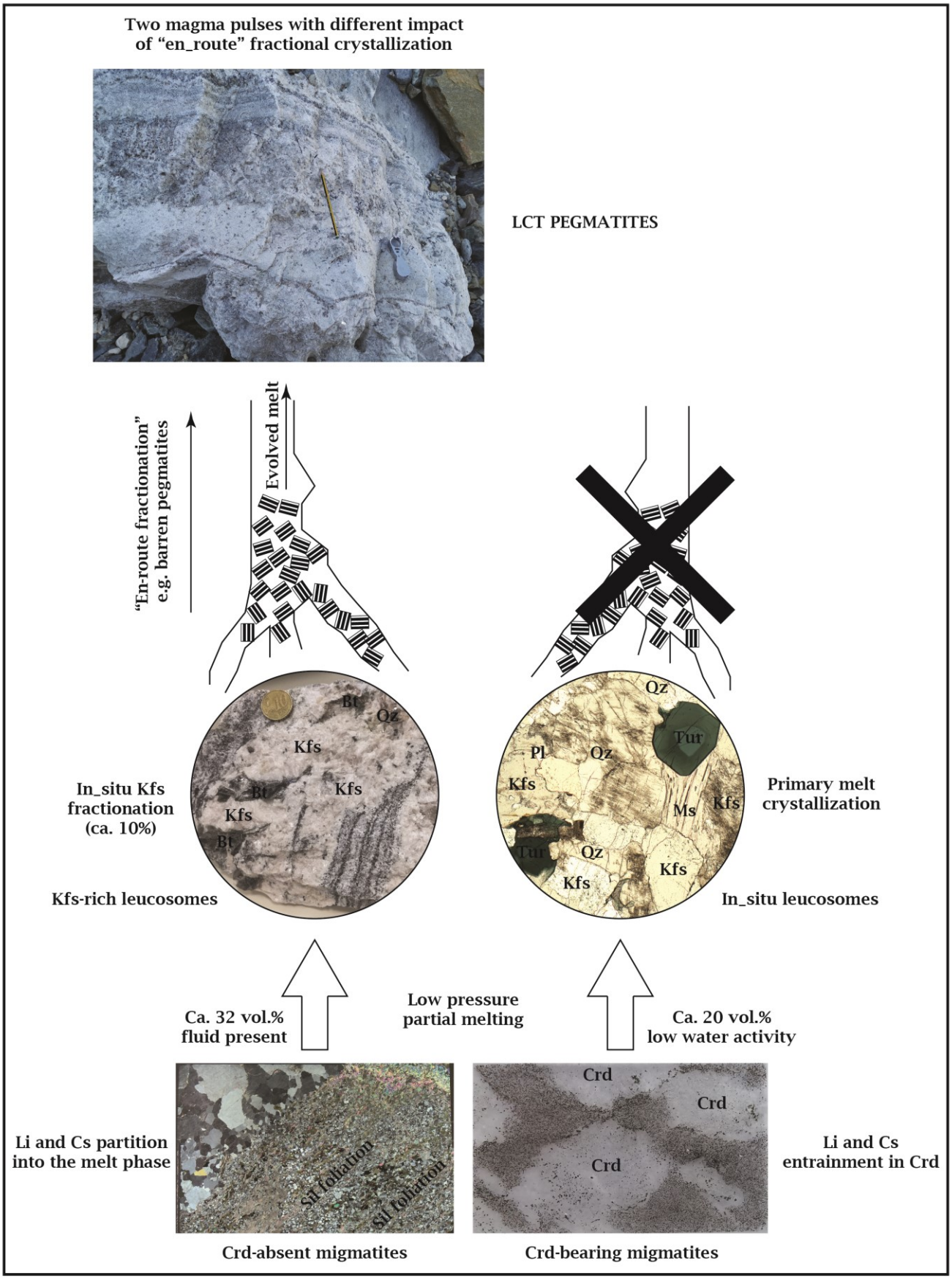

Figure 5-8 Flow chart explaining the formation of LCT pegmatites in the Forcel Rosso area.

that normal pelites featuring Li contents of ca. 60 ppm, similar to those of the mean pelite composition (Wedepohl, 1995), may originate Li-enriched melts in the right conditions. We then propose this set of requirements in a genetic model for anatectic LCT pegmatites (Fig. 5-7) that involves: i) thermal perturbation of a fertile pelitic source; ii) low to medium degree of partial melting under fluid fluxedconditions and without cordierite formation; iii) early fractionation of Kfs-rich leucosomes and barren pegmatites; iv) injection into large fractures in the upper crust expressing several tens of degrees °C of undercooling, in the case of the Forcel Rosso area 80°C (Magnani et al., 2022, data from Crd geothermometer) in agreement with the observations of London et al. (2014). In-source fractionation and injection in undercooled conditions are key elements necessary to express pegmatitic textures versus S-type anatectic granites. More work will be needed to further validate this genetic model for anatectic LCT pegmatites, applying it to other scenarios where the geological conditions we constrained can be recognized (e.g. Jung et al., 2001; Garcia-Arias et al., 2011 and 2015; Gerbi et al., 2006 and references therein). Many different pegmatitic dykes are thoroughly described in nature and classified based on chemical and structural parameters (e.g. Černý&Ercit, 2005), this advocates for many different P-T conditions under which these bodies may have originated, opening new and exciting ways to interpret new discoveries and to, maybe, reinterpret older bodies of uncertain origin. The most important implication for resources exploitation is the ability to target metamorphic fields with the right P-T conditions that evolved in favourable fluids regimes in order to be able to find new LCT pegmatites prospects that may present potential economic value, given the increasing role of lithium as a strategic resource. Since this work focused on melts produced in a restricted range of P-T conditions, it is also possible that pressure may play an important role in the formation of Li-enriched melts in the crust by destabilizing Crd and stabilizing garnet. Experiments suggest that this mineral tends to have lower affinity for lithium (e.g. Jolliff et al., 1992; Klemme et al., 2002; Adam&Green, 2006) than cordierite, although peritectic garnet may behave like peritectic cordierite and be characterized by higher partition coefficients for lithium than expected (Bea et al., 1994a), which remains to be thourougly determined. In the case of higher pressures though, melt productivity would in turn raise causing the formation of more abundant melt fraction, which would in turn be less rich in lithium and would require even more “in-source” fractionation in order to form Li-rich magmatic bodies. More data are needed in this field to correctly constrain lithium movements during partial melting of the continental crust at variable P-T-H_2O and kinetic conditions.

5.10 Acknowledgements

This publication is part of the PhD project of Lorenzo Magnani. Andrea Risplendente is thanked for the EPMA–WDS analyses. The authors acknowledge the Italian Ministry of Education and University (MIUR) for the support through the project "Dipartimenti di Eccellenza 2018–2022 – Le Geoscienze per la società: Risorse e loro evoluzione". The Centro Nazionale Ricerche, CNR-IGG Pisa, is thanked for its fundamental contribution to the whole rock isotopic determinations.

5.11 References

Adam, J., & Green, T. (2006). Trace element partitioning between mica-and amphibole-bearing garnet lherzolite and hydrous basanitic melt: 1. Experimental results and the investigation of controls on partitioning behaviour. Contributions to Mineralogy and Petrology, 152(1), 1-17.

Ayres, M., & Harris, N. (1997). REE fractionation and Nd-isotope disequilibrium during crustal anatexis: constraints from Himalayan leucogranites. Chemical Geology, 139(1-4), 249-269.

Ballouard, C., Elburg, M. A., Tappe, S., Reinke, C., Ueckermann, H., & Doggart, S. (2020). Magmatic-hydrothermal evolution of rare metal pegmatites from the Mesoproterozoic Orange River pegmatite belt (Namaqualand, South Africa). Ore Geology Reviews, 116, 103252.

Bartels, A., Vetere, F., Holtz, F., Behrens, H., Linnen, R.L., 2011. Viscosity of flux-rich pegmatitic melts. Contributions to Mineralogy and Petrology, 162(1), 51-60.

Bartels, A., Behrens, H., Holtz, F., Schmidt, B.C., 2015. The effect of lithium on the viscosity of pegmatite forming liquids. Chemical Geology, 410, 1-11.

Bea F., Pereira M.D., Stroh A. (1994a). Mineral/leucosome trace-element partitioning in a peraluminous migmatite (a laser ablation-ICP-MS study). Chemical Geology, 117(1-4), 291-312.

Bea, F., Pereira, M. D., Corretgé, L. G., & Fershtater, G. B. (1994b). Differentiation of strongly peraluminous, perphosphorus granites: The Pedrobernardo pluton, central Spain. Geochimica et Cosmochimica Acta, 58(12), 2609-2627.

Bigazzi, G., Del Moro, A., & Macera, P. (1986). A quantitative approach to trace element and Sr isotope evolution in the Adamello batholith (northern Italy). *Contributions to Mineralogy and Petrology*, *94*(1), 46-53.

Burnham, A. D. (2020). Key concepts in interpreting the concentrations of the rare earth elements in zircon. Chemical Geology, 551, 119765.

Černý, P. (1991). Rare-element granitic pegmatites. Part I: Anatomy and internal evolution of pegmatite deposits. Geoscience Canada, 18(2), 49-67.

Černý, P., Ercit, T.S. (2005). The classification of granitic pegmatites revisited. The Canadian Mineralogist, 43(6).

Chakraborty, T., & Upadhyay, D. (2020). The geochemical differentiation of S-type pegmatites: constraints from major–trace element and Li–B isotopic composition of muscovite and tourmaline. *Contributions to Mineralogy and Petrology*, *175*(7), 1-25.

Chappell, B. W., & White, A. J. R. (1992). I-and S-type granites in the Lachlan Fold Belt. *Earth and Environmental Science Transactions of the Royal Society of Edinburgh*, *83*(1-2), 1-26.

Chappell, B. W., Bryant, C. J., Wyborn, D., White, A. J. R., & Williams, I. S. (1998). High-and low-temperature I-type granites. Resource Geology, 48(4), 225-235.

Chassé, M., Griffin, W. L., Alard, O., O'reilly, S. Y., & Calas, G. (2018). Insights into the mantle geochemistry of scandium from a meta-analysis of garnet data. Lithos, 310, 409-421.

Christmann, P., Gloaguen, E., Labbé, J. F., Melleton, J., & Piantone, P. (2015). Global lithium resources and sustainability issues. In Lithium process chemistry (pp. 1-40). Elsevier.

Diella, V., Pezzotta, F., Bocchio, R., Marinoni, N., Cámara, F., Langone, A., Lanzafame, G. (2018). Gem-Quality Tourmaline from LCT Pegmatite in Adamello Massif, Central Southern Alps, Italy: An Investigation of Its Mineralogy, Crystallography and 3D Inclusions. Minerals, 8(12), 593.

Evensen, J. M., London, D. (2003). Experimental partitioning of Be, Cs, and other trace elements between cordierite and felsic melt, and the chemical signature of S-type granite. Contributions to Mineralogy and Petrology, 144(6), 739-757.

Farina, F., & Stevens, G. (2011). Source controlled 87Sr/86Sr isotope variability in granitic magmas: the inevitable consequence of mineral-scale isotopic disequilibrium in the protolith. *Lithos*, *122*(3-4), 189-200.

Finger, F., & Schiller, D. (2012). Lead contents of S-type granites and their petrogenetic significance. Contributions to Mineralogy and Petrology, 164(5), 747-755.

Floess, D., Baumgartner, L. (2013). Formation of garnet clusters during polyphase metamorphism. Terra Nova, 25(2), 144-150.

Floess D., Baumgartner L.P. (2015). Constraining magmatic fluxes through thermal modelling of contact metamorphism. From: Caricchi L., Blundy J.D. (eds) Chemical, Physical and Temporal Evolution of Magmatic Systems. Geological Society, London, Special Publications 422.

Floess, D., Baumgartner, L.P., Vonlanthen, P., 2015. An observational and thermodynamic investigation of carbonate partial melting. Earth and Palentary Science Letters 409, 147-156.

García-Arias, M., Corretgé, L. G., & Castro, A. (2011). Trace element behavior during partial melting of Iberian orthogneisses: An experimental study. Chemical Geology, 292, 1-17.

García-Arias, M., Corretgé, L. G., Fernández, C., & Castro, A. (2015). Water-present melting in the middle crust: the case of the Ollo de Sapo gneiss in the Iberian Massif (Spain). *Chemical Geology*, *419*, 176-191.

Gerbi, C. C., Johnson, S. E., & Koons, P. O. (2006). Controls on low-pressure anatexis. *Journal of Metamorphic Geology*, *24*(2), 107-118.

Guillong, M., Meier, D.L., Allan, M.M., Heinrich, C.A., & Yardley, B.W. (2008). Appendix A6: SILLS: A MATLAB-based program for the reduction of laser ablation ICP-MS data of homogeneous materials and inclusions. *Mineralogical Association of Canada Short Course*, *40*, 328-333.

Halden, N. M., & Hawthorne, F. C. (1993). The fractal geometry of oscillatory zoning in crystals: Application to zircon. American Mineralogist, 78(9-10), 1113-1116.

Harris, N., Ayres, M., & Massey, J. (1995). Geochemistry of granitic melts produced during the incongruent melting of muscovite: implications for the extraction of Himalayan leucogranite magmas. Journal of Geophysical Research: Solid Earth, 100(B8), 15767-15777.

Hoskin, P. W. (2005). Trace-element composition of hydrothermal zircon and the alteration of Hadean zircon from the Jack Hills, Australia. Geochimica et cosmochimica acta, 69(3), 637-648.

Hoskin, P. W., & Schaltegger, U. (2003). The composition of zircon and igneous and metamorphic petrogenesis. Reviews in mineralogy and geochemistry, 53(1), 27-62.

Icenhower, J., & London, D. (1995). An experimental study of element partitioning among biotite, muscovite, and coexisting peraluminous silicic melt at 200 MPa (H2O). American Mineralogist, 80(11-12), 1229-1251.

Ilickovic, T., Schuster, R., Mali, H., Onuk, P., & Horschinegg, M. (2017). Genesis of spodumene pegmatites in the Austroalpine unit (Eastern Alps): isotopic and geochemical investigations. Abstracts

and proceedings of the Geological Society of Norway (8th International Symposion on Granitic Pegmatites, Kristiansand, 14.–19.06. 2017), 2(2017), 54-57.

Inger, S., & Harris, N. (1993). Geochemical constraints on leucogranite magmatism in the Langtang Valley, Nepal Himalaya. Journal of Petrology, 34(2), 345-368.

Jolliff, B. L., Papike, J. J., & Shearer, C. K. (1992). Petrogenetic relationships between pegmatite and granite based on geochemistry of muscovite in pegmatite wall zones, Black Hills, South Dakota, USA. Geochimica et Cosmochimica Acta, 56(5), 1915-1939.

Jung, S., Mezger, K., & Hoernes, S. (2001). Trace element and isotopic (Sr, Nd, Pb, O) arguments for a mid-crustal origin of Pan-African garnet-bearing S-type granites from the Damara orogen (Namibia). Precambrian Research, 110(1-4), 325-355.

Kagami, H., Ulmer, P., Hansmann, W., Dietrich, V., & Steiger, R. H. (1991). Nd-Sr isotopic and geochemical characteristics of the southern Adamello (northern Italy) intrusives: Implications for crustal versus mantle origin. Journal of Geophysical Research: Solid Earth, 96(B9), 14331-14346.

Kavanagh, L., Keohane, J., Garcia Cabellos, G., Lloyd, A., & Cleary, J. (2018). Global lithium sources—industrial use and future in the electric vehicle industry: a review. *Resources*, *7*(3), 57.

Kesler, S. E., Gruber, P. W., Medina, P. A., Keoleian, G. A., Everson, M. P., & Wallington, T. J. (2012). Global lithium resources: Relative importance of pegmatite, brine and other deposits. Ore geology reviews, 48, 55-69.

Klemme, S., Blundy, J. D., & Wood, B. J. (2002). Experimental constraints on major and trace element partitioning during partial melting of eclogite. *Geochimica et Cosmochimica Acta*, *66*(17), 3109-3123.

Knoll, T., Schuster, R., Huet, B., Mali, H., Onuk, P., Horschinegg, M., Giester, G. (2018). Spodumene pegmatites and related leucogranites from the Austroalpine Unit (eastern Alps, central Europe): field relations, petrography, geochemistry, and geochronology. *The Canadian Mineralogist*, *56*(4), 489-528.

Kroslakova, I., & Günther, D. (2007). Elemental fractionation in laser ablation-inductively coupled plasma-mass spectrometry: evidence for mass load induced matrix effects in the ICP during ablation of a silicate glass. Journal of Analytical Atomic Spectrometry, 22(1), 51-62.

London, D. (2005). Granitic pegmatites: an assessment of current concepts and directions for the future. Lithos, 80(1-4), 281-303.

London, D. (2014). A petrologic assessment of internal zonation in granitic pegmatites. Lithos, 184, 74-104.

Loucks, R. R., Fiorentini, M. L., & Henríquez, G. J. (2020). New magmatic oxybarometer using trace elements in zircon. Journal of Petrology, 61(3), egaa034.

Magnani, L., Farina, F., Pezzotta, F., Dini, A., Mayne, M. J., & Bartoli, O. (2022). Role of aqueous fluids during low pressure partial melting of pelites in the Adamello pluton contact aureole (Italy). *Lithos*, *430*, 106853.

Michaud, J. A. S., Pichavant, M., & Villaros, A. (2021). Rare elements enrichment in crustal peraluminous magmas: insights from partial melting experiments. Contributions to Mineralogy and Petrology, 176(11), 1-33.

Moyen, J. F., Janoušek, V., Laurent, O., Bachmann, O., Jacob, J. B., Farina, F., ... & Villaros, A. (2021). Crustal melting vs. fractionation of basaltic magmas: Part 1, granites and paradigms. Lithos, 402, 106291.

Morfin, S., Sawyer, E. W., & Bandyayera, D. (2014). The geochemical signature of a felsic injection complex in the continental crust: Opinaca Subprovince, Quebec. *Lithos*, *196*, 339-355.

Morgan Vi, G. B., & London, D. (1999). Crystallization of the Little Three layered pegmatite-aplite dike, Ramona District, California. Contributions to Mineralogy and Petrology, 136(4), 310-330.

Müller, A., Simmons, W., Beurlen, H., Thomas, R., Ihlen, P. M., Wise, M., ... & Zagorsky, V. (2022). A proposed new mineralogical classification system for granitic pegmatites–Part I: History and the need for a new classification. The Canadian Mineralogist, 60(2), 203-227.

Nash, W. P., & Crecraft, H. R. (1985). Partition coefficients for trace elements in silicic magmas. Geochimica et Cosmochimica Acta, 49(11), 2309-2322.

Pearce, N. J., Perkins, W. T., Westgate, J. A., Gorton, M. P., Jackson, S. E., Neal, C. R., & Chenery, S. P. (1997). A compilation of new and published major and trace element data for NIST SRM 610 and NIST SRM 612 glass reference materials. *Geostandards newsletter*, *21*(1), 115-144.

Peters D., Pettke T. (2016). Evaluation of major to ultra trace element bulk rock chemical analysis of nanoparticulate pressed powder pellets by LA-ICP-MS. Geostandards and Geoanalytical Research, vol. 41, n. 1, pp. 5-28.

Sawyer, E. W. (1987). The role of partial melting and fractional crystallization in determining discordant migmatite leucosome compositions. *Journal of Petrology*, *28*(3), 445-473.

Sawyer, E. W., & Barnes, S. J. (1988). Temporal and compositional differences between subsolidus and anatectic migmatite leucosomes from the Quetico metasedimentary belt, Canada. *Journal of Metamorphic Geology*, *6*(4), 437-450.

Schaltegger U., Nowak A., Ulianov A., Fisher C.M., Gerdes A., Spikings R., Whitehouse M.J., Bindeman I., Hanchar J.M., Duff J., Vervoort J.D., Sheldrake T., Caricchi L., Brack P.and Müntener O. (2019). Zircon Petrochronology and $^{40}Ar/^{39}Ar$ Thermochronology of the Adamello Intrusive Suite, N. Italy: Monitoring the Growth and Decay of an Incrementally Assembled Magmatic System. Journal of Petrology 60, vol. 4, 701-722.

Schoene, B., Schaltegger, U., Brack, P., Latkoczy, C., Stracke, A., & Günther, D. (2012). Rates of magma differentiation and emplacement in a ballooning pluton recorded by U–Pb TIMS-TEA, Adamello batholith, Italy. Earth and Planetary Science Letters, 355, 162-173.

Schuster, R., Huet, B., Knoll, T., & Paulick, H. (2019, January). Anatectic origin of albite-spodumene pegmatites: a geochemical model. In Geophysical Research Abstracts (Vol. 21).

Seydoux-Guillaume, A. M., Montel, J. M., Bingen, B., Bosse, V., de Parseval, P., Paquette, J. L., ... & Wirth, R. (2012). Low-temperature alteration of monazite: Fluid mediated coupled dissolution–precipitation, irradiation damage, and disturbance of the U–Pb and Th–Pb chronometers. Chemical Geology, 330, 140-158.

Shaw, D. M. (1954). TRACE ELEMENTS IN PELITIC ROCKS: PART I: VARIATION DURING METAMORPHISM. Geological Society of America Bulletin, 65(12), 1151-1166.

Simmons, Wm. B., E. E. Foord, and A. U. Falster, 1996. Anatectic Origin of Granitic Pegmatites, Western Maine, USA. GAC-MAC Annual meeting, Winnipeg. Abstracts with Programs.

Simmons, W.B., Foord, E.E., Falster, A.U. & King, V.T. (1995): Evidence for an anatectic origin of granitic pegmatites, western Maine, USA. Geol. Soc. Amer. Annual Meeting., Abstr Programs 27, (6), A411.

Simmons, W.B.S., Webber, K.L. (2008). Pegmatite genesis: state of the art. European Journal of Mineralogy, 20(4), 421-438.

Simmons, W., Falster, A., Webber, K., Roda-Robles, E., Boudreaux, A. P., Grassi, L. R., & Freeman, G. (2016). Bulk composition of Mt. Mica pegmatite, Maine, USA: Implications for the origin of an LCT type pegmatite by anatexis. The Canadian Mineralogist, 54(4), 1053-1070.

Sláma, J., Košler, J., Condon, D. J., Crowley, J. L., Gerdes, A., Hanchar, J. M., Whitehouse, M. J. (2008). Plešovice zircon—a new natural reference material for U–Pb and Hf isotopic microanalysis. Chemical Geology, 249(1-2), 1-35.

Sliwinski, J. T., Guillong, M., Liebske, C., Dunkl, I., Von Quadt, A., & Bachmann, O. (2017). Improved accuracy of LA-ICP-MS U-Pb ages of Cenozoic zircons by alpha dose correction. Chemical Geology, 472, 8-21.

Soman, A., Geisler, T., Tomaschek, F., Grange, M., & Berndt, J. (2010). Alteration of crystalline zircon solid solutions: a case study on zircon from an alkaline pegmatite from Zomba–Malosa, Malawi. Contributions to Mineralogy and Petrology, 160(6), 909-930.

Stepanov, A., A Mavrogenes, J., Meffre, S., & Davidson, P. (2014). The key role of mica during igneous concentration of tantalum. *Contributions to Mineralogy and Petrology*, *167*(6), 1-8.

Tomascak P.B., Krogstad E.J., Walker R.J. (1998) Sm-Nd isotope systematics and the derivation of pegmatites in southwestern Maine. *The Canadian Mineralogist 36*, 327-337.

Tropper, P., Wyhlidal, S., Haefeker, U. A., & Mirwald, P. W. (2018). An experimental investigation of Na incorporation in cordierite in low P/high T metapelites. Mineralogy and Petrology, 112(2), 199-217.

Ulmer, P., Callegari, E., & Sonderegger, U. C. (1983). Genesis of the mafic and ultramafic rocks and their genetical relations to the tonalitic-trondhjemitic granitoids of the southern part of the Adamello batholith (Northern Italy). Memorie della Società Geologica Italiana, 26(1), 171-222.

Ushikubo, T., Kita, N. T., Cavosie, A. J., Wilde, S. A., Rudnick, R. L., & Valley, J. W. (2008). Lithium in Jack Hills zircons: Evidence for extensive weathering of Earth's earliest crust. Earth and Planetary Science Letters, 272(3-4), 666-676.

Van Hinsberg, V. J. (2011). Preliminary experimental data on trace-element partitioning between tourmaline and silicate melt. The Canadian Mineralogist, 49(1), 153-163.

Villaros, A., Stevens, G., Moyen, J. F., & Buick, I. S. (2008). The trace element compositions of S-type granites: evidence for disequilibrium melting and accessory phase entrainment in the source. Contributions to Mineralogy and Petrology, 158(4), 543-561.

Villaros, A., Pichavant, M. (2019). Mica-liquid trace elements partitioning and the granite-pegmatite connection: The St-Sylvestre complex (Western French Massif Central). *Chemical Geology, 528*, 119-265.

Wang, Y., & Trail, D. (2022). Experimental partitioning of Li between zircon and different silicate melts: implications for Li contents in the Hadean and modern crust. Contributions to Mineralogy and Petrology, 177(1), 1-14.

Wedepohl, K. H. (1995). The composition of the continental crust. Geochimica et cosmochimica Acta, 59(7), 1217-1232.

Wise, M. A., Müller, A., & Simmons, W. B. (2022). A proposed new mineralogical classification system for granitic pegmatites. The Canadian Mineralogist, 60(2), 229-248.

Wolf, M., Romer, R. L., & Glodny, J. (2019). Isotope disequilibrium during partial melting of metasedimentary rocks. *Geochimica et Cosmochimica Acta*, *257*, 163-183.

Chapter 6

Pegmatitic zircons and age of the pegmatites

6.1 Introduction

Zircon ($ZrSiO_4$) is a mineral of singular importance in Earth science as its widespread use in geochronology, based on the decay of uranium (U) to lead (Pb), has established it as Earth's best timekeeper. It is extremely variable both in terms of external morphology and internal textures and these features reflect its geologic history, especially the relevant episode(s) of magmatic or metamorphic crystallization (and recrystallization) and the strain imposed by both external forces, internal metamictization-induced volume expansion, and chemical alteration.

Zircon has become one of the most widely used minerals for the extraction of information on the genesis and evolution of magmatic rocks. Apart from its geological suitability as a geochronometer based on the decay of U (and Th) to Pb, its REE and other trace elements abundances, alongside the application of the radiogenic isotopic tracer Hf, can help define the affinity of the magmas from which zircons crystallized. All these data yield useful clues concerning the history of the host rock, and in some case also the parent rock from which they derived (Corfù et al., 2003).

Zircons in pegmatites and aplites have been widely studied (e.g. Neves et al., 1974; Tilton et al., 1957; Schaltegger et al., 2015; Soman et al., 2010; Uher and Černý, 1998; Wang et al., 2007) but they are so peculiar that a comprehensive review study able to classify them is still missing. The same is true for zircons from extremely evolved granitic melts (e.g. Troch et al., 2018). The fractionated nature of rare elements-enriched pegmatitic melts determines an extreme enrichment of zircon in REEs, U and Th contents. This phenomenon is connected to the partial solid solution between the isomorphs zircon, thorite ($ThSiO_4$), coffinite ($USiO_4$) and xenotime [$(Y,HREE)PO_4$] (e.g. Förster, 2006) ultimately leading to the deformation of the zircon structure. In some cases these minerals may also exsolute from the zircon crystals generating honeycomb textures (e.g. Troch et al., 2018), making it difficult to obtain inclusion-free signals during in-situ analyses. The incorporation of excess U and Th, in turn, tends to destroy the crystal lattice through radioactive decay, because of the extremely high alpha dose these zircons are subjected to after crystallization. The likely result of these outstanding features is that Th- and U-enriched zircons older than a few hundred million years tend to become extremely difficult to study since they cannot be annealed for fear of inclusions contamination, they cannot be chemically abraded because they may dissolve completely, together with their many inclusions, and they are likely prone to U and Pb loss, making their U-Pb age determination tricky at best. In this work we

study young pegmatitic and aplitic zircons from the two different families of pegmatites described in the Forcel Rosso area in order to date the ages of intrusion and use trace elements concentrations in order to determine temperature and oxygen fugacity conditions at the time of emplacement and to identify compositional peculiarities of each melt that could help in tracing back their geochemical affinity. Ultimately, we try to define if zircons in young pegmatites can indeed be used in order to determine wheter pegmatites are anatectic or pluton-derived.

6.2 Previous studies on the Adamello batolith zircons

The Adamello batholith zircon petrochronology and trace elements have been widely studied by several authors that contributed to its in-depth knowledge and to the overall evolution of magmatic systems. Schaltegger et al. (2009) and Schoene et al. (2012) investigated the timing of intrusion and rates of magma differentiation in the Re di Castello pluton using high-precision zircon U-Pb geochronology, finding that it formed through incremental accretion that progressed for ca. 1.5 Ma. Zircon Hf isotopes with largely positive εHf values made the authors suggest that their parent magma was of depleted mantellic origin. Tiepolo et al. (2011) date the mafic intrusions of the Mt. Cadino and Mattoni between at ca. 44 and 40 Ma using U-Pb zircon geochronology and the zircon chemistry suggest ultramafic crustal material assimilation by the amphibole-forming melt.

Schaltegger et al. (2019) and Ji et al. (2019) investigated the timing and duration of magmatism on the whole Adamello batolith identifying a prolonged assembly process ca. 10-12 Ma long from ca. 44 to 33 Ma, with maximum intra-unit age dispersion of ca. 2.3 Ma (Re di Castello pluton) using SIMS and LA-ICP-MS zircon U-Pb dating. Zircon in-situ Hf isotopes, oxygen isotopes and trace elements suggest a continuous evolution through magmatic differentiation and increasing crustal material assimilation towards the younger and more evolved Avio and Presanella plutons. The Adamello pluton in particular features age of 38.23 ± 0.24 Ma at the Forcel Rosso pass, εHf values between ca. -1 and -9 suggesting important crustal contamination, oxygen fugacity (calculated using Trail et al., 2011) between -10 (MH) and -15 (FMQ) and crystallization temperature (Loucks et al., 2020) of 803 ± 50°C.

6.3 Methods

Zircon trace element concentrations and U-Pb ages were determined by LA-ICP-MS at the Geochemistry, Geochronology and Isotope Geology laboratory of the Earth Science Department, Università degli Studi di Milano (Italy). The instrument couples an Analyte Excite 193 nm ArF excimer laser microprobe system equipped with a double volume chamber cell HelEx II (Teledyne Cetac Technologies) to a single-quadrupole ICP-MS (iCAP-RQ, Thermo Fisher Scientific).

Conditions for trace element determinations in zircon were: spot diameter of 25 μm, repetition rate of 10 Hz and a fluence of 2 J/cm^2. He gas flow rates were 0.5 1/min in the sample cell, and 0.21/min in the cup. The SiO_2 concentration in zircon was considered at the stoichiometric value of 32.78 wt.% and used as internal standard during calculations using the Glitter software (Griffin et al., 2008). Glass reference materials NIST-SRM612 (Jochum et al., 2011) and BCR-2G (Jochum et al., 2005) were used respectively as external standard and as quality control. On the glass references the spot diameter was set at 40 μm, repetition rate at 10 Hz and fluence at respectively 6 J/cm^2 ($NIST_{SRM}612$) and 3 J/cm^2 (BCR-2G). For U-Pb in zircon geochronology, the analyses were carried out with a laser spot of 25 μm, fluence set at 3 J/cm^2, and repetition rate of 7 Hz. Helium gas flow rate was set at 0.5 l/min in the sample cell, and at 0.2 l/min in the cup. The unknown were standardized on zircon 91500 (Wiedenbeck et al., 1995, 2004) using Plesovice zircon (Slama et al., 2008) for quality control. Data treatment was performed on Glitter (Griffin et al., 2008) and final U-Pb ages for the zircon groups were obtained through IsoplotR (Veermesch, 2018).

6.4 Zircon Petrography

. Zircons were classified into three types, defined on the basis of textural characters (Fig. 6-1).

- Type I zircons are only found in the lithium-rich pegmatites, hosted in the metapelites. They have subhedral crystalline habits, often elongated to form needle-like crystals, and are completely transparent without external signs of metamictization. They appear homogeneously dark in CL and show no zoning, either in CL or BSE. Inclusions found in Type I zircons are limited to smaller zircons (which are rare) and micrometric to submicrometric inclusions of Yb-rich xenotime.
- Type II zircons are found in the biotite-bearing pluton-hosted pegmatites: they are characterized by euhedral to subhedral crystalline habits, often resorbed, showing rounded embayements (Fig. 6-1) and resorption along fractures without overgrowths. They are also transparent and show no evident sign of metamictization. They appear dark in CL and show no clear compositional zoning both in CL and BSE. Rarely, the most euhedral crystals show a preferential incorporation of inclusions clustering into cryptic oscillatory zoning. Most of the grains are rich in inclusion of thorite, K-feldspar, apatite and rare plagioclase but rare zircons free of inclusions also occur, mainly featuring euhedral crystal habit.
- Type III zircons are found in the biotite-bearing pluton-hosted pegmatites and are particularly abundant in the aplitic dykes hosted within the Adamello pluton. Aplitic samples yielded only

Type III zircons. They are oscillatory zoned and reactive to CL, usually euhedral with crystalline habits mainly expressing {110} and {101} as their dominant form. The majority of cores are homogenous either dark or bright and are surrounded by oscillatory zoned rim. These cores are often rounded and show evidence of partial resorption but clear truncation between core and rims is rarely observed.

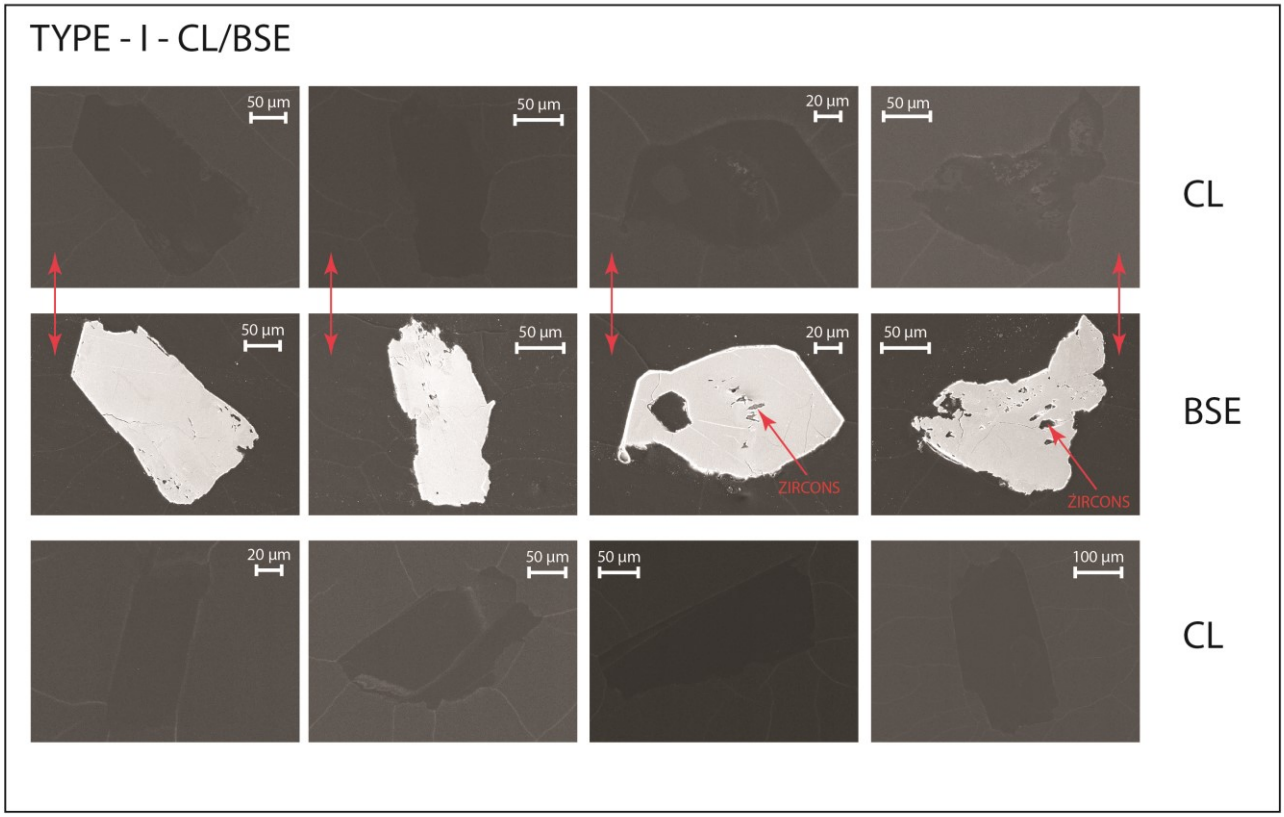

Figure 6-1.1 LCT pegmatites-hosted Type I zircons

Inclusions are invariably composed of decimicrometric apatite crystals. Their crystal habits and zonations are very similar to those of the Adamello pluton zircons of Schaltegger et al., (2019) and other authors and also the inclusions are composed only of decamicrometric apatite crystals, which are common in pluton-related crystals while they are never found in any Type I or II zircons.

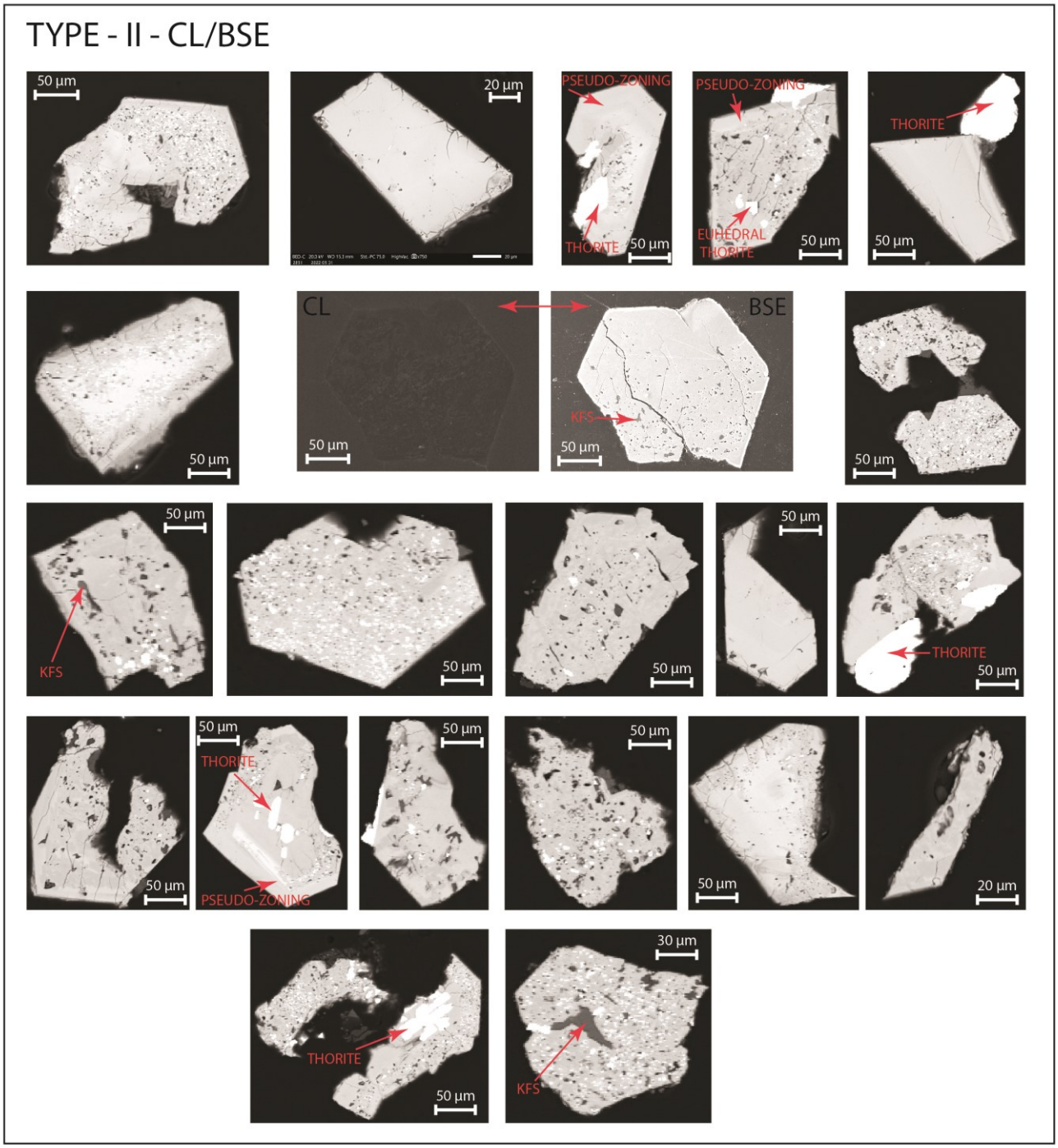

Figure 6-1.2 Pluton pegmatites-hosted Type II zircons

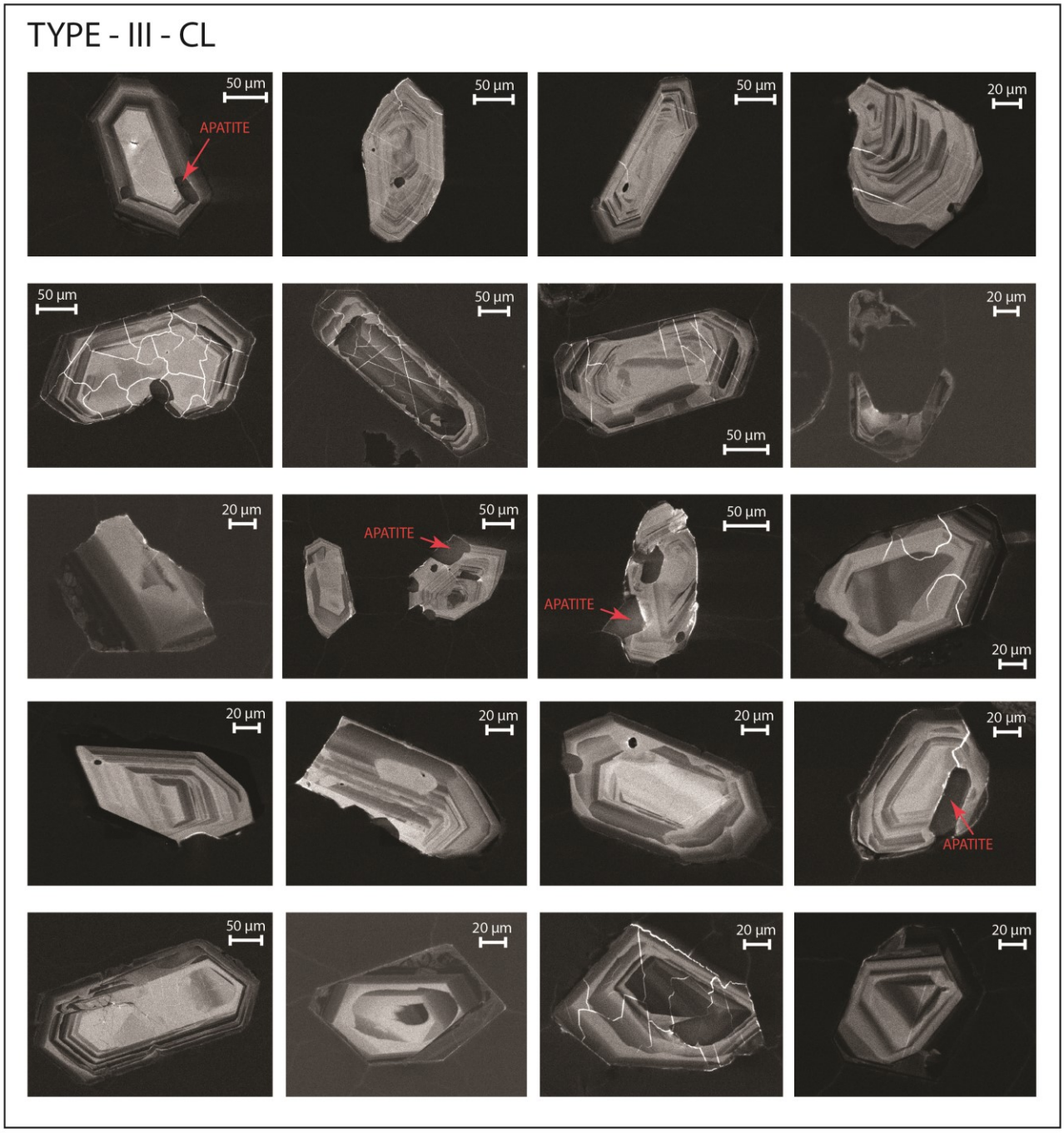

Figure 6-1.3 Pluton aplites-hosted Type III zircons

6.5 Zircon trace elements composition

Zircon trace elements composition supports the textural subdivision and expands our capacity to define the chemical systems they crystallized from (Fig. 6-2). All data are reported in Tables C1.1 (Type I), C1.2 (Type II) and C1.3 (Type III) in appendix C.

- Type I zircons are Li-rich (20 to 60 ppm Li), Ti-poor (1 to 5 ppm Ti) and extremely enriched in Y (0.7 to 2.2 wt.%), HREE, Hf (0.9 to 2 wt.%), Th (200 to 900 ppm) and U (0.9 to 3.3 wt.%).

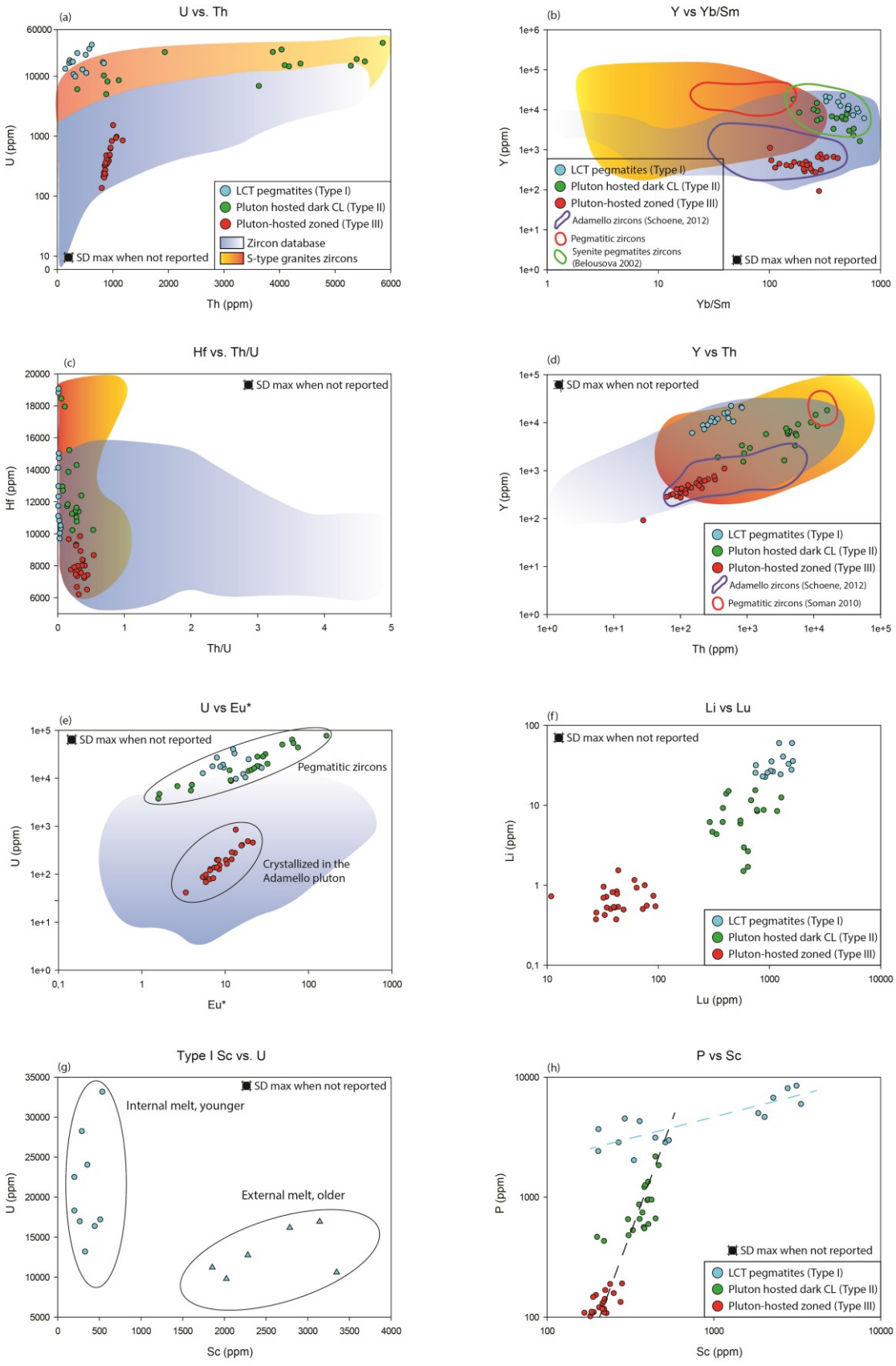

Figure 6-2 Zircons trace elements diagram, for description refer to the text. S-type granitic zircons from Breiter et al. (2014); Zircon database from Carley et al. (2014), Caliborne et al. (2010), Farina (unpublished), Lukacks et al. (2021), Reimink et al.(2020), Schoene et al. (2012), Shen et al. (2015).

Sc is sometimes extremely enriched as it is comprised between 200 and 3300 ppm. Two subgroups, determined by chemical zoning, can be identified among these zircons: the cores, which are cryptic and cannot be readily identified through CL or BSE, are characterized by extremely high Sc (Fig. 6-2g, h, between 1800 and 3400 ppm) and the highest P, HREEs and Y contents in the group, while the zircons rims are characterized by normal Sc contents (200 to 550 ppm), higher U (16000 up to 33000 ppm), Hf (11000 to 20000 ppm) and Ta (c15 up to 70 ppm) compared to the cores.

- Type II zircons feature low to moderately high Li (1 to 15 ppm Li), Ti content ranging from ca. 4 to 7 ppm, they are Y-rich (0.1 to 1.4 wt.%) and HREE-rich, even if less than Type I zircons, and extremely enriched in Hf (1 to 2.1 wt.%), Th (300 ppm to 1 wt.%) and U (0.4 to 4.1 wt.%). Sc content ranges between 200 to 470 ppm without any discernible cheminal zoning. Nb and Ta contents are comparable and invariably higher than in Type I zircons, ranging respectively from 40 to 200 ppm Nb and 20 to 210 ppm Ta.
- Type III zircons are extremely Li-poor (up to 1.5 ppm), have medium Ti content (from ca 2 to 7 ppm), higher than type I but comparable with type II zircons. They have low Y (90 to 1000 ppm), HREE, Nb (up to 5 ppm) and Ta (up to 2 ppm), Th (60 to 500 ppm) and U (under 1500ppm) compared with Type I and II zircons. Hf is comprised between 0.6 and 1 wt.%.

6.6 Zircon U-Pb ages

U-Pb ages were obtained from the set of zircons separated from LCT and pluton-related pegmatites using LA-ICP-MS (Fig. 6-3). As the analyzed zircons are relatively young, the age has been calculated as a weighted mean of their $^{206}Pb/^{238}U$ values. Results in Tables C2.1 (I), C2.2 (II), C2.3 (III).

In the LCT pegmatites, ten Type I zircons were dated yielding a weighted mean $^{206}Pb/^{238}U$ age of 39.62 ± 0.32 Ma (MSWD 0.9, n.8) with no discernible differences between cores and rims.

In the pluton-related pegmatites, Type II and Type III zircons were recognized. In total, 22 Type II zircons and 21 Type III zircons from four samples of pegmatites and aplites were dated. Type II zircons data are the most scattered because of their main inclusions and many are characterized by lead loss. We plotted all data on a Tera Wasserburg discordia plot obtaining an age of 39.78 ± 0.25 Ma (MSWD 3). Using a 95% concordance filter we determined a $^{206}Pb/^{238}U$ weighted mean age of 39.86 ± 0.32 Ma (MSWD 1.8, n.10). Type III zoned zircons yield a good weighted mean age of 37.36 ± 0.19 Ma (MSDW 1.6, n.35), but applying the same 95% concordance filter we can find an even better age of 37.67± 0.29 (MSWD 1.3, n.16). One inherited zircon core dating at ca. 373 Ma was identified in a Type III zircon. All age uncertainties are referred to the 95% confidence level.

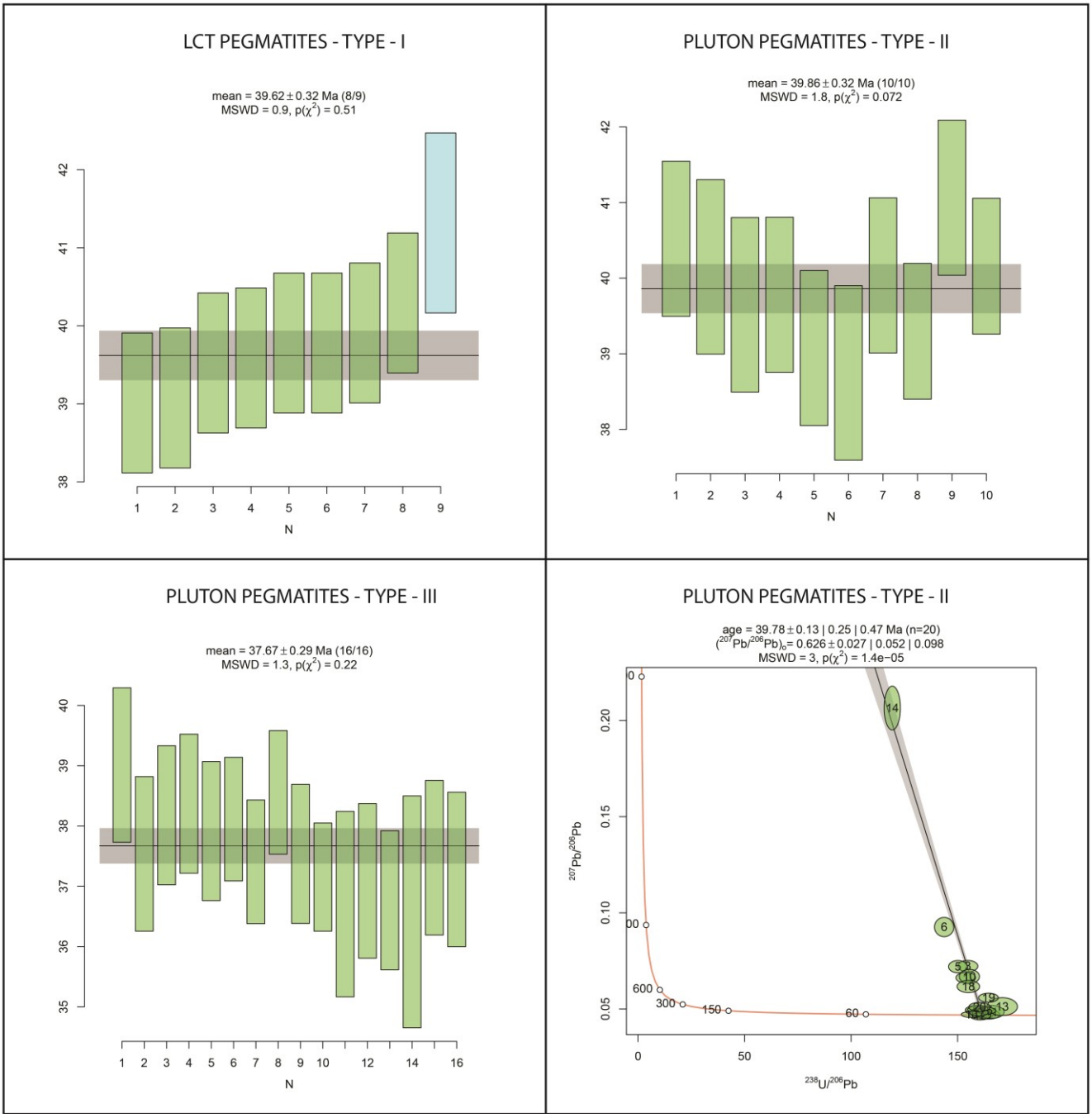

Figure 6-3 U-Pb ages for Type I-II-III zircons; top left 6/38 age of Type II zircons; bottom left Tera Wasserburg age of Type II zircons

6.7 Discussion

6.7.1 Zircon textures

Textures and inclusions concur in defining the three zircon types identified in the Forcel Rosso pegmatites. Interestingly, all zircon types appear to be not too damaged by radioactive decay, since they do not appear reddish like may other zircons from LCT and other evolved pegmatites described in literature (e.g. McCauley&Bradley, 2014 and references therein; Bradley et al., 2016; Goncalves et al.,

2019). Type I zircons are completely homogeneous, with rare zircon inclusions but show submicrometric exsolutions of Yb-xenotime [(Y,HREE)PO_4], suggesting these zircons grew from a P and Y-rich melt. On the other hand, Type II zircons formed in evolved pluton-hosted pegmatites are still homogeneous but extremely rich in thorite ($ThSiO_4$), Kfs and Pl inclusions suggesting they grew from a Th-rich melt. The inclusions in Type II zircons define honeycomb textures, with some zircons so full of them that we were not able to perform any non-mixed in-situ analyses. Similar textures are described in the cores of the Yellowstone rhyolitic magmatic units zircons (Troch et al., 2018 and references therein) and in granulite-hosted dykes of the IVZ (Bonazzi et al., 2020) and defined as "spongy". As in their case, in some grains, the inclusions follow primary growth zones ("ghost textures"), whereas neighbouring zones with lower trace element contents remain inclusion-free. Thorite is present as a mineral phase in pluton-hosted pegmatites and we observe that many Type II zircons include euhedral to subhedral crystals of this mineral at their core, suggesting that they formed after it. The presence of extremely fine-grained anhedral thorite inclusions disseminated in the zircon crystals, sometimes aligned along pseudo-zonations suggest that this may have formed through zircon recrystallization from a thorite-zircon solid solution (e.g. Troch et al., 2018). Moreover, as thorite is isostructural to zircon, the anhedral inclusions observed in pseudo-zoning areas resemble the dissolution reprecipitation patterns described by Geisler et al. (2007). The existence of rare inclusion-free euhedral Type II zircon crystals suggests the protracted crystallization of zircon after thorite exahustion. We identify that thorite inclusions in zircons in fractionated felsic rocks may be a good proxy for identifiyng mantle derived fractionates from crustal melting products. These zircon inclusions seem to be characteristic of the terminal stages of I-type mantle derived granitoids with variable stages of crustal contamination (e.g. Adamello pluton, this work and Yellowstone volcanics, Troch et al., 2018 and references therein). Although these inclusions are rare, they may be useful in identifying the geochemical affinity of some evolved vulcanites, pegmatites and granitoids. Type III zircons are oscillatory zoned and similar to normal magmatic crystals, with large apatite inclusions that are not present in Type II zircons. The textural differences existing between Type II and III zircons suggest that they may have formed from different systems as no Type III zircons overgrowths are observed on Type II zircons or the other way around.

6.7.2 Age of the pegmatitic bodies

The age of the pegmatitic bodies in the Forcel Rosso area, both hosted in the metapelites of the Verrucano Lombardo formation and in the Adamello pluton, is compatible with that of the Adamello batholith intrusion, marking them as contemporaneous to the periadriatic magmatic event. Type I and

Type II zircons yield similar $^{206}Pb/^{238}U$ ages, respectively 39.62 ± 0.32 Ma and 39.86 ± 0.32 Ma while Type III zircons are younger, at 37.67 ± 0.29 Ma. The Adamello pluton, that we infer to be indirectly correlated with Type I zircons (of the LCT pegmatites) and in which the pegmatites hosting Type II and III zircons are intruded, is dated at 38.23 ± 0.24 Ma (Schaltegger et al., 2019, LA-ICP-MS) at the Forcel Rosso pass. This pluton has a concentric structure (e.g. Blundy, 1989) and the most external zones, in which our pegmatites are intruded, are the oldest, most rigid and cold portions of the magmatic mass, capable of cracking under stress. Field relationships suggest that pluton-hosted pegmatites are slightly younger than their host as they intrude it with sharp contacts, emplaced following decompression during fractures opening. The observed plastic deformation is a sign that the magmatic mass was still at moderately high temperatures when they intruded it. Type III zircons yield ages compatible with these observations, marking them as possibly pluton-derived, but Type II zircons are slightly too old for them to be formed during the pegmatites intrusion in the partially cooled Adamello pluton. They either predate the Adamello pluton and were transported in the pegmatites from the older Re di Castello pluton (the only one with compatible age) or the LA-ICP-MS age determination was disturbed by the high to extremely high U and Th contents characterizing zircon Types I and II, which generated extremely high α-doses (Mattinson, 2010; Sliwinski et al., 2018a) during their geological history. Since there is no field evidence that both pluton-hosted and metapelites-hosted LCT pegmatites could have been produced by the Re di Castello pluton and several verticalized metacarbonates septa separate it from the Adamello pluton at the Forcel Rosso, the difference should be linked to the radiation damage affecting the zircon crystals, which should be corrected. Unfortunately, thermal annealing and chemical abrasion couldn't be applied to the studied zircons because they are either full of Pb-bearing inclusions (Type II), that would have caused mixed CA analyses or may present Li-rich inclusions (Type I) that may have caused Li diffusion in the zircon crystals (Sliwinski et al., 2018b). In order to make it possible to compare our LA-ICP-MS analyses with annealed zircons data (e.g. Schaltegger et al., 2019), we applied the α-dose correction proposed by Sliwinski et al. (2018a) allowing for radiation damage correction. This work is based on the fact that the most important factor impacting crystal lattice deformation, ultimately influencing the LA-ICP-MS age determination compared to CA-ID-TIMS data (Allen and Campbell, 2012), is the degree of metamictization and that zircon crystals thermal annealing cannot always be performed. Our ages have been corrected by putting our raw data in the program developed by Sliwinski et al. (2018a) and using them to calculate α-dose corrected weighted mean ages for all types of zircons found in the Forcel Rosso pegmatites. Corrected $^{206}Pb/^{238}U$ ages (Fig. 6-4) are 38.35 ± 0.23 Ma (2σ, MSWD 2.6, n.8) for Type I zircons and 37.85 ± 0.26 Ma (2σ, MSWD 1, n.7) for Type II zircons calculated after

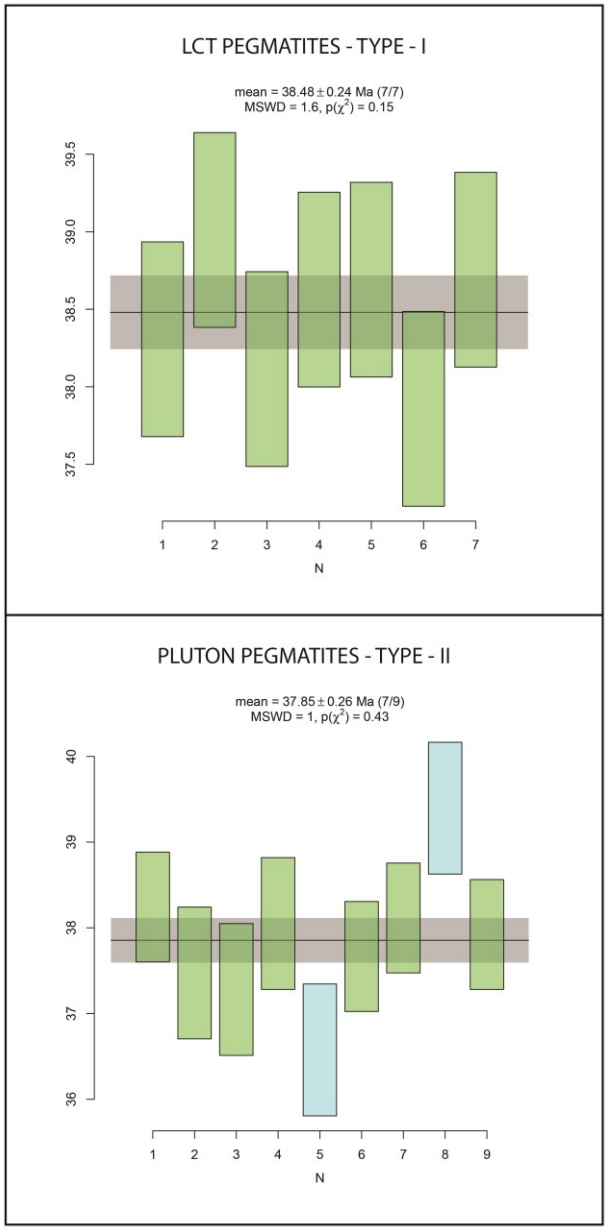

Figure 6-4 Corrected 6/38 ages for Type I and II zircons

rejection of discordant ages using a 95% concordance filter. Type I corrected zircon age is concordant within uncertainty with the the Adamello pluton intrusion age, directly correlating it to the metapelites partial melting event as expected (chapter 4 and 5). Type II (corrected) and III zircons ages are undistinguishable within uncertainty and are compatible with the Adamello pluton age at the Forcel Rosso Pass, showing that the pluton-hosted pegmatites formed slightly after the most external shell of the Adamello pluton began cooling down. This data is indistinguishable from the age of the Adamello pluton intrusion (38.23 ± 0.24 Ma, Schaltegger et al., 2019) and the only way to have more precise ages and better resolve this complex geological situation without resorting to numerical corrections would involve CA-ID-TIMS high precision techniques. Unfortunately, only zircons Type I and III could be anlyzed with this technique as Type II zircons are too rich in inclusions hosting initial Pb as Kfs, Pl and thorite.The presence of an inherited core dating at ca. 373 Ma, derived from the digested country rocks (e.g. Schaltegger et al., 2009) only in the Type III zircon group suggests that these zircons may be xenocrystic, having crystallized within the plutonic mass until they were incorporated into the pegmatites. This would explain why we don't observe any Type II core inside Type III zircons, differently from what was observed in the Yellowstone magmatic units (Bindeman et al., 2008; Matthews et al., 2015; Troch et al., 2018).

6.7.3 Zircon crystallization temperatures and oxygen fugacity conditions

Zircon trace elements are used to discriminate between the sources of the studied pegmatites, alongside zircon pressure-dependent crystallization temperatures and oxygen fugacity in the systems (Fig. 6-5) based on Loucks et al. (2020). Pressure was calculated at ca. 300 MPa using phase equilibria modelling. SiO_2 activity was determined at 1 for all types of pegmatitic bodies as quartz is a stable phase. TiO_2 activity was determined at 1 for LCT pegmatites as they are rutile-bearing with clear indicators that both mineral phases crystallized early on, as they are included into Kfs crystals. TiO_2 activity in pluton-hosted pegmatites was estimated at 0.5 as titanite is the main Ti-bearing phase present in these magmatic bodies and no ilmenite is recognized (e.g. Schiller&Finger, 2019).

Type I zircons of the LCT metapelites-hosted pegmatites yield temperatures ranging between 618 and 745°C, with a mean of 679 ± 36°C and oxygen fugacity (fO_2) values between ca. -21.8 and -17.5, with a mean value of -19.78 ± 1.36. Type II zircons in the pluton-hosted pegmatites yield a mean crystallization temperature of 827 ± 29°C at 0.5 $aTiO_2$ after rejection of three outlier values characterized by ca. 5 times the Ti content of the bulk of the analyses, which probably sampled Ti-bearing microinclusions of titanite. The oxygen fugacity mean value for this zircon group is -14.75 ± 1.02 after outliers rejection.

Type III zircons in the pluton-hosted aplites feature a mean crystallization temperature of 782 ± 30°C and fO_2 mean value of -15.76 ± 0.60.

The temperature calculated for Type I zircons is compatible within error with the 687 ± 12°C calculated in the migmatites using the Na in Crd geothermometer (Tropper et al., 2018) and the 680 to 690°C obtained from phase equilibria modelling in the inferred source for magma production. Since the peak temperature of the metapsammitic rocks hosting the LTC pegmatites is calculated at 616 ± 14°C, estimated through the Na in Crd geothermometer, the 679 ± 36°C temperature characterizing the zircons defines undercooling conditions during LCT pegmatites intrusion between 13 and 113°C. These conditions are argued to be necessary for the expression of pegmatitic textures (e.g. London, 2018). While the LCT pegmatites crystallization temperature is compatible with that of the anatectic system, pluton-hosted pegmatites show crystallization temperatures comparable with those characterizing the injection of large calc-alkaline magma batches (e.g. Roberts&Clemens, 1993) as they formed at temperatures 100 to 150°C higher than their metapelites-hosted lithium-enriched counterparts. Type II and III zircons yield overlapping crystallization temperatures between 750 and 850°C and are mostly This temperature is reasonably similar to the Val Fredda Tonalite zircon saturation temperatures identified by Broderick et al (2015) in the Re di Castelo pluton (850-870°C).

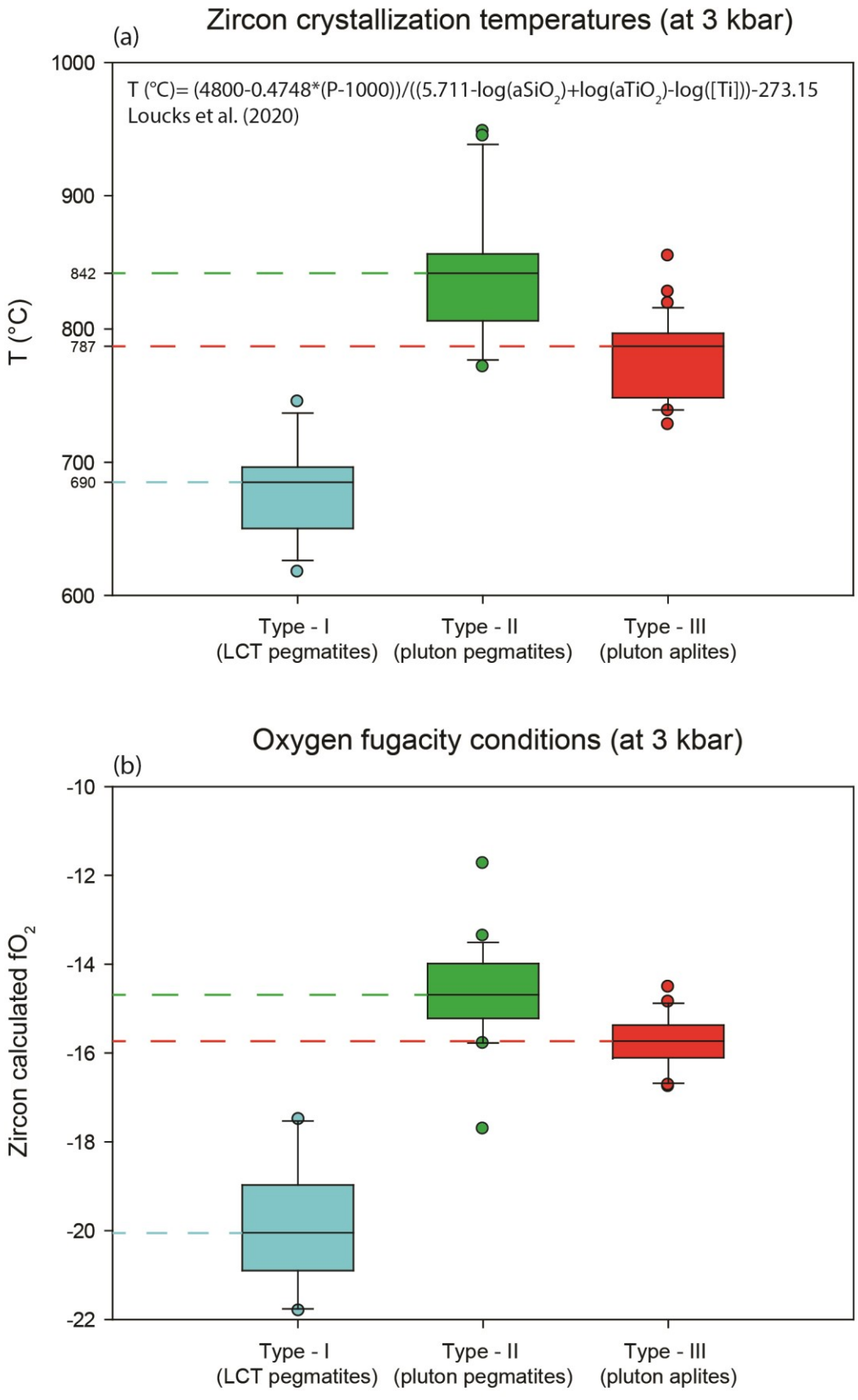

Figure 6-5 a) Crystallization temperatures of Forcel Rosso pegmatites zircons; b) oxygen fugacity conditions during zircon crystallization. Equations from Loucks et al., (2020).

Type I zircons oxygen fugacity data are distinct and much lower than their pluton-hosted counterparts, which are in turn compatible inside their standard deviation, suggesting that those two types of zircons may have formed from the same source and in a similar, more oxidised environment. Type I zircons yield fO_2 values between ca. -18 and -21 matching the values of S-type granites originating from graphite-bearing metapelites (e.g. Dos Santos Dias et al., 2019), suggesting that a graphitic component may have been locally present where this anatectic melt originated. Overall, type II and III zircons oxygen fugacity values are compatible with the values for calc-alkaline granitoid suites reported in Loucks et al. (2020) and near the FMQ buffer. Although the NNO buffer is considered extremely important during calc-alkaline differentiation by many experimental works (e.g. Ulmer et al., 2018; Marxer&Ulmer, 2019) the values we obtained are slightly more reduced, suggesting a contribution from crustal assimilation of reduced material.

6.7.4 Zircon trace elements

The three different zircon types from the Forcel Rosso pegmatites are characterized by important differences in trace elements chemistry that can help us differentiate them and pinpointing their source. We note that highly concentrated elements (e.g., U, Th) generally vary linearly with lower-concentration elements in our analyses suggesting that partitioning follows Henrian behaviour even for the most evolved compositions. Although strange and extremely enriched, the compositions of our zircons are not unique, as Fig. 6-2a and c show that almost all the analyzed zircon types are comprised in the compilation of granitic (type-S and -I) and pegmatitic zircons available in the literature. Fig. 6-2b confirms the perfect overlapping between the trace elements compositions of type III zircons with those reported by Schoene et al. (2014) in the Re di Castello Pluton, while type I and II zircons perfectly overlap the field of the syenitic pegmatites zircons reported by Belousova et al. (2002) even if they are completely different from pegmatitic zircons reported by Soman et al. (2010).

Fig. 6-2d and e diagrams are the best for discriminating between the different types of zircons of the Forcel Rosso pegmatites. The Y vs. Th diagram in Fig. 6-2d shows two distinct trends: one enriched in Y identified by type I LCT pegmatites zircons and one enriched in Th formed by type II and III zircons. Type III zircons are comparable to the zircons of Schoene et al. (2012), while type II zircons are definitely richer in Y and Th even if they remain on the same trending line. This diagram confirms the oxybarometer data and support the hypothesis that LCT pegmatites have a different origin than the pluton-hosted pegmatites and that type II and III zircons are probably the product of a continous fractionation process. Type II and III zircons Th enrichment is concordant with the observed high whole rock Th/U ratio in the I-type Adamello pluton.

Fig. 6-2e defines the three zircon groups on the basis of U and Eu* parameters, clearly differentiating the pegmatitic zircons (Type I and II), extremely enriched in U, from the pluton-linked zircons of type III. Type I and II zircons feature similarly negative Eu anomaly values suggesting that they developed from a melt that fractionated Kfs and/or Pl while Type III zircons feature a much less pronounced Eu anomaly that suggest they developed from a less fractionated magma.

Fig. 6-2f shows the positive correlation existing between Li and HREEs. Lithium enters zircon in the coupled substitution: Li^{1+}(interstitial) + (Y; REE)$^{3+}$ = Zr^{4+} + vacancy, required to balance Y and HREE (e.g. Ushikubo et al., 2008; Wang and Trail, 2022). Given the high crystallization temperature of these zircons, no Li-bearing mineral inclusion should be present and zircon Li concentration should mirror the parental melt lithium enrichment. Type I zircons are the most Li-enriched (up to ca. 70 ppm) and the most Lu (and HREE) enriched, type II zircons feature moderate lithium contents (up to ca. 15 ppm) while type III zircons are Li and HREE-poor. Scandium contents (Fig. 6-2g and h) is almost constant in all zircon types at ca. 150-500 ppm except for Type I zircons where it helps us distinguishing the otherwise cryptic cores from the rims. Sc enters zircon in the coupled substitution Sc^{3+} + P^{5+} = Zr^{4+} + Si^{4+} (e.g. Halden et al., 1993; Hoskin and Schaltegger, 2003) and the most rich analyses points are indeed the most P-rich analyses. Several trace elements, Sc included, concur in suggesting that cores and rims formed from melts with different compositions but with age differences that were impossible to resolve with LA-ICP-MS in-situ U-Pb age determinations. The “younger melt”, which formed the zircon rims, was tendentially richer in U, Hf and Ta than the “older melt” which formed the zircon cores, suggesting that the former was already more fractionated when it mixed with the latter. The “older melt” comparative enrichment in Y and HREEs is coupled to an enrichment in phosphorous, suggesting that while both cores and rims are characterized by xenotime substitution, its impact differed in magnitude. The Sc in zircon data is in agreement with our Sr-Nd whole rock isotopic data showing that the LCT pegmatites are composed of two distinct melt batches, one older and less fractionated, and one younger and extremely fractionated. High scandium contents in pegmatitic melts are not common (Williams-Jones&Vasyukova, 2018), probably because they are often originated from highly fractionated granites. Sc in metapelites is particularly compatible in garnet (e.g. Chassè et al., 2018) while in pegmatites it can be enriched in Nb-Ta minerals (Wise et al., 1998) and Ti minerals like ilmenite and rutile. The Sc enrichment observed in the older melt could be directly linked to the anatectic source for our LCT pegmatites, which are garnet-free metapelites and to the fact that this melt crystallized zircon without forming Nb and Ta minerals because it was not fractionated enough to do so3. On the other hand, the lower Sc content of the “internal melt”-linked zircon rims suggest the contemporaneous crystallization of Nb-Ta minerals, rutile and zircon shortly after injection, which is supported by the mineralogical analyses of the pegmatitic zones reported in the research paper 2.

6.8 Conclusions

Zircon data highlight the differences existing between pegmatitic zircons linked to plutonic versus anatectic origins. The chemistry of the pegmatitic melt played an extremely important role in zircon morphology and trace elements incorporation. We highlighted how several trace elements, particularly Y and Th can be used in order to differentiate evolved granitic pegmatites deriving from metasediments anatexis from those deriving from fractional crystallization of I-type granitoids. Fig. 6-6 synthetizes the features of three zircon types described in this chapter. More data is needed in order to evaluate how to recognize anatectic LCT pegmatites from pluton-derived LCT pegmatites. More studies featuring detailed comparisons between barren pluton-derived pegmatites and anatectic barren pegmatites, which in our case were not found, are needed in order to integrate our dataset in order to create a comprehensive model of how zircons can be used in order to define origin and affinity of pegmatites. More data on Hf isotopes on the studied zircons are needed in order to define if they confirm the geochemical affinity suggested by Sr and Nd whole rock isotopes.

		Zonations	Inclusions	Trace elements enrichment	U-Pb Age (corrected)	Oxygen fugacity	Temperature
Type I	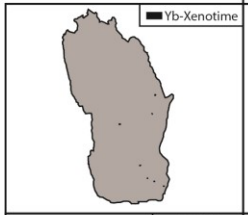	Not zoned	Yb-Xenotime	Li, Sc, Y, Yb, Lu, U	38.48 ± 0.23 Ma	-19.87 ± 1.36	697 ± 36°C
Type II	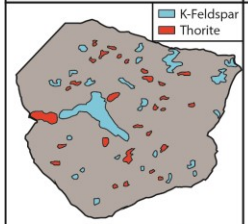	Not zoned	Thorite K-Feldspar	Yb, Lu, Th, U	37.85 ± 0.26 Ma	-14.75 ± 1.02	827 ± 29°C
Type III	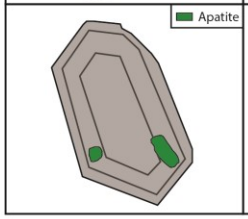	Oscillatory zoned	Apatite	Normal pattern	37.67 ± 0.29 Ma	-15.76 ± 0.70	782 ± 30°C

Figure 6-6 Cartoons sytethizig the main features of zircon Type I to III.

6.9 References

Allen, C. M., & Campbell, I. H. (2012). Identification and elimination of a matrix-induced systematic error in LA–ICP–MS 206Pb/238U dating of zircon. Chemical Geology, 332, 157-165

Belousova, E. A., Griffin, W. L., O'Reilly, S. Y., & Fisher, N. I. (2002). Apatite as an indicator mineral for mineral exploration: trace-element compositions and their relationship to host rock type. Journal of Geochemical Exploration, 76(1), 45-69.

Bindeman, I. N., Fu, B., Kita, N. T., & Valley, J. W. (2008). Origin and evolution of silicic magmatism at Yellowstone based on ion microprobe analysis of isotopically zoned zircons. Journal of Petrology, 49(1), 163-193.

Blundy, J. D. (1989). The geology of the southern Adamello Massif, Italy (Doctoral dissertation, University of Cambridge).

Bonazzi, M., Langone, A., Tumiati, S., Dellarole, E., Mazzucchelli, M., Giovanardi, T., & Zanetti, A. (2020). Mantle-Derived Corundum-Bearing Felsic Dykes May Survive Only within the Lower (Refractory/Inert) Crust: Evidence from Zircon Geochemistry and Geochronology (Ivrea–Verbano Zone, Southern Alps, Italy). Geosciences, 10(8), 281.

Bradley, D., Shea, E., Buchwaldt, R., Bowring, S., Benowitz, J., O'Sullivan, P., & McCauley, A. (2016). Geochronology and tectonic context of lithium-cesium-tantalum pegmatites in the Appalachians. The Canadian Mineralogist, 54(4), 945-969.

Breiter, K., Lamarão, C. N., Borges, R. M. K., & Dall'Agnol, R. (2014). Chemical characteristics of zircon from A-type granites and comparison to zircon of S-type granites. Lithos, 192, 208-225.

Broderick, C., Wotzlaw, J.F., Frick, D.A., Gerdes, A., Ulianov, A., Günther, D., Schaltegger, U., 2015. Linking the thermal evolution and emplacement history of an upper-crustal pluton to its lower-crustal roots using zircon geochronology and geochemistry (southern Adamello batholith, N. Italy). Contributions to Mineralogy and Petrology, 170(3), 1-17.

Burnham, A. D. (2020). Key concepts in interpreting the concentrations of the rare earth elements in zircon. Chemical Geology, 551, 119765.

Carley, T. L., Miller, C. F., Wooden, J. L., Padilla, A. J., Schmitt, A. K., Economos, R. C., ... & Jordan, B. T. (2014). Iceland is not a magmatic analog for the Hadean: Evidence from the zircon record. Earth and Planetary Science Letters, 405, 85-97.

Černý, P., Ercit, T.S. (2005). The classification of granitic pegmatites revisited. The Canadian Mineralogist, 43(6).

Chappell, B. W., Bryant, C. J., Wyborn, D., White, A. J. R., & Williams, I. S. (1998). High-and low-temperature I-type granites. Resource Geology, 48(4), 225-235.

Chassé, M., Griffin, W. L., Alard, O., O'reilly, S. Y., & Calas, G. (2018). Insights into the mantle geochemistry of scandium from a meta-analysis of garnet data. Lithos, 310, 409-421.

Claiborne, L. L., Miller, C. F., & Wooden, J. L. (2010). Trace element composition of igneous zircon: a thermal and compositional record of the accumulation and evolution of a large silicic batholith, Spirit Mountain, Nevada. Contributions to Mineralogy and Petrology, 160(4), 511-531.

Corfu, F., Hanchar, J. M., Hoskin, P. W., & Kinny, P. (2003). Atlas of zircon textures. Reviews in mineralogy and geochemistry, 53(1), 469-500.

Dos Santos Dias, J. C., Gonçalves, L., & Gonçalves, C. C. (2019). Contrasting oxygen fugacity of I- and S-type granites from the Araçuaí orogen, SE Brazil: an approach based on opaque mineral assemblages. Mineralogy and Petrology, 113(5), 667-686.

Förster, H. J. (2006). Composition and origin of intermediate solid solutions in the system thorite–xenotime–zircon–coffinite. Lithos, 88(1-4), 35-55.

Geisler, T., Schaltegger, U., & Tomaschek, F. (2007). Re-equilibration of zircon in aqueous fluids and melts. Elements, 3(1), 43-50.

Gonçalves, A. O., Melgarejo, J. C., Alfonso, P., Amores, S., Paniagua, A., Neto, A. B., ... & Camprubí, A. (2019). The distribution of rare metals in the LCT pegmatites from the Giraúl Field, Angola. Minerals, 9(10), 580.

Griffin, W. L. (2008). GLITTER: data reduction software for laser ablation ICP-MS. Laser Ablation ICP-MS in the Earth Sciences: Current practices and outstanding issues, 308-311.

Grimes, C. B., Wooden, J. L., Cheadle, M. J., & John, B. E. (2015). "Fingerprinting" tectono-magmatic provenance using trace elements in igneous zircon. Contributions to Mineralogy and Petrology, 170(5), 1-26.

Halden, N. M., & Hawthorne, F. C. (1993). The fractal geometry of oscillatory zoning in crystals: Application to zircon. *American Mineralogist*, *78*(9-10), 1113-1116.

Hoskin, P. W. (2005). Trace-element composition of hydrothermal zircon and the alteration of Hadean zircon from the Jack Hills, Australia. Geochimica et cosmochimica acta, 69(3), 637-648.

Hoskin, P. W., & Schaltegger, U. (2003). The composition of zircon and igneous and metamorphic petrogenesis. Reviews in mineralogy and geochemistry, 53(1), 27-62.

Jochum, K. P., Willbold, M., Raczek, I., Stoll, B., & Herwig, K. (2005). Chemical Characterisation of the USGS Reference Glasses GSA-1G, GSC-1G, GSD-1G, GSE-1G, BCR-2G, BHVO-2G and

BIR-1G Using EPMA, ID-TIMS, ID-ICP-MS and LA-ICP-MS. Geostandards and Geoanalytical Research, 29(3), 285-302.

Jochum, K. P., Weis, U., Stoll, B., Kuzmin, D., Yang, Q., Raczek, I., ... & Enzweiler, J. (2011). Determination of reference values for NIST SRM 610–617 glasses following ISO guidelines. Geostandards and Geoanalytical Research, 35(4), 397-429.

London, D. (2018). Ore-forming processes within granitic pegmatites. Ore Geology Reviews, 101, 349-383.

Loucks, R. R., Fiorentini, M. L., & Henríquez, G. J. (2020). New magmatic oxybarometer using trace elements in zircon. Journal of Petrology, 61(3), egaa034.

Lukács, R., Guillong, M., Bachmann, O., Fodor, L., & Harangi, S. (2021). Tephrostratigraphy and Magma Evolution Based on Combined Zircon Trace Element and U-Pb Age Data: Fingerprinting Miocene Silicic Pyroclastic Rocks in the Pannonian Basin. Frontiers in Earth Science, 9, 615768.

Marxer, F., & Ulmer, P. (2019). Crystallisation and zircon saturation of calc-alkaline tonalite from the Adamello Batholith at upper crustal conditions: an experimental study. Contributions to Mineralogy and Petrology, 174(10), 1-29.

Mattinson, J. M. (2011). Extending the Krogh legacy: development of the CA–TIMS method for zircon U–Pb geochronology. Canadian Journal of Earth Sciences, 48(2), 95-105.

Matthews, N. E., Vazquez, J. A., & Calvert, A. T. (2015). Age of the L ava C reek supereruption and magma chamber assembly at Yellowstone based on 40 A r/39 A r and U-P b dating of sanidine and zircon crystals. Geochemistry, Geophysics, Geosystems, 16(8), 2508-2528.

McCauley, A., & Bradley, D. C. (2014). The global age distribution of granitic pegmatites. The Canadian Mineralogist, 52(2), 183-190.

Neves, J. M., Nunes, J. E., & Sahama, T. G. (1974). High hafnium members of the zircon-hafnon series from the granite pegmatites of Zambézia, Mozambique. Contributions to Mineralogy and Petrology, 48(1), 73-80.

Reimink, J. R., Davies, J. H., Bauer, A. M., & Chacko, T. (2020). A comparison between zircons from the Acasta Gneiss Complex and the Jack Hills region. Earth and Planetary Science Letters, 531, 115975.

Roberts, M. P., & Clemens, J. D. (1993). Origin of high-potassium, calc-alkaline, I-type granitoids. Geology, 21(9), 825-828.

Schaltegger, U., Brack, P., Ovtcharova, M., Peytcheva, I., Schoene, B., Stracke, A., ... & Bargossi, G. M. (2009). Zircon and titanite recording 1.5 million years of magma accretion, crystallization and initial cooling in a composite pluton (southern Adamello batholith, northern Italy). Earth and Planetary Science Letters, 286(1-2), 208-218.

Schaltegger, U., Ulianov, A., Müntener, O., Ovtcharova, M., Peytcheva, I., Vonlanthen, P., ... & Girlanda, F. (2015). Megacrystic zircon with planar fractures in miaskite-type nepheline pegmatites formed at high pressures in the lower crust (Ivrea Zone, southern Alps, Switzerland). American Mineralogist, 100(1), 83-94.

Schaltegger U., Nowak A., Ulianov A., Fisher C.M., Gerdes A., Spikings R., Whitehouse M.J., Bindeman I., Hanchar J.M., Duff J., Vervoort J.D., Sheldrake T., Caricchi L., Brack P.and Müntener O. (2019). Zircon Petrochronology and 40Ar/39Ar Thermochronology of the Adamello Intrusive Suite, N. Italy: Monitoring the Growth and Decay of an Incrementally Assembled Magmatic System. Journal of Petrology 60, vol. 4, 701-722.

Schiller, D., & Finger, F. (2019). Application of Ti-in-zircon thermometry to granite studies: problems and possible solutions. Contributions to Mineralogy and Petrology, 174(6), 1-16.

Schoene, B., Schaltegger, U., Brack, P., Latkoczy, C., Stracke, A., & Günther, D. (2012). Rates of magma differentiation and emplacement in a ballooning pluton recorded by U–Pb TIMS-TEA, Adamello batholith, Italy. Earth and Planetary Science Letters, 355, 162-173.

Shen, P., Hattori, K., Pan, H., Jackson, S., & Seitmuratova, E. (2015). Oxidation condition and metal fertility of granitic magmas: Zircon trace-element data from porphyry Cu deposits in the Central Asian orogenic belt. Economic Geology, 110(7), 1861-1878.

Sláma, J., Košler, J., Condon, D. J., Crowley, J. L., Gerdes, A., Hanchar, J. M., Whitehouse, M. J. (2008). Plešovice zircon—a new natural reference material for U–Pb and Hf isotopic microanalysis. Chemical Geology, 249(1-2), 1-35.

Sliwinski, J. T., Guillong, M., Liebske, C., Dunkl, I., Von Quadt, A., & Bachmann, O. (2017). Improved accuracy of LA-ICP-MS U-Pb ages of Cenozoic zircons by alpha dose correction. Chemical Geology, 472, 8-21.

Soman, A., Geisler, T., Tomaschek, F., Grange, M., & Berndt, J. (2010). Alteration of crystalline zircon solid solutions: a case study on zircon from an alkaline pegmatite from Zomba–Malosa, Malawi. Contributions to Mineralogy and Petrology, 160(6), 909-930.

Tilton, G. R., Davis, G. L., Wetherill, G. W., & Aldrich, L. T. (1957). Isotopic ages of zircon from granites and pegmatites. Eos, Transactions American Geophysical Union, 38(3), 360-371.

Troch, J., Ellis, B. S., Schmitt, A. K., Bouvier, A. S., & Bachmann, O. (2018). The dark side of zircon: textural, age, oxygen isotopic and trace element evidence of fluid saturation in the subvolcanic reservoir of the Island Park-Mount Jackson Rhyolite, Yellowstone (USA). Contributions to Mineralogy and Petrology, 173(7), 1-17.

Tropper, P., Wyhlidal, S., Haefeker, U. A., & Mirwald, P. W. (2018). An experimental investigation of Na incorporation in cordierite in low P/high T metapelites. Mineralogy and Petrology, 112(2), 199-217.

Uher, P., & Černý, P. (1998). Zircon in Hercynian granitic pegmatites of the Western Carpathians, Slovakia. Geologica Carpathica, 49, 261-270.

Ulmer, P., Callegari, E., & Sonderegger, U. C. (1983). Genesis of the mafic and ultramafic rocks and their genetical relations to the tonalitic-trondhjemitic granitoids of the southern part of the Adamello batholith (Northern Italy). Memorie della Società Geologica Italiana, 26(1), 171-222.

Ulmer, P., Kaegi, R., & Müntener, O. (2018). Experimentally derived intermediate to silica-rich arc magmas by fractional and equilibrium crystallization at 1· 0 GPa: an evaluation of phase relationships, compositions, liquid lines of descent and oxygen fugacity. Journal of Petrology, 59(1), 11-58.

Ushikubo, T., Kita, N. T., Cavosie, A. J., Wilde, S. A., Rudnick, R. L., & Valley, J. W. (2008). Lithium in Jack Hills zircons: Evidence for extensive weathering of Earth's earliest crust. Earth and Planetary Science Letters, 272(3-4), 666-676.

Vermeesch, P. (2018). IsoplotR: A free and open toolbox for geochronology. Geoscience Frontiers, 9(5), 1479-1493.

Villaros, A., Stevens, G., Moyen, J. F., & Buick, I. S. (2009). The trace element compositions of S-type granites: evidence for disequilibrium melting and accessory phase entrainment in the source. Contributions to Mineralogy and Petrology, 158(4), 543-561.

Wang, T., Tong, Y., Jahn, B. M., Zou, T. R., Wang, Y. B., Hong, D. W., & Han, B. F. (2007). SHRIMP U–Pb Zircon geochronology of the Altai No. 3 Pegmatite, NW China, and its implications for the origin and tectonic setting of the pegmatite. Ore geology reviews, 32(1-2), 325-336.

Wang, Y., & Trail, D. (2022). Experimental partitioning of Li between zircon and different silicate melts: implications for Li contents in the Hadean and modern crust. Contributions to Mineralogy and Petrology, 177(1), 1-14.

Williams-Jones, A. E., & Vasyukova, O. V. (2018). The economic geology of scandium, the runt of the rare earth element litter. Economic Geology, 113(4), 973-988.

Wiedenbeck, M. A. P. C., Alle, P., Corfu, F. Y., Griffin, W. L., Meier, M., Oberli, F. V., ... & Spiegel, W. (1995). Three natural zircon standards for U-Th-Pb, Lu-Hf, trace element and REE analyses. Geostandards newsletter, 19(1), 1-23.

Wiedenbeck, M., Hanchar, J. M., Peck, W. H., Sylvester, P., Valley, J., Whitehouse, M., Zheng, Y. F. (2004). Further characterisation of the 91500 zircon crystal. Geostandards and Geoanalytical Research, 28(1), 9-39.

Wise, M. A., Černý, P., & Falster, A. U. (1998). Scandium substitution in columbite-group minerals and ixiolite. The Canadian Mineralogist, 36(2), 673-680.

Chapter 7

The evolution of an anatectic system through the eye of tourmaline.

7.1 Introduction

Tourmaline is the main boron (B) host mineral in many magmatic and metamorphic rocks. It is characterized by a complex crystalline structure, with a general formula of $XY_3Z_6T_6O_{18}(BO_3)_3V_3W$ featuring three different atomic sites that can host a great variety of elements of widely different charge and ionic radius (e.g. Bosi, 2018). In the last two decades, an increasing number of works demonstrated the ability of tourmaline to remain stable in high pressure and high temperature environments, extending from surface conditions below 150 °C (e.g. Dietrich 1985; Dutrow&Henry,. 2011) to high-grade metamorphic and magmatic conditions of .850 °C at pressures between 0.1 and 0.5 GPa (e.g. Robbins & Yoder 1962; Manning & Pichavant 1983) up to ca. 150 km depth (e.g. Marschall et al., 2009). These features, coupled with the low B diffusivities in its structure (Marschall et al., 2008) make tourmaline an ideal petrogenetic indicator for several prograde and retrograde metamorphic processes, as mica destabilization, s and magmatic differentiation processes, such as pegmatites and leucogranites crystallization. Stable isotope studies of Tur major elements O, B, Si and H (e.g. Jiang&Palmer, 1998; Dyar et al. 1999) have been successfully applied to decipher the fluid history of fluid–melt–rock systems. Among them, boron is particularly interesting for its fluid mobility, speciation variability at low temperature, relatively low mass and large mass difference between its isotopes (~10%), which contribute in making this element a sensitive tracer of a variety of geochemical processes (e.g., Palmer & Swihart 1996, 2008). Boron has an atomic mass of 10.81 and has two stable isotopes: ^{10}B (~20%) and ^{11}B (~80%). Boron isotopic variation is reported using delta notation: $\delta^{11}B(‰) = [(^{11}B/^{10}B_{sample})/ (^{11}B/^{10}B_{STD})-1]*1000$ where $^{11}B/^{10}B$standard is the boron isotopic composition of National Institute of Standards and Technology (NIST) Standard Reference Material SRM 951 boric acid (Catanzaro et al. 1970). In many natural systems boron is bound to oxygen in either a tetrahedral complex, such as $B(OH)_4$ (borate ion), or a trigonal complex, such as $B(OH)_3$ (boric acid). Natural fractionation between the two isotopes is governed principally by their distribution between these complexes, with the ^{11}B incorporated preferentially in the more strongly bonded trigonal molecules. The large B isotopic fractionation at low temperatures has led to the use of the tourmaline B stable isotope system in fluids circulation tracking and to constrain the fluid influx in

metamorphic terranes (e.g. Slack et al., 1989) as tourmaline may retain information of multiple prograde stages of evolution of the host rocks metamorphic history.

7.2 Methods

The mineralogy, microstructures and textural relationships of tourmaline and muscovite from pelitic and pegmatitic samples were characterized on 40 thin sections observed by optical microscopy, of which 16 were analyzed by electron microprobe. Electronic microprobe analyses were conducted at the "Ardito Desio" Earth Sciences Department of the University of Milan (Italy) on a JEOL JXA-8200 using wavelength-dispersive spectrometry. Operating conditions were 15 kV accelerating voltage and beam current of 5 nA, with a beam diameter of 1 µm. The trace element composition of muscovite, previously analyzed by EMPA were obtained at the the Geochemistry, Geochronology and Isotope Geology laboratory of the Department of Earth Sciences, Università degli Studi di Milano (Italy). using an iCAP ICP-MS quadrupole coupled with a 193 nm Ar-F excimer laser. Operating conditions were: spot size of 40 µm spot size, 10 Hz and 2 J/cm^2 fluence. The runs were standardized using the international glass standard NIST612 (Pearce et al., 1997) analyzed using a 40 µm spot size at 10 Hz and 4 J/cm^2; SiO2 was used as internal standard. Data reductions were performed using the Glitter package (Griffin et al., 2008). In-situ boron isotopes determination on tourmaline was carried out as described in chapter 3.3 of the methods section of this PhD thesis with accuracy results shown in Fig. 7-1.

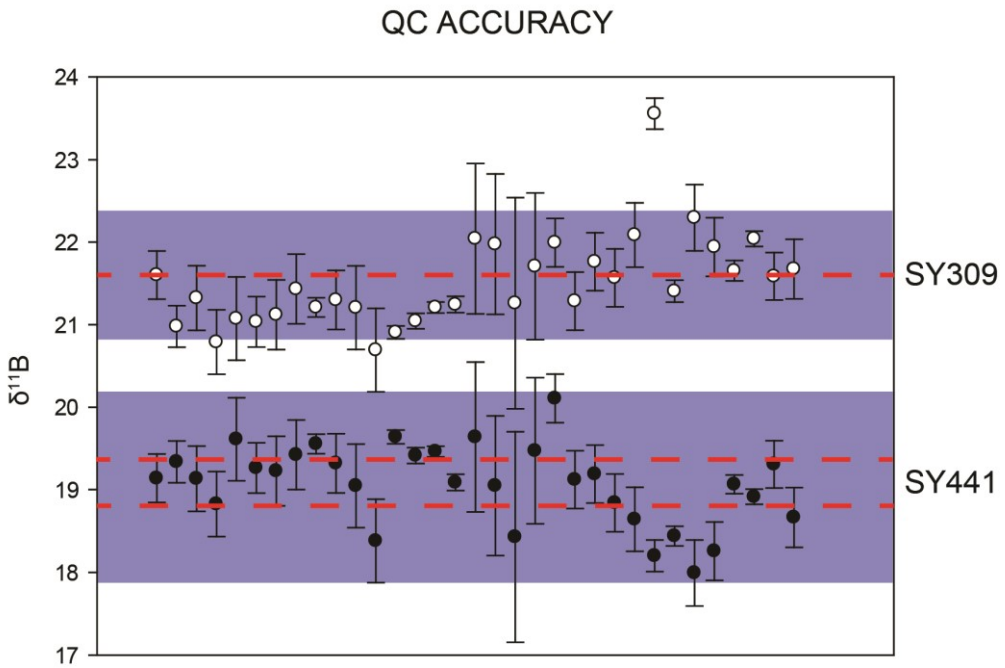

Figure 7-1 Syros tourmalines SY309 and SY441 quality control analitycal results

7.3 Tourmaline petrography

Tourmaline is ubiquitous in the Verrucano Lombardo pelites and metapelites of the Forcel Rosso area, inside the Adamello pluton thermal aureole, and also characterizes all the connected in-situ leucosomes and anatectic barren to lithium enriched pegmatites. Petrographic analysis on tourmaline was performed using optical microscopy on the complete range of rocks described in the previous chapters of the PhD thesis from pelites which experienced only diagenetic processes to high amphibolitic facies, their connected leucosomes and on anatectic, tourmaline-bearing pegmatites (Fig. 7-2). The complete mineral assemblages for all rock types here described can be found in chapter 4.

7.3.1 Unmetamorphosed samples

Unmetamorphosed Verrucano Lombardo pelites that did not experience the Adamello pluton contact metamorphic imprint are rich in clay minerals, dominated by illite, that form up to 30 to 35 vol.% of modal amount of the mineral assemblage (Magnani et al., 2022). These rocks (samples V1, V3, V4, V4-2) are characterized by rare anhedral, rounded tourmaline crystals of various colours under transmitted light, ranging from light brown to light green to yellowish (referred hereafter as Type 0 tourmaline), almost always overgrown by anhedral and uneven dark green tourmaline (referred hereafter as Type I tourmaline, Fig. 7-2.1). The modal abundance of types 0 and I tourmalines are about 0.01 vol.%.

7.3.2 Greenschist facies samples

Greenschist facies onset can be recognized in the Verrucano Lombardo pelites through the gradual disappearance of clay minerals in favor of micrometric intergranular muscovite and biotite crystals and aggregates. Quartz (Qz) and K-feldspar (Kfs) grain boundaries become more distinct and their relationships with phyllosilicates become clearer. Also in these samples, the two groups of tourmaline crystals previously identified in the unmetamorphosed rock-suite can be recognized: Type 0 + Type I zoned crystals, where the Type I overgrowth is usually thicker and better expressed than in unmetamorphosed pelites (Fig. 7-2a), and homogeneous, neogenic, light to dark green subhedral to euhedral tourmaline crystals of micrometric size (referred hereafter as Type II tourmaline; Fig. 7-2.1).

7.3.3 Amphibolite facies samples

Magnani et al. (2022) distinguished two types of metapelites that underwent amphibolite facies metamorphism and low to medium degrees of partial melting: cordierite (Crd)-absent metatexites

underwent partial melting in a fluid rich environment while Crd-bearing metapelites underwent partial melting reactions with much lower fluids influx. In both rock types, tourmaline crystals are characterized by euhedral crystalline habits and homogeneous appearance. No zoned crystals have been observed in the investigated metatexites samples. Crd-bearing metapelites tourmaline are small (tens of µm) and range from dark green to almost black colour under transmitted light and will be referred to as Type III tourmaline (Fig. 7-2.1). Crd-absent metatexites tourmaline crystals are millimetric in size and much lighter under transmitted light, between light brown and dark green and will be referred to as Type IV tourmaline (Fig. 7-2.1).

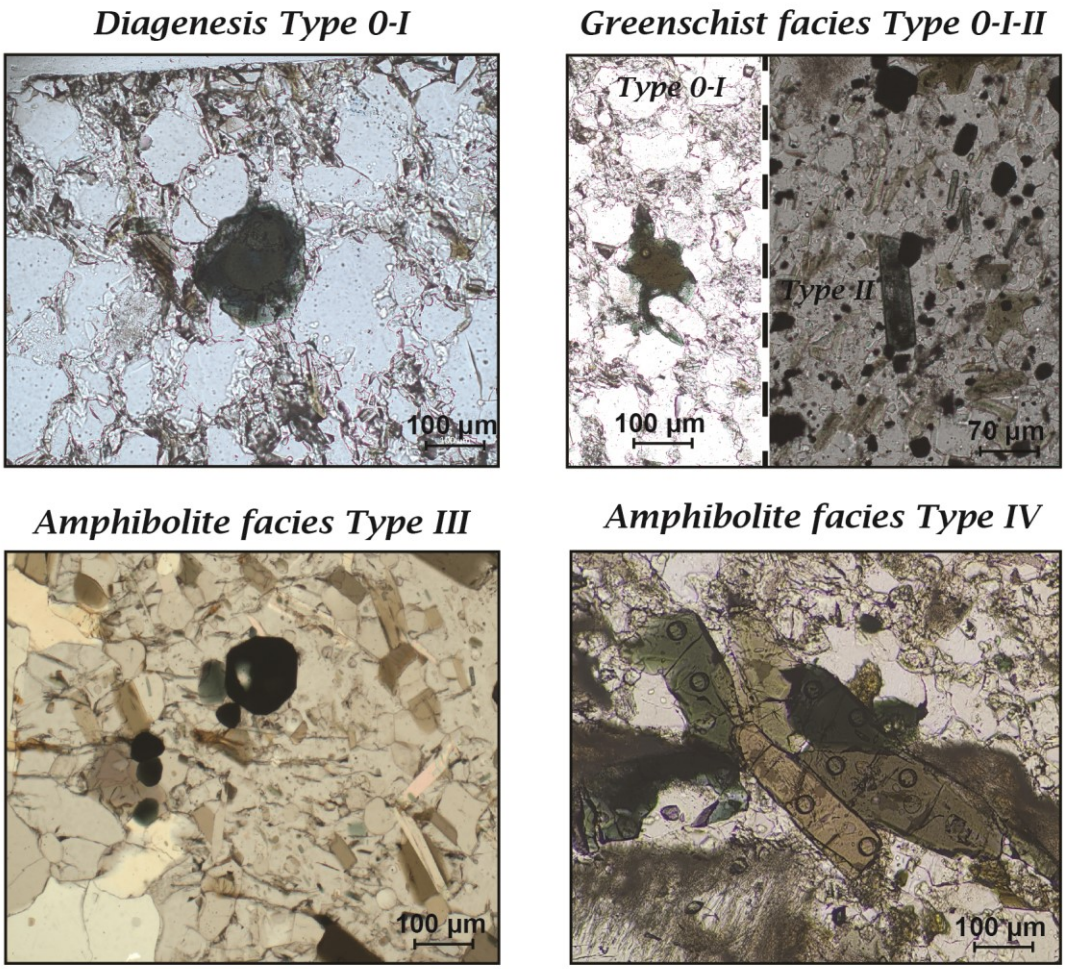

Figure 7-2.1 Tourmaline from Type 0 to IV with mean compositions of the tourmaline categories

7.3.4 Tourmaline-bearing leucosomes

In-situ leucosomes directly connected to Crd-bearing metatexites contain black tourmaline as their main mafic mineral phase, forming up ca. 5-10 vol.% of their modal mineralogy. These tourmalines are millimetric in size and euhedral, with small zonations in the otherwise homogenous crystals. Tourmaline from these structures will be referred to as Type V tourmaline (Fig. 7-2.2).

7.3.5 Anatectic barren pegmatites

Two types of barren pegmatites are recognized in the area between the partially melted metapelites and the LCT pegmatites: a Kfs+Qz+Pl+Ms+Tur common type, forming up the small interconnected pegmatitic network connecting source rocks and anatectic LCT pegmatites, and a rare Qz+Kfs+Ms+Tur+And type found only near the main LCT pegmatitic dykes featuring euhedral andalusite crystals. Tourmaline from these structures is anhedral to euhedral and always strongly zoned with light green cores and darker green rims. Tourmalines cut perpendicular to the *C*-axis often show different crystalline habits between core and rim. Tourmaline in andalusite-bearing pegmatites always occur as inclusions hosted in And crystals, showing that it is one of the first mineral phase to crystallize in the magmatic assemblage. No significant differences can be observed between tourmaline from the two types of pegmatites, therefore they will be referred to as Type VI tourmaline (Fig. 7-2.2).

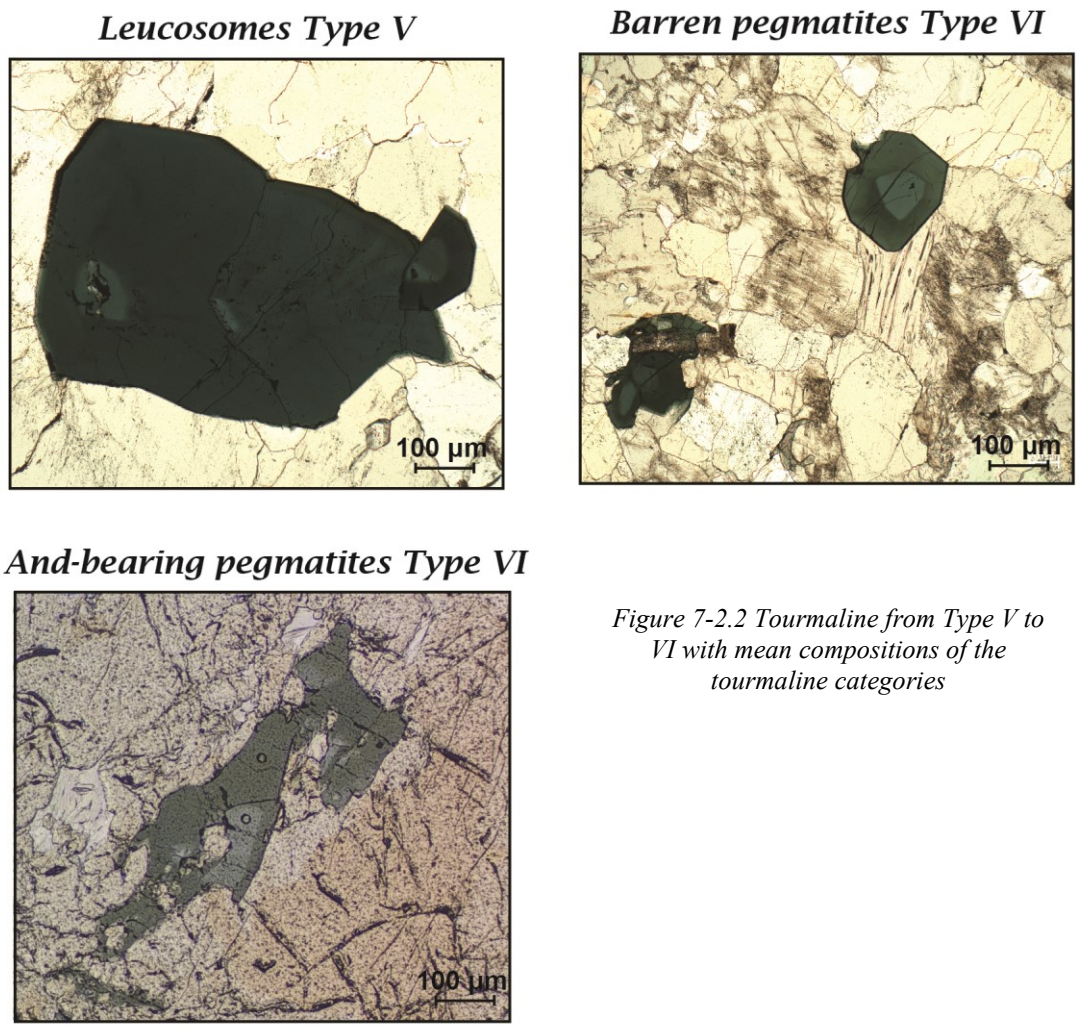

Figure 7-2.2 Tourmaline from Type V to VI with mean compositions of the tourmaline categories

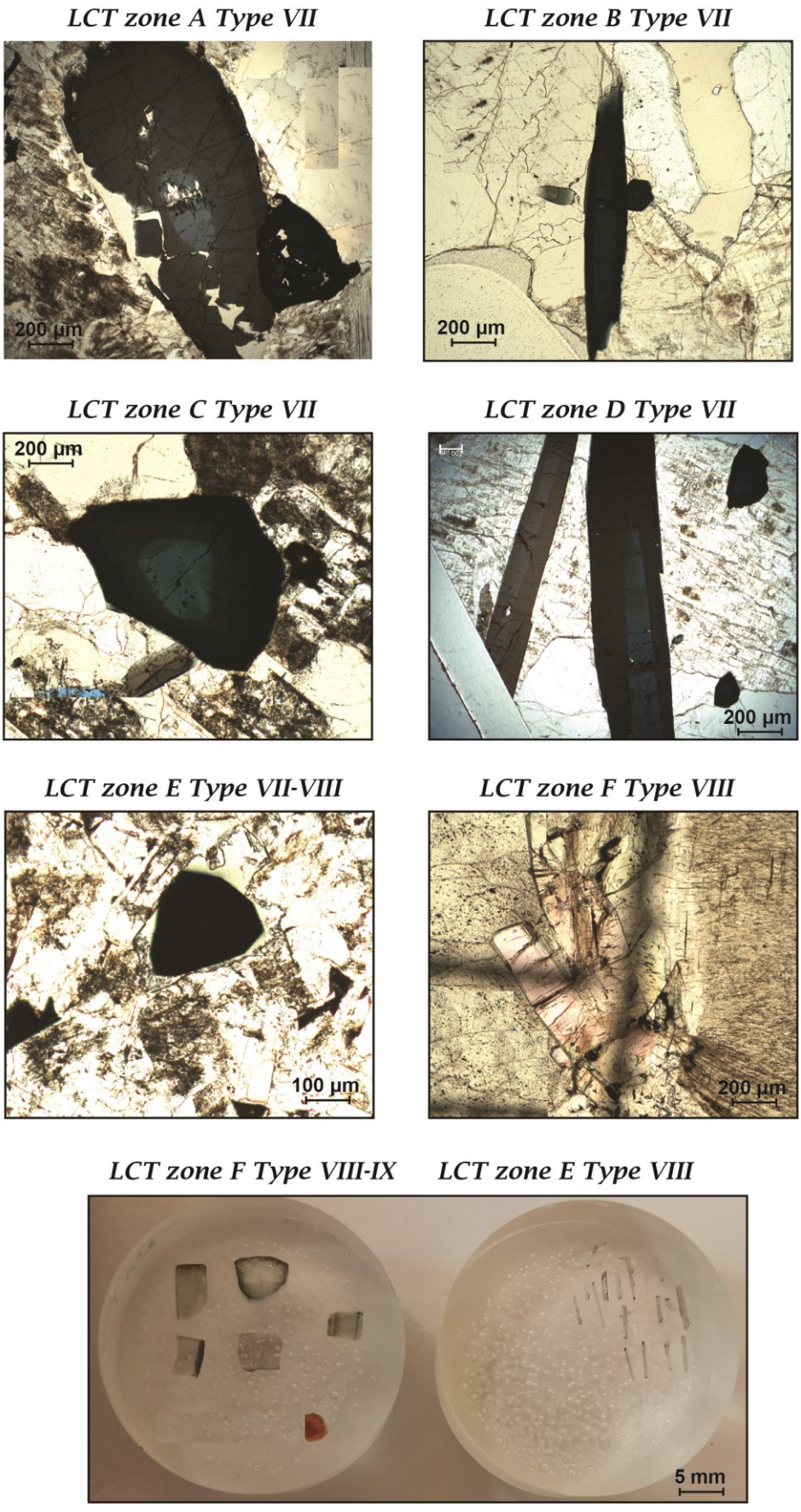

Figure 7-2.3 Tourmaline from Type VII to IX with mean compositions of the tourmaline categories

7.3.6 Anatectic LCT pegmatites

These pegmatites represent the most evolved anatectic melts produced in the Forcel Rosso area, they are produced through low grade partial melting and subsequent Kfs fractionation of fluid fluxed metapelites-derived magma (Magnani et al., 2022; chapter 4 and 5 of this thesis). Zonation in these samples is defined by different textures and mineral paragenesis where tourmaline is always a rock-forming mineral. Type VII (Fig. 7-2.3) tourmaline is found throughout zone from A to E, from the grapich granite external zone to the internal aplite zone and in the palisade zone. It is characterized by light green to brownish cores and dark green to black rims that, towards zone E, form up almost all the crystals. Type VIII (Fig. 7-2.3) tourmaline is found as rims around black tourmaline in the internal aplite (zone E), in the lithium enriched internal pegmatitic zone (F) and in the pockets of zone E-F as euhedral crystals. It is characterized by homogeneous transparent to light green and pink tourmaline crystals. Finally, Type IX tourmaline (Fig. 7-2.3) is found only in extremely thin black caps on top of green pocket tourmalines in zone F.

7.4 Results

7.4.1 Tourmaline chemistry

Tourmaline major elements mineral chemistry was investigated for all described tourmalines types (0 to IX). The complete set of analyses, more than 600 EMPA data, are reported in Table D1 in appendix D. Figure 7-3 shows tourmaline chemical compositions and tourmaline mineral species attribution on the basis of X and Y-sites occupancy (Henry et al., 2011) subdivided into sedimentary/metamorphic rocks and magmatic rocks. In Fig. 7-2 are reported the mean values for each tourmaline types described above. The majority of the analyses lies within the alkali tourmalines group on the X-site diagrams (Fig. 7-3), with rare vacancy dominated tourmalines, mainly among the magmatic rocks-hosted tourmalines, and one single calcic tourmaline analysis in the metapelites. The X-site ternary diagram for sedimentary/metamorphic rocks highlights a Ca-enrichment trend starting from diagenesis/greenschist facies (Type 0 to Type II tourmaline) towards amphibolite facies (Type III and IV tourmaline). On the other hand, the magmatic rocks X-site ternary diagram highlights a weak alkali enrichment trend during the differentiation of the system, that is particularly well expressed in the late stages and most evolved zones of the LCT pegmatitic dykes (Type VIII and IX). All the analyses lying outside of the alkali fields are near the arbitrary fields subdivisions and would require single crystal XRD crystal refinement in order to be rigorously classified, which is beyond the scope of this work. Vacancy dominated tourmalines are mainly Mg-Foititic, both in the metamorphic and magmatic rocks and only two analyses can be classified as foititic. The single calcic tourmaline (Type III) analysis can

be classified as uvitic and is found in metapelitic rocks at the limit with the basal metacarbonates of the Servino formation. Alkali tourmalines are the most abundant and therefore can better describe the

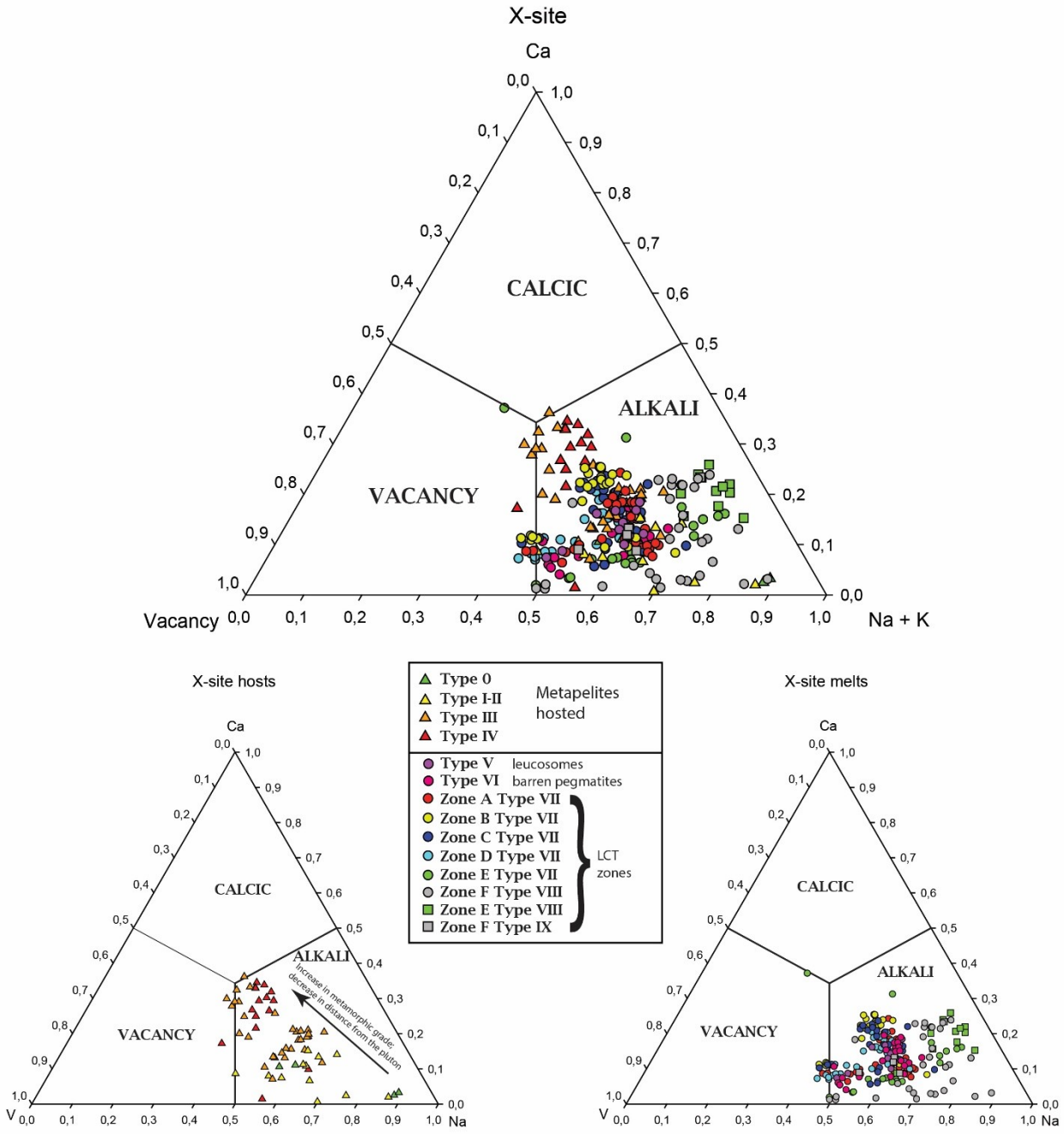

Figure 7-3 X-site classification for the Forcel Rosso tourmalines (Henry et al., 2011)

evolution of the studied systems (Fig. 7-4). Alkali group tourmalines of sedimentary/metamorphic rocks (Types 0 to IV) largely fall into the dravitic field and only three tourmalines of schorlitic composition are recongnized, two of which are detrital grains of sedimentary origin (Type 0). The diagrams of Fig. 7-4 featuring metapelites-hosted tourmaline analyses do not express any clear trend concerning the chemical evolution of tourmaline during prograde metamorphism, aside from the Ca

enrichment, suggesting that tourmaline chemical composition was internally buffered for the entirety of the Verrucano Lombardo metapelites prograde metamorphic history. On the other hand, the

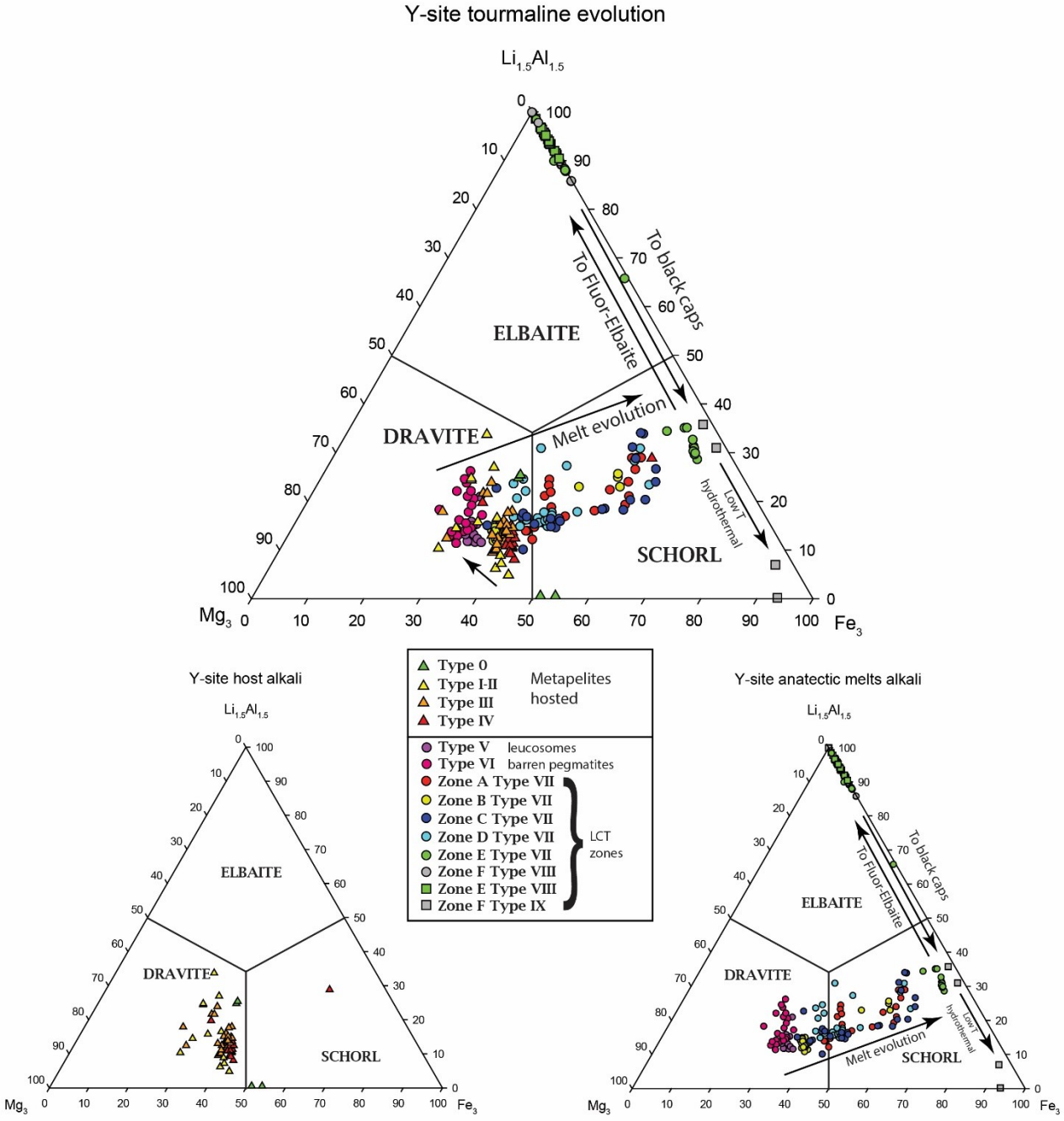

Figure 7-4 Y-site classification for the Forcel Rosso tourmalines (Henry et al., 2011)

alkali group tourmalines of the anatectic magmatic system featured in Fig. 7-4 are the most interesting as they define a clear chemical trend that is continuous from metapelitic rocks (Type I to IV) through in-situ leucosomes (Type V), barren pegmatites (Type VI) and the most external zones of the LCT pegmatites (Type VII) towards the pockets of the most evolved pegmatites (Type VIII). Tourmalines from in-situ leucosomes and barren pegmatites (Types V and VI) exhibit the most dravitic

compositions among anatectic melts, with a dravitic component higher than the metamorphic tourmalines of their source rocks. These two groups of tourmalines form almost overlapping, well definite groups unmixed with Type VII tourmalines compositions. From this Mg-rich primitive composition, tourmaline Y-site occupancy evolves throughout zones A to E of the LCT pegmatites: in zones from A to D, dravitic cores of composition similar to Type V tourmalines are overgrown by schorlitic rims while, in zone E, tourmalines are homogeneously schorlitic in composition. The subsequent dramatic evolution of the system is recorded by the disappearance of Mg and Fe-dominated tourmalines and the appearance of Li-dominated fluor-elbaite (Type VIII) that is present in zone E as overgrowths on schorlitic tourmaline, and in zone F where it is the dominant tourmaline species. The Type XI black caps that overgrow the terminations of zone F pocket tourmalines show again schorlitic composition. The MnO *vs.* Mg# diagram in Fig. 7-5 highlights a marked increase in tourmaline Mn content alongside the magmatic differentiation inside the LCT pegmatites, marking the most evolved tourmalines as also the most Mn-rich. The black caps (Type IX) at the top of Type VIII tourmaline crystals are, conversely, Mn poor.

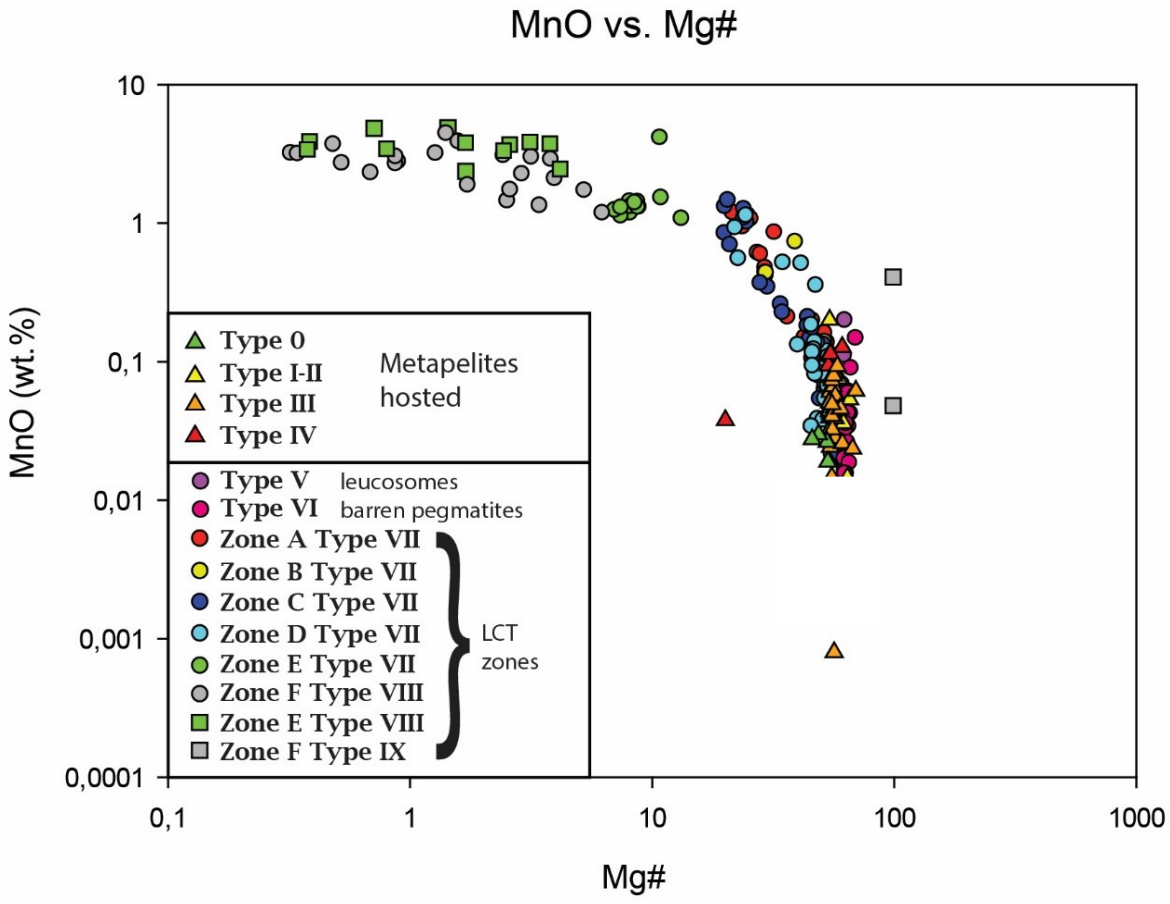

Figure 7-5 MnO vs. Mg# diagram for the Forcel Rosso tourmalines showing the enrichment with pegmatitic differentiation

7.4.2 Trace elements

7.4.2.1 Whole rock

Whole rock B determination (table D2), together with in-situ trace elements on muscovite (Table D3), were carried out in order to define the various minerals contributions to the B budget during the metamorphic prograde history of the Verrucano Lombardo pelites. Mineral modal abundances on thin sections were estimated through visual observation and validated using image analyses techniques with ImageJ on both photomicrographs and SEM images. Boron concentration for tourmaline was assumed to be equal to the stochiometric value of 3.08 wt% as B_2O_3. Clay minerals, because of their extremely small sizes were not possible to directly analyze through LA-ICP-MS, so the whole rock value of unmetamorphosed pelites was investigated both using the PPP technique and in neutronic activation, yielding B contents between 125 and 205 ppm. Greenschist to lower amphibolitic facies metapelites show whole rock B contents ranging from 122 to 184 ppm. Metapelites from upper amphibolite facies that underwent low degrees of partial melting show much lower whole rock B concentrations ranging from 50 to 90 ppm. Data available in Table D2.

7.4.2.2 Muscovite trace elements

Muscovite is relatively B-poor, with contents ranging from 31 to 50 ppm. Data available in Table D3. Biotite and cordierite are extremely B-poor with B contents in the order of 1-5 ppm (Chapter 5).

7.4.3 Tourmaline $\delta^{11}B$ in-situ isotopic data

Boron isotopes data ($\delta^{11}B$) were measured on all tourmaline Types from 0 to XI (Fig.7-6) and are reported in table X. Type 0 detrital tourmaline cores show a wide range of $\delta^{11}B$ compositions from -13.62±0.82 to -8.19±0.71‰, measured on detrital cores in unmetamorphosed and greenschist facies rocks. Type I detrital tourmaline rims yield $\delta^{11}B$ values ranging between 0.56±1.02 and 6.91±0.71‰. Type II greenschist facies tourmalines are characterized by negative $\delta^{11}B$ values ranging from -6.00±0.84‰ to -3.09±0.85‰‰, completely different from Type I rims. Type III tourmalines of the Crd-bearing metatexites, hosting the in-situ leucosomes, yield closely cropped $\delta^{11}B$ values between +0.41±0.99‰ and +1.43±0.99‰. Type IV tourmalines hosted in Crd-absent metatexites yield slightly negative $\delta^{11}B$ values between -3.53±0.57‰ and -2.35±0.76‰. Type V tourmalines, from in in-situ leucosomes, representing a primary melt and connected to fluid assisted partial melting, are characterized by $\delta^{11}B$ values between ca. -2.56±0.19‰ and -1.15±0.21‰. Type VI tourmalines hosted in barren pegmatites are characterized by $\delta^{11}B$ values of -0.68±0.23‰ (2SD). Type VII tourmalines are characterized by variable $\delta^{11}B$ values, with means of -1.6 ± 0.4‰ in LCT pegmatites zone A, -2.58 ± 0.58‰ (2SD) in zone B, -0.35 ± 0.81‰ (2SD) in zone C, -0.34 ± 0.44‰ (2SD) in zone D and -0.94

± 0.32‰ (2SD), in zone E. Type VIII elbaitic tourmalines show $\delta^{11}B$ values ranging from ca. -2.14±0.71‰ to -0.75±0.57‰. Finally, Type IX black cap tourmalines yield mean $\delta^{11}B$ value of 0.04±0.15‰ (2SD). All data is reported in Table D4.

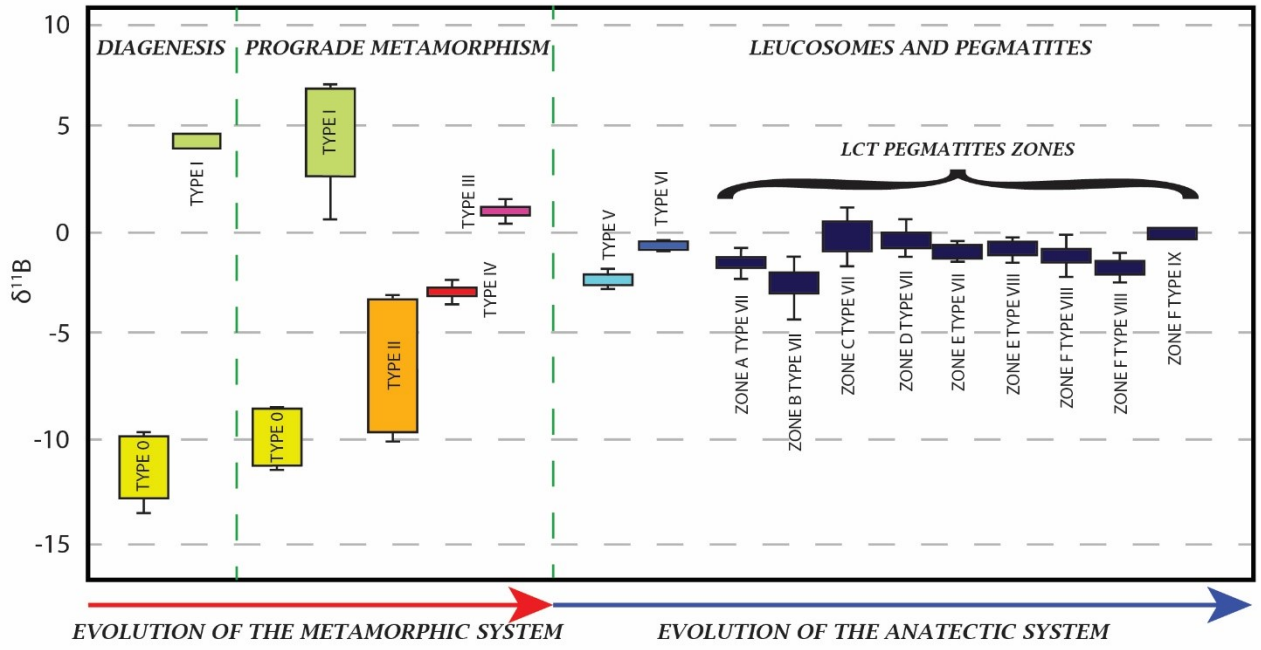

Figure 7-6 Evolution of the boron isotopic signature of tourmaline during prograde metamorphism and LCT pegmatites crystallization. The data show a systematic tendence to homogeneization at high temperature.

7.5 Discussion

7.5.1 Boron budget in pelites and metapelites

In the Forcel Rosso area we have the possibility to study the B budget of the thermometamorphic system spanning from unmetamorphosed pelites up to metapelitic metatexites. This allows us to measure B contents at several prograde metamorphic increments and to be able to identify its allocation in the various main boron-bearing minerals composing the rock. The excellent similarity between unmetamorphosed and greenschist facies pelitic rocks B concentrations show that the low-grade metamorphism did not create the conditions for the metamorphic system to open, thus maintaining the original B contents. This overlap in B content suggests that no influx of B-rich fluids was registered during the onset of the metamorphic history. The decrease in whole rock B contents from low-grade metapelites to migmatites is interpreted as related to melt production and partial tourmaline destabilization in an open system. This is consistent with the geochemical behavior of B, which is highly mobile in fluids and tends to be strongly partitioned into the fluid phase and in the melt. This result in depleting the connected restitic parts of the metatexites during processes of magma extraction.

Boron partitioning into the main mineral phases was calculated based on: i) the standard structural B content of tourmaline, 30800 ppm; ii) LA-ICP-MS-measured muscovite B contents in leucosomes and pegmatites which yielded concentrations in the range from 31 to 50 ppm; iii) LA-ICP-MS-measured biotite B contents in greenschist facies and upper amphibolite facies metatexites which yielded concentrations in the range from 1 to 5 ppm, ca. ten times less than muscovite; iv) the assumption that in the unmetamorphosed pelites the B hosted in muscovite and biotite is negligible as just respectively 5 to 10 crystals of detrital muscovite and 1-2 crystals of biotite are found in every analized thin section.

In unmetamorphosed pelites, tourmaline modal content is as low as 0.1 vol.%, estimated on 10 thin sections of different rock samples, suggesting that the total amount of detrital tourmaline-hosted boron in these rocks is around 30 ppm. Subtracting the tourmaline-hosted boron and assuming that muscovite and biotite B contents are negligible, we calculate that ca. 90 to 170 ppm of B may be hosted in clay minerals aggregates, mainly composed of illite (Riklin, 1983). This is unfortunately the only possible type of analysis of the B content of these minerals given the nanometric scale of the single crystals and the extremely thin films they form over and between Kfs and Qz crystals.

In greenschist facies metapelites, tourmaline modal amount increases significatively to around 0.2-0.3 vol.% as tourmalines show growth rims around detrital cores and new tourmalines are formed. Following the same approach used in the unmetmaorphosed pelites case, the maximum boron contribution from tourmaline can here be calculated as ca. 90 ppm. Clay minerals are not present anymore in these lithotypes as submicrometric to micrometric muscovite and biotite crystals replaced the original aggregates. Also in this case, the extremely small size of the crystals makes it impossible to analyze them with LA-ICP-MS, therefore the best approximation of the microcrystalline Ms and Bt B content ranges from ca. 30 to ca. 90 ppm, assuming the muscovite B concentration data obtained from muscovites from other samples.

In upper amphibolitic facies metatexites, tourmaline does not increase in modal abundance, remaining around 0.2-0.3 vol.%, even if it is completely recrystallized. The contribution of the bulk B hosted in tourmaline is estimated to be around 60-90 ppm, based on previous calculation. According to petrographic observation, muscovite is no longer stable as it was involved in dehydration reactions forming sillimanite and K-feldspar, as observed in Magnani et al. (2022). From the differences in whole rock B contents existing between the same strata of unmetamorphosed and migmatitic pelites, we calculate that nearly 50% of the initial B leaves the system hosted in fluid or melt phases during these reactions, causing the high-grade metapelites to be depleted in B compared to their low-grade counterparts. In this case, tourmaline-hosted B is enough to explain the whole rock B content, thus

suggesting that biotite is not a major important B host in the system, in agreement with our LA-ICP-MS investigation.

Summarizing, we quantified the different minerals contribution on B budget in the metamorphic system: (i) in the unmetamorphosed pelites, tourmaline represents 15-20% of the total B budget while clay minerals amount to 80-85% of the total B content; (ii) in low-grade metapelites tourmalines represents 35-50% of the total B budget while muscovite and biotite amount to 50-65%; (iii) finally, at higher metamorphic grades, tourmaline is the only stable B-bearing phase hosting all the B budget.

7.5.2 Tourmaline chemical evolution

Tourmaline chemical evolution defines several trends helping to reconstruct the metamorphic and anatectic history of the Forcel Rosso metapelites and pegmatites system.

X-site chemical variations in metamorphic tourmalines show a progressive enrichment in Ca, substituting for Na and K, up to uvite composition (one analysis) with increasing metamorphic grade (Fig. X). It should be noted that Ca-enrichment is relegated to the migmatites that are near the contact with the basal carbonate layer of the Servino formation. This may be explained through the circulation of external fluids sourced from these rocks, as suggested in Magnani et al. (2022). These fluids may have provided Ca and CO_2 from carbonates into the metapelitic formation. This chemical exchange process at open system condition is also supported by the presence of carbonates in the terminal stages of the LCT pegmatites, that could have formed only through CO_2 enrichment of the anatectic melt.

The *X*-site ternary diagram (Fig. 7-3) for the anatectic melts shows only a weak trend toward more alkalic (Na-rich) tourmalines during the latest stages of LCT pegmatites differentiation, coincident with the appearance of fluor-elbaitic tourmaline as the stable species.

The *Y*-site ternary diagram (Fig. 7-4) for metamorphic tourmalines gives very few information while, on the other hand, the Y-site diagram for the anatectic melts reveals a complex history during which tourmaline chemical composition evolved from Fe and Mg-dominated to Li-Al-dominated. Starting from in-situ leucosomes compositions of Type IV and V tourmaline, the MgO content decreases in favor of the increase in FeO through Type VI, barren pegmatites hosted, and Type VII tourmaline, up to the onset of the elbaitic transition. Neither of these three tourmalines type composition overlaps with the other, well defining each group, but together they define a well-defined evolution trend that supports the idea of a the same anatectic system. The onset of fluor-elbaitic tourmaline formation of Type VIII tourmaline crystallization is abrupt as testified by the rims in zone E. The increase of Li activity inside the LCT pegmatites (Chapter 5), exhaustion of the MgO and FeO components towards the end of the internal aplite (Zone E) crystallization determined the expression of fluor-elbaitic

tourmaline, which completely dominates the internal zones of the LCT pegmatites. These crystals are invariably Fluorine-rich. The last change in the tourmaline chemical composition history of the anatectic system is represented by Type IX F-poor, FeO rich, schorlitic tourmaline forming the black caps. Manganese content in tourmaline steadily increases during the differentiation of the LCT pegmatitic dykes, reaching its peak at 4.5 wt.% in crystal F2. Interestingly, MnO content decreases during Type IX tourmaline formation, which should represent the terminal stage of the hydrothermal system forming the pocket elbaitic tourmalines (Fig. 7-5). "Testa di Moro" tourmalines are commonly observed in Elba island pockets and are thorougly described (e.g., Bosi et al., 2022; Pezzotta et al., 2000) and attributed to opening of the miarolitic pockets during the terminal stages of tourmaline crystallization. In our case, we infer that this feature may indeed have been developed at the latest stages of low temperature hydrothermal crystallization and have been connected to the partial opening of the miarolitic cavities and small internal fluids recirculation, since iron was exhausted much earlier during fractional crystallization of the pegmatitic body.

7.5.3 Tourmaline δ11B evolution

In-situ $\delta^{11}B$ data on tourmaline, coupled with petrographic observations, reveal that the B isotopic composition of tourmaline is sensitive to several metamorphic reactions and in well constrained cases, it can be used as a proxy to identify the reactions of the system. The $\delta^{11}B$ prograde evolution of tourmaline progresses from strongly negative (detrital tourmalines) to slighltly negative in the anatectic melts to slightly positive in the Crd-bearing metatexites. This evolution marks an ^{11}B-enrichment signature during the metamorphic history compatible with the values of the metapelites-connected anatectic melts of the Forcel Rosso area.

7.5.3.1 Metamorphic system

Detrital Type 0 tourmalines show negative $\delta^{11}B$ values compatible with common metamorphic tourmaline values (e.g. Marschall et al., 2009). The rounded shapes of the tourmalines belonging to this group and their variable colours led us to believe they are detrital in origin. Tracing back their provenence proves to be difficult since the Variscan basement from which the Verrucano Lombardo pelites and psammites derive is tourmaline-poor. The most probable source for the identified detrital tourmaline is represented by the sedimentary products of the Collio Formation, that in the Adamello area host tourmaline-rich breccia veins (e.g. Zhang et al, 1994), particularly near older contact intrusions near the investigated area (De Capitani et al., 1996; Moroni, 1994).

Type I tourmaline, mainly forming rims around detrital grains, is characterized by positive δ11B values ca. 4.41±1.48‰ (2SD), which we interpret to be linked to the circulation of low temperature

fluids with positive B isotopic signature. Their origin may either be external (magmatic or metamorphic) or internal, deriving from low-T devolatilization of rock-forming minerals. Clay minerals, and particularly illite, tend to liberate adsorbed fluids during prograde recrystallization as micrometric trioctahedral micas. Since illite composes up to 35 vol.% of the studied unmetamorphosed pelites it is possibile that a significative amount of boron may have been liberated at the onset of prograde metamorphism thus allowing for neogenic tourmaline development. The devolatilization-linked fluid, produced by release of adsorbed water from the clay should be enriched in 11B compared to the clay minerals it derives from ($\Delta^{11}B_{illite\text{-}fluid}$ = -13‰ to -16‰, at 300-350°C Williams et al., 2001a,b), also Palmer et al. (1987) investigated the B-isotope fractionation of illite surface-adsorbed B, finding it to be 23.4– to 34‰ lighter than the B dissolved in the coexisting seawater ($\delta^{11}B$ = + 39.61 ± 0.04‰; Foster et al. 2010) at 4-50°C. Following this approach, we expect the $\delta^{11}B$ values of illite-produced fluids to be extremely positive, between +26 and +30‰ $\delta^{11}B$, thus able of producing the observed tourmaline rims. The circulation of external fluids needs to be excluded as they would have been characterized by typically negative B isotopic signature (e.g. Trumbull & Slack, 2018). Furthermore, low temperature fluids circulation would have remained localized and limited to the immediate surroundings of the related fractures system.

Type II tourmalines, coexisting with zoned Type 0-I grains but found only at higher greenschist facies conditions, are characterized by negative $\delta^{11}B$ values which we interpret as possibly linked to the advanced stages of muscovite dehydration. White mica devolatilization is an important metamorphic process which leads to partial melting and can thus liberate boron at relatively low temperatures. White mica is usually characterized by negative $\delta^{11}B$ values, therefore tendentially generating $\delta^{11}B$ negative, boron-rich fluids at high T which can allow for tourmaline neoformation at low pressures (e.g. Nakano&Nakamura, 2001).

Unfortunately, establishing the B isotope composition of the microcrystalline muscovite was not possible using LA-MC-ICP-MS because of the extremely small crystal size, but, since greenschist facies temperatures cannot cause destabilization of tourmaline and the lack of B diffusion in the tourmaline structure in geological times (e.g. Van Hinsberg & Schumacher, 2007), we can argue that this $\delta^{11}B$ negative tourmaline may be neoformed during white mica destabilization during prograde metamorphic reactions.

Type III and IV tourmalines are hosted, respectively, in the Crd-bearing and Crd-absent migmatites. The former tourmaline type III is characterized by positive $\delta^{11}B$ signature, around +1‰, that we interpret to be the result of the complete recrystallization of tourmaline causing the homogenization of Type 0, I and II tourmalines and determining their inheritance of the initial whole rock $\delta^{11}B$ signature

of unmetamorphosed pelites. The latter tourmaline type IV, found in Crd-absent migmatites, is characterized by negative $\delta^{11}B$ of -2.99 ± 0.37‰ (2SD). Since partial melting of metapelites in the Adamello pluton thermal aureole progressed at ca. 700°C, we can assume little to no isotopic fractionation was involved during melt production (Meyer et al., 2008?) and that the anatectic melts connected to this metatexites roughly had the same $\delta^{11}B$ signature (e.g. Trumbull et al. 2008, 2013). Interestingly, Type IV tourmaline boron isotopic signature perfectly matches the ca. -2‰ $\delta^{11}B$ signature of the external part of the studied LCT pegmatites, which we infer to be directly connected to this migmatites, further supporting our hypothesis. The differences existing between Type III and IV tourmalines are difficult to decipher but they may have been derived by the slightly different B signature of their two protolith rocks. Alternatively, the possibility that the slightly more negative values of Type IV tourmalines may be connected to the external metamorphic fluids circulation that determined the fluid fluxed conditions during partial melting.

7.5.3.2 Anatectic system

Type V tourmaline is found in in-situ leucosomes directly correlated to the Crd-bearing metatexites. Their mean $\delta^{11}B$ value is -2.16 ± 0.42‰ and, although different from the slightly positive signature of type III tourmaline (0.97 ± 0.30‰), the correlation between these values is compatible with their partial melting and subsequent crystallization at ca. 500-600°C considering -2 to -3‰ cumulative fractionation between melt and tourmaline. (Trumbull 2008). Tourmaline in these leucosomes presents $\delta^{11}B$ values similar to the external zones of the LCT pegmatites.

Type VII tourmalines in the LCT pegmatites are as variable in $\delta^{11}B$ as they are in chemical composition. Type VII tourmaline yields well definite values in all pegmatitic zones, allowing for the interpretation of the internal evolution of the pegmatites. We observe several events that modified the $\delta^{11}B$ signature of the pegmatitic melt throughout its history, all recorded by Type VII tourmaline: in the most external zones of the pegmatites (A and B), tourmaline expresses a tendence in decreasing its $\delta^{11}B$ values, from a mean of -1.58 ± 0.38‰ of zone A, , to the -2.58 ± 0.81‰ (2SD) value of zone B, the lowest found inside the LCT pegmatites. Zone B, a line rock zone enriched in tourmaline, is interpreted as an extreme tourmaline fractionation event with en-masse tourmaline fractionation in which the most MgO-rich cores are recognized. The $\delta^{11}B$ evolution from Crd-absent migmatites (Tur Type IV) through barren pegmatites (Tur Type VI) to the external LCT zones A and B is complex and difficult to interpret. Since these tourmaline types $\delta^{11}B$ signatures are different, this can be interpreted as a function of boron fractionation during pegmatites crystallization. At 700°C, the temperature inferred for partial melting in chapter 4, isotopic fractionation should be very limited and therefore tourmaline Type IV (-2.99 ± 0.37‰ $\delta^{11}B$) should have recorded the magma's boron signature with a 0

to +1 fractionation effect (Trumbull et al., 2008). Cooling the pegmatitic melt from ca. 700°C to ca. 500°C causes $\Delta^{11}B_{tur\text{-}melt}$ fractionation to rise up to ca. -3‰ (Trumbull et al., 2008) which could have produced the observed progressive decrease in tourmaline $\delta^{11}B$ up to zone A. In order to explain zone B boron signature we have to remember that the "internal melt" injected along this zonation, causing a re-heating of the system to ca. 700°C, causing the B isotopic fractionation to go back to ca. 0. Between zone B and C (Tur-rich line rock and aplite), $\delta^{11}B$ signature increases of ca. 2‰. This shift could have only been caused by the injection of a new magma batch, as supported by the Sr-Nd whole rock isotopic signature of the LCT pegmatitic dykes described in chapter 5. This melt, comparatively richer in ^{11}B than the first, then fractionated tourmaline in zones C and D (-0.25 ± 0.94‰ and -0.38 ± 0.52‰ respectively), then E (-0.94 ± 0.32‰). The B isotopic composition of the "external melt" is more negative compared to the one featured by the "internal melt" and this could be explained by their small scale source, as it was the case for Sr and Nd (chapter 5). Tourmaline at the top of the formation in the Crd-absent migmatites was more negative compared to the tourmaline at the base (in the Crd-bearing migmatites analyzed here) therefore explaining this difference as source-derived. This may have been caused by a more prominent activity of low temperature fluids during diagenesis at the base of the formation compared to the top of it or by the circulation of negative $\delta^{11}B$ fluids at the top of the formation after muscovite dehydration.

In zone E Type VIII, elbaitic tourmaline makes its first appearance in rims around schorlitic cores. This dramatic compositional change does not seem to impact the B isotopes fractionation as Type VIII rims do not differ from schorlitic tourmaline and pocket tourmalines of zone E yield similar $\delta^{11}B$ values of -0.79 ± 0.36‰. Type VIII evolves throughout zone F with similar $\delta^{11}B$ values of -1.08 ± 0.47‰ but only in the pockets it really shows an important $\delta^{11}B$ evolution. (Fig. 7-7). Our data reveal two different behaviors in the fluid-related growth of Type VIII tourmaline: i) from core to rim, perpendicular to the *C*-axis, tourmaline F3 exhibits a definite decrease in $\delta^{11}B$ values from -1.5 to -2.1‰; ii) from base to tip, parallel to the *C*-axis, crystal F1 shows a slight increase in $\delta^{11}B$ values from -1.2 to -0.4‰ towards the black cap.

Finally, the schorlitic black caps of Type IX tourmaline (Fig. 7-7, top crystals) yield an invariably slightly positive $\delta^{11}B$ value of +0.04 ± 0.15‰ (2SD/SE), the only positive value recorded in the LCT pegmatites of the Forcel Rosso area. This B isotopic value marks the formation of the black caps as completely hydrothermal as the formation of a few micrometers thick B-positive tourmaline layer is not enough to justify a new heating event up to 700°C but could be explained by the enrichment in ^{11}B of the terminal pegmatitic fluids.

7.5.3.3 General observations

The observed metamorphic evolution is complex and unfortunately no single zoned tourmaline grain is able to record it completely. Prograde evolution of tourmaline during high pressure metamorphism in metasedimentary rocks is described by Nakano and Nakamura (2001) and that observe a decrease in $\delta^{11}B$ values in core-to-rim profiles in tourmalines. Our data show that, starting from negative B isotope composition in detrital tourmaline, the $\delta^{11}B$ values increase in response to clay minerals evolution,

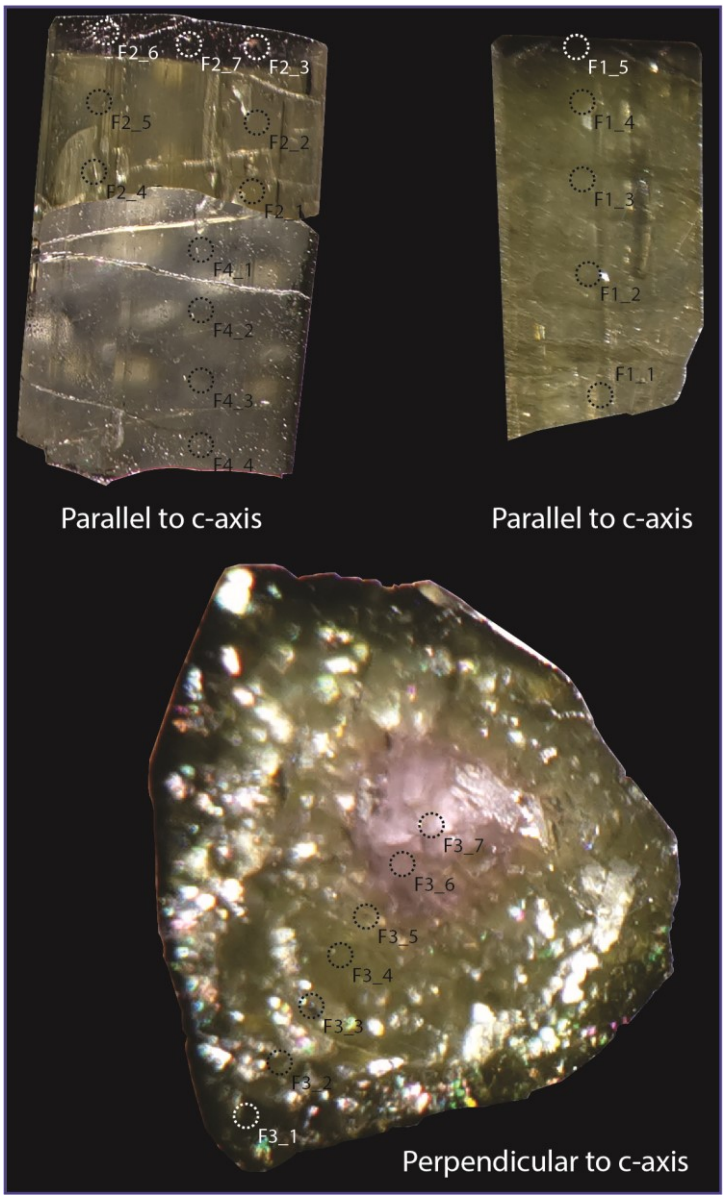

Figure 7-7 Traverses on tourmaline crystals from the LCT pegmatites miarolitic cavities. At the top, black-capped tourmalines analyzed along the C-axis, at the bottom a watermelon tourmaline analyzed perpendicular to the C-axis.

determining a final homogeneous tourmaline composition of ca. +1‰ (Type III). These results, obtained on previously unmetamorphosed pelites, are discordant with the more common observations that tourmalines tend to become progressively more negative as metamorphic grade increases (ref.)

and they suggest that the origin of the sediments (marine vs. continental) and precursor? metamorphic history of the sediments determine tourmaline B isotopic evolution and signature at high metamorphic grades.

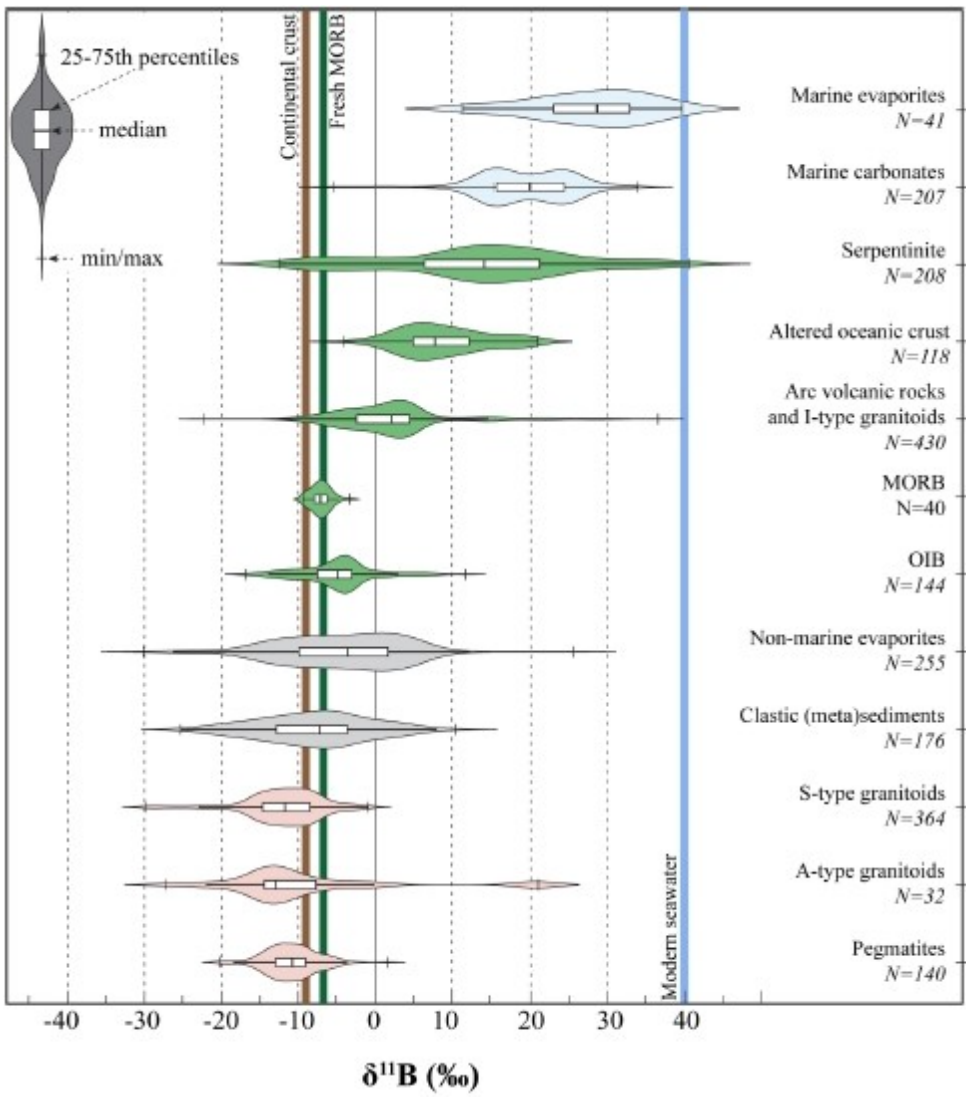

Figure 7-8 Distribution of the $\delta^{11}B$ values across multiple reservoirs, from Trumbull et al. 2020. This diagram highlights how the bulk of the available isotopic B data for pegmatites ranges from -16‰ to ca. -5‰.

Finally, the $\delta^{11}B$ values observed in the Forcel Rosso LCT pegmatites are comprised between -4.3 to +0.1‰ which, although in the range of the $\delta^{11}B$ data available in the literature for this kind of magmatic bodies (Fig. 7-8), are completely different from well-known pluton derived LCT pegmatites. For instance, Elba Island LCT pegmatites are characterized by $\delta^{11}B$ between -9.6 to -8.5‰ (Tonarini et al., 1998), much of the Borborema province tourmalines yield -17 to -9‰ values, with a strong maximum between -13 and -15‰ (Beurlen et al., 2011; Trumbull et al., 2013) and finally tourmaline

from pegmatites of the CMC in the Sierra San Luis yield values from -10.3 to -7.8‰ (Montenegro et al., 2021). These observations suggest that tourmaline boron signature may be the best way to differentiate between anatectic and plutonic-derived LCT pegmatites. More data will be needed in order to validate this hypotesis in other pegmatitic dykes with similar B isotopic signature.

7.6 Conclusions

We calculated that the initial boron budget of the pelites and metapelites of the Verrucano Lombardo formation in the Forcel Rosso area is mainly controlled by sedimentary and diagenetic clay minerals, muscovite and tourmaline. This study shows that high-temperature tourmaline tends to acquire the whole rock $\delta^{11}B$ signature of the protolith rocks, if the system remains closed to external boron influxes, therefore suggesting that the origin of the sediments (marine vs. continental) and their metamorphic history can be interpreted from high temperature tourmaline B isotopic signature. Also, the $\delta^{11}B$ values observed in the Forcel Rosso LCT pegmatites are completely different from well-known pluton derived LCT pegmatites suggesting that slightly negative $\delta^{11}B$ tourmaline values may be the best way to differentiate between anatectic and plutonic-derived LCT pegmatites. The next step will be to analyze the Li isotopic signature of the same crystals in order to study their coupled variations

7.7 References

Bebout, G. E., & Nakamura, E. (2003). Record in metamorphic tourmalines of subduction-zone devolatilization and boron cycling. Geology, 31(5), 407-410.

Beurlen, H., Muller, A., Silva, D., & Da Silva, M. R. R. (2011). Petrogenetic significance of LA-ICP-MS trace-element data on quartz from the Borborema Pegmatite Province, northeast Brazil. Mineralogical Magazine, 75(5), 2703-2719.

Bosi, F. (2018). Tourmaline crystal chemistry. American Mineralogist: Journal of Earth and Planetary Materials, 103(2), 298-306.

Bosi, F., Pezzotta, F., Altieri, A., Andreozzi, G. B., Ballirano, P., Tempesta, G., ... & Evans, R. J. (2022). Celleriite,□(Mn 2 2+ Al) Al6 (Si6O18)(BO3) 3 (OH) 3 (OH), a new mineral species of the tourmaline supergroup. American Mineralogist: Journal of Earth and Planetary Materials, 107(1), 31-42.

Catanzaro, E. J. (1970). Boric acid: isotopic and assay standard reference materials (Vol. 260, No. 17). National Bureau of Standards, Institute for Materials Research.

De Capitani, L. U. I. S. A., Moroni, M., & Rodeghiero, F. (1999). Geological and geochemical characteristics of Permian tourmalinization at Val Trompia (southern Alps, northern Italy) and relationship with the Orobic tourmalinites. Periodica Mineral, 68, 185-212.

Dietrich, R. V., & Dietrich, R. V. (1985). The tourmaline group (p. 300). New York: Van Nostrand Reinhold.

Dyar, D., Guidott, C. V., Core, D. P., Wearn, K. M., Wise, M. A., Francis, C. A., ... & Cross, L. R. (1999). Stable isotope and crystal chemistry of tourmaline across pegmatite-country rock boundaries at Black Mountain and Mount Mica, southwestern Maine, USA. European Journal of Mineralogy, 11, 281.

Dutrow, B. L., & Henry, D. J. (2011). Tourmaline: a geologic DVD. Elements, 7(5), 301-306.

Floess, D., Baumgartner, L.P., 2015. Constraining magmatic fluxes through thermal modelling of contact metamorphism. From: Caricchi L., Blundy J.D. (eds) Chemical, Physical and Temporal Evolution of Magmatic Systems. Geological Society, London, Special Publications 422.

Floess, D., Baumgartner, L.P., Vonlanthen, P., 2015. An observational and thermodynamic investigation of carbonate partial melting. Earth and Palentary Science Letters 409, 147-156.

Griffin, W. L. (2008). GLITTER: data reduction software for laser ablation ICP-MS. Laser Ablation ICP-MS in the Earth Sciences: Current practices and outstanding issues, 308-311.

Henry, D. J., Novák, M., Hawthorne, F. C., Ertl, A., Dutrow, B. L., Uher, P., & Pezzotta, F. (2011). Nomenclature of the tourmaline-supergroup minerals. American Mineralogist, 96(5-6), 895-913.

Jiang, S. Y., & Palmer, M. R. (1998). Boron isotope systematics of tourmaline from granites and pegmatites; a synthesis. European Journal of Mineralogy, 10(6), 1253-1265.

London, D. (2011). Experimental synthesis and stability of tourmaline: a historical overview. The Canadian Mineralogist, 49(1), 117-136.

Magnani, L., Farina, F., Pezzotta, F., Dini, A., Mayne, M. J., & Bartoli, O. (2022). Role of aqueous fluids during low pressure partial melting of pelites in the Adamello pluton contact aureole (Italy). Lithos, 430, 106853.

Manning, D. A. C., & Pichavant, M. (1983). The role of fluorine and boron in the generation of granitic melts. In High grade metamorphism, migmatites and melting. Meeting of the Geochemical Group of the Mineralogical Society (pp. 94-109).

Marschall, H. R., Altherr, R., Kalt, A., & Ludwig, T. (2008). Detrital, metamorphic and metasomatic tourmaline in high-pressure metasediments from Syros (Greece): intra-grain boron isotope patterns determined by secondary-ion mass spectrometry. Contributions to Mineralogy and Petrology, 155(6), 703-717.

Marschall, H. R., Korsakov, A. V., Luvizotto, G. L., Nasdala, L., & Ludwig, T. (2009). On the occurrence and boron isotopic composition of tourmaline in (ultra) high-pressure metamorphic rocks. Journal of the Geological Society, 166(4), 811-823.

Meyer, C., Wunder, B., Meixner, A., Romer, R. L., & Heinrich, W. (2008). Boron-isotope fractionation between tourmaline and fluid: an experimental re-investigation. Contributions to Mineralogy and Petrology, 156(2), 259-267.

Montenegro, T., Wul, J., de Luchi, M. L., Ribacki, E., & Trumbull, R. B. (2021). Chemical and boron isotope composition of tourmaline from pegmatites and their host rocks, Sierra de San Luis, Argentina. The Canadian Mineralogist, 59(3), 467-494.

Moroni, M. (1994). Identification of W-Sn mineralization associated with boron metasomatism in the crystalline basement of the Southern Italian Alps: Preliminary observations on a new finding. Chronique de la recherche minière, (514), 38-42.

Nakano, T., & Nakamura, E. (2001). Boron isotope geochemistry of metasedimentary rocks and tourmalines in a subduction zone metamorphic suite. Physics of the Earth and Planetary Interiors, 127(1-4), 233-252.

Palmer, M. R., Spivack, A. J., & Edmond, J. M. (1987). Temperature and pH controls over isotopic fractionation during adsorption of boron on marine clay. Geochimica et Cosmochimica Acta, 51(9), 2319-2323.

Palmer, M. R., Swihart, G. H., Grew, E. S., & Anovitz, L. M. (1996). Boron: Mineralogy, Petrology and Geochemistry. Rev. Mineral, 33, 709-744.

Palmer, M. R., & Swihart, G. H. (2018). Boron isotope geochemistry: an overview. Boron, 709-744.

Pearce, N. J., Perkins, W. T., Westgate, J. A., Gorton, M. P., Jackson, S. E., Neal, C. R., & Chenery, S. P. (1997). A compilation of new and published major and trace element data for NIST SRM 610 and NIST SRM 612 glass reference materials. Geostandards newsletter, 21(1), 115-144.

Pezzotta, F. (2000). Internal structures, parageneses and classification of the miarolitic Li-bearing complex pegmatites of Elba Island (Italy). Memorie della Società Italiana di Scienze Natuarli e del Museo Civico di Storia Naturale di Milano, 30, 29-43.

Riklin, K. (1983). Contact metamorphism of the permian «Red Sandstone» in the Adamello area. Memorie della Società Geologica Italiana, 26(1), 159-169.

Robbins, C. R., & Yoder Jr, H. S. (1962). Stability relations of dravite, a tourmaline. Carnegie Institution of Washington, Yearbook, 61, 106-108.

Schaltegger, U., Nowak, A., Ulianov, A., Fisher, C. M., Gerdes, A., Spikings, R., ... & Müntener, O. (2019). Zircon petrochronology and 40Ar/39Ar thermochronology of the Adamello intrusive suite, N. Italy: monitoring the growth and decay of an incrementally assembled magmatic system. Journal of Petrology, 60(4), 701-722.

Slack, J. F., Palmer, M. R., & Stevens, B. P. (1989). Boron isotope evidence for the involvement of non-marine evaporites in the origin of the Broken Hill ore deposits. Nature, 342(6252), 913-916.

Tonarini, S., Dini, A., Pezzotta, F., & Leeman, W. P. (1998). Boron isotopic composition of zoned (schorlelbaite) tourmalines, Mt. Capanne Li-Cs pegmatites, Elba (Italy). European Journal of Mineralogy-Ohne Beihefte, 10(5), 941-952.

Tonarini, S., Pennisi, M., Adorni-Braccesi, A., Dini, A., Ferrara, G., Gonfiantini, R., ... & Gröning, M. (2003). Intercomparison of boron isotope and concentration measurements. Part I: Selection, preparation and homogeneity tests of the intercomparison materials. Geostandards Newsletter, 27(1), 21-39.

Trumbull, R. B., Krienitz, M. S., Gottesmann, B., & Wiedenbeck, M. (2008). Chemical and boron-isotope variations in tourmalines from an S-type granite and its source rocks: the Erongo granite and tourmalinites in the Damara Belt, Namibia. Contributions to Mineralogy and Petrology, 155(1), 1-18.

Trumbull, R. B., Beurlen, H., Wiedenbeck, M., & Soares, D. R. (2013). The diversity of B-isotope variations in tourmaline from rare-element pegmatites in the Borborema Province of Brazil. Chemical Geology, 352, 47-62.

Trumbull, R. B., & Slack, J. F. (2018). Boron isotopes in the continental crust: granites, pegmatites, felsic volcanic rocks, and related ore deposits. In Boron Isotopes (pp. 249-272). Springer, Cham.

Trumbull, R. B., Codeço, M. S., Jiang, S. Y., Palmer, M. R., & Slack, J. F. (2020). Boron isotope variations in tourmaline from hydrothermal ore deposits: a review of controlling factors and insights for mineralizing systems. Ore Geology Reviews, 125, 103682.

Van Hinsberg, V. J., & Schumacher, J. C. (2007). Intersector element partitioning in tourmaline: a potentially powerful single crystal thermometer. Contributions to Mineralogy and Petrology, 153(3), 289-301.

Von Goerne, G., Franz, G., & Robert, J. L. (1999). Upper thermal stability of tourmaline+ quartz in the system MgO-Al 2 O 3-SiO 2-B 2 O 3-H 2 O and Na 2 O-MgO-Al 2 O 3-SiO 2-B 2 O 3-H 2 O-HCl in hydrothermal solutions and siliceous melts. The Canadian Mineralogist, 37(4), 1025-1039.

Williams, L. B., Hervig, R. L., Holloway, J. R., & Hutcheon, I. (2001a). Boron isotope geochemistry during diagenesis. Part I. Experimental determination of fractionation during illitization of smectite. Geochimica et Cosmochimica Acta, 65(11), 1769-1782.

Williams, L. B., Hervig, R. L., & Hutcheon, I. (2001b). Boron isotope geochemistry during diagenesis. Part II. Applications to organic-rich sediments. Geochimica et Cosmochimica Acta, 65(11), 1783-1794.

Wunder, B., Meixner, A., Romer, R. L., Wirth, R., & Heinrich, W. (2005). The geochemical cycle of boron: constraints from boron isotope partitioning experiments between mica and fluid. Lithos, 84(3-4), 206-216.

Zhang, J. S., Passchier, C. W., Slack, J. F., Fliervoet, T. F., & De Boorder, H. (1994). Cryptocrystalline Permian tourmalinites of possible metasomatic origin in the Orobic Alps, Northern Italy. Economic Geology, 89(2), 391-396.

Chapter 8

Conclusions and geological implications

This PhD projects produced several interesting results that may have geological implications for: i) pegmatitic lithium resources targeting, ii) the overall knowledge of lithium behaviour during low pressure partial melting, iii) migmatites and their connection to migrating anatectic melts, ii) and iv) the evolution of tourmaline during prograde contact metamorphism.

Paper one (chapter 4) determined that in migmatitic terrains at low pressure the fluids regime during metamorphism and anatexis may be extremely variable even at the scale of hundreds of meters. In this paper it is argued that melt produced from a migmatitic area, even at the metric scale, could be characterized by both “fluid absent” and “fluid present” signatures as the source could feature extreme heterogenities in water activity. Also, from this work, it appears clear that evolved Li-rich pegmatites found emplaced in migmatitic fields could be traced back to their source on the basis of the melts major elements compositions. The fundamental link connecting these evolved magmatic bodies to their origin is the the early fractionation of Kfs-rich cumulates, in-situ or during the initial stages of melt migration.

Paper two (chapter 5) determined the definite Sr-Nd isotopic crustal imprint of the metapelites-hosted LCT pegmatites, confirming their anatectic origin from the nearby migmatites and excluding the possibility of a direct connection with the nearby Adamello batholith, featuring a mantle-derived geochemical signature. The identification of these nearly in-situ anatectic Li-enriched pegmatites helped us expanding our understanding of how lithium could concentrate in anatectic melts at low pressure. We observe that the most important conditions for Li enrichment in crustal magmas are: i) the thermal perturbation of a fertile pelitic source; ii) low to medium degree of partial melting under fluid fluxed conditions and without cordierite formation; iii) early fractionation of Kfs-rich cumulates. In our study, we identify that normal pelites featuring Li contents of ca. 60 ppm, similar to those of the mean pelite composition (Wedepohl, 1995) may originate Li-enriched melts after partial melting in the absence of cordierite and in-source fractionation of the anatectic primary melt. Kfs-rich cumulates fractionation is the key to achieve proper Li and rare elements contents in order for them to be expressed as minable resources. The fact that anatectic Li-rich pegmatites may be formed from direct partial melting of metapelites of normal composition suggests that low pressure migmatitic fields may become new interesting prospects for pegmatitic lithium deposits in the future, therefore potentially increasing the projected Li resources for many countries and contributing in strenghtening the lithium supply chain.

Zircons data from Forcel Rosso pegmatites (chapter 6) offer interesting results that confirm our previous findings: their chemical composition reflects the enrichment of peculiar elements of the LCT system, they can be used to determine the ages of the bodies they crystallized in and they provide informations on the crystallization temperatures and the systems redox state. The main takeaway from this work is that zircon inclusions and trace elements chemistry can help us pinpointing the source of pegmatites and other evolved melts. We observe that zircons deriving from metapelites anatexis are tendentially enriched in Y while zircons deriving from the crystal fractionation and differentiation processes of mantle-derived felsic magmas are tendentially enriched in Th. We identify that thorite inclusions and exsolutions in/from zircons in felsic rocks may be a good proxy for identifiyng mantle derived fractionates from crustal melting products. Although these inclusions are rare, they may be useful in identifying the geochemical affinity of some evolved vulcanites, pegmatites and granitoids.
Chapter 7 delves into the topic of tourmaline evolution during prograde metamorphism, partial melting and crystallization of anatectic magmas. The area we studied is a great example of a metamorphic-anatectic system in which pelites from unmetamorphosed up to migmatites can be directly sampled and where the products of anatexis remained almost all in-situ. Tourmaline data supports the succession of events discussed in the previous chapters (4, 5, 6) and registered almost every major event through its chemical and isotopical composition. This study shows that high-temperature tourmaline tends to acquire the whole rock $\delta^{11}B$ signature of the protolith rocks, if the system remains closed to external boron influxes, therefore suggesting that the origin of the sediments (marine vs. continental) and their metamorphic history can be interpreted from high temperature tourmaline B isotopic signature. Also, the $\delta^{11}B$ values observed in the Forcel Rosso LCT pegmatites are completely different from well-known pluton derived LCT pegmatites suggesting that tourmaline boron signature may be one of the best ways to differentiate between anatectic and plutonic-derived LCT pegmatites.

8.1 References

Wedepohl, K. H. (1995). The composition of the continental crust. Geochimica et cosmochimica Acta, 59(7), 1217-1232.

Ackowledgments

I deeply thank all the members of the Geochemistry group of the Università degli Studi d Milano that supported me and made this whole work possible. The biggest thank goes to Federico Farina, my tutor, that believed in me from the start and never stopped even during the thoughest times.
I dedicate this work to my family, that never ceased to support me and provided me with everything that made me who I am today, to Silvia, the ray of sunshine that guided me through everything and withouth which I would not be here today, and finally to Antida that couldn't be here to see this day but will always be in my heart.

Dedico questo lavoro alla mia famiglia che non ha mai smesso di supportarmi e di provvedere a tutto ciò che mi ha reso quello che sono, a Silvia, il raggio di sole che mi ha guidato attraverso tutto e senza la quale non sarei qui oggi, e infine ad Antida che non è potuta essere qui con noi a vedere questo giorno ma che rimarrà per sempre nel mio cuore. Grazie nonna.

I thank Antonio Langone and Gary Steves for the precious insights that allowed for the improvement of this manuscript.
The author acknowledges the Italian Ministry of Education and University (MIUR) for the support through the project "Dipartimenti di Eccellenza 2018–2022 – Le Geoscienze per la societa: Risorse e loro evoluzione". The Stellenbosch University (SA) Center for Analytical Facilities (CAF) is thanked for their contribution in the XRF analyses.

Appendix A: Additional text for Chapter 4

A.1 Calcium enrichment and high An plagioclase origin

CaO values in the performed analyses of the same stratigraphic level of Verrucano Lombardo pelites at different conditions of metamorphism varies between 0.06 wt% and 0.64 wt%. The CaO content of unmetamorphosed VER pelites is the lowest, being always under 0.1 wt% as the collected samples completely lack detrital plagioclase. On the other hand, the CaO content in low grade metamorphic pelites is higher, being comprised between 0.49 wt% and 0.64 wt%. Although small, this difference can produce a dramatic increase in predicted plagioclase in pseudosections and it was one of the motives behind the use of a low grade metamorphic rock as compositional proxy during phase equilibria modeling, instead of the unmetamorphosed counterpart. Plagioclase is present in all the sampled VER metapelites in the Adamello pluton aureole. While low grade to metatexite grade plagioclase varies between An15 and An40, high anorthite (An86-95) plagioclase can be found in the banded stromatic metatexites as euhedral to subhedral crystals disseminated in and near the foliation. Similar high-An plagioclases were observed by Marger&Mueller, 2014 in the Southern Adamello Massif. Calculated T-X pseudosections, obtained through Perplex, predict a maximum An content of 45 in the fluid assisted case and of 58 in the fluid excess case at the inferred P-T field. While the first value correctly explains the low grade to metatexite plagioclase, the second value fails to correctly model the composition of the plagioclase observed in the banded metapelites. Madlakana&Stevens (2018) describe similar highly anorthitic plagioclases in the Bandelierkop Quarry (South Africa) as euhedral to subhedral inclusions in peritectic garnet in melt transfer zones and interpreted it as formed by disequilibrium melting products in water absent conditions. Their evaluations are based on the experiment of Morse (1984) in which plagioclase reacts in water rich medium. Morse's data showed that Na-Ca diffusion in plagioclase single crystals is very slow and at melting temperatures it is too slow to give a complete reequilibration of the plagioclase even in geological times, only allowing for the formation of rims showing isles and peninsulas reaction profiles with CaO contents higher than the core. Following Morse's experiment, the plagioclase found in the Forcel Rosso low grade metapelites (An15-40) cannot ever become so rich in CaO to form An86 to An95 crystals by simple intracrystalline cationic diffusion. T-X models calculated with PerpleX for each composition discussed in chapter 4 predict in fact that for the given bulk the An content of the plagioclase should be An67 or lower for any given water content between 0 and 10 wt.% H_2O in the reactive system. Given that phase equilibria modeling cannot correctly predict the residual plagioclase composition with equilibrium reactions, the only possible explanation is that a disequilibrium o metasomatic process is

responsible for its formation in our case. The observed plagioclases are often ehuedral and included in schlieren of neoformed biotite. They can be observed, other than in the banded metapelites, in low grade Verrucano Lombardo metapelites where matasomatized carbonatic nodules and caliches are present, which are now composed of Ca-Mg-amphiboles with phlogopite rims. Around the matasomatized nodules, for several centimeters, the same subhedral An86-88 plagioclases that can be observed in the banded metatexites compose from the 20 vol.% up to 50 vol.% of the rock. This suggests a fluid metasomatism of the original carbonatic portions of the rock causing the formation of abundant anorthite in the immediate surroundings that remained metastable during partial melting and that developed an higher An92-95 border in a fluid rich environment as described by Morse's experiments. The low titanium content of the phlogopite rims in the nodules suggests a low temperature metasomatism prior to the Adamello pluton intrusion during which the metasomatic anorthite formed, probably linked to the the Re di Castello intrusion. The Ca enrichment observed in the low-grade metamorphic rocks versus their unmetamorphosed counterparts may then be linked to this phenomenon. Furthermore, Verrucano Lombardo metapelites that were in contact with the basal carbonates of the Servino formation show Ca enrichment that could have originated during a similar, very limited, Ca-rich fluids circulation.

References

Madlakana, N., & Stevens, G. (2018). Plagioclase disequilibrium induced during fluid-absent biotite-breakdown melting in metapelites. Journal of Metamorphic Geology, 36(9), 1097-1116.

Marger, K., & Mueller, T. (2014, May). Formation of contact metamorphic reaction rims in the southern Adamello Massif, N-Italy: A natural study on transport controlled growth mechanisms. In EGU General Assembly Conference Abstracts (p. 5119).

Morse, S. A. (1984). Cation diffusion in plagioclase feldspar. Science, 225(4661), 504-505.

Appendix A: Modal proportions, whole rock compositions, phase equilibria results

Table A1

	Unmetamorphosed pelites	Foliated metapelites	Spotted metapelites	Orbicular metapelites	Banded metapelites
Aspect	Homogeneous	Finely foliated, dispersed but isooriented micas	Finely foliated, with black spots and white coronas interrupting the foliation	White, rounded spots united to form leucocratic levels, separated by biotite schlieren. Zones with recrystallized fine foliation.	Parallel leucocratic and melanocratic levels. Foliation defined by Bt+Sil schlieren
Main Al phases	Illite and Smectite	Microcrystalline muscovite and biotite	Muscovite, andalusite, biotite	Biotite, rare Sillimanite	Biotite and Sillimanite
Leucosomes	No	No	No, only subsolidus segregation in the bleached coronas	In-situ, Ms-Tur bearing, concordant with the main foliation	Bt-bearing, perpendicular to the foliation and connected to extraction structures

Table 1) Synthesys of main pelites and metapelites rock characteristics.

Table A2

vol. %	Unmetamorphosed pelites (1*)	Foliated metapelites (2*)	Spotted metapelites (3*)	Orbicular metapelites(4*)	Banded metapelites (5*)	Orbicular metapelites leucosomes (6*)	Banded metapelites leucosomes (7*)	Barren pegmatites (8*)
Quartz	45-55	30-35	25-30	18-22	15-18	32	12	16
Plagioclase	4-5	10-12	8-10	4-5	2-3	22	1	20
K-feldspar	12-10	12-14	20-22	27-30	25-27	30	82	53
Biotite		13-15	13-15	10-15	18-20		5	
Muscovite (prograde, retrograde, magmatic)	5-6	20-25	10-12		10-11	12		7
Sillimanite			5-6	1-4	8-10			
Andalusite			8-10	1-2	2-3			
Cordierite				8-12				
Tourmaline	ca. 0.1	ca. 0.2-0.3	ca. 0.2-0.3	ca. 0.2-0.3	ca. 0.2-0.3	4		4
Illite	30-35							

1* (4 samples, 8 thin sections), 2* (3 samples, 8 thin sections), 3* (2 samples, 4 thin sections)
4* (6 samples, 9 thin sections), 5* (4 samples, 6 thin sections)
6* (3 samples, 5 thin sections), 7* (5 samples, 5 thin sections), 8* (3 samples, 3 thin sections)

Table 2) Mineral modal abundance of metapelitc lithotypes and related leucosomes.

Table A3

	Na2O	MgO	Al2O3	SiO2	P2O5	K2O	CaO	TiO2	MnO	FeO
Unit	wt%	wt%	wt%	wt%	wt%	wt%	wt%	wt%	wt%	wt%
ML6	0.8	1.8	25.5	56.0	0.1	8.6	0.8	0.7	0.1	4.1
ML6B	0.9	1.7	25.8	54.5	0.1	10.2	0.7	0.7	0.1	4.2
ML118	1.4	3.0	19.1	63.7	0.1	5.4	0.6	0.7	0.1	4.9
ML119	1.2	3.0	21.3	60.2	0.1	6.3	0.4	0.8	0.1	4.9
ML153	2.1	2.0	20.2	63.8	0.0	5.4	0.4	0.9	0.0	3.5
ML152	1.6	2.2	16.7	68.3	0.1	5.0	1.1	0.7	0.1	2.9
ML5	1.1	1.8	16.8	68.1	0.0	4.4	0.1	0.7	0.0	3.6
ML161	1.5	1.3	16.9	66.1	0.1	6.1	0.55	0.8	0.0	4.7
ML163	2.7	1.7	15.6	67.9	0.1	6.9	0.7	0.7	0.0	3.1
V1	0.4	0.9	16.4	68.9	0.0	5.2	0.1	0.7	0.0	3.8
V1S	0.3	0.8	14.9	71.3	0.0	5.7	0.0	0.7	0.0	4.6
V4	0.8	1.0	16.6	68.7	0.0	5.5	0.1	0.7	0.0	3.2
V4S	0.8	0.9	15.6	70.2	0.0	6.2	0.1	0.6	0.0	3.9
V3	0.8	0.7	13.5	74.6	0.0	5.2	0.1	0.6	0.0	3.4
V4-2	0.9	0.9	15.3	70.8	0.0	6.2	0.0	0.6	0.0	3.8
ML6L	1.3	0.4	17.1	66.7	0.1	12.7	0.3	0.1	0.0	0.8
ML168L	2.9	0.6	15.8	72.0	0.1	5.8	0.9	0.1	0.0	0.7
ML121A	1.6	0.1	15.1	73.7	0.1	6.5	0.5	0.1	0.0	0.6
ML121B	1.4	0.4	15.5	73.5	0.1	4.9	0.5	0.2	0.1	1.1
ML121C	3.4	0.1	14.9	74.0	0.1	4.2	1.6	0.0	0.0	0.4
ML121D	3.5	0.3	15.0	75.0	0.1	2.0	2.3	0.0	0.0	0.6
ML121E	7.0	0.0	15.6	74.1	0.1	0.9	1.0	0.0	0.3	0.2
ML121F	3.7	0.0	11.3	80.3	0.1	1.9	0.8	0.0	0.1	0.2
Mean pegmatite	4.3	0.1	14.0	76.3	0.1	2.1	1.4	0.0	0.1	0.4
Barren pegs	2.7	0.2	12.3	74.9	0.1	8.5	0.3	0.1	0.0	0.3

Table 3) Whole rock compositions. Unmetamorphosed samples were collected in the same stratigraphic position as ML6, 118, 119, 152, 153, 161 but in a different area of the Adamello pluton thermal aureole.

Table A4

No.	SiO2	TiO2	Al2O3	FeO	MnO	MgO	CaO	Na2O	K2O	Total	#Mg	Ti apfu		
1	36.5	2.94	17.9	19.0	0.46	9.8	0.00	0.11	9.79	96.5	34.1	0.3	Banded metapelites	
2	35.8	3.06	17.0	19.1	0.43	10.0	0.05	0.11	9.67	95.2	34.4	0.4		
3	36.6	2.96	18.1	18.9	0.50	9.8	0.00	0.10	9.63	96.6	34.2	0.3		
4	36.8	2.85	17.9	18.8	0.45	10.0	0.01	0.10	9.87	96.8	34.7	0.3		
5	36.3	2.64	18.7	18.7	0.47	9.7	0.02	0.12	9.71	96.3	34.1	0.3		
6	35.9	2.90	18.0	19.3	0.47	9.7	0.00	0.18	9.71	96.2	33.4	0.3		
7	36.2	3.02	17.6	17.8	0.44	9.2	0.07	0.14	9.39	93.8	34.1	0.3		
8	35.6	2.46	16.7	18.4	0.46	10.1	0.01	0.15	9.38	93.2	35.5	0.3		
9	36.2	3.21	16.9	18.8	0.40	9.8	0.00	0.14	9.33	94.7	34.3	0.4		
10	35.0	2.99	18.7	19.3	0.43	9.1	0.03	0.11	9.65	95.4	31.9	0.3		
11	35.7	3.01	19.1	19.4	0.39	9.5	0.03	0.16	9.73	97.1	33.0	0.3		
12	35.2	2.94	19.4	18.8	0.39	9.5	0.04	0.18	9.55	96.0	33.7	0.3		
13	35.6	2.98	18.9	19.1	0.36	9.6	0.01	0.13	9.66	96.3	33.4	0.3		
14	35.5	2.86	18.9	18.8	0.46	9.8	0.02	0.15	9.71	96.1	34.3	0.3		
15	35.6	2.79	18.7	18.7	0.34	9.7	0.00	0.17	9.8	95.9	34.2	0.3		
16	38.8	0.38	18.1	14.3	0.18	14.8	0.00	0.07	9.89	96.6	50.8	0.0	Orbicular metapelites	
17	40.0	1.63	15.3	14.2	0.12	14.9	0.00	0.00	10.06	96.4	51.2	0.2		
18	38.6	1.24	17.6	14.8	0.19	15.0	0.00	0.08	9.63	97.2	50.3	0.1		
19	39.2	0.94	18.2	14.3	0.22	14.0	0.00	0.17	9.57	96.5	49.5	0.1		
20	35.7	2.42	19.0	17.5	0.23	11.0	0.01	0.19	9.59	95.7	38.6	0.3		
21	36.3	2.53	19.5	16.8	0.20	10.8	0.02	0.18	9.69	96.1	39.2	0.3		
22	36.0	2.62	19.3	17.2	0.23	10.3	0.00	0.11	9.67	95.6	37.4	0.3		
23	36.6	2.61	19.2	17.8	0.19	10.7	0.01	0.13	9.46	96.9	37.4	0.3		
24	36.8	2.63	19.1	17.6	0.20	10.8	0.04	0.19	9.43	97.0	38.0	0.3		
25	35.6	2.82	18.7	18.6	0.18	10.2	0.05	0.13	9.5	95.9	35.5	0.3		
26	36.3	2.73	19.5	18.2	0.11	9.9	0.07	0.13	9.35	96.4	35.3	0.3		
27	37.0	2.70	19.8	18.2	0.12	10.0	0.02	0.11	9.61	97.7	35.5	0.3		

28	35.0	2.98	18.6	18.1	0.12	10.5	0.04	0.12	9.59	95.1	36.8	0.3	
29	35.3	3.09	18.8	18.1	0.17	10.5	0.05	0.17	9.57	95.7	36.8	0.4	
30	36.6	2.77	19.5	17.9	0.17	10.7	0.01	0.15	9.55	97.4	37.3	0.3	
31	35.8	2.78	18.9	17.8	0.19	10.5	0.08	0.16	9.3	95.6	37.0	0.3	
32	36.4	2.90	19.4	18.3	0.09	10.4	0.04	0.10	9.45	97.1	36.3	0.3	
33	35.9	3.26	17.6	18.3	0.19	9.4	0.02	0.17	9.42	94.2	33.9	0.4	
34	37.0	2.35	18.7	17.2	0.09	11.7	0.03	0.14	9.66	96.9	40.5	0.3	
35	36.5	3.08	18.6	17.8	0.13	10.2	0.00	0.13	9.82	96.3	36.4	0.3	
36	36.8	2.57	19.4	17.0	0.10	11.0	0.03	0.17	9.63	96.6	39.3	0.3	
37	36.5	2.70	18.8	17.9	0.13	10.5	0.01	0.16	9.63	96.4	36.9	0.3	
38	36.3	2.88	18.4	17.7	0.15	10.7	0.05	0.10	9.6	95.9	37.6	0.3	
39	36.3	2.71	17.8	17.1	0.11	11.8	0.01	0.08	9.52	95.4	40.8	0.3	
40	36.6	2.54	18.9	17.0	0.11	12.0	0.00	0.12	9.37	96.6	41.3	0.3	
41	37.3	2.48	19.2	17.3	0.11	11.6	0.00	0.18	9.39	97.4	40.2	0.3	
42	37.2	2.91	17.9	16.7	0.49	11.4	0.01	0.16	9.77	97.3	40.6	0.3	
43	37.4	2.49	18.6	16.7	0.42	11.6	0.04	0.24	9.7	97.9	41.1	0.3	
44	37.9	2.66	19.0	16.1	0.47	12.0	0.03	0.17	9.78	98.9	42.7	0.3	
45	37.6	2.50	18.6	15.8	0.38	11.8	0.01	0.19	9.83	97.3	42.7	0.3	
46	36.8	2.66	18.3	14.9	0.29	12.6	0.02	0.13	9.96	96.3	45.9	0.3	
47	37.8	2.39	18.5	14.7	0.38	13.5	0.01	0.11	10.03	98.2	47.8	0.3	
48	37.7	2.26	19.0	14.4	0.39	13.4	0.02	0.15	9.96	98.0	48.1	0.2	
49	37.7	2.54	19.0	13.3	0.48	13.6	0.08	0.12	9.68	97.2	50.7	0.3	
50	38.0	2.26	19.7	13.4	0.49	13.6	0.01	0.11	9.84	98.4	50.4	0.2	
51	37.2	2.00	18.9	11.9	0.39	14.2	0.05	0.19	9.64	95.4	54.5	0.2	
52	33.9		19.6	15.3	0.45	11.7	0.05	0.17	9.51	91.5	43.3		
53	33.4		18.7	15.4	0.45	12.2	0.03	0.22	9.74	90.8	44.1		
54	34.2		18.9	15.7	0.49	11.3	0.01	0.17	9.92	91.4	41.7		
55	37.1		19.4	16.1	0.47	11.6	0.04	0.16	9.76	95.3	41.9		
56	37.5	2.84	18.1	15.8	0.19	12.1	0.00	0.07	9.83	96.3	43.2	0.3	
57	37.4	2.56	18.4	16.2	0.25	11.8	0.03	0.13	9.84	96.6	42.2	0.3	
58	36.7	2.73	17.9	16.1	0.19	11.8	0.03	0.07	9.85	95.4	42.3	0.3	

59	36.1	2.73	17.7	16.0	0.14	12.4	0.01	0.06	9.79	94.8	43.6	0.3	Spotted and foliated metapelites
60	36.9	2.28	18.3	15.7	0.21	12.8	0.00	0.14	9.64	96.0	44.9	0.3	
61	36.1	2.86	17.9	16.4	0.22	11.8	0.01	0.06	9.79	95.0	41.9	0.3	
62	36.3	2.80	18.2	16.4	0.16	11.5	0.03	0.04	9.82	95.2	41.1	0.3	
63	36.6	2.64	18.2	16.4	0.26	11.9	0.00	0.06	9.82	96.0	41.9	0.3	
64	37.1	2.84	18.4	16.8	0.20	11.7	0.02	0.11	9.76	97.0	40.9	0.3	
65	37.0	2.66	18.1	17.2	0.17	11.6	0.00	0.10	9.57	96.4	40.2	0.3	
66	36.6	3.11	17.9	18.3	0.18	10.4	0.05	0.06	9.67	96.3	36.2	0.4	
67	36.6	2.90	17.8	17.4	0.21	10.5	0.00	0.07	9.77	95.3	37.6	0.3	
68	36.5	3.01	17.4	17.1	0.21	11.3	0.00	0.11	9.69	95.3	39.8	0.3	
69	36.7	3.06	18.0	17.6	0.17	10.4	0.01	0.07	9.74	95.7	37.1	0.3	
70	36.7	2.02	18.2	15.9	0.16	12.4	0.00	0.09	9.78	95.3	43.9	0.2	
71	38.5	2.76	19.3	15.4	0.78	12.5	0.02	0.08	9.7	99.0	44.9	0.3	
72	37.2	1.66	18.7	14.3	0.75	13.4	0.04	0.05	9.65	95.8	48.4	0.2	
73	37.2	1.61	18.9	14.1	0.69	13.6	0.08	0.10	9.83	96.1	49.1	0.2	
74	37.4	1.16	18.9	13.7	0.69	13.8	0.00	0.10	9.93	95.6	50.2	0.1	
75	37.1	2.62	17.7	15.6	0.71	12.7	0.00	0.10	9.71	96.1	44.9	0.3	
76	36.7	3.01	17.7	15.8	0.73	12.1	0.01	0.10	9.98	96.2	43.3	0.3	
77	36.8	2.76	18.2	15.5	0.76	12.2	0.04	0.09	9.97	96.3	44.1	0.3	

Table 4) Biotite major elements composition (EMPA analyses).

Table A5

No.	SiO2	Al2O3	FeO	MnO	MgO	CaO	Na2O	Total	Mg#		
1	49.5	32.4	6.98	0.35	9.02	0.01	0.27	98.5	56.4		
2	49.0	32.7	7.24	0.32	8.97	0.02	0.26	98.6	55.3		
3	48.9	31.8	7.02	0.32	9.07	0.03	0.31	97.5	56.4	Orbicular metapelites	
4	49.4	33.3	6.84	0.28	9.20	0.01	0.33	99.3	57.3		
5	49.0	32.8	7.02	0.33	8.95	0.02	0.32	98.4	56.0		
6	49.5	33.2	7.00	0.33	9.05	0.03	0.29	99.4	56.4		
7	49.5	32.8	7.13	0.28	8.79	0.01	0.28	98.8	55.2		
8	49.8	32.9	6.81	0.30	9.12	0.01	0.23	99.2	57.2		
9	49.1	32.9	6.76	0.33	8.76	0.02	0.61	98.5	56.4		
10	49.4	33.3	6.97	0.33	9.07	0.03	0.28	99.3	56.5		
11	49.1	33.2	7.07	0.37	8.95	0.02	0.31	99.0	55.9	Table 5) Cordierite major	
12	49.2	32.2	7.19	0.34	8.86	0.00	0.31	98.2	55.2		
13	49.6	32.4	6.69	0.36	9.32	0.00	0.27	98.6	58.2	elements composition	
14	49.6	32.6	6.95	0.29	9.00	0.04	0.26	98.8	56.4		
15	48.6	33.2	6.72	0.54	8.54	0.06	0.54	98.3	55.9	(EMPA analyses).	
16	48.2	33.1	6.57	0.47	8.75	0.05	0.50	97.7	57.1		
17	49.1	33.4	6.62	0.53	8.62	0.02	0.40	98.8	56.5		
18	48.6	33.1	6.52	0.56	9.06	0.04	0.42	98.4	58.1		
19	49.0	33.2	7.55	0.40	8.19	0.04	0.46	98.8	52.0		
20	49.0	32.9	7.21	0.48	7.85	0.04	0.46	98.0	52.1		
21	49.0	33.3	7.26	0.47	8.33	0.00	0.43	98.8	53.4		
22	48.9	33.0	7.40	0.46	8.03	0.00	0.31	98.1	52.0		
23	48.3	33.3	7.47	0.49	8.15	0.01	0.50	98.2	52.1		
24	48.5	33.4	7.62	0.48	8.31	0.03	0.39	98.7	52.1		
25	48.9	33.6	7.49	0.53	8.46	0.02	0.36	99.3	53.0		
26	48.6	33.3	7.30	0.42	8.26	0.03	0.44	98.4	53.1		
27	49.1	33.2	7.46	0.39	8.83	0.02	0.25	99.3	54.2		
28	49.1	33.5	7.71	0.35	8.72	0.02	0.26	99.7	53.1		
29	48.9	33.5	7.36	0.40	8.83	0.00	0.22	99.2	54.5		
30	49.1	33.6	7.40	0.36	8.80	0.03	0.32	99.7	54.3		

31	48.8	34.0	7.11	0.41	8.78	0.02	0.26	99.5	55.2	
32	49.0	33.7	7.11	0.36	8.79	0.04	0.33	99.4	55.3	
33	48.9	34.0	6.44	0.29	9.11	0.03	0.29	99.1	58.6	
34	49.0	33.9	7.08	0.37	8.95	0.02	0.26	99.6	55.8	
35	48.7	33.9	6.63	0.38	9.06	0.01	0.27	99.0	57.7	
36	48.5	33.8	6.86	0.34	8.96	0.02	0.26	98.7	56.6	
37	48.9	34.1	6.98	0.44	8.98	0.02	0.29	99.7	56.2	
38	49.3	33.7	6.94	0.44	8.87	0.02	0.31	99.6	56.1	
39	49.2	34.0	6.83	0.47	9.00	0.02	0.24	99.7	56.8	
40	48.9	34.1	6.98	0.44	8.19	0.06	0.22	98.9	53.9	
41	49.1	33.8	7.05	0.40	8.97	0.00	0.28	99.6	55.9	
42	49.0	34.2	6.82	0.39	9.08	0.04	0.27	99.8	57.1	
43	48.8	33.8	7.07	0.34	8.78	0.00	0.26	99.1	55.3	
44	48.9	33.9	6.02	0.26	9.31	0.00	0.55	98.9	60.7	
45	48.8	34.1	6.05	0.25	9.41	0.02	0.49	99.1	60.8	
46	49.2	33.8	5.77	0.28	9.29	0.02	0.42	98.8	61.6	
47	49.7	34.0	6.02	0.19	9.33	0.01	0.43	99.7	60.7	
48	49.2	33.6	7.39	0.08	8.49	0.03	0.48	99.3	53.4	
49	49.1	34.0	7.45	0.12	8.76	0.02	0.39	99.8	54.0	
50	48.7	33.6	7.24	0.14	8.80	0.03	0.48	99.0	54.8	
51	48.9	33.6	7.27	0.15	8.78	0.03	0.36	99.1	54.7	
52	49.1	34.0	6.34	0.22	9.51	0.01	0.40	99.6	60.0	
53	49.4	34.0	5.62	0.24	9.62	0.00	0.43	99.3	63.1	
54	49.5	33.8	6.35	0.18	9.21	0.01	0.44	99.5	59.1	
55	49.1	33.5	6.10	0.22	9.39	0.02	0.41	98.7	60.6	
56	49.8	34.0	5.91	0.21	9.68	0.00	0.50	100.1	62.0	
57	49.2	33.6	7.40	0.12	8.79	0.01	0.39	99.5	54.2	
58	49.3	33.8	7.02	0.13	9.11	0.00	0.38	99.8	56.4	

Table A6

0.3 Gpa, vol %	Quartz	Plagioclase	K-feldspar	Biotite	Sillimanite	Cordierite	Melt
Fluid limited 690°C	29	7	39	13	6	4	1
Fluid limited 700°C	25	7	42	8	4	11	2
Fluid assisted 690°C	22	6	28	13	6	2	21
Fluid assisted 700°C	19	5	30	9	3	9	23
Extracted fluid assisted mean	26	6	37	15	6	8	
Fluid rich 690°C	14	4	15	12	6	1	41
Extracted fluid rich 690°C	28	6	32	22	10		35

Table 6) Mineral and melt modal abundances from phase equilibria modelling.

Table A7

Melt composition									
	Al_2O_3	CaO	FeO	K_2O	MgO	Na_2O	SiO_2	H_2O	A/CNK
Fluid assisted	13.07	0.30	0.08	5.75	0.01	2.60	71.91	6.28	1.51
	13.95	0.32	0.08	6.14	0.01	2.78	76.73	0.00	
	Al_2O_3	CaO	FeO	K_2O	MgO	Na_2O	SiO_2	H_2O	A/CNK
Fluid rich	12.97	0.31	0.06	5.81	0.01	2.51	71.85	6.45	1.50
	13.87	0.33	0.06	6.22	0.01	2.68	76.83	0.00	

Table 7) Predicted melt compositions at 3 kbar and 690°C.

Additional figure A1: SEM images

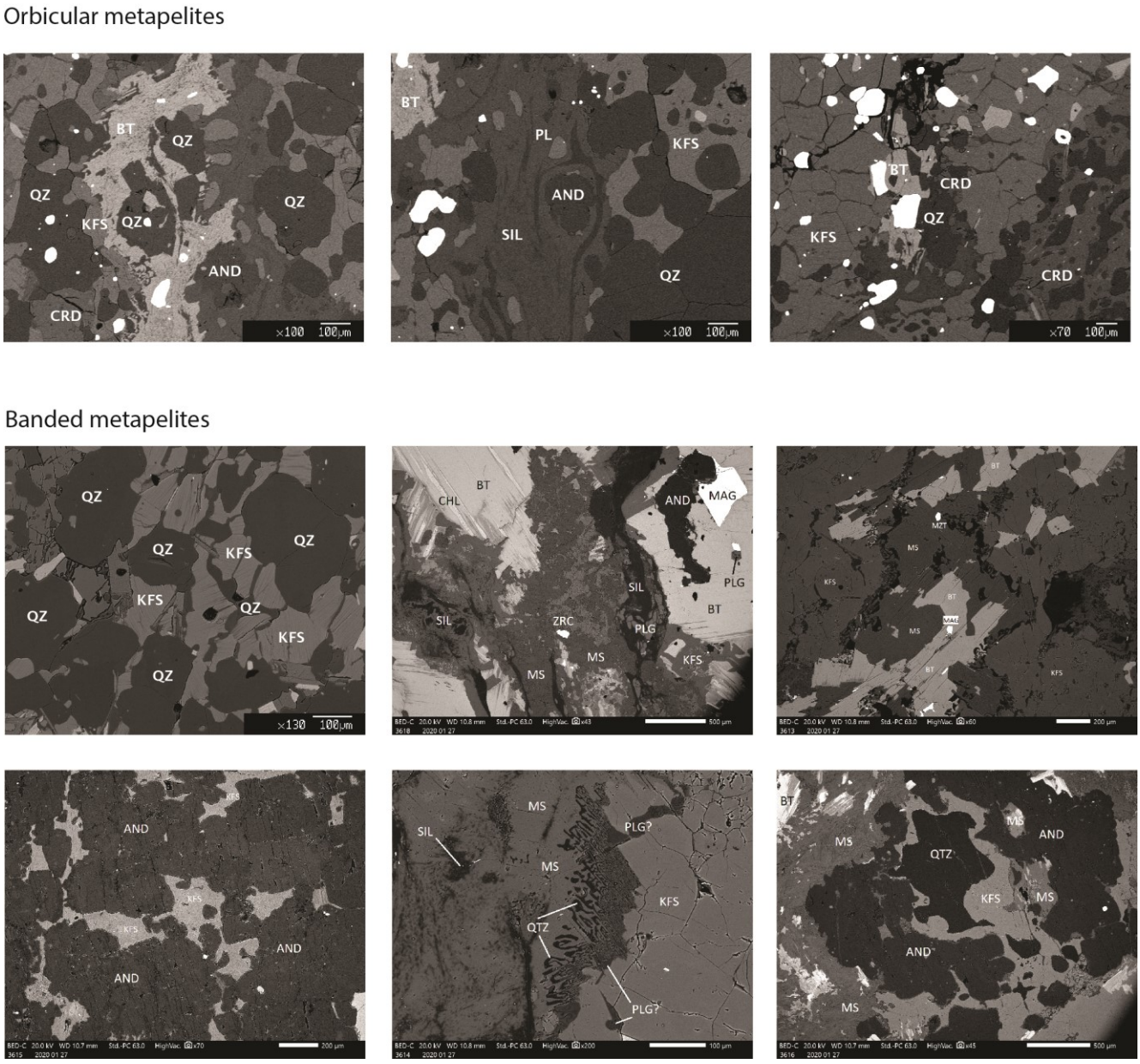

Figure A1 – SEM images of orbicular and banded metatexites not present in the published article.

Appendix B: Whole rock chemistry, Sr-Nd isotopes, Bt-Crd traces

Table B1

		Low grade metapelite		High grade metapelite		Crd-absent migmatites				Crd-bearing migmatites				Kfs-rich leucosomes	
		ML161	SD	ML153	SD	ML6	SD	ML6B	SD	ML118	SD	ML119	SD	ML6L	SD
SiO2	wt%	66.1	0.2	63.8	0.3	56.0	0.4	54.5	0.4	63.7	0.4	60.2	0.2	66.65	0.47
TiO2	wt%	0.8	0.0	0.9	0.0	0.7	0.0	0.7	0.0	0.7	0.0	0.8	0.0	0.14	0.0
Al2O3	wt%	16.9	0.1	20.2	0.3	25.5	0.3	25.8	0.2	19.1	0.3	21.3	0.2	17.11	0.43
Fe2O3t	wt%	4.7	0.1	3.5	0.1	4.1	0.1	4.2	0.0	4.9	0.1	4.9	0.1	0.77	0.0
MnO	wt%	0.0	0.0	0.0	0.0	0.1	0.0	0.1	0.0	0.1	0.0	0.1	0.0	0.02	0.0
MgO	wt%	1.3	0.0	2.0	0.0	1.8	0.1	1.7	0.0	3.0	0.0	3.0	0.0	0.35	0.01
CaO	wt%	0.5	0.0	0.4	0.0	0.8	0.0	0.7	0.0	0.6	0.0	0.4	0.0	0.26	0.01
Na2O	wt%	1.5	0.0	2.1	0.0	0.8	0.0	0.9	0.2	1.4	0.0	1.2	0.0	1.31	0.02
K2O	wt%	6.1	0.1	5.4	0.0	8.6	0.1	10.2	0.0	5.4	0.1	6.3	0.0	12.73	0.18
P2O5	wt%	0.1	0.0	0.0	0.0	0.1	0.0	0.1	0.0	0.1	0.0	0.1	0.0	0.09	0.00
Li	ppm	63.9	1.7	109.4	1.1	96.5	2.3	97.0	2.0	110.8	1.4	107.3	1.7	26.9	0.26
Be	ppm	4.7	0.1	6.2	0.3	2.7	0.1	2.9	0.1	7.7	0.4	6.7	0.2	0.3	0.06
B	ppm	183.8	8.3	50.6	1.3	89.4	1.4	90.2	1.4	60.5	1.3	99.0	2.8	25.5	0.58
Sc	ppm	18.4	0.3	15.9	0.5	20.6	0.2	18.1	0.4	18.7	0.5	22.9	0.5	7.9	0.1
V	ppm	82.8	1.4	76.2	3.7	89.4	0.7	79.5	0.5	58.4	1.6	69.0	1.9	16.6	0.4
Cr	ppm	55.0	1.5	37.1	1.5	43.6	0.7	48.0	1.3	50.5	1.3	55.6	3.3	3.5	0.4
Co	ppm	6.8	0.2	8.7	0.1	10.5	0.3	75.8	1.2	6.7	0.2	6.7	0.2	2.1	0.1
Ni	ppm	19.8	0.6	15.0	0.4	18.3	0.5	23.9	0.1	15.4	0.4	17.9	1.3	3.5	0.2
Cu	ppm	1.2	0.1	1.3	0.1	1.1	0.1	5.6	0.1	1.0	0.1	1.0	0.1	1.3	0.2
Zn	ppm	38.3	1.9	28.5	1.7	40.0	1.6	39.8	0.2	33.5	1.7	33.4	2.1	15.3	0.8
Ga	ppm	18.6	0.7	16.6	0.3	25.5	0.5	24.2	0.6	21.7	0.5	21.6	0.3	11.2	0.3
Ge	ppm	2.0	0.1	2.4	0.1	2.8	0.1	2.1	0.2	2.0	0.1	2.1	0.1	2.9	0.2
Rb	ppm	245.8	4.4	187.0	1.9	384.7	8.8	368.0	7.6	262.2	7.8	281.0	4.5	517.7	7.1
Sr	ppm	64.8	1.7	149.5	4.5	200.8	4.8	210.0	3.2	114.0	3.9	131.5	2.8	342.1	10.9
Y	ppm	33.7	5.8	61.9	4.6	58.7	4.4	54.7	1.7	39.2	5.6	41.8	8.2	22.7	2.4
Zr	ppm	312.8	26.2	431.8	32.4	767.5	13.5	667.6	7.7	199.1	14.3	191.6	12.9	18.3	1.6
Nb	ppm	19.4	0.5	26.0	0.5	18.9	0.3	17.1	0.7	20.8	0.8	21.8	0.6	4.6	0.2
Mo	ppm	0.2	0.0	0.1	0.0	0.2	0.0	0.4	0.1	0.1	0.0	0.1	0.0	0.1	0.0
Cd	ppm	0.0	0.0	BDL	BDL	0.1	0.0	BDL	BDL	0.0	0.0	BDL		0.1	
In	ppm	0.1	0.0	0.1	0.0	0.1	0.0	BDL	BDL	0.1	0.0	0.1	0.0	0.0	0.0
Sn	ppm	5.3	0.2	5.4	0.3	5.3	0.1	BDL	BDL	5.9	0.2	6.7	0.2	1.2	0.1
Sb	ppm													0.3	0.0
Cs	ppm	19.8	0.6	23.9	0.3	55.0	1.2	47.6	1.1	27.3	0.7	26.6	0.5	32.3	0.5
Ba	ppm	400.8	10.7	565.0	10.4	1510.9	18.8	1669.5	4.9	938.8	18.8	1026.5	19.0	2025.8	59.4
La	ppm	37.3	3.3	50.1	2.9	66.3	5.7	64.5	0.8	47.1	3.2	43.3	1.4	11.1	1.6
Ce	ppm	75.8	6.4	106.8	5.3	137.0	12.0	125.7	1.1	101.8	6.4	89.5	2.3	25.2	3.6
Pr	ppm	9.0	1.0	12.1	0.7	16.8	1.5	14.9	0.5	10.9	0.7	9.8	0.2	2.8	0.4
Nd	ppm	31.6	3.0	46.6	2.6	60.1	5.0	60.8	1.5	39.4	3.0	35.8	1.0	9.8	2.1
Sm	ppm	6.3	0.5	10.2	0.5	12.3	0.9	12.2	0.3	7.9	0.6	7.3	0.2	2.5	0.5
Eu	ppm	1.0	0.1	1.7	0.1	1.9	0.1	1.8	0.1	1.1	0.1	1.2	0.0	1.1	0.0
Gd	ppm	5.7	0.5	9.8	0.5	10.9	1.3	10.3	0.5	7.1	0.7	6.9	0.3	2.7	0.5
Tb	ppm	0.9	0.1	1.6	0.1	1.7	0.2	1.5	0.0	1.1	0.1	1.1	0.1	0.5	0.1
Dy	ppm	6.0	0.9	10.2	0.6	10.9	1.0	10.3	0.2	7.1	0.9	7.2	1.0	3.6	0.5
Ho	ppm	1.2	0.2	2.1	0.1	2.2	0.2	2.0	0.0	1.4	0.2	1.5	0.2	0.7	0.1
Er	ppm	3.7	0.6	6.2	0.5	6.4	0.5	6.0	0.3	4.3	0.7	4.3	0.8	2.2	0.4
Tm	ppm	0.6	0.1	0.9	0.1	1.0	0.1	0.9	0.0	0.6	0.1	0.7	0.1	0.4	0.0
Yb	ppm	3.6	0.5	5.7	0.4	6.5	0.6	6.4	0.3	3.7	0.4	4.1	1.0	2.5	0.4
Lu	ppm	0.5	0.1	0.8	0.1	0.9	0.1	1.0	0.0	0.5	0.1	0.6	0.1	0.3	0.0
Hf	ppm	8.7	0.6	11.3	0.8	20.2	0.7	17.8	0.0	6.1	0.4	5.8	0.4	0.4	0.0
Ta	ppm	1.5	0.0	2.6	0.1	2.1	0.0	1.8	0.0	1.4	0.1	1.5	0.1	0.6	0.0
W	ppm	9.5	0.7	3.9	0.2	1.7	0.1	3.0	0.1	2.6	0.2	2.2	0.2	0.3	0.0
Pb	ppm	15.8	0.5	11.9	0.2	14.2	0.4	15.1	0.2	11.4	0.3	13.4	0.3	32.1	0.4
Th	ppm	13.4	0.9	18.8	1.2	27.0	3.6	25.9	0.5	18.1	1.3	17.5	0.4	4.7	1.2
U	ppm	3.4	0.3	3.0	0.3	5.8	0.9	5.9	0.2	3.3	0.3	3.4	0.4	2.8	0.7

Table B1) Whole rock chemical analyses.

		Unfractionated leucosomes		LCT pegmatites zonations															
		ML168L	SD	ML121A	SD	ML121B	SD	ML121C	SD	ML121D	SD	ML121E	SD	ML121F	SD	ML121G	SD	LCT mean comp	SD
SiO2	wt%	71.97	0.32	73.7	0.3	73.5	0.2	74.0	0.3	75.0	0.3	74.1	0.4	80.3	0.3	84.9	0.2	443.7	60.0
TiO2	wt%	0.13	0.0	0.1	0.0	0.2	0.0	0.0	0.0	0.0	0.0	0.0	0.0	0.0	0.0	0.1	0.0	4.3	0.7
Al2O3	wt%	15.79	0.34	15.1	0.2	15.5	0.1	14.9	0.2	15.0	0.2	15.6	0.2	11.3	0.2	8.8	0.2	947.1	118.8
Fe2O3t	wt%	0.74	0.0	0.6	0.0	1.1	0.0	0.4	0.0	0.6	0.0	0.2	0.0	0.2	0.0	1.9	0.0	4.1	0.5
MnO	wt%	0.01	0.0	0.0	0.0	0.1	0.0	0.0	0.0	0.0	0.0	0.3	0.0	0.1	0.0	0.1	0.0	0.2	0.0
MgO	wt%	0.60	0.00	0.1	0.0	0.4	0.0	0.1	0.0	0.3	0.0	0.0	0.0	0.0	0.0	0.5	0.0	13.6	1.5
CaO	wt%	0.87	0.02	0.5	0.0	0.5	0.0	1.6	0.0	2.3	0.1	1.0	0.0	0.8	0.0	0.2	0.0	76.9	8.0
Na2O	wt%	2.88	0.03	1.6	0.0	1.4	0.0	3.4	0.1	3.5	0.1	7.0	0.1	3.7	0.1	1.1	0.0	0.1	0.0
K2O	wt%	5.82	0.06	6.5	0.1	4.9	0.1	4.2	0.1	2.0	0.0	0.9	0.0	1.9	0.1	0.8	0.0	2.0	0.2
P2O5	wt%	0.10	0.01	0.1	0.0	0.1	0.0	0.1	0.0	0.1	0.0	0.1	0.0	0.1	0.0	0.1	0.0	1.3	0.2
Li	ppm	26.4	0.32	292.9	4.7	446.8	8.9	177.8	4.7	152.3	3.2	154.7	4.6	1153.9	45.1	46.2	1.2	8.3	1.2
Be	ppm	1.3	0.11	1.4	0.1	1.9	0.2	3.2	0.2	2.3	0.2	8.0	0.4	4.5	0.3	3.5	0.2	0.0	0.0
B	ppm	625.9	10.54	154.8	6.8	1368.0	25.5	621.4	13.2	1537.7	38.0	333.9	15.6	269.6	13.5	3807.2	57.4	2.8	0.4
Sc	ppm	9.7	0.2	11.7	0.4	20.1	0.5	10.7	0.2	10.2	0.3	5.8	0.3	7.6	0.4	5.1	0.2	0.8	0.2
V	ppm	14.8	0.1	11.6	0.2	22.4	0.8	5.2	0.1	3.3	0.2	0.4	0.0	0.7	0.1	5.3	0.2	0.1	0.0
Cr	ppm	6.4	0.6	1.1	0.3	1.0	0.2	0.8	0.0	0.6	0.1	0.8	0.2	0.6	0.1	2.4	0.5	0.5	0.1
Co	ppm	1.7	0.1	0.4	0.0	2.3	0.0	0.7	0.0	1.2	0.1	0.1	0.0	0.1	0.0	2.5	0.1	0.7	0.1
Ni	ppm	2.8	0.2	0.7	0.1	1.9	0.1	0.5	0.1	0.4	0.0	0.3	0.0	0.4	0.1	1.8	0.2	0.5	0.1
Cu	ppm	1.6	0.2	1.1	0.1	0.4	0.1	1.1	0.2	0.6	0.1	0.5	0.2	0.7	0.1	2.4	0.4	0.8	0.2
Zn	ppm	18.1	1.5	20.5	0.4	38.0	3.4	17.4	0.7	19.5	0.6	21.3	1.5	27.0	1.5	88.0	1.6	27.4	3.9
Ga	ppm	14.4	0.6	17.2	0.5	18.5	0.5	15.3	0.4	14.2	0.5	16.5	0.3	16.6	0.5	15.4	0.3	15.8	2.0
Ge	ppm	2.8	0.2	3.1	0.1	2.9	0.2	3.9	0.2	2.6	0.2	7.0	0.4	6.2	0.4	4.2	0.3	4.9	0.8
Rb	ppm	252.6	2.1	566.8	10.4	440.0	10.4	448.6	12.7	160.6	3.6	139.7	3.0	445.9	16.7	102.6	3.7	275.2	35.7
Sr	ppm	168.3	4.5	44.3	0.9	38.2	0.4	57.9	1.6	55.0	1.5	8.0	0.3	11.2	0.3	27.2	1.5	29.2	3.8
Y	ppm	26.3	3.6	32.6	4.2	40.8	5.1	17.8	1.9	51.9	4.0	12.2	0.6	11.2	3.7	18.5	1.1	25.4	5.4
Zr	ppm	97.4	6.1	23.2	2.3	15.7	2.5	14.4	1.9	45.2	2.3	22.0	7.5	33.1	9.9	41.7	8.8	32.7	9.4
Nb	ppm	13.0	0.5	21.6	0.8	33.1	1.3	11.8	0.9	4.5	0.1	22.0	2.5	30.2	2.5	25.8	2.0	19.1	3.5
Mo	ppm	0.1	0.0	0.1	0.0	0.1	0.0	0.1	0.0	0.1	0.0	0.1	0.0	0.1	0.0	0.2	0.0	0.1	0.0
Cd	ppm	BDL		0.0	0.0	bdl		0.1	0.0	0.1	0.0	0.1	0.0	0.1	0.0	0.1	0.0		
In	ppm	0.0	0.0	0.0	0.0	0.1	0.0	0.0	0.0	0.0	0.0	bdl		0.0	0.0	0.0	0.0		
Sn	ppm	2.1	0.1	1.0	0.1	2.8	0.1	0.9	0.1	0.5	0.1	0.2	0.1	0.3	0.0	0.4	0.1	0.5	0.1
Sb	ppm	0.3	0.0	1.7	0.2	2.7	0.3	3.1	0.6	3.5	0.6	7.4	0.5	13.9	2.4	0.5	0.1	7.0	1.7
Cs	ppm	22.8	0.3	80.1	2.0	100.7	2.6	85.8	2.9	39.2	1.1	52.4	1.4	439.9	11.4	23.1	1.1	161.4	20.5
Ba	ppm	1076.1	23.7	210.1	4.3	161.4	2.8	101.3	3.4	14.9	0.3	2.6	0.1	4.7	0.2	9.4	0.3	25.0	3.2
La	ppm	16.6	1.4	24.7	1.8	24.5	2.2	5.8	0.6	11.9	1.1	2.5	0.2	3.6	0.6	52.2	5.0	10.7	2.1
Ce	ppm	36.1	3.0	52.7	3.8	52.0	4.3	12.3	1.5	24.7	2.4	5.5	0.4	8.0	1.3	122.8	8.9	23.5	4.5
Pr	ppm	4.1	0.4	6.3	0.6	6.1	0.6	1.5	0.2	3.0	0.3	0.7	0.0	1.0	0.2	13.5	1.0	2.8	0.5
Nd	ppm	14.3	1.3	23.4	2.6	21.9	2.0	5.5	0.6	11.1	0.9	2.2	0.3	3.6	0.6	46.1	4.2	9.8	2.0
Sm	ppm	3.1	0.3	5.6	0.6	5.5	0.5	1.8	0.1	3.7	0.2	1.1	0.1	1.4	0.2	10.6	0.8	2.9	0.5
Eu	ppm	0.5	0.0	0.7	0.1	0.6	0.0	0.4	0.0	0.5	0.0	0.0	0.0	0.1	0.0	0.6	0.0	0.3	0.0
Gd	ppm	3.0	0.2	5.4	0.5	5.6	0.5	2.1	0.2	5.1	0.4	1.1	0.1	1.5	0.4	6.1	0.4	3.1	0.6
Tb	ppm	0.6	0.0	0.9	0.1	1.0	0.1	0.4	0.0	1.1	0.1	0.3	0.0	0.3	0.1	0.9	0.0	0.6	0.1
Dy	ppm	4.1	0.1	6.1	0.8	6.8	0.8	2.9	0.3	8.2	0.8	2.0	0.2	1.9	0.6	4.1	0.1	4.2	0.9
Ho	ppm	0.9	0.0	1.2	0.1	1.3	0.2	0.5	0.0	1.6	0.1	0.3	0.0	0.3	0.1	0.7	0.0	0.8	0.2
Er	ppm	2.9	0.2	3.3	0.3	4.0	0.6	1.6	0.1	5.2	0.4	1.0	0.1	1.0	0.4	1.7	0.1	2.4	0.5
Tm	ppm	0.5	0.0	0.5	0.0	0.7	0.1	0.3	0.0	0.9	0.1	0.2	0.0	0.2	0.1	0.3	0.0	0.4	0.1
Yb	ppm	3.4	0.4	3.4	0.3	4.5	0.7	1.8	0.2	6.3	0.6	2.2	0.2	1.5	0.6	1.9	0.2	3.2	0.8
Lu	ppm	0.5	0.1	0.5	0.0	0.6	0.1	0.3	0.0	0.9	0.1	0.3	0.0	0.2	0.1	0.3	0.0	0.5	0.1
Hf	ppm	2.6	0.2	0.8	0.1	0.8	0.1	0.7	0.2	1.4	0.1	1.4	0.4	1.8	0.3	2.6	0.8	1.5	0.4
Ta	ppm	1.7	0.1	2.7	0.2	4.4	0.4	1.6	0.1	0.6	0.1	5.8	0.8	5.8	0.6	4.0	0.4	3.7	0.8
W	ppm	3.5	0.1	9.3	0.1	14.3	0.3	3.7	0.1	2.1	0.2	2.3	0.1	9.5	1.5	2.8	0.2	4.9	1.0
Pb	ppm	15.6	0.6	8.3	0.3	5.6	0.1	8.5	0.4	5.8	0.1	3.3	0.1	4.1	0.2	11.2	0.3	5.4	0.7
Th	ppm	8.0	0.9	9.4	0.7	11.5	0.9	2.7	0.7	6.5	0.5	1.5	0.2	2.1	0.1	55.7	5.3	7.7	1.5
U	ppm	2.9	0.5	3.9	0.4	4.3	0.4	1.9	0.1	5.9	0.4	3.7	0.7	5.5	1.7	14.7	4.0	5.6	1.6

						Barren pegmatites		Adamello pluton	
		"external melt"	SD	"internal melt"	SD	ML169P	SD	ML12C	SD
SiO2	wt%	173.8	20.7	484.4	65.9	74.85	0.27	56.92	0.34
TiO2	wt%	2.6	0.4	4.6	0.7	0.05	0.0	0.77	0.0
Al2O3	wt%	2374.9	275.3	731.4	95.2	12.34	0.21	20.07	0.24
Fe2O3t	wt%	1.3	0.2	4.5	0.6	0.32	0.0	5.57	0.1
MnO	wt%	0.4	0.0	0.1	0.0	0.01	0.0	0.12	0.0
MgO	wt%	11.6	1.4	13.9	1.6	0.15	0.00	2.83	0.04
CaO	wt%	80.0	8.2	76.4	7.9	0.29	0.01	7.69	0.18
Na2O	wt%	0.1	0.0	0.1	0.0	2.73	0.07	2.65	0.02
K2O	wt%	3.1	0.4	1.9	0.2	8.48	0.15	1.42	0.02
P2O5	wt%	0.3	0.1	1.4	0.2	0.11	0.00	0.15	0.00
Li	ppm	9.1	1.2	8.2	1.2	18.0	0.37	25.9	0.43
Be	ppm	0.1	0.0	0.0	0.0	0.4	0.05	2.1	0.06
B	ppm	9.5	1.2	1.8	0.3	222.1	8.01	7.9	0.20
Sc	ppm	1.8	0.6	0.7	0.2	8.6	0.2	21.2	0.6
V	ppm	0.1	0.0	0.1	0.0	6.2	0.1	165.0	2.9
Cr	ppm	1.4	0.2	0.4	0.1	2.2	0.6	9.0	0.3
Co	ppm	1.9	0.2	0.5	0.1	0.4	0.0	13.3	0.2
Ni	ppm	1.5	0.3	0.4	0.1	1.0	0.1	5.0	0.1
Cu	ppm	1.8	0.5	0.6	0.2	0.7	0.1	6.6	0.2
Zn	ppm	60.9	7.6	22.3	3.4	16.3	1.2	68.1	2.4
Ga	ppm	16.4	2.0	15.7	2.0	17.8	0.6	16.5	0.2
Ge	ppm	3.7	0.6	5.0	0.8	3.8	0.2	1.9	0.1
Rb	ppm	288.2	35.4	273.2	35.8	403.3	4.6	58.9	1.8
Sr	ppm	33.9	4.6	28.5	3.6	49.8	0.7	407.6	9.7
Y	ppm	25.7	5.1	25.4	5.4	1.9	0.3	22.0	0.6
Zr	ppm	32.7	9.3	32.7	9.4	11.4	1.2	119.0	3.4
Nb	ppm	25.5	4.1	18.1	3.4	5.1	0.1	11.7	0.2
Mo	ppm	0.1	0.0	0.1	0.0	0.1	0.0	0.1	0.0
Cd	ppm					BDL		0.1	0.0
In	ppm					0.0	0.0	0.1	0.0
Sn	ppm	0.9	0.2	0.4	0.1	0.7	0.0	1.6	0.0
Sb	ppm	1.1	0.2	7.9	2.0	0.4	0.0		
Cs	ppm	50.6	6.7	178.2	22.5	37.3	0.5	2.3	0.1
Ba	ppm	90.4	10.9	15.2	2.0	222.9	3.6	407.9	9.3
La	ppm	40.2	7.7	6.2	1.3	0.7	0.0	34.9	1.8
Ce	ppm	92.2	15.9	13.1	2.7	1.4	0.0	60.8	2.4
Pr	ppm	10.3	1.9	1.6	0.3	0.1	0.0	7.0	0.2
Nd	ppm	36.0	7.0	5.8	1.2	0.4	0.0	24.5	0.5
Sm	ppm	8.4	1.5	2.1	0.4	0.1	0.0	4.7	0.1
Eu	ppm	0.6	0.1	0.2	0.0	0.1	0.0	1.2	0.1
Gd	ppm	5.8	1.0	2.6	0.6	0.2	0.0	3.9	0.1
Tb	ppm	0.9	0.2	0.6	0.1	0.0	0.0	0.6	0.0
Dy	ppm	5.1	0.9	4.1	0.9	0.3	0.1	3.8	0.1
Ho	ppm	0.9	0.2	0.8	0.2	0.1	0.0	0.8	0.0
Er	ppm	2.5	0.5	2.4	0.6	0.2	0.1	2.3	0.1
Tm	ppm	0.4	0.1	0.4	0.1	0.0	0.0	0.3	0.0
Yb	ppm	2.7	0.6	3.3	0.8	0.4	0.1	2.2	0.1
Lu	ppm	0.4	0.1	0.5	0.1	0.1	0.0	0.3	0.0
Hf	ppm	1.8	0.7	1.5	0.4	0.4	0.0	3.0	0.1
Ta	ppm	3.6	0.7	3.8	0.8	0.5	0.0	0.8	0.0
W	ppm	6.3	0.8	4.7	1.1	4.2	0.1	0.3	0.0
Pb	ppm	9.6	1.2	4.8	0.7	21.4	0.9	10.4	0.1
Th	ppm	35.8	6.9	3.4	0.7	0.2	0.0	10.5	0.6
U	ppm	10.1	3.4	4.9	1.4	0.9	0.1	1.7	0.3

Table B2

								Propagation	
Sample type	Rb (ppm)	Rb err (%)	Sr (ppm)	Sr err (%)	87/86Sr meas	87/86Sr iniz	2sigma	Min 87/86Sr iniz	Max 87/86Sr iniz
Crd-absent metatexites	384.7	2%	200.8	2%	.724344	0.721386	0.000015	0.721266	0.721502
Crd-bearing metatexites	281.0	2%	131.5	2%	.730395	0.727094	0.000007	0.726960	0.727224
Low grade metapelites	245.8	2%	64.8	3%	.739450	0.733586	0.000011	0.733283	0.733870
LCT pegmatites external	440.0	2%	38.2	1%	.744275	0.726459	0.000019	0.725919	0.726988
LCT pegmatites internal	445.9	2%	11.2	1%	.782562	0.720120	0.000017	0.717370	0.722355
Kfs-rich leucosomes (cumulates)	517.7	1%	342.1	3%	.725155	0.720497	0.000019	0.720401	0.720588
Barren pegmatites	403.3	1%	54.6	1%	.731277	0.719867	0.00001	0.719636	0.720092
Unfractionated leucosomes	252.6	1%	168.3	3%	.724452	0.722135	0.000013	0.722039	0.722225
Pluton pegmatite	236.6	2%	136.6	3%	.709384	0.706714	0.000012	0.706576	0.706844
Pluton pegmatite	121.7	1%	152.2	2%	.708481	0.707249	0.000011	0.707211	0.707285
Unmetamorphosed pelites	239.3	1%	45.0	3%	.745607	0.737381	0.000015	0.737041	0.737544

Table B2) Sr-Nd whole rock analyses

									Propagation	
Sample type	Sm (ppm)	Sm err (%)	Nd (ppm)	Nd err (%)	143/144Nd meas	143/144Nd iniz	2sigma	eNd	Min eNd	Max eNd
Crd-absent metatexites	12.3	7%	60.1	8%	0.512206824	0.51217578	3.24E-05	-8.06	-8.15	-7.97
Crd-bearing metatexites	7.3	3%	35.8	3%	0.512359757	0.51232893	1.38E-05	-5.07	-5.11	-5.03
Low grade metapelites	6.3	8%	31.6	9%	0.512565101	0.51253496	2.57E-05	-1.05	-1.15	-0.96
LCT pegmatites external	5.5	9%	21.9	9%	0.512274106	0.51223614	4.86E-05	-6.88	-7.03	-6.76
LCT pegmatites internal	1.4	17%	3.6	17%	0.512146593	0.51208781	1.62E-05	-9.77	-10.24	-9.44
Kfs-rich leucosomes (cumulates)	2.5	20%	9.8	21%	0.512079082	0.51204052	1.58E-04	-10.70	-11.07	-10.44
Barren pegmatites	0.1	8%	0.4	7%	0.513783714	0.51374591	8.84E-06	22.57	22.45	22.68
Unfractionated leucosomes	3.1	11%	14.3	9%	0.512212664	0.5121799	1.23E-04	-7.98	-8.14	-7.86
Pluton pegmatite	1.3	6%	3.6	3%	0.512469039	0.51241445	1.21E-05	-3.40	-3.51	-3.29
Pluton pegmatite	2.6	2%	13.9	6%	0.512452429	0.51242415	2.92E-05	-3.21	-3.23	-3.17
Unmetamorphosed pelites	8.6	5%	41.7	5%	0.512166783	0.51216678	1.51E-05	-9.19	-8.91	-8.78

Table B3.1

Table B3.1) Biotite trace elements compositions, in red near or below detection limits elements.

Element	Crd-absent migmatites					Low grade metapelites					Crd-bearing migmatites					
Li	527	525	551	522	499	371	409	415	446	447	171	162	175	173	171	178
Be	0	0	0	0	0	2	2	2	3	2	BDL	0	BDL	BDL	BDL	0
B	BDL	BDL	BDL	BDL	BDL	4	BDL	BDL	BDL	BDL	BDL	BDL	BDL	BDL	2	BDL
Mg	66296	67905	66951	68657	68149	82259	84199	84892	87673	86453	75350	73573	76650	75973	74332	73984
Si	167484	170943	167998	172064	168839	172158	173747	171504	173186	173654	172999	170382	171877	170662	169727	169587
Sc	50	53	45	44	41	6	8	9	8	8	58	58	51	66	66	64
Ti	18179	18827	18164	20146	19166	16862	17122	18771	18657	18724	19427	19481	19485	20176	19422	20495
V	295	304	304	307	285	143	170	174	167	166	244	243	241	281	273	269
Cr	77	80	103	104	111	122	80	71	3542	3463	239	228	242	237	349	248
Mn	3263	3402	3321	3389	3309	5061	5351	5580	5465	5418	1038	1025	1016	1041	1019	982
Co	57	58	57	58	60	74	77	80	71	70	43	43	44	44	42	42
Ni	110	112	111	117	110	280	297	289	240	242	158	155	160	151	150	157
Cu	2	1	1	1	1	1	BDL	1	1	2	1	1	1	1	1	1
Zn	275	284	285	280	287	219	243	245	234	243	207	203	210	213	206	203
As	BDL	BDL	BDL	1	1	BDL	1	BDL	BDL	1	1	1	1	1	1	BDL
Rb	852	841	861	908	857	692	741	727	740	736	1026	1025	1016	1012	1004	1011
Sr	2	2	1	1	2	1	1	1	1	1	1	1	1	1	1	1
Y	0	BDL	0	BDL	0	0	1	0	0	0	0	0	BDL	BDL	BDL	BDL
Zr	1	0	0	0	0	0	45	0	0	0	0	0	0	0	0	0
Nb	100	103	95	100	97	6	9	11	9	9	9	10	9	6	10	8
Cd	BDL	BDL	BDL	BDL	BDL	BDL	BDL	BDL	BDL	BDL	BDL	BDL	BDL	BDL	BDL	BDL
Sb	1	1	1	1	1	1	1	1	1	1	0	0	0	0	0	0
Cs	132	113	164	202	111	141	151	156	158	156	102	107	117	118	118	112
Ba	403	444	404	415	524	115	122	119	132	131	308	301	293	299	302	310
La	BDL	BDL	0	BDL	0	0	0	0	BDL	0	BDL	0	BDL	BDL	0	BDL
Ce	BDL	0	BDL	BDL	0	0	0	0	0	0	BDL	0	BDL	0	BDL	0
Pr	BDL	BDL	BDL	0	0	0	0	0	BDL	0	BDL	BDL	0	BDL	0	BDL
Nd	BDL	BDL	BDL	BDL	0	0	BDL	0	BDL	0	BDL	0	0	BDL	0	BDL
Sm	BDL	BDL	BDL	BDL	0	BDL	0	BDL	BDL	0	0	BDL	0	BDL	BDL	0
Eu	0	0	0	BDL	BDL	0	BDL	BDL	BDL	BDL	0	0	0	0	BDL	BDL
Gd	BDL	0	BDL	BDL	0	0	BDL	0	BDL	0	BDL	BDL	BDL	0	BDL	0
Tb	BDL	BDL	BDL	0	BDL	BDL	0	0	0	0	BDL	BDL	BDL	BDL	BDL	BDL
Dy	BDL	BDL	BDL	BDL	BDL	0	0	BDL	0	0	0	BDL	BDL	BDL	BDL	0
Ho	0	BDL	BDL	BDL	BDL	0	0	BDL	BDL	BDL	0	BDL	BDL	0	BDL	BDL
Er	BDL	BDL	BDL	BDL	BDL	0	0	0	BDL	0	BDL	BDL	BDL	BDL	0	BDL
Tm	BDL	BDL	0	BDL	BDL	BDL	0	0	BDL	BDL	0	0	BDL	BDL	0	BDL
Yb	BDL	BDL	0	BDL	BDL	BDL	1	0	0	0	BDL	0	BDL	BDL	0	BDL
Lu	BDL	BDL	0	0	0	0	0	0	0	BDL	BDL	0	0	BDL	0	0
Hf	0	0	0	0	0	BDL	1	0	BDL	BDL	0	0	0	0	0	0
Ta	8	8	8	9	9	0	2	3	1	1	0	0	0	0	0	0
W	4	4	4	5	4	1	0	0	0	0	1	2	3	3	2	2
Pb	1	1	1	1	1	1	1	1	1	1	1	1	1	1	1	1
Th	BDL	BDL	BDL	BDL	BDL	0	1	0	0	0	BDL	BDL	BDL	BDL	BDL	BDL
U	0	0	0	0	0	0	2	0	0	0	0	0	0	0	0	0
Li/Cs	4	5	3	3	4	3	3	3	3	3	2	2	1	1	1	2

Table B3.2

Table B3.2) Cordierite trace elements compositions, in red near or below detection limits elements.

Element	Crd-bearing migmatites													
Li	431.65	437.8	448.72	396.25	390.72	398.98	425.93	450.25	417.8	476.06	495.99	494.84	477.63	455.24
Be	20.29	19.07	20.45	18.82	17.54	17.41	27	25.03	27.06	26.94	24.12	25.34	25.66	24.93
B	2.48	BDL	BDL	3.11	BDL	BDL	BDL	BDL	3.85	BDL	BDL	BDL	BDL	BDL
Mg	63625.85	62052.83	61245.04	60133.62	54709.86	51709.42	62069.28	58989.12	56104.23	59068.33	58305.88	58216.53	58776.37	56697.89
Si	231195.6	231289.1	232597.8	230073.7	231896.7	231990.2	231195.6	231195.5	231195.5	231195.5	228531.1	228531.1	228531.1	228531.1
Sc	3.19	2.79	3.23	2.45	3.65	2.74	2.93	3.02	2.91	2.83	2.81	3.1	3.43	3.35
Ti	4.2	BDL	9.14	3.02	BDL	7.17	BDL	BDL	BDL	BDL	BDL	BDL	5.84	3.29
V	BDL	0.203	BDL	BDL	BDL	BDL	BDL	BDL	BDL	BDL	BDL	BDL	BDL	BDL
Cr	BDL	BDL	BDL	BDL	BDL	BDL	BDL	BDL	BDL	BDL	BDL	BDL	BDL	BDL
Mn	2248.69	2257.86	2314.85	2053.31	1948.79	1847.75	2160.76	2099.89	2040.53	2109.16	2111.69	2124.32	2121.76	2049.58
Co	9.28	8.95	8.86	9.11	8.8	7.59	8.95	9.63	9.55	9.05	7.17	8.74	7.93	8.39
Ni	12.76	12.47	12.12	8.92	11.24	10.48	10.99	10.04	9.97	10.32	8.43	10.26	8.37	9.02
Cu	BDL	BDL	BDL	BDL	BDL	BDL	BDL	BDL	BDL	BDL	BDL	BDL	BDL	BDL
Zn	55.5	54.71	56.84	64.29	52.14	53.26	64.08	54.98	55.93	57.05	56.08	56.21	59.49	53.95
As	1.05	1.23	BDL	1.09	BDL	0.79	1.03	BDL	BDL	1.18	BDL	BDL	0.65	BDL
Rb	1.26	1.16	0.716	0.87	1.16	3.7	1.32	1.43	1.45	1.13	0.6	0.62	0.56	0.58
Sr	0.059	0.16	0.048	0.43	BDL	4.49	BDL	BDL	BDL	0.137	BDL	BDL	BDL	BDL
Y	BDL	BDL	BDL	0.476	0.081	0.028	0.019	BDL	BDL	BDL	BDL	0.0149	0.073	0.039
Zr	BDL	BDL	0.0033	0.813	5.39	0.26	1.67	0.233	BDL	0.632	BDL	0.083	2.02	2.32
Nb	BDL	BDL	BDL	0.0114	BDL	BDL	BDL	BDL	BDL	BDL	BDL	BDL	BDL	0.025
Cd	BDL	BDL	BDL	BDL	BDL	BDL	BDL	0.39	BDL	BDL	BDL	BDL	BDL	BDL
Sb	BDL	BDL	BDL	BDL	BDL	BDL	BDL	BDL	BDL	BDL	BDL	BDL	BDL	BDL
Cs	26.22	26.33	23.8	25.39	24.21	24.34	26.68	27.59	27.63	27	24.37	25.91	24.06	25.89
Ba	BDL	BDL	BDL	0.41	0.066	2.66	BDL	BDL	0.041	0.035	BDL	BDL	BDL	BDL
La	0.0041	BDL	BDL	0.0111	BDL	0.0338	BDL	BDL	BDL	BDL	0.0062	BDL	0.0027	BDL
Ce	0.0082	BDL	0.0013	BDL	BDL	0.0247	BDL	BDL	0.0132	BDL	0.0016	0.002	BDL	BDL
Pr	BDL	BDL	0.0042	0.0029	0.0013	0.0103	BDL	BDL	0.002	BDL	0.0012	0.0015	0.0021	0.0012
Nd	0.012	BDL	BDL	0.042	0.023	0.057	BDL	BDL	BDL	0.0067	BDL	BDL	BDL	0.0135
Sm	0.014	BDL	BDL	BDL	BDL	0.01	BDL	BDL	BDL	BDL	0.016	BDL	BDL	BDL
Eu	BDL	BDL	0.0038	BDL	BDL	BDL	BDL	BDL	BDL	BDL	BDL	BDL	BDL	BDL
Gd	BDL	BDL	BDL	BDL	BDL	BDL	BDL	BDL	BDL	BDL	BDL	BDL	BDL	BDL
Tb	BDL	BDL	BDL	0.0077	BDL	BDL	BDL	BDL	BDL	0.001	BDL	BDL	BDL	0.0042
Dy	BDL	BDL	0.0078	0.076	0.0198	0.028	BDL	BDL	BDL	BDL	BDL	0.0171	BDL	BDL
Ho	0.00097	BDL	BDL	0.0027	0.0036	0.0054	BDL	BDL	BDL	BDL	BDL	BDL	BDL	BDL
Er	0.0042	BDL	0.0083	0.063	0.0157	0.017	BDL	BDL	0.0081	0.0046	BDL	BDL	BDL	BDL
Tm	0.00095	BDL	BDL	BDL	BDL	0.004	BDL	BDL	BDL	0.0021	BDL	0.0041	BDL	BDL
Yb	BDL	BDL	0.0059	0.049	BDL	BDL	0.029	BDL	0.012	0.0066	0.0136	BDL	0.012	0.0134
Lu	BDL	BDL	BDL	0.0105	0.0072	0.0013	BDL	0.0032	BDL	BDL	0.0032	BDL	0.0083	BDL
Hf	BDL	0.0042	BDL	0.047	0.257	BDL	0.072	0.036	BDL	0.024	BDL	BDL	0.046	0.084
Ta	BDL	BDL	BDL	BDL	0.0024	0.0027	BDL	BDL	BDL	0.0011	0.0011	0.0134	BDL	BDL
W	0.0041	0.008	0.0121	BDL	BDL	BDL	0.02	BDL	BDL	BDL	BDL	BDL	BDL	BDL
Pb	BDL	BDL	BDL	BDL	BDL	0.638	BDL	BDL	BDL	BDL	BDL	BDL	BDL	BDL
Th	BDL	BDL	BDL	0.0055	0.0089	0.0028	0.0122	0.0011	BDL	0.0034	BDL	BDL	0.0081	0.0057
U	0.0195	0.0274	0.0257	0.0344	0.134	0.048	0.055	0.0218	0.018	0.0247	0.0101	0.0121	0.102	0.144
Li/Cs	16.46262	16.62742	18.85378	15.60654	16.13879	16.39195	15.96439	16.31932	15.12125	17.63185	20.35248	19.09842	19.85162	17.58362

Table B4

Mineral	Biotite		Ilmenite		K-feldspar		Plagioclase		Quartz		Cordierite	
Min	Min	Max	Min	Max	Min	Max	Min	Max	Min	Max	Min	Max
Rb[a]	2	5	0.01	0.05	0.3	3	0.04	0.3	0.001	0.01	0.106066	0.106066
Sr[a]	0.1	0.45	0.05	0.75	1	5	3	6	0.001	0.01	0.187083	0.187083
Ba[a]	4.5	12	0.01	0.05	2	15	0.5	1.5	0.001	0.01	0.022361	0.022361
Nb[a]	2	10	40	80	0.01	0.15	0.05	0.6	0.001	0.01	0.031623	0.031623
Ta[a]	2	10	20	100	0.001	0.01	0.02	0.06	0.001	0.01	0.031623	0.031623
Li[b]	1	1.7	0.00001	0.00002	0.01	0.05	0.02	0.1	0.05	0.05	0.12[d]	0.444[d]
Cs[c]	0.27	0.4	0.00001	0.00002	0.09	0.13	0.005	0.16	0.0002	0.0002	0.19[d]	0.19[d]

a FROM LAURENT ET AL., 2013
b FROM ICENHOWER&LONDON, 1995
c FROM EVENSEN&LONDON, 2002
d FROM EVENSEN&LONDON, 2004

Table B4) Partition coefficients

Appendix C: Zircon age and trace elements composition

Table C1.1

Table C1.1) Type I zircons trace elements compositions

Element	ML121_1.1	ML121_1.2	ML121_2.1	ML121_2.2	ML121_2.3	ML121_3.1	ML121_3.2	ML121_3.3	ML121_4.1	ML121_4.2	ML121_4.3	ML121_5.1	ML121_5.2	ML121_7.1	ML121_7.2
Li	24.2	40.2	26.1	31.4	22.4	27.6	35.4	26.8	22.7	25.3	25.2	32.6	59.3	35.0	59.2
P	6697.5	4272.7	5930.8	3106.6	4628.0	8426.5	8036.4	4976.1	2402.4	2839.9	2018.9	3662.1	4489.3	2843.1	2963.5
Sc	2281.6	360.5	3345.9	447.4	2023.4	3143.2	2784.8	1854.4	203.6	269.5	332.8	203.8	293.5	513.9	539.7
Ti	1.9	1.0	2.3	2.4	2.7	4.7	4.3	2.5	1.3	1.2	0.9	2.8	2.2	2.0	2.3
Mn	0.5	0.6	BDL	3.2	1.6	0.3	2.2	BDL	BDL	0.4	0.3	2.3	0.8	3.9	5.0
Fe	52.8	BDL	BDL	400.3	30.8	8.5	BDL	9.5	BDL	BDL	BDL	BDL	18.2	BDL	17.5
Rb	2.1	2.1	1.9	1.9	1.8	3.1	4.2	2.3	1.3	1.4	1.0	2.8	2.9	2.1	1.4
Sr	2.3	2.3	1.8	1.8	1.5	2.6	2.6	1.7	1.4	1.7	1.1	2.5	2.9	1.8	2.2
Y	15326.8	11777.1	12294.3	8606.8	10071.1	21136.5	20045.3	12172.3	7168.0	8779.7	6005.3	16002.9	21888.4	10462.4	10355.0
Zr	335768.1	351992.3	367781.0	373319.5	335398.1	378553.1	364515.0	355633.9	349558.3	357650.7	364019.8	381198.4	553004.1	498274.0	434915.4
Nb	17.3	12.9	19.4	10.9	18.0	28.3	27.9	20.0	22.6	15.7	15.6	18.5	23.6	16.2	90.4
La	0.0	0.0	0.0	0.6	0.1	0.0	0.1	0.0	0.0	0.0	0.0	0.3	0.0	0.0	0.1
Ce	16.6	8.0	13.5	9.7	11.9	26.3	27.6	17.7	9.5	8.8	5.4	19.3	13.1	7.1	12.6
Pr	0.1	0.1	0.1	0.3	0.1	0.2	0.2	0.1	0.1	0.0	0.0	0.4	0.1	0.1	0.2
Nd	2.9	1.7	1.7	2.2	1.8	4.8	4.9	2.5	1.3	1.1	0.7	4.9	4.4	1.4	2.8
Sm	17.1	14.8	12.5	10.6	10.6	30.3	27.6	14.6	8.8	9.0	5.9	25.9	24.4	9.3	14.0
Eu	6.0	2.1	4.7	1.4	3.6	9.5	8.7	4.7	1.0	1.3	0.9	4.1	3.7	1.5	1.5
Gd	189.1	142.2	143.5	86.1	117.1	287.4	283.8	158.3	75.7	97.1	63.3	213.3	266.1	84.4	114.1
Tb	100.5	78.9	74.7	52.5	65.4	155.5	142.7	84.2	46.5	58.9	39.5	112.0	143.6	64.9	67.5
Dy	1458.0	1220.4	1226.1	845.3	1025.0	2310.5	2087.9	1323.9	731.4	868.0	596.4	1690.0	1709.2	927.0	894.9
Ho	561.3	408.9	459.6	288.9	385.2	782.3	780.0	478.2	260.9	311.2	213.5	554.9	612.1	325.1	314.0
Er	2717.7	2088.5	2377.9	1558.7	1987.6	3796.7	3786.7	2347.6	1337.4	1621.8	1107.5	2565.3	2911.5	1630.6	1787.8
Tm	685.2	617.5	614.9	464.1	522.2	967.7	1009.3	620.7	408.2	474.8	339.3	736.1	857.1	497.3	540.3
Yb	7136.7	7570.4	6507.7	5341.5	5533.3	9829.2	9707.7	6370.8	4982.2	5735.6	4190.8	8470.2	11244.2	5749.5	7167.1
Lu	1265.5	1334.7	1081.2	759.7	920.3	1588.5	1637.1	1031.6	874.5	968.1	754.1	1495.1	1606.6	1050.1	1229.4
Hf	10016.0	12956.2	10809.8	11087.4	9690.8	10338.5	10329.2	10503.3	11720.7	12310.6	14117.8	14707.7	15005.8	18797.9	19052.9
Ta	10.6	15.6	15.7	14.7	13.5	16.3	16.6	13.4	28.6	19.0	21.1	34.0	40.4	22.7	68.2
W	2.6	1.8	2.2	3.0	2.0	3.6	3.3	2.2	1.2	1.5	1.0	2.9	3.8	2.0	3.4
Pb	2.0	1.4	1.3	2.3	1.5	3.1	3.1	2.1	0.9	0.8	0.6	2.4	2.5	1.3	2.4
Th	459.9	366.5	299.8	220.0	328.3	827.1	844.3	528.9	229.3	259.4	151.5	517.6	581.9	286.8	627.0
U	12759.9	24009.7	10607.6	16340.0	9798.2	16948.8	16189.3	11217.0	18274.6	16935.0	13149.6	22476.5	28207.6	17167.2	33142.5
U/Th	27.7	65.5	35.4	74.3	29.8	20.5	19.2	21.2	79.7	65.3	86.8	43.4	48.5	59.9	52.9
LREE-I	595.2	796.2	810.7	471.2	662.6	557.5	506.0	631.3	633.4	915.0	947.8	409.3	454.9	781.2	380.0
T (°C) at 3kb	669.6	626.2	685.6	689.6	697.5	745.4	736.8	693.2	643.8	639.9	617.6	701.0	683.9	675.5	684.9
T (K) at 3kb	942.8	899.4	958.8	962.8	970.6	1018.5	1010.0	966.3	917.0	913.1	890.8	974.2	957.0	948.7	958.1
deltaFMQ	-1.6	-2.9	-2.0	-3.0	-2.3	-1.8	-1.6	-1.6	-2.6	-2.6	-2.9	-2.2	-2.9	-3.4	-3.1
Oxygen fugacity	-19.2	-21.8	-19.1	-20.0	-19.1	-17.5	-17.5	-18.6	-20.9	-21.0	-21.8	-18.9	-20.1	-20.8	-20.3
REE+Y	29483.4	25265.0	24812.4	18028.2	20655.2	40925.5	39549.5	24627.1	15905.5	18935.3	13322.6	31894.7	41284.6	20810.9	22501.4
Nb/Ta	1.6	0.8	1.2	0.7	1.3	1.7	1.7	1.5	0.8	0.8	0.7	0.5	0.6	0.7	1.3
Yb/Sm	417.8	512.2	519.4	504.9	520.0	324.0	351.3	437.6	568.7	635.2	715.1	326.5	460.1	617.6	511.2
U/Yb	1.8	3.2	1.6	3.1	1.8	1.7	1.7	1.8	3.7	3.0	3.1	2.7	2.5	3.0	4.6
Y/Hf	1.5	0.9	1.1	0.8	1.0	2.0	1.9	1.2	0.6	0.7	0.4	1.1	1.5	0.6	0.5
Sc/Th	5.0	1.0	11.2	2.0	6.2	3.8	3.3	3.5	0.9	1.0	2.2	0.4	0.5	1.8	0.9
Yb/Hf	0.7	0.6	0.6	0.5	0.6	1.0	0.9	0.6	0.4	0.5	0.3	0.6	0.7	0.3	0.4

Table C1.2

Element	ML158_2.1	ML158_2.2	ML158_6.1	ML158_6.2	ML157_2.1	ML157_2.2	ML157_2.3	ML157_3.1	ML157_3.2	ML107_10	ML107_15	ML107_16	ML107_X	ML107_17.2	ML107_20	ML107_22.2	ML107_24.1	ML107_24.2	ML107_25.1	ML107_25.2
Li	4.6	4.3	6.1	6.1	1.5	2.9	1.7	5.9	2.6	8.4	6.4	13.8	8.4	12.4	14.9	8.6	11.4	8.7	9.2	15.2
P	464.0	429.3	661.0	592.7	559.7	938.5	951.5	653.4	946.6	1204.0	545.6	527.6	1836.7	2170.1	478.4	1253.8	739.6	1336.3	651.2	864.2
Sc	200.1	220.2	449.1	406.3	381.1	400.9	406.9	360.3	424.8	384.7	384.8	328.2	468.9	448.2	309.4	389.4	374.6	405.0	307.1	357.4
Ti	15.7	3.2	7.4	16.2	6.4	5.7	4.3	7.5	3.4	6.5	3.9	6.5	5.6	14.8	7.2	6.4	5.1	4.0	6.7	7.4
Mn	1.4	1.9	4.2	1.9	1.2	3.7	1.6	4.0	0.4	1.8	0.5	6.4	3.2	5.7	5.1	2.7	BDL	0.3	4.0	4.1
Fe	39.4	23.3	31.7	43.7	18.2	11.3	BDL	517.4	BDL	29.1	18.6	855.6	42.8	35.1	775.6	42.4	13.7	BDL	211.9	73.1
Rb	0.3	0.5	1.9	1.5	1.9	1.5	1.2	4.5	1.2	2.2	1.1	1.0	3.5	5.9	6.9	1.8	1.3	1.2	4.3	1.2
Sr	0.6	0.6	1.6	1.0	1.0	1.0	1.0	1.1	0.9	1.5	1.2	0.9	2.0	2.3	2.7	1.5	1.3	1.1	1.0	1.8
Y	1516.2	1870.4	2919.8	2248.9	5839.8	5711.1	6040.4	5362.6	6550.7	9092.0	5686.9	1617.9	14387.9	17908.7	3299.5	9976.6	6697.5	7491.4	3276.1	8395.2
Zr	299975.2	314225.8	346775.3	312997.8	346241.1	362937.1	337620.0	348556.3	382400.2	311514.6	293950.3	269626.1	316979.9	288052.7	315030.4	299691.7	312837.2	354316.1	328378.0	328124.8
Nb	66.6	71.9	119.1	109.0	87.3	46.8	41.2	63.8	43.1	193.2	112.0	100.0	64.0	266.2	61.2	158.8	103.2	53.7	55.1	122.2
La	0.3	0.1	0.3	0.3	0.1	0.3	0.1	0.2	0.0	0.1	0.0	0.3	0.1	0.4	0.2	0.2	0.1	0.1	0.4	0.2
Ce	8.0	8.1	16.0	11.8	76.4	51.7	54.9	61.8	58.1	143.7	62.1	15.7	127.4	259.3	35.6	131.1	73.2	69.7	35.0	104.0
Pr	0.2	0.1	0.3	0.2	0.1	0.2	0.1	0.3	0.1	0.2	0.1	0.5	0.3	0.8	0.2	0.3	0.1	0.1	0.6	0.4
Nd	1.0	0.5	2.4	1.4	2.5	2.8	1.9	3.4	1.8	4.2	1.3	2.8	6.6	14.4	1.8	5.7	2.1	1.7	5.1	7.2
Sm	1.3	1.0	3.4	2.8	9.9	6.3	7.2	9.8	7.1	16.5	6.8	2.9	22.9	43.4	4.0	18.5	9.4	8.0	5.6	20.3
Eu	0.2	0.2	0.3	0.3	2.9	2.3	2.3	2.7	2.4	1.2	1.2	0.4	3.7	3.1	0.6	1.9	1.6	1.5	0.8	2.4
Gd	8.3	10.6	22.1	17.0	74.5	61.8	64.9	68.1	72.9	121.9	55.6	13.0	174.9	279.0	31.2	131.4	75.1	78.5	34.3	125.9
Tb	3.8	4.8	8.5	6.9	29.8	26.6	28.0	26.1	28.9	47.1	25.7	5.2	67.9	101.3	12.5	53.3	30.8	33.5	13.4	46.1
Dy	72.6	86.9	132.4	108.0	445.6	420.5	454.9	398.9	460.6	705.1	403.3	71.3	1004.2	1412.6	211.0	737.3	495.1	532.9	229.9	658.6
Ho	39.1	43.2	59.5	48.7	201.8	178.4	198.4	170.5	205.2	287.2	172.6	36.8	409.8	522.1	94.4	305.8	208.9	229.8	102.3	248.4
Er	250.9	289.8	363.9	294.8	1067.3	978.0	1075.1	928.2	1125.3	1467.6	960.0	264.6	2205.7	2601.2	527.7	1619.7	1115.4	1263.3	605.4	1271.4
Tm	88.0	100.7	120.0	97.2	273.2	259.6	265.4	239.3	295.4	392.0	267.8	99.3	554.0	651.6	167.6	415.1	295.4	339.3	180.6	341.7
Yb	1422.6	1473.5	1769.7	1590.6	2879.2	2927.7	2896.8	2657.0	3204.8	4497.4	3333.7	1898.0	6149.1	7211.0	2329.9	4638.7	3436.2	3976.8	2116.1	3791.1
Lu	308.3	336.1	382.1	292.2	588.4	592.4	643.5	550.7	644.2	781.1	551.1	410.6	1179.8	1285.7	431.3	892.2	688.3	775.6	384.3	750.1
Hf	15208.7	18432.5	21548.2	17934.2	11002.5	10745.9	11330.8	11372.3	11430.3	13850.1	12925.4	10218.4	10204.9	11609.4	12676.1	11228.3	11708.8	11822.6	12368.8	14273.3
Ta	214.0	210.6	154.4	146.2	41.1	21.9	21.1	34.2	22.5	112.5	63.7	142.2	31.4	124.1	53.7	90.2	55.7	32.7	41.5	87.4
W	3.7	1.1	1.5	1.0	1.1	1.4	1.1	1.3	1.0	1.7	0.9	1.9	2.2	2.5	0.7	2.0	1.2	1.3	1.1	1.4
Pb	2.0	1.9	5.3	3.6	20.8	18.3	15.1	25.1	16.6	26.0	10.6	19.4	47.8	61.2	10.2	45.3	17.1	15.9	38.4	52.4
Th	886.7	367.5	1112.6	910.5	5392.4	4175.0	4097.0	5540.0	4381.3	5860.0	1942.2	3633.1	10754.0	15960.7	844.6	9189.0	4040.9	3883.6	5286.7	11433.7
U	4958.4	5959.5	8431.5	8034.3	18879.5	14359.3	14984.1	17362.9	15945.8	35370.2	24814.8	6763.1	47826.6	55481.0	10067.6	41803.1	27436.3	24932.3	14722.5	39519.8
U/Th	0.2	0.1	0.1	0.1	0.3	0.3	0.3	0.3	0.3	0.2	0.1	0.5	0.2	0.3	0.1	0.2	0.1	0.2	0.4	0.3
U/Th	5.6	16.2	7.6	8.8	3.5	3.4	3.7	3.1	3.6	6.0	12.8	1.9	4.4	3.5	11.9	4.5	6.8	6.4	2.8	3.5
LREE-I	129.8	252.9	93.5	118.4	226.2	216.8	305.5	157.2	323.6	208.9	367.0	50.1	197.1	130.4	170.8	170.4	288.6	374.9	86.3	123.7
T (°C) at 3kb	945.1	771.8	857.1	948.7	842.0	828.7	802.3	858.6	778.1	842.8	792.6	843.0	826.9	937.0	854.3	842.0	818.7	794.6	846.2	857.1
deltaFMQ	-3.9	-2.6	-2.5	-3.7	-0.4	-0.7	-0.4	-0.8	-0.1	0.2	-0.5	-2.2	-0.1	0.1	-1.2	-0.1	-0.6	-0.3	-1.5	-0.6
FMQ	-11.7	-15.1	-13.3	-11.7	-13.6	-13.8	-14.4	-13.3	-14.9	-13.6	-14.6	-13.6	-13.8	-11.8	-13.3	-13.6	-14.1	-14.5	-13.5	-13.3
Oxygen fugacity	-15.6	-17.7	-15.8	-15.3	-14.0	-14.5	-14.8	-14.1	-15.0	-13.4	-15.1	-15.8	-14.0	-11.7	-14.6	-13.7	-14.6	-14.9	-15.0	-13.9
REE+Y	3720.8	4225.8	5800.7	4721.2	11491.5	11219.6	11733.7	10479.6	12657.4	17557.4	11528.0	4439.3	26294.1	32294.6	7147.7	18927.7	13129.0	14801.9	6989.9	15763.0
Nb/Ta	0.3	0.3	0.8	0.7	2.1	2.1	2.0	1.9	1.9	1.7	1.8	0.7	2.0	2.1	1.1	1.8	1.9	1.6	1.3	1.4
Yb/Sm	1061.6	1416.8	525.1	574.2	290.8	464.0	404.6	270.6	451.4	271.9	489.5	654.5	268.1	166.1	576.7	251.1	366.7	499.6	379.2	186.7
U/Yb	3.5	4.0	4.8	5.1	6.6	4.9	5.2	6.5	5.0	7.9	7.4	3.6	7.8	7.7	4.3	9.0	8.0	6.3	7.0	10.4
Y/Hf	0.1	0.1	0.1	0.1	0.5	0.5	0.5	0.5	0.6	0.7	0.4	0.2	1.4	1.5	0.3	0.9	0.6	0.6	0.3	0.6
Sc/Th	0.2	0.6	0.4	0.4	0.1	0.1	0.1	0.1	0.1	0.1	0.2	0.1	0.0	0.0	0.4	0.0	0.1	0.1	0.1	0.0
Yb/Hf	0.1	0.1	0.1	0.1	0.3	0.3	0.3	0.2	0.3	0.3	0.3	0.2	0.6	0.6	0.2	0.4	0.3	0.3	0.2	0.3

Table C1.2) Type II zircons trace elements compositions

Table C1.3

Element	ML108_1.1	ML108_1.2	ML108_2.1	ML108_2.2	ML108_3.1	ML108_3.2	ML108_5.1	ML108_5.2	ML108_6.1	ML108_6.2	ML108_7.1	ML108_7.2	ML108_8	ML158_1.1	ML158_1.2	ML158_8	ML158_4	ML158_5	ML107_1.1	ML107_1.2	ML107_2.1	ML107_2.2	ML107_4	ML107_5	ML107_7
Li	1.2	1.0	BDL	0.7	BDL	BDL	0.7	1.5	BDL	BDL	BDL	BDL	BDL	BDL	0.7	0.7	0.8	0.4	0.5	0.8	1.0	0.8	0.9	BDL	0.4
P	187.7	107.3	157.4	108.6	129.4	84.6	61.7	116.3	95.8	119.9	134.6	132.9	101.2	109.4	107.4	110.1	167.0	85.0	152.0	95.5	108.1	146.3	189.5	116.5	141.1
Sc	239.7	228.1	251.9	221.5	216.0	190.7	157.8	220.9	216.7	205.9	220.2	277.0	182.1	191.3	186.7	185.6	224.2	177.6	197.2	158.8	168.2	189.5	282.8	215.3	222.7
Ti	4.3	2.3	4.1	2.3	4.3	2.2	2.9	3.7	2.3	3.8	3.7	3.7	3.1	4.1	3.4	3.9	5.2	2.2	5.6	1.9	3.8	3.9	7.3	3.9	4.1
Mn	BDL	BDL	BDL	BDL	BDL	BDL	0.3	BDL	BDL	BDL	0.4	BDL	BDL	BDL	BDL	1.4	0.4	BDL	BDL	BDL	0.8	BDL	BDL	BDL	BDL
Fe	BDL	BDL	BDL	BDL	BDL	BDL	BDL	BDL	BDL	BDL	BDL	BDL	BDL	BDL	BDL	34.1	BDL	BDL	BDL	BDL	BDL	BDL	BDL	BDL	BDL
Rb	0.1	0.1	0.2	0.1	0.2	0.1	2.7	0.1	0.1	0.1	0.1	0.1	0.1	0.1	0.1	0.1	0.2	0.1	0.2	0.1	0.4	0.1	0.2	0.1	0.1
Sr	0.2	0.1	0.2	0.2	0.2	0.1	2.2	0.1	0.2	0.1	0.1	0.2	0.1	0.1	0.1	0.1	0.2	0.1	0.2	0.1	0.2	0.1	0.2	0.1	0.1
Y	584.2	641.4	1092.7	652.2	536.2	441.3	90.7	427.1	605.6	383.5	307.3	752.2	436.9	282.3	287.3	349.8	480.9	267.6	490.4	331.8	404.7	421.6	643.8	319.7	401.9
Zr	344338.7	387900.7	394700.8	358437.3	350047.7	365541.4	373630.6	372079.3	383244.2	370324.3	383194.0	389377.0	347147.3	341294.3	349888.6	362246.3	345608.1	357728.3	314309.8	306517.0	312311.9	324848.2	381898.5	390657.5	407613.3
Nb	2.5	4.5	2.1	5.0	1.0	1.3	0.5	2.3	4.1	0.9	0.9	4.9	0.9	1.0	1.2	0.7	2.1	1.4	1.6	1.7	0.7	1.8	2.7	1.0	1.5
La	0.0	0.0	0.0	0.0	0.0	0.0	0.0	0.0	0.0	0.0	0.0	0.0	0.0	0.0	0.0	0.0	0.0	0.0	0.0	0.0	0.0	0.0	0.0	0.0	0.0
Ce	13.2	18.9	16.1	13.5	8.6	8.0	3.4	12.1	15.8	6.7	5.4	21.7	7.5	6.0	6.7	5.9	10.3	8.5	10.6	8.4	6.6	8.0	12.1	5.9	7.3
Pr	0.0	0.0	0.2	0.0	0.1	0.0	0.0	0.0	0.0	0.0	0.0	0.0	0.1	0.0	0.0	0.0	0.0	0.0	0.0	0.0	0.1	0.0	0.0	0.0	0.0
Nd	0.8	0.5	3.0	0.4	1.4	0.5	0.1	0.5	0.4	0.7	0.2	0.5	0.9	0.4	0.3	1.1	0.5	0.1	0.9	0.3	0.8	0.5	0.7	0.4	0.4
Sm	1.1	1.1	4.7	1.2	2.4	1.2	0.2	1.1	0.9	1.2	0.6	1.5	1.7	0.7	0.7	1.6	1.4	0.6	1.2	0.9	1.3	1.2	1.2	0.7	0.9
Eu	0.5	0.4	1.5	0.4	0.7	0.5	0.1	0.4	0.4	0.5	0.3	0.5	0.5	0.4	0.3	0.5	0.4	0.1	0.6	0.2	0.5	0.4	0.7	0.3	0.3
Gd	7.6	7.5	22.3	7.1	9.9	7.0	1.3	5.8	6.2	6.5	4.3	8.9	8.4	4.3	4.1	7.4	6.6	3.3	8.5	4.6	8.4	5.7	9.2	4.9	5.3
Tb	3.2	2.8	7.2	2.9	3.3	2.5	0.5	2.1	2.5	2.2	1.7	3.5	2.9	1.6	1.6	2.1	2.5	1.3	2.9	1.7	2.6	2.1	3.5	1.6	2.0
Dy	44.4	43.3	92.9	47.1	44.4	35.6	6.3	32.0	38.8	30.5	24.1	54.7	35.8	21.4	21.8	29.2	37.6	19.6	38.1	25.5	34.5	32.1	53.5	22.0	29.7
Ho	18.5	19.7	35.2	20.5	17.9	14.5	2.5	13.8	18.1	11.8	10.0	23.9	13.8	8.8	9.0	11.6	15.8	8.0	16.4	10.7	13.3	13.3	21.0	9.5	12.7
Er	98.1	113.5	172.3	123.1	86.6	75.2	15.0	73.3	108.5	63.4	53.4	132.9	70.2	48.4	50.1	59.6	80.8	43.9	82.6	55.3	64.5	70.1	112.5	53.8	70.4
Tm	27.5	31.4	41.1	36.2	21.7	19.3	4.5	18.9	29.8	16.5	14.0	36.6	18.9	12.6	14.3	15.2	20.6	12.6	21.6	16.2	16.5	19.6	28.9	13.9	17.8
Yb	327.3	364.7	474.8	440.8	249.2	219.4	58.0	253.6	364.0	194.1	169.7	430.6	212.8	150.3	176.5	175.9	238.2	157.1	260.8	207.2	192.0	234.3	336.7	149.8	195.2
Lu	61.3	76.0	95.0	91.0	49.1	43.8	10.9	44.0	73.1	37.5	34.6	79.2	40.8	27.9	34.3	32.3	42.6	27.7	40.0	39.0	32.4	42.9	64.3	33.2	42.1
Hf	7665.2	9828.6	8639.2	9638.8	7400.5	9311.7	7733.9	7856.3	9236.9	7539.4	7653.6	8896.5	7991.6	7330.3	7451.2	7994.8	7216.9	7975.4	6187.4	7884.1	6487.4	6652.8	7312.2	8332.1	8352.0
Ta	1.3	2.8	1.2	3.5	0.7	1.0	0.4	1.5	2.5	0.6	0.6	2.6	0.8	0.6	0.9	0.6	1.1	1.1	0.9	1.3	0.5	1.2	1.4	0.7	0.9
W	0.1	0.1	0.2	0.1	0.1	0.1	0.0	BDL	0.1	0.1	BDL	0.1	0.1	0.1	0.1	0.2	BDL	0.1	0.1	0.0	0.1	0.1	0.1	0.1	0.1
Pb	0.8	1.3	1.8	1.1	0.7	0.7	1.1	1.1	0.9	0.5	0.3	1.3	0.7	0.3	0.3	0.4	0.7	0.5	0.6	0.4	0.4	0.5	0.7	0.3	0.4
Th	207.4	333.8	460.8	263.1	175.3	134.8	28.0	211.7	234.4	119.2	72.3	323.6	146.5	63.5	88.4	100.7	192.2	102.0	131.8	121.6	101.0	105.4	195.6	77.7	89.0
U	615.9	966.3	837.2	1504.5	383.5	472.0	134.8	632.6	819.2	331.5	244.5	918.2	352.5	210.6	316.7	267.4	469.9	329.9	405.3	471.5	224.6	355.0	482.1	201.4	233.8
U/Th	0.3	0.3	0.6	0.2	0.5	0.3	0.2	0.3	0.3	0.4	0.3	0.4	0.4	0.3	0.3	0.4	0.4	0.3	0.3	0.3	0.4	0.3	0.4	0.4	0.4
U/Th	3.0	2.9	1.8	5.7	2.2	3.5	4.8	3.0	3.5	2.8	3.4	2.8	2.4	3.3	3.6	2.7	2.4	3.2	3.1	3.9	2.2	3.4	2.5	2.6	2.6
LREE-I	99.1	128.1	50.9	155.1	50.6	96.3	72.4	90.6	148.3	68.3	141.7	136.4	60.1	83.7	98.7	46.7	95.6	238.4	72.6	128.6	66.7	95.6	116.7	90.6	113.6
T (°C) at 3kb	802.0	743.1	797.0	741.6	801.4	738.8	764.2	785.8	743.1	790.2	787.1	785.8	769.4	797.0	779.7	791.4	819.5	741.2	828.2	728.4	789.4	791.7	854.9	792.9	796.5
deltaFMQ	-0.1	0.7	0.0	-0.3	-0.4	-0.1	-0.8	-0.1	0.5	-0.6	-0.7	0.6	-0.3	-0.5	-0.5	-0.7	-0.4	0.3	-0.3	0.0	-0.3	-0.4	-0.5	-0.4	-0.2
FMQ	-15.1	-16.4	-15.2	-16.4	-15.1	-16.5	-15.9	-15.4	-16.4	-15.4	-15.4	-15.4	-15.8	-15.2	-15.6	-15.3	-14.8	-16.5	-14.5	-16.8	-15.4	-15.3	-14.0	-15.3	-15.2
Oxygen fugacity	-15.2	-15.7	-15.2	-16.7	-15.5	-16.6	-16.7	-15.5	-15.9	-16.0	-16.1	-14.8	-16.1	-15.7	-16.1	-16.0	-15.2	-16.2	-14.9	-16.8	-15.7	-15.7	-14.5	-15.7	-15.4
REE+Y	1187.7	1321.2	2059.0	1436.4	1031.5	868.7	193.8	884.9	1263.8	755.1	625.7	1546.7	851.2	565.1	607.0	692.1	938.2	550.3	974.6	701.6	778.2	851.6	1288.1	615.7	786.0
Nb/Ta	1.9	1.6	1.7	1.4	1.4	1.3	1.3	1.5	1.7	1.5	1.4	1.9	1.2	1.6	1.3	1.3	1.9	1.3	1.7	1.3	1.5	1.6	1.9	1.6	1.7
Yb/Sm	300.3	328.5	101.9	380.0	104.7	189.1	281.5	230.6	413.6	157.8	292.5	289.0	123.7	208.8	245.1	113.5	167.7	261.9	213.8	235.4	143.3	200.3	273.8	205.2	219.4
U/Yb	1.9	2.6	1.8	3.4	1.5	2.2	2.3	2.5	2.3	1.7	1.4	2.1	1.7	1.4	1.8	1.5	2.0	2.1	1.6	2.3	1.2	1.5	1.4	1.3	1.2
Y/Hf	0.1	0.1	0.1	0.1	0.1	0.0	0.0	0.1	0.1	0.1	0.0	0.1	0.1	0.0	0.0	0.0	0.1	0.0	0.1	0.0	0.1	0.1	0.1	0.0	0.0
Sc/Th	1.2	0.7	0.5	0.8	1.2	1.4	5.6	1.0	0.9	1.7	3.0	0.9	1.2	3.0	2.1	1.8	1.2	1.7	1.5	1.3	1.7	1.8	1.4	2.8	2.5
Yb/Hf	0.0	0.0	0.1	0.0	0.0	0.0	0.0	0.0	0.0	0.0	0.0	0.0	0.0	0.0	0.0	0.0	0.0	0.0	0.0	0.0	0.0	0.0	0.0	0.0	0.0

Table C1.3) Type III zircons trace elements compositions

Table C2.1

								Age correction (after Sliwinski 2018)				
Type I	Pb207/U235	1se	Pb206/U238	1se	rho	Age 06/38	2σ	Corrected age	1se	Corrected 06/38	Corrected 1se	corrected rho
ML121_5_1	0.03921	0.00065	0.00607	0.00007	0.695653276	39.01	0.90	37.44	0.63	0.005825747	4.88787E-05	0.506117396
ML121_7_2	0.04191	0.00075	0.00619	0.00007	0.631922456	39.78	0.90	38.32	0.63	0.005962686	4.91992E-05	0.461076216
ML121_7_3	0.04172	0.00071	0.00627	0.00007	0.656019049	40.29	0.90	39.01	0.64	0.00607007	4.96335E-05	0.480471151
ML121_8_4	0.22416	0.00566	0.01759	0.00021	0.472819242	112.41	2.66	106.11	1.81	0.01660466	0.000143013	0.341103208
ML121_9_5	0.04215	0.00098	0.00643	0.00009	0.602009077	41.32	1.15	39.90	0.82	0.006209692	6.38433E-05	0.442198001
ML121_1_6	0.03969	0.00071	0.00615	0.00007	0.636276194	39.52	0.90	38.14	0.63	0.005934906	4.93482E-05	0.464815227
ML121_2_7	0.04112	0.00072	0.00619	0.00007	0.645844552	39.78	0.90	38.61	0.64	0.006008229	4.98713E-05	0.47405071
ML121_2_8	0.04019	0.00073	0.00616	0.00007	0.625622665	39.59	0.90	38.68	0.65	0.006018069	5.04712E-05	0.461723054
ML121_3_9	0.03975	0.0007	0.00608	0.00007	0.653782895	39.08	0.90	37.84	0.64	0.005887438	4.9669E-05	0.479068903
ML121_4_10	0.04153	0.00074	0.00621	0.00007	0.632610872	39.91	0.90	38.73	0.64	0.006027098	4.98673E-05	0.464342129

Table C2.1) Type I zircons U-Pb ages. On the left uncorrected data, on the right corrected data after alpha dose correction (Sliwinski et al, 2018a)

Table C2.2

								Age correction (after Sliwinski 2018)				
Type II	Pb207/U235	1se	Pb206/U238	1se	rho	Age 06/38	2σ	Corrected age	1se	Corrected 06/38	Corrected 1se	corrected rho
ML107_8_1	0.05934	0.00123	0.0065	0.00008	0.593771107	41.77	1.02	39.53	0.70	0.006150798	5.4928E-05	0.430828823
ML107_10_2	0.04291	0.00101	0.00631	0.00008	0.538638967	40.55	1.02	38.21	0.69	0.005945432	5.45034E-05	0.389473168
ML107_10_3	0.06435	0.00134	0.00646	0.00008	0.594704496	41.51	1.02	39.38	0.70	0.006128112	5.51515E-05	0.432189724
ML107_12_11	0.04214	0.0012	0.00625	0.00009	0.50568	40.16	1.15	37.44	0.77	0.005825972	5.99179E-05	0.361161599
ML107_13_8	0.06609	0.00144	0.00666	0.00008	0.551301301	42.79	1.02	40.70	0.71	0.006334862	5.54187E-05	0.401506678
ML107_16_10	0.08883	0.00228	0.00696	0.00009	0.503799909	44.71	1.15	43.64	0.83	0.006793251	6.51185E-05	0.373466619
ML107_15_9	0.04098	0.00123	0.00617	0.00009	0.485986481	39.65	1.15	37.25	0.78	0.005795949	6.07308E-05	0.349101006
ML107_18_15	0.04048	0.00102	0.00619	0.00008	0.512908233	39.78	1.03	38.07	0.71	0.005923846	5.5455E-05	0.37151575
ML107_17_14	0.0395	0.00097	0.00608	0.00008	0.535811177	39.08	1.03	36.56	0.69	0.005688472	5.33141E-05	0.381655938
ML107_21_17	0.07389	0.00192	0.00774	0.0001	0.497214147	49.7	1.28	48.43	0.92	0.007542318	7.1951E-05	0.367126901
ML107_20_16	0.05926	0.00154	0.00643	0.00008	0.478762295	41.32	1.02	39.33	0.71	0.006120443	5.54822E-05	0.348828349
ML107_24_19	0.04029	0.00129	0.00603	0.00009	0.466157584	38.76	1.15	36.56	0.78	0.005688358	6.11975E-05	0.336011563
ML107_22_18	0.04025	0.00104	0.00623	0.00008	0.496974935	40.04	1.03	37.65	0.69	0.005857871	5.37812E-05	0.355323105
ML107_25_20	0.04131	0.00169	0.00585	0.0001	0.417842513	37.6	1.28	35.68	0.88	0.005550882	6.85085E-05	0.301682971
ML107_27_21	0.23846	0.00623	0.00838	0.00011	0.50243069	53.8	1.41	52.12	1.00	0.008117549	7.81323E-05	0.368411599
ML157_2_3	0.0414	0.00077	0.00612	0.00007	0.614973262	39.33	0.90	38.12	0.64	0.005931747	4.97575E-05	0.451009808
ML157_2_4	0.04152	0.00076	0.00639	0.00008	0.68396343	41.06	1.02	39.39	0.72	0.006129523	5.62344E-05	0.501209706
ML157_3_5	0.04147	0.00078	0.00625	0.00007	0.595466667	40.16	0.90	38.89	0.64	0.006052148	4.96687E-05	0.436327652
ML158_2_3	0.05483	0.00138	0.00645	0.00009	0.554398382	41.45	1.15	40.41	0.83	0.006287611	6.50008E-05	0.410744693
ML158_2_4	0.04681	0.00097	0.00608	0.00007	0.555598888	39.08	0.90	37.95	0.64	0.005904613	4.99504E-05	0.408239122
ML158_6_5	0.04388	0.00101	0.00624	0.00008	0.556994161	40.1	1.03	39.16	0.74	0.006093067	5.75358E-05	0.4102487

Table C2.2) Type II zircons U-Pb ages. On the left uncorrected data, on the right corrected data after alpha dose correction (Sliwinski et al, 2018a).

Table C2.3

Table C2.3)
Type III zircons
U-Pb ages.

								Age correction (after Sliwinski 2018)				
Type III	Pb207/U235	1se	Pb206/U238	1se	rho	Age 06/38	2σ	Corrected age	1se	Corrected 06/38	Corrected 1se	corrected rho
ML157_1_1	0.04321	0.00254	0.00628	0.00009	0.24379984	40.36	1.15	41.52	0.94	0.006460346	7.30468E-05	0.192351671
ML157_1_2	0.04208	0.00184	0.00591	0.00008	0.309571103	37.99	1.03	38.85	0.82	0.006044362	6.42691E-05	0.243169789
ML158_1_1	0.03869	0.00306	0.00607	0.0001	0.208299685	39.01	1.28	40.55	1.06	0.006309911	8.26153E-05	0.165544424
ML158_1_2	0.03737	0.00221	0.00584	0.0001	0.289546272	37.54	1.28	37.81	1.01	0.005881928	7.89429E-05	0.226946855
ML158_8_6	0.03801	0.00209	0.00594	0.00009	0.275554589	38.18	1.15	39.07	0.93	0.006078585	7.26051E-05	0.217228111
ML158_4_9	0.03822	0.00207	0.00597	0.00009	0.278348263	38.37	1.15	39.33	0.93	0.006118506	7.27427E-05	0.219515167
ML158_4_10	0.04119	0.00257	0.00577	0.00009	0.249991571	37.09	1.15	38.41	0.95	0.005974892	7.38999E-05	0.198231488
ML158_5_11	0.03675	0.00197	0.0059	0.00009	0.284565086	37.92	1.15	38.98	0.94	0.006064033	7.30778E-05	0.224809828
ML158_5_12	0.04187	0.00159	0.00594	0.00008	0.354657688	38.18	1.03	38.81	0.82	0.006038496	6.3726E-05	0.277903215
ML108_1_1	0.0391	0.0019	0.00593	0.00008	0.277624922	38.11	1.03	39.02	0.83	0.006071174	6.44162E-05	0.218346335
ML108_1_2	0.03896	0.00163	0.00582	0.00008	0.328547636	37.41	1.03	38.16	0.82	0.005937068	6.40357E-05	0.257798965
ML108_2_3	0.0414	0.00152	0.00591	0.00008	0.368688218	37.99	1.03	38.56	0.81	0.005999348	6.35256E-05	0.288403938
ML108_2_4	0.04006	0.00129	0.006	0.00008	0.414056848	38.56	1.03	38.81	0.80	0.006037994	6.25108E-05	0.321501688
ML108_3_5	0.03738	0.00255	0.00584	0.00009	0.225906527	37.54	1.15	38.76	0.94	0.006030323	7.36273E-05	0.178977138
ML108_3_6	0.04086	0.00197	0.00567	0.00008	0.292643623	36.45	1.03	37.35	0.83	0.005809667	6.45743E-05	0.23053683
ML108_4_7	0.03741	0.00118	0.00578	0.00007	0.383951088	37.15	0.90	37.56	0.71	0.005843945	5.51822E-05	0.299363401
ML108_5_8	0.03952	0.00253	0.0058	0.00009	0.242387897	37.28	1.15	38.58	0.95	0.006002336	7.38397E-05	0.192161321
ML108_5_9	0.04161	0.00358	0.00592	0.00011	0.215966141	38.05	1.41	39.81	1.18	0.006194197	9.20682E-05	0.172758507
ML108_6_10	0.0368	0.00363	0.00571	0.00012	0.213052351	36.70	1.54	38.52	1.30	0.005993017	0.00010154	0.171764408
ML108_6_11	0.03913	0.00128	0.00572	0.00007	0.374112216	36.77	0.90	36.88	0.69	0.005737638	5.41867E-05	0.288708322
ML108_7_12	0.03783	0.00336	0.00577	0.0001	0.195128745	37.09	1.28	38.72	1.07	0.006024333	8.31686E-05	0.155434539
ML108_7_13	0.0404	0.00168	0.00568	0.00008	0.33869886	36.51	1.03	37.38	0.83	0.005815099	6.45133E-05	0.266786572
ML108_8_14	0.04121	0.00223	0.0059	0.00009	0.281895569	37.92	1.15	39.11	0.94	0.006084453	7.34738E-05	0.223156054
ML107_1_4	0.03683	0.00227	0.00572	0.00009	0.255283263	36.77	1.15	37.94	0.94	0.005902946	7.36051E-05	0.202308961
ML107_1_5	0.03868	0.0021	0.00568	0.00008	0.259423206	36.51	1.03	37.58	0.83	0.005846238	6.49696E-05	0.204691943
ML107_2_6	0.03976	0.00246	0.00569	0.00009	0.255647477	36.58	1.15	37.84	0.95	0.005886217	7.38232E-05	0.202706556
ML107_2_7	0.04037	0.00269	0.00567	0.0001	0.264681392	36.45	1.28	37.61	1.05	0.005850895	8.20668E-05	0.210499857
ML107_3_12	0.03951	0.00186	0.00572	0.00008	0.297090007	36.77	1.03	37.65	0.83	0.005857699	6.44475E-05	0.233707821
ML107_3_13	0.03685	0.00455	0.00569	0.00015	0.213503544	36.58	1.92	39.01	1.68	0.006067892	0.000131034	0.174893091
ML107_4_22	0.04125	0.00204	0.00583	0.00009	0.312153163	37.47	1.15	38.48	0.94	0.005987183	7.30178E-05	0.246603858
ML107_4_23	0.03733	0.00297	0.00583	0.0001	0.215592171	37.47	1.28	39.02	1.06	0.006070688	8.29444E-05	0.171731864
ML107_5_24	0.03615	0.00273	0.00585	0.0001	0.226354842	37.60	1.28	39.05	1.06	0.00607485	8.26577E-05	0.180174563
ML107_5_25	0.0389	0.00226	0.00564	0.00009	0.274665788	36.26	1.15	37.49	0.95	0.005831662	7.3824E-05	0.217894626
ML107_6_27	0.03897	0.00295	0.0058	0.0001	0.227761543	37.28	1.28	38.85	1.06	0.006044571	8.30234E-05	0.181444261
ML107_7_28	0.14463	0.00948	0.00679	0.00016	0.359501128	43.62	2.05	46.27	1.76	0.007201894	0.000137748	0.291802472
ML107_7_29	0.04032	0.00198	0.00567	0.00009	0.323232323	36.45	1.15	37.48	0.94	0.005830014	7.32232E-05	0.255761194

Appendix D: Tourmaline compositional and isotopic data

Table D1

Analysis	SiO2	TiO2	Al2O3	FeO	MnO	MgO	CaO	Na2O	K2O	F	Total	Mg#		F	B	Si	Ti	Al	Fe	Mn	Mg	Ca	Na	K
ML121EB-1-c	35.33		34.71	14.18	1.42	0.7624	0.4092	1.86	0.0476	0.3388	89.0581	8.747302		0.3388	3	5.829376	0	6.749368	1.956401	0.198429	0.187537	0.072333	0.594976	0.010018
ML121EB-1-r1	35.27		38.39	7.4	2.33	0.0721	0.6577	2.24	0.0201	1.02	87.4	1.707442		1.02	3	5.777663	0	7.411309	1.013635	0.323252	0.017608	0.115424	0.711382	0.0042
ML121EB-1-r2	51.73		31.69	0.3246	1.52	0.0223	2.32	0.9005	0.0072	1.41	89.9771	10.91184		1.41	3	7.707513	0	5.564474	0.040441	0.191802	0.004953	0.370324	0.260114	0.001368
ML121EB-2-c1	35.89		36.87	13.29	1.1807	0.6605	0.1823	1.71	0.0366	0.1933	90.0135	8.139511		0.1933	3	5.787536	0	7.006861	1.792043	0.16125	0.158788	0.031494	0.534595	0.007529
ML121EB-2-c2	35.59		36.57	13.27	1.1223	0.5992	0.1895	1.71	0.0228	0.1722	89.3261	7.450679		0.1722	3	5.788267	0	7.009315	1.804657	0.154585	0.145284	0.033018	0.539169	0.00473
ML121EB-2-r1	35.06		35.79	13.85	1.43	0.6851	0.3888	1.96	0.04	0.3802	89.5842	8.104396		0.3802	3	5.74395	0	6.910199	1.897368	0.198415	0.167331	0.068241	0.622534	0.008359
ML121EB-2-r2	36.91		39.72	2.66	4.51	0	0.7923	2.26	0.0173	1.52	88.4184	0		1.52	3	5.905426	0	7.489391	0.35587	0.611114	0	0.135806	0.70101	0.003531
ML121EB-3-c	34.93		34.86	13.07	1.2373	0.5552	0.0982	1.48	0.0475	0.2658	86.5441	7.040287		0.2658	3	5.867227	0	6.900678	1.835748	0.176014	0.13903	0.017671	0.481953	0.010177
ML121EB-3-r	34.66		35.87	13.86	1.31	0.693	0.5049	1.94	0.0414	0.3843	89.2636	8.18477		0.3843	3	5.702601	0	6.95514	1.906825	0.182538	0.169982	0.088996	0.618806	0.008689
ML121EB-3-c2	35.58		35.83	13.74	1.29	0.6222	0.3589	1.97	0.0595	0.3073	89.761	7.470429		0.3073	3	5.79826	0	6.881271	1.872327	0.178041	0.151163	0.06266	0.622395	0.012369
ML121EB-3-c3	35.62		35.93	12.53	1.076	1.0747	0.357	2.02	0.047	0.5551	89.2098	13.26354		0.5551	3	5.813409	0	6.910736	1.709981	0.148726	0.261486	0.06242	0.639141	0.009785
ML121EB-3-r2	36.8		39.9	2.04	4.12	0.1388	1.004	2.12	0.0301	1.4	87.5804	10.81825		1.4	3	5.904962	0	7.545226	0.273718	0.559893	0.033203	0.172594	0.659498	0.006161
ML121EB-5-s	35.04		34.97	13.93	1.3	0.7572	0.3439	1.92	0.0419	0.2916	88.5947	8.835052		0.2916	3	5.799267	0	6.820791	1.927806	0.182218	0.186829	0.060977	0.616054	0.008846
ML121EB-5-r1	37.37		39.45	1.77	4.8	0.0146	0.8673	2.29	0.0229	1.44	88.0263	1.449309		1.44	3	5.975946	0	7.434652	0.236679	0.650075	0.003481	0.148585	0.709949	0.004671
ML121EB-5-r2	37.08		39.6	1.1442	4.94	0	0.9291	2.39	0.0128	1.44	87.5362	0		1.44	3	5.952284	0	7.491507	0.153585	0.671598	0	0.159782	0.74379	0.002621
ML121EB-5-c	35.31		35.1	13.86	1.3	0.7465	0.3929	1.73	0.0444	0.3703	88.8541	8.761279		0.3703	3	5.821724	0	6.820106	1.910822	0.181525	0.183488	0.0694	0.552979	0.009338
ML121EB-6-c	35.32		35.32	14.05	1.4	0.7332	0.3988	1.84	0.0595	0.3688	89.4903	8.512007		0.3688	3	5.793926	0	6.82815	1.927222	0.1945	0.179308	0.070086	0.585165	0.01245
ML121EB-6-r1	36.92		39.56	2.71	4.74	0.011	0.9065	2.37	0.0154	1.55	88.8967	0.718478		1.55	3	5.898632	0	7.448622	0.362045	0.641367	0.00262	0.15516	0.734085	0.003138
ML121EB-6-r2	37.74		41.3	0.3959	3.35	0	1.84	1.63	0.0101	1.28	87.5461	0		1.28	3	5.957127	0	7.682722	0.052254	0.447836	0	0.311154	0.498805	0.002034
ML121FB-1-c	38.36		38.33	2.41	3.86	0.0218	0.7569	2.52	0.0119	1.55	87.9955	1.587132		1.55	3	6.140369	0	7.230774	0.322579	0.523289	0.005202	0.1298	0.782032	0.00243
ML121FB-1-m	38.03		40.53	1.0054	3.34	0	0.925	2.19	0.0112	1.29	87.3639	0		1.29	3	6.03075	0	7.57446	0.133317	0.44857	0	0.157148	0.673283	0.002266
ML121FB-1-s	39.41		42.52	0.0729	0.866	0	1.0902	1.56	0.014	1.01	86.6902	0		1.01	3	6.13168	0	7.796441	0.009484	0.114112	0	0.181719	0.47055	0.002778
ML121FB-1-1	37.85		40.89	0.9423	3.07	0.0132	0.7761	2.21	0.0067	1.22	87.0059	2.43665		1.22	3	6.007197	0	7.648093	0.125054	0.412651	0.003123	0.131961	0.679996	0.001356
ML121FB-1-2	37.94		40.71	0.9367	3.52	0	0.6478	2.18	0.03	1.19	87.1545	0		1.19	3	6.018873	0	7.611128	0.124257	0.472933	0	0.110098	0.670475	0.006071
ML121FB-2-c	38.72		41.91	2.34	1.87	0.0232	0.3431	2.1	0.0384	0.5649	87.9097	1.736937		0.5649	3	6.021996	0	7.681621	0.304316	0.246312	0.005379	0.057167	0.633188	0.007618
ML121FB-2-r	37.61		39.68	3.19	2.77	0.0162	0.6451	2.38	0.0196	1.47	87.781	0.897287		1.47	3	6.006319	0	7.468043	0.42599	0.374648	0.003857	0.110371	0.736869	0.003993
ML121FB-2-u	37.57		39.56	2.74	2.7	0.0081	1.2684	2.06	0.017	1.34	87.2636	0.524292		1.34	3	6.014982	0	7.464135	0.366815	0.366097	0.001933	0.217556	0.639394	0.003472
ML121FB-3-c	38.28		39.79	2.71	2.68	0.0134	0.6116	2.37	0.0303	1.39	87.8986	0.873867		1.39	3	6.07318	0	7.439577	0.359515	0.360096	0.003169	0.103952	0.728955	0.006132
ML121A-2-1	36.12		34.54	9.63	0.1266	5.28	1.0621	1.8	0.0613	0.3181	88.9611	49.43182		0.3181	3	5.81237	0	6.550251	1.295791	0.017254	1.266672	0.183102	0.561547	0.012583
ML121A-2-3c	36.44		32.89	9.69	0.1427	5.41	1.1059	1.65	0.0715	0.2662	87.7353	49.8846		0.2662	3	5.946317	0	6.325045	1.322198	0.019721	1.316109	0.193334	0.52199	0.014883
ML121A-2-3r	36.01		33.83	11.55	0.8528	3.06	0.5533	2.03	0.0865	0.4595	88.4322	32.08123		0.4595	3	5.906011	0	6.538878	1.584004	0.118456	0.7482	0.09722	0.645469	0.018097
ML121A-3-1c	36.22		34.26	9.41	0.1473	5.48	1.062	1.74	0.0688	0.1676	88.5558	50.93892		0.1676	3	5.83677	0	6.506412	1.267993	0.020103	1.316526	0.183346	0.543603	0.014142
ML121A-3-1r	34.75		35.92	11.71	1.136	2.18	0.5132	2.01	0.0618	0.4504	88.7315	24.91989		0.4504	3	5.693328	0	6.9355	1.604248	0.157626	0.532467	0.090078	0.638434	0.012915
ML121A-4-1c	35.57		35.08	8.55	0.1369	5.4	1.1833	1.73	0.0486	0.6608	88.3653	52.96394		0.6608	3	5.754365	0	6.688107	1.156599	0.018757	1.302363	0.205083	0.542585	0.010029
ML121A-4-1r	34.83		35.25	12.04	1.0753	2.24	0.5748	2.02	0.0559	0.456	88.7052	24.90792		0.456	3	5.730904	0	6.83532	1.65653	0.149844	0.549468	0.101323	0.644361	0.011732
ML121A-4-2c	36.34		34.36	8.35	0.0598	6.42	1.41	1.66	0.0547	0.503	89.1576	57.81993		0.503	3	5.812373	0	6.476671	1.116756	0.0081	1.530835	0.241607	0.514737	0.01116
ML121A-4-2r	35.29		36.73	11.47	1.0682	2.22	0.5574	2.02	0.0614	0.5156	90.0144	25.65461		0.5156	3	5.691588	0	6.981244	1.546851	0.145906	0.533777	0.09631	0.631599	0.012632
ML121A-5-1c	36.64		35.65	9.4	0.1428	4.69	0.5706	1.67	0.0514	0.2119	89.0643	47.07714		0.2119	3	5.846696	0	6.704165	1.254256	0.019298	1.115714	0.097546	0.51663	0.010462
ML121A-5-1r	34.93		36.46	11.98	0.936	2.09	0.5957	1.95	0.0336	0.3519	89.3272	23.72447		0.3519	3	5.675414	0	6.981451	1.627642	0.128799	0.506256	0.103693	0.614245	0.006964
ML121A-5-2c	36.33		34.75	9.81	0.1325	4.63	0.6366	1.76	0.0419	0.309	88.4303	45.69528		0.309	3	5.866557	0	6.613066	1.324616	0.018121	1.114612	0.11013	0.550984	0.008631
ML121A-5-2r	35.04		35.42	12.11	0.609	2.56	0.6259	1.86	0.0423	0.3807	88.648	27.37269		0.3807	3	5.736479	0	6.833764	1.657787	0.084438	0.624807	0.109776	0.590341	0.008833
ML121A-7-1	35.67		34.99	12.55	0.5939	2.75	0.5634	1.89	0.0472	0.2606	89.3725	28.09224		0.2606	3	5.796873	0	6.701388	1.705444	0.081742	0.666267	0.098091	0.595471	0.009785
ML121A-7-2c	35.25		35.09	9.82	0.1141	4.98	1.0296	1.68	0.0556	0.3507	88.3701	47.48308		0.3507	3	5.718247	0	6.708374	1.332044	0.015676	1.204365	0.178935	0.52835	0.011505
ML121A-7-2r	35.43		35.74	12.13	0.9725	1.99	0.4751	2.04	0.042	0.5002	89.3199	22.63008		0.5002	3	5.768211	0	6.857324	1.65133	0.134091	0.483001	0.082866	0.643885	0.008722
ML121A-6-1	37.11		35.94	9.25	0.1738	4.39	0.3694	1.65	0.0321	0.1444	89.0598	45.83306		0.1444	3	5.896387	0	6.729816	1.228966	0.023387	1.039883	0.06288	0.508262	0.006506
ML121A-6-2	35.17		36.06	11.83	1.1891	1.82	0.4317	2.08	0.0296	0.5074	89.1866	21.52487		0.5074	3	5.736968	0	6.932117	1.613608	0.164273	0.442595	0.075442	0.657782	0.006159
ML121A-6-3	36.62		36.13	9.35	0.1978	4.47	0.4901	1.62	0.0528	0.2035	89.1343	46.0145		0.2035	3	5.830158	0	6.778912	1.244734	0.02667	1.060949	0.083593	0.500018	0.010723
ML121A-6-4	36.51		35.97	9.56	0.1728	4.51	0.5224	1.65	0.0615	0.2144	89.2087	45.68423		0.2144	3	5.82095	0	6.758534	1.274509	0.023333	1.071972	0.089229	0.510005	0.012507
ML121A-6-5	35.09		35.49	10.54	0.1484	4.43	1.0491	1.82	0.0444	0.204	88.8948	42.83592		0.204	3	5.679217	0	6.769259	1.426425	0.020341	1.068892	0.181905	0.571064	0.009166
ML121A-6-6	35.26		35.28	11.54	0.2097	3.7	0.8861	1.83	0.0582	0.1783	89.0357	36.37193		0.1783	3	5.721379	0	6.746477	1.565768	0.028817	0.895045	0.154036	0.575676	0.012046
ML121A-6-7	37.42		36.72	8.2	0.1599	4.93	0.5146	1.47	0.0296	0.2466	89.6951	51.73515		0.2466	3	5.873513	0	6.792458	1.076245	0.021256	1.153628	0.086534	0.447322	0.005926
ML121A-6-8	37.16		36.49	8.19	0.0855	4.85	0.505	1.42	0.0311	0.0997	88.8314	51.35702		0.0997	3	5.876944	0	6.80111	1.083086	0.011452	1.143517	0.085564	0.435384	0.006274
ML121A-6-9	36.17		35.2	9.47	0.1215	5.57	1.0596	1.69	0.0586	0.2514	89.5912	51.18716		0.2514	3	5.76551	0	6.612443	1.262241	0.016402	1.323638	0.180948	0.522257	0.011915
ML121A-6-10	35.56		35.14	9.86	0.1434	4.88	1.0289	1.73	0.045	0.2803	88.7266	46.87628		0.2803	3	5.743492	0	6.688768	1.331663	0.019616	1.175057	0.178037	0.541712	0.009271
ML121A-6-11	34.98		35.21	12.54	0.4734	2.93	0.7413	1.95	0.0365	0.1286	88.9899	29.40713		0.1286	3	5.707121	0	6.770074	1.710795	0.065413	0.712672	0.129573	0.616794	0.007596
ML121B-1-1	35.65		34.28	8.66	0	6.17	1.44	1.52	0.055	0.2466	88.0217	55.95198		0.2466	3	5.769391	0	6.537946	1.171903	0	1.488608	0.249663	0.476895	0.011354
ML121B-1-2	35.8		35.03	8.34	0.0494	6.26	1.2685	1.6	0.0528	0.1565	88.5573	57.23257		0.1565	3	5.739578	0	6.618615	1.118063	0.006708	1.496222	0.217876	0.497308	0.010798
ML121B-1-3	35.89		34.44	8.61	0.028	6.35	1.47	1.52	0.0497	0.175	88.5328	56.80157		0.175	3	5.768533	0	6.523567	1.157173	0.003811	1.521565	0.253123	0.473635	0.01019

Analysis	SiO2	TiO2	Al2O3	FeO	MnO	MgO	CaO	Na2O	K2O	F	Total	Mg#		F	B	Si	Ti	Al	Fe	Mn	Mg	Ca	Na	K
ML121B-1-4c	35.71		35.28	10.41	0.7287	3.75	0.4737	2.2	0.0462	0.7013	89.2999	39.10783		0.7013	3	5.779912	0	6.729612	1.408916	0.099889	0.904873	0.08214	0.690339	0.009539
ML121B-1-4r	35.93		34.81	8.03	0.0302	6.28	1.397	1.47	0.0627	0.493	88.503	58.23468		0.493	3	5.773893	0	6.592432	1.079022	0.00411	1.504513	0.240508	0.45797	0.012853
ML121B-1-6	37.1		35.96	7.65	0.0487	5.74	0.6352	1.41	0.0323	0.1967	88.7729	57.22367		0.1967	3	5.870571	0	6.705887	1.012211	0.006526	1.354076	0.107681	0.432548	0.00652
ML121B-2-1c	37.43		36.31	7.7	0.0864	5.65	0.6929	1.39	0.056	0.1431	89.5321	56.6765		0.1431	3	5.874384	0	6.715816	1.0105	0.011484	1.321952	0.116502	0.422927	0.011211
ML121B-2-1r	36.1		34.83	8.38	0.0471	6.42	1.3583	1.58	0.0391	0.3376	89.0922	57.73244		0.3376	3	5.76562	0	6.55575	1.119144	0.006371	1.528617	0.232411	0.48922	0.007966
ML121B-2-2c	36.81		36.4	7.47	0.0368	5.69	0.6483	1.42	0.0633	0.2416	88.8176	57.59194		0.2416	3	5.82445	0	6.787668	0.988355	0.004931	1.342228	0.109897	0.435598	0.012776
ML121B-2-2r	35.54		35.45	8.19	0.0492	6.08	1.3242	1.57	0.0554	0.1956	88.4545	56.96247		0.1956	3	5.70309	0	6.704079	1.098955	0.006686	1.454525	0.22765	0.488428	0.01134
ML121B-2-3c	35.51		35.13	8.37	0.0316	6.26	1.47	1.52	0.0646	0.2071	88.605	57.14465		0.2071	3	5.702314	0	6.648271	1.123904	0.004298	1.498648	0.252895	0.473208	0.013233
ML121B-2-3r	35.97		35.07	9.04	0.1387	5.45	1.075	1.54	0.0403	0.2558	88.6172	51.80386		0.2558	3	5.782321	0	6.643969	1.21516	0.018883	1.30612	0.185137	0.479944	0.008264
ML121B-3-1	35.89		35.51	8.15	0.0434	6.23	1.2845	1.63	0.0461	0.1859	88.9914	57.67846		0.1859	3	5.72174	0	6.671683	1.086464	0.00586	1.480702	0.219387	0.503791	0.009375
ML121B-3-2	36.85		36.19	7.53	0.0221	5.68	0.6723	1.38	0.0695	0	88.4099	57.35342		0	3	5.841249	0	6.760626	0.998082	0.002967	1.342275	0.11417	0.424088	0.014053
ML121B-3-3	35.61		35.38	8.04	0.1081	6.18	1.2992	1.63	0.0468	0.157	88.4512	57.81341		0.157	3	5.709996	0	6.685775	1.078011	0.01468	1.477329	0.223183	0.50671	0.009572
ML121B-3-4	35.89		35.05	8.08	0.0405	6.19	1.2804	1.53	0.0646	0.221	88.3465	57.73178		0.221	3	5.760095	0	6.629402	1.084353	0.005505	1.481057	0.220153	0.476054	0.013225
ML121B-4-1c	35.67		34.46	8.47	0.072	6.2	1.45	1.42	0.0723	0.1098	88.0415	56.61715		0.1098	3	5.763877	0	6.562314	1.144454	0.009853	1.493579	0.251016	0.444845	0.014902
ML121B-4-1r	35.49		35.32	11.61	0.4185	2.74	0.5337	1.77	0.0575	0.2796	88.2893	29.61541		0.2796	3	5.801009	0	6.803749	1.586839	0.057934	0.667687	0.093458	0.560892	0.011989
ML121B-4-2c	35.79		34.53	8.12	0.0309	6.25	1.2814	1.45	0.0567	0.199	87.7081	57.84663		0.199	3	5.785202	0	6.577843	1.097529	0.00423	1.506127	0.221903	0.454395	0.011691
ML121B-4-2m	35.99		34.98	8.19	0.0287	6.23	1.2428	1.52	0.0527	0.1469	88.3854	57.5589		0.1469	3	5.770085	0	6.609221	1.097962	0.003897	1.489064	0.213463	0.472446	0.010778
ML121B-4-2r	35.32		36.01	11.62	0.4383	2.71	0.5434	1.92	0.0362	0.2014	88.8736	29.36857		0.2014	3	5.73487	0	6.890585	1.577655	0.060272	0.65599	0.094525	0.604383	0.007498
ML121B-4-3c	35.67		34.6	8.42	0.0736	6.21	1.3786	1.6	0.0657	0.1656	88.1835	56.80207		0.1656	3	5.7519	0	6.575282	1.135334	0.010051	1.492879	0.23816	0.500192	0.013514
ML121B-4-3r	35		36.15	12.01	0.4371	2.84	0.6449	1.92	0.067	0.3232	89.3923	29.65655		0.3232	3	5.673333	0	6.905715	1.627858	0.060005	0.686299	0.111991	0.603365	0.013853
ML121B-4-4c	37.34		36.06	7.42	0.0744	5.51	0.6571	1.3424	0.0407	0.1362	88.5809	56.96969		0.1362	3	5.904482	0	6.719907	0.981103	0.009964	1.298925	0.111317	0.411526	0.008209
ML121B-4-4r	35.77		34.25	8.35	0.0265	6.27	1.3637	1.68	0.0612	0.2146	87.9861	57.2423		0.2146	3	5.782067	0	6.524614	1.128636	0.003628	1.510973	0.236159	0.52648	0.012619
ML121DB-1-1c	37.4		35.72	8.02	0.0663	5.15	0.4711	1.5	0.0409	0	88.4116	53.37704		0	3	5.935778	0	6.681094	1.064348	0.008912	1.218535	0.080102	0.461536	0.00828
ML121DB-1-1m	36.25		34.95	8.59	0.0759	5.63	1.089	1.63	0.0439	0.3926	88.7926	53.88565		0.3926	3	5.816216	0	6.608605	1.152468	0.010314	1.346684	0.18719	0.507024	0.008985
ML121DB-1-1r	35.27		35.47	10.89	0.1316	4.1	0.8576	1.59	0.0495	0.2828	88.689	40.16418		0.2828	3	5.720205	0	6.779496	1.476853	0.018076	0.991322	0.149009	0.499933	0.01024
ML121DB-1-2c	37.5		36.08	7.97	0.079	5.3	0.4997	1.57	0.0317	0.1054	89.2905	54.24604		0.1054	3	5.908718	0	6.69975	1.050083	0.010542	1.244981	0.084352	0.47959	0.006371
ML121DB-1-2r	36.03		34.92	9.07	0.1032	5.61	1.1771	1.7	0.0633	0.2477	89.0134	52.44324		0.2477	3	5.778032	0	6.599637	1.216259	0.014016	1.341231	0.202233	0.528534	0.012949
ML121DB-2-1c	37.17		36.02	8.19	0.0539	4.98	0.4281	1.57	0.0329	0.0795	88.5245	52.01753		0.0795	3	5.900604	0	6.738724	1.087154	0.007247	1.178577	0.072807	0.483183	0.006662
ML121DB-2-1r	35.59		35.08	9.81	0.1207	5	1.0927	1.65	0.0561	0.2932	88.6928	47.60845		0.2932	3	5.745698	0	6.674281	1.324302	0.016503	1.203399	0.18899	0.516425	0.011553
ML121DB-2-2c	36.89		35.96	8.57	0.1025	5.09	0.6127	1.65	0.0429	0.0961	89.0545	51.43059		0.0961	3	5.850903	0	6.721466	1.136575	0.013768	1.20353	0.104108	0.507349	0.008679
ML121DB-2-2r	35.33		34.82	10.04	0.1155	4.94	1.1561	1.66	0.0621	0.1557	88.2795	46.73011		0.1557	3	5.733939	0	6.659909	1.362531	0.015876	1.195257	0.201014	0.522307	0.012856
ML121DB-2-3c	36.51		35.44	8.31	0.0966	5.32	0.631	1.54	0.0506	0.0846	88.1589	53.30126		0.0846	3	5.852804	0	6.695391	1.113926	0.013115	1.271419	0.108369	0.478609	0.010347
ML121DB-2-3r	35.79		35.13	9.77	0.0818	5.05	0.9319	1.67	0.0433	0.4799	88.9699	47.95866		0.4799	3	5.765241	0	6.669051	1.315993	0.01116	1.212752	0.160823	0.521532	0.008897
ML121DB-2-4c	37.63		36.43	7.89	0.0399	5.42	0.4817	1.46	0.0423	0	89.4187	55.05093		0	3	5.897401	0	6.728461	1.033967	0.005296	1.266341	0.080877	0.443596	0.008456
ML121DB-2-4r	36.11		34.56	9.5	0.0789	5.07	0.8294	1.79	0.0479	0.1287	88.115	48.75721		0.1287	3	5.838153	0	6.58494	1.284324	0.010803	1.222027	0.143659	0.56106	0.009879
ML121DB-2-5c	36.19		36.41	9.56	0.5082	3.8	0.5762	1.77	0.0357	0.3993	89.2896	41.47514		0.3993	3	5.787976	0	6.862604	1.278496	0.068835	0.906038	0.098726	0.548807	0.007283
ML121DB-2-5r	35.86		35.05	9.96	0.1835	4.69	0.9231	1.67	0.0485	0.3728	88.8485	45.63823		0.3728	3	5.787904	0	6.66698	1.34423	0.025083	1.128519	0.159618	0.52256	0.009985
ML121DB-3-1	35.52		34.82	11.47	0.5174	3.44	0.7358	1.87	0.0315	0.5623	88.967	34.84103		0.5623	3	5.787254	0	6.685878	1.562666	0.071394	0.83557	0.128434	0.590676	0.006547
ML121DB-3-2	37.39		35.9	7.98	0.1183	5.11	0.4966	1.52	0.0371	0	88.5768	53.30742		0	3	5.922932	0	6.702021	1.05703	0.015871	1.206777	0.084277	0.466803	0.007497
ML121DB-3-3	35.61		34.82	9.64	0.0384	5.09	1.0282	1.77	0.0454	0.2978	88.4177	48.49011		0.2978	3	5.766288	0	6.644819	1.305282	0.005266	1.22876	0.178371	0.555656	0.009378
ML121DB-6-1c	36.99		36.36	8.16	0.3543	4.16	0.6504	1.46	0.0389	0.3928	88.5781	47.61431		0.3928	3	5.895589	0	6.829625	1.087517	0.047825	0.988465	0.111057	0.451132	0.007909
ML121DB-6-1m	37.27		35.75	8.69	0.1375	4.56	0.401	1.48	0.0405	0	88.4475	48.33509		0	3	5.93671	0	6.711083	1.157469	0.018549	1.08287	0.068431	0.457042	0.008229
ML121DB-6-1r	36.12		35.41	9.99	0.138	5.01	1.1942	1.6	0.0382	0.1803	89.7412	47.20493		0.1803	3	5.760197	0	6.654962	1.332166	0.018638	1.191111	0.204027	0.494673	0.007771
ML121DB-6-2c	36.46		34.33	9.13	0.0377	5.35	0.8777	1.72	0.0565	0.2567	88.2187	51.09383		0.2567	3	5.880927	0	6.525788	1.231411	0.00515	1.286494	0.151669	0.537856	0.011625
ML121DB-6-2r	35.98		34.83	9.79	0.1221	4.82	0.9137	1.72	0.0607	0.2438	88.4804	46.74565		0.2438	3	5.811218	0	6.629635	1.322184	0.016702	1.160588	0.1581	0.538571	0.012506
ML121DB-4-1c	36.07		35.1	10	0.1123	4.9	0.9358	1.69	0.0472	0.1881	89.0434	46.62711		0.1881	3	5.790261	0	6.640323	1.342317	0.015268	1.172662	0.160937	0.525953	0.009665
ML121DB-4-1r	35.53		35.88	11.86	0.9217	1.89	0.358	1.83	0.0465	0.4382	88.7545	22.12554		0.4382	3	5.795913	0	6.897777	1.617761	0.127337	0.459635	0.062565	0.578743	0.009676
ML121DB-5-1	37.15		36.38	8.41	0.0819	4.85	0.4199	1.41	0.0125	0.1121	88.978	50.69461		0.1121	3	5.880915	0	6.787016	1.113231	0.01098	1.144597	0.071212	0.432727	0.002524
ML121DB-5-2	36.07		35.01	9.67	0.0805	4.88	1.0458	1.7	0.0717	0.2892	88.8173	47.36111		0.2892	3	5.803518	0	6.63846	1.300992	0.010969	1.17055	0.180267	0.530277	0.014715
ML121DB-5-3	35.54		35.51	10.14	0.1164	4.88	1.0998	1.67	0.0503	0.211	89.2349	46.17962		0.211	3	5.708405	0	6.721685	1.361879	0.015834	1.168536	0.189249	0.520023	0.010306
ML121DB-5-4	34.87		35.69	13	0.5546	2.15	0.6363	1.82	0.0579	0.2782	89.057	22.77161		0.2782	3	5.700782	0	6.876368	1.77717	0.076789	0.524018	0.111446	0.576849	0.012075
ML121DB-X-c	37.71		36.1	8.04	0.1081	5.2	0.4408	1.48	0.0512	0	89.1301	53.55546		0	3	5.93221	0	6.692637	1.057595	0.014402	1.219518	0.074289	0.451367	0.010274
ML121DB-X-r	36.14		35.19	10.08	0.034	4.76	0.9238	1.73	0.058	0.1589	89.1558	45.70867		0.1589	3	5.796797	0	6.651955	1.351959	0.004619	1.138235	0.158745	0.537965	0.011867
ML121DB-Y-c	35.26		35.54	11.91	1.1323	2.17	0.5604	2.03	0.0349	0.4362	89.0739	24.5192		0.4362	3	5.755706	0	6.836972	1.625665	0.156537	0.528081	0.098002	0.642422	0.007267
ML121DB-Y-r	35.39		34.84	10.06	0.0929	4.84	1.1595	1.67	0.0485	0.2286	88.3685	46.17192		0.2286	3	5.743353	0	6.663358	1.365168	0.012768	1.170995	0.201594	0.525424	0.01004
ML121CA-1-1c	35.96		33.85	10.34	0.1469	4.76	1.0977	1.61	0.0633	0.2629	88.0909	45.07742		0.2629	3	5.857756	0	6.498309	1.40843	0.020266	1.155962	0.191565	0.508447	0.013153
ML121CA-1-1m	36.22		33.42	9.61	0.0626	5.78	1.1678	1.67	0.0568	0.4817	88.469	51.74501		0.4817	3	5.871696	0	6.384864	1.302692	0.008595	1.396908	0.202818	0.524856	0.011746
ML121CA-1-1r	34.67		36.19	12.93	0.842	1.81	0.7209	1.89	0.0609	0.3306	89.4445	19.97282		0.3306	3	5.655921	0	6.95774	1.763808	0.116332	0.440203	0.125993	0.59775	0.012673
ML121CA-1-2c	37.06		35.51	7.29	0.0613	5.68	0.6521	1.43	0.042	0.0815	87.8503	58.14374		0.0815	3	5.910493	0	6.674198	0.972185	0.00828	1.35049	0.111418	0.442143	0.008544

Analysis	SiO2	TiO2	Al2O3	FeO	MnO	MgO	CaO	Na2O	K2O	F	Total	Mg#		F	B	Si	Ti	Al	Fe	Mn	Mg	Ca	Na	K
ML121CA-1-2m	36.37		34.77	8.64	0.0711	6.06	1.2774	1.49	0.0435	0.2108	88.9329	55.56525		0.2108	3	5.810111	0	6.545998	1.154139	0.009619	1.44324	0.21862	0.461462	0.008864
ML121CA-1-2r	35.33		35.41	11.44	1.2617	2.03	0.3327	1.82	0.0466	0.4018	88.255	24.03337		0.4018	3	5.806671	0	6.858665	1.572218	0.175622	0.497399	0.058581	0.579914	0.00977
ML121CA-2-1	35.75		34.99	8.85	0.0751	5.41	1.2227	1.46	0.0666	0.1614	88.0131	52.15019		0.1614	3	5.775617	0	6.661874	1.195553	0.010275	1.303	0.211624	0.457281	0.013725
ML121CA-2-2	35.43		34.89	10.32	0.2091	4.58	0.965	1.72	0.0464	0.2618	88.563	44.17271		0.2618	3	5.752308	0	6.67578	1.401051	0.028752	1.108565	0.16785	0.541387	0.009609
ML121CA-2-3	35.14		35.3	13.16	0.6957	1.97	0.5825	1.78	0.0382	0.2903	88.9923	21.06654		0.2903	3	5.755425	0	6.81366	1.802332	0.096502	0.481024	0.10221	0.565202	0.007981
ML121CA-3-1c	35.69		34.86	8.65	0.045	5.87	1.3619	1.57	0.0636	0.2487	88.3593	54.74876		0.2487	3	5.750866	0	6.619789	1.165483	0.006141	1.410099	0.235101	0.49045	0.013072
ML121CA-3-1m	35.62		34.86	10.44	0.1806	4.61	0.9039	1.77	0.0455	0.2513	88.7145	44.04866		0.2513	3	5.76671	0	6.651073	1.413311	0.024762	1.112654	0.156775	0.555541	0.009396
ML121CA-3-1r	34.77		35.41	12.58	0.3439	3.04	0.8409	1.8	0.0579	0.2929	89.1527	30.11092		0.2929	3	5.673	0	6.808698	1.716295	0.04752	0.739446	0.146985	0.569363	0.01205
ML121CA-3-2c	36.07		34.61	8.57	0.0213	5.97	1.3081	1.55	0.0502	0.2202	88.3699	55.39661		0.2202	3	5.800857	0	6.559605	1.152471	0.002901	1.431348	0.225377	0.483266	0.010298
ML121CA-3-2m	35.13		35.05	10.18	0.1748	4.87	1.1938	1.6	0.0513	0.2856	88.5356	46.03082		0.2856	3	5.699786	0	6.701909	1.38112	0.024019	1.17797	0.207508	0.503279	0.010617
ML121CA-3-2r	34.58		35.39	12.56	0.368	2.75	0.85	1.87	0.0561	0.2665	88.6907	28.07616		0.2665	3	5.670987	0	6.839814	1.72237	0.051112	0.672344	0.149339	0.594543	0.011736
ML121CA-3-2f	32.3		31.57	12.07	1.0116	2.22	0.5052	2.03	0.0363	0.4912	82.3744	24.69424		0.4912	3	5.76789	0	6.64384	1.802291	0.15299	0.591007	0.09665	0.702779	0.008269
ML121CA-5-1c	35.53		35.08	8.8	0.0692	5.32	1.1994	1.53	0.0515	0.2397	87.8199	51.87289		0.2397	3	5.756344	0	6.69794	1.192168	0.009495	1.284955	0.208179	0.480564	0.010643
ML121CA-5-1m	35.06		34.2	9.36	0.0537	5.14	1.2442	1.8	0.0528	0.184	87.0947	49.47094		0.184	3	5.756263	0	6.617362	1.285014	0.007467	1.258104	0.218847	0.572941	0.011058
ML121CA-5-1r	34.9		35.12	11.8	0.2579	3.43	0.9313	1.85	0.0674	0.275	88.6704	34.13441		0.275	3	5.703513	0	6.763969	1.612509	0.035695	0.835672	0.163053	0.586134	0.01405
ML121CA-5-2m	37.21		34.58	7.83	0.0634	6.41	1.3057	1.5	0.0587	0.3089	89.2668	59.3421		0.3089	3	5.896938	0	6.458356	1.037604	0.008509	1.514432	0.221683	0.460857	0.011866
ML121CA-5-2r	35.01		36.61	11.66	1.31	1.6405	0.5154	1.79	0.047	0.296	88.879	20.05382		0.296	3	5.704619	0	7.030146	1.588679	0.180778	0.398507	0.089971	0.565452	0.009769
ML121CA-DX-c	37.37		35.63	7.34	0.003	5.62	0.6493	1.41	0.0359	0.2955	88.3538	57.71835		0.2955	3	5.932559	0	6.665994	0.974357	0.000403	1.330087	0.11043	0.433957	0.00727
ML121CA-DX-m	35.75		35.1	10.04	0.1051	4.8	0.9699	1.62	0.0446	0.2016	88.66	46.01517		0.2016	3	5.768931	0	6.675081	1.354741	0.014364	1.154743	0.167675	0.506807	0.00918
ML121CA-DX-r	35.17		35.2	11.81	1.0883	2.1	0.4901	1.97	0.0668	0.51	88.4053	24.0712		0.51	3	5.784154	0	6.822448	1.624129	0.151585	0.514887	0.086352	0.628119	0.014014
ML121CA-DX-v	35.75		35.66	11.52	1.46	1.68	0.3156	1.79	0.033	0.2883	88.497	20.63512		0.2883	3	5.838923	0	6.863855	1.573303	0.201952	0.409064	0.055222	0.566785	0.006875
ML121CA-SX-c	37.43		35.79	7.55	0.0796	5.51	0.5977	1.35	0.0549	0	88.3623	56.54341		0	3	5.927566	0	6.679568	0.999785	0.010676	1.300867	0.101406	0.414475	0.01109
ML121CA-SX-m	35.73		34.91	9.04	0.1324	5.3	1.2491	1.56	0.0493	0.2449	88.2158	51.10674		0.2449	3	5.773293	0	6.647686	1.221412	0.018118	1.276707	0.216227	0.488679	0.010161
ML121CA-SX-r	34.85		34.28	11.57	0.2257	3.45	0.9461	1.71	0.0653	0.2643	87.3615	34.70997		0.2643	3	5.768289	0	6.686751	1.60133	0.031638	0.851311	0.167766	0.548717	0.013787
ML167A-1-1	34.97		34.63	7.28	0.0302	6.63	1.0471	1.82	0.0581	0.0629	86.6017	61.88578		0.0629	3	5.708819	0	6.662439	0.993768	0.004175	1.613575	0.183131	0.57601	0.012099
ML167A-1-2	35.77		33.94	7.26	0.0236	6.83	0.5668	1.89	0.0304	0.1463	86.4645	62.64867		0.1463	3	5.831968	0	6.521359	0.989774	0.003259	1.660129	0.099003	0.597402	0.006322
ML167A-1-3	35.35		34.53	7.55	0.0273	6.74	0.9614	1.84	0.0536	0.0777	87.1301	61.41384		0.0777	3	5.736634	0	6.603807	1.024514	0.003752	1.630619	0.167145	0.578887	0.011095
ML167A-2-2	36.11		35.92	6.81	0.065	6.11	0.4998	1.59	0.0431	0.0271	87.2877	61.53278		0.0271	3	5.794431	0	6.792814	0.913763	0.008834	1.46167	0.085921	0.494639	0.008822
ML167A-2-c	35.17		34.63	7.54	0.0686	6.62	0.8175	1.8	0.0548	0.0715	86.8791	61.0188		0.0715	3	5.727442	0	6.646162	1.026746	0.009461	1.607205	0.142626	0.568289	0.011384
ML167A-2-m	35.23		35.01	7.2	0.1159	6.47	0.6906	1.95	0.0568	0.0935	86.8285	61.56971		0.0935	3	5.724481	0	6.70418	0.978271	0.015949	1.567302	0.120219	0.61428	0.011773
ML167A-2-r	35.68		35.08	7.15	0.1107	6.63	0.6712	1.9	0.047	0.1795	87.4485	62.30987		0.1795	3	5.754075	0	6.667152	0.964184	0.015119	1.594003	0.115964	0.594036	0.009668
ML167A-3-c	34.19		34.77	6.35	0.0369	6.08	0.4071	1.47	0.0218	0.0253	83.5602	63.05971		0.0253	3	5.732458	0	6.870313	0.890264	0.00524	1.519743	0.073125	0.477823	0.004662
ML167A-3-m	33.95		34.24	7.6	0.0487	6.43	0.7486	1.82	0.0377	0.0808	84.9559	60.13409		0.0808	3	5.658322	0	6.725301	1.059167	0.006874	1.597658	0.133666	0.588068	0.008015
ML167A-3-r	34.96		34.86	6.89	0.1986	6.5	0.7347	1.81	0.0299	0.0642	86.0475	62.71385		0.0642	3	5.720645	0	6.722504	0.942749	0.027523	1.585666	0.128797	0.574196	0.006241
ML167A-4-3	33.64		34.25	7.02	0.0502	6.68	0.9261	1.69	0.0304	0.1513	84.4381	62.91528		0.1513	3	5.631704	0	6.757321	0.982707	0.007117	1.66719	0.166098	0.548503	0.006492
ML167A-4-4	33.91		34.25	6.8	0.048	6.65	0.8953	1.6	0.0334	0.1438	84.3306	63.55088		0.1438	3	5.669501	0	6.748507	0.950669	0.006797	1.657538	0.160364	0.518615	0.007123
ML118-2-1	34.15	0.4026	31.9	7.79	0.0604	5.2	1.03	1.2358	0.1115	0	82.0011	54.34022		0	3	5.892629	0.05225	6.486929	1.123981	0.008827	1.337663	0.190405	0.413404	0.024542
ML118-2-2	36.2	0.2747	33.76	8.46	0	5.99	0.9	1.75	0.0506	0.0161	87.4015	55.79808		0.0161	3	5.866148	0.033481	6.447287	1.146352	0	1.447092	0.156246	0.549782	0.010459
ML118-2-3	36.01	0.3691	33.8	8.56	0.0147	5.91	0.9119	1.71	0.0405	0.0539	87.3962	55.17576		0.0539	3	5.843977	0.045053	6.464459	1.161615	0.00202	1.429874	0.158546	0.538009	0.008384
ML118-6-1	35.73	0.4868	33.65	8.41	0.0508	6.05	1.0436	1.75	0.0637	0.0855	87.4067	56.18974		0.0855	3	5.811609	0.059553	6.45028	1.143833	0.006998	1.467046	0.181853	0.551836	0.013216
ML118-6-2	36.21	0.5434	33.41	8.52	0.0464	6.19	1.1109	1.83	0.0532	0.0695	88.0381	56.43285		0.0695	3	5.848495	0.066013	6.359488	1.15069	0.006347	1.490497	0.192226	0.573027	0.010961
ML118-6-3	36.31	0.5551	33.45	8.41	0.025	6.03	0.89	1.86	0.0543	0.08	87.6645	56.10821		0.08	3	5.874995	0.067553	6.378337	1.137838	0.003426	1.454533	0.154274	0.583449	0.011207
ML118-6-4	36.08	0.5029	33.66	8.57	0.0008	6.24	1.0602	1.78	0.0641	0.0846	88.0427	56.48677		0.0846	3	5.823546	0.061051	6.40273	1.156658	0.000109	1.501518	0.183329	0.556993	0.013197
ML118-7-1	35.62	0.6844	33.72	8.68	0.056	6.08	1.1825	1.7	0.073	0.0559	87.9152	55.53256		0.0559	3	5.771412	0.083405	6.438813	1.17601	0.007684	1.468644	0.205263	0.534005	0.015088
ML118-7-2	35.93	0.6151	33.19	8.46	0.0825	6.51	1.1819	1.91	0.0885	0.1707	88.2005	57.84026		0.1707	3	5.811218	0.074825	6.326264	1.144151	0.011301	1.569697	0.204792	0.598896	0.018258
ML118-5-1	36.45	0.2996	34.1	8.22	0.0663	5.87	0.7628	1.75	0.0451	0.0379	87.6018	56.00866		0.0379	3	5.880811	0.036356	6.483719	1.108957	0.009059	1.411896	0.131848	0.547376	0.009282
ML118-5-2	36.2	0.4887	33.42	8.53	0.0066	6.46	1.2015	1.75	0.0558	0.1473	88.2988	57.45083		0.1473	3	5.834811	0.059245	6.348261	1.149663	0.000901	1.5523	0.207474	0.546845	0.011473
ML118-5-3	34.24	0.5547	32.32	8.61	0.0331	5.78	1.1743	1.59	0.0745	0.1963	84.6535	54.48066		0.1963	3	5.779818	0.070426	6.429569	1.215309	0.004732	1.454565	0.212364	0.520338	0.016042
ML118-8-1	36.23	0.5165	33.75	8.39	0.039	6.24	1.1043	1.82	0.0675	0.0731	88.4029	57.00779		0.0731	3	5.830488	0.062517	6.400892	1.12902	0.005315	1.497084	0.190391	0.567827	0.013856
ML118-8-2	36.25	0.4714	33.31	8.57	0.028	6.4	1.2176	1.8	0.0586	0.1167	88.3387	57.10801		0.1167	3	5.846365	0.057182	6.33115	1.155745	0.003824	1.538802	0.21038	0.562806	0.012055
ML118-8-3	35.88	0.583	33.45	8.45	0.0567	6.3	1.1478	1.82	0.0497	0.1326	87.8699	57.06766		0.1326	3	5.810053	0.071005	6.383427	1.144162	0.007776	1.520874	0.19912	0.571357	0.010266
ML118-10-1	36.42	0.4911	34.25	8.56	0.0324	6	0.8465	1.71	0.0558	0.011	88.42	55.54926		0.011	3	5.837516	0.059204	6.46962	1.147268	0.004398	1.43372	0.145357	0.531365	0.011409
ML118-10-2	49.24	0.0585	32.95	7.2	0.4328	8.94	0.0218	0.3154	0.0059	0	99.1645	0		0										
ML118-10-3	36.54	0.3712	34.76	8.25	0.0406	5.72	0.7669	1.68	0.0537	0.1153	88.3639	55.27986		0.1153	3	5.850022	0.044698	6.558414	1.10445	0.005505	1.365243	0.131538	0.521443	0.010967
ML168A-1-1r	36.29	0.448	34.3	7.16	0	6.66	0.904	1.87	0.0454	0.0573	87.7347	62.38305		0.0573	3	5.825847	0.054093	6.489277	0.961144	0	1.593937	0.155476	0.581999	0.009297
ML168A-1-1c	37.44	0.2205	35.41	6.68	0.0163	6.38	0.4324	1.6	0.0283	0.0242	88.2651	63.00146		0.0242	3	5.919807	0.026222	6.598235	0.883184	0.002183	1.503894	0.073245	0.490456	0.005708
ML168A-1-1r2	36.71	0.426	33.8	7.14	0.0133	6.72	0.7094	1.94	0.0572	0.093	87.6868	62.65875		0.093	3	5.898145	0.051479	6.399968	0.959251	0.00181	1.609627	0.122108	0.604284	0.011723
ML168A-1-2	35.97	0.4874	33.59	6.86	0.0376	6.85	0.7526	2.08	0.0404	0.2052	86.8789	64.03239		0.2052	3	5.840817	0.059527	6.427961	0.931452	0.005171	1.658245	0.130924	0.654794	0.008368
ML168A-1-2r	35.97	0.5556	34.18	7.23	0	6.25	0.88	1.76	0.0553	0.2169	87.1354	60.64876		0.2169	3	5.826743	0.067692	6.525107	0.979325	0	1.509351	0.152718	0.552722	0.011427

Analysis	SiO2	TiO2	Al2O3	FeO	MnO	MgO	CaO	Na2O	K2O	F	Total	Mg#		F	B	Si	Ti	Al	Fe	Mn	Mg	Ca	Na	K
ML168A-2-1c	37.69	0.2796	35.42	5.85	0.0052	6.68	0.6254	1.47	0.0516	0.0282	88.1	67.06012		0.0282	3	5.942232	0.033155	6.581155	0.771227	0.000694	1.570091	0.105634	0.449313	0.010377
ML168A-2-1r	37.02	0.5042	34.5	6.58	0.034	6.97	0.9499	1.86	0.0567	0.1474	88.6223	65.38056		0.1474	3	5.868032	0.060111	6.444738	0.872138	0.004564	1.647076	0.161308	0.57158	0.011464
ML168A-2-2c	36.51	0.5784	34.38	6.68	0.0606	7.11	1.0159	1.83	0.0454	0.1216	88.3319	65.48921		0.1216	3	5.816213	0.069302	6.454527	0.889832	0.008176	1.688585	0.173381	0.565181	0.009226
ML168A-2-2r	36.23	0.4789	34.02	6.78	0	7.12	1.0117	1.84	0.0445	0.1814	87.7382	65.18452		0.1814	3	5.820591	0.057868	6.441146	0.910818	0	1.705311	0.17413	0.573093	0.009119
ML168A-3-1	36.49	0.5257	33.81	6.93	0.0591	7.27	1.1333	1.69	0.0703	0.0666	88.0465	65.16104		0.0666	3	5.838639	0.063266	6.375482	0.927202	0.008009	1.734192	0.194269	0.524243	0.014348
ML168A-3-2	36.42	0.5585	34.29	6.54	0.0894	7.38	1.1039	1.84	0.0718	0.1828	88.5254	66.79806		0.1828	3	5.799552	0.066891	6.435052	0.870834	0.012057	1.752007	0.188324	0.568042	0.014584
ML168A-3-3	36.42	0.4559	34.18	6.48	0.0421	7.22	0.9358	1.86	0.0688	0.1329	87.7956	66.51575		0.1329	3	5.831396	0.054903	6.449629	0.867582	0.005709	1.723434	0.160523	0.57737	0.014052
ML168A-4-1	36.25	0.5352	34.81	7.12	0.0221	6.88	0.8717	1.88	0.0455	0.1533	88.5679	63.27285		0.1533	3	5.772481	0.064101	6.532638	0.948064	0.00298	1.633307	0.148711	0.580391	0.009242
ML168A-4-2	37.55	0.2441	35.51	6.41	0.0118	6.51	0.4988	1.73	0.0365	0.0892	88.5904	64.42158		0.0892	3	5.914341	0.028917	6.591393	0.844224	0.001574	1.52863	0.084168	0.528264	0.007333
ML168A-4-3	37.06	0.3899	35.02	6.78	0	6.67	0.7171	1.84	0.0322	0.1487	88.658	63.68856		0.1487	3	5.86549	0.046413	6.531984	0.897288	0	1.5738	0.121591	0.564579	0.006501
ML168A-4-4	36.29	0.4653	34.18	7.04	0.0199	6.63	0.8709	1.89	0.0471	0.0828	87.5161	62.67328		0.0828	3	5.838445	0.056303	6.480558	0.947079	0.002711	1.590189	0.150107	0.589495	0.009666
ML168A-5-1c	37.99	0.2735	36.44	6.13	0.0422	6.44	0.3554	1.62	0.0222	0	89.3148	65.19367		0	3	5.908206	0.031992	6.678744	0.797168	0.005558	1.493128	0.059214	0.488438	0.004404
ML168A-5-1r	36.84	0.3472	34.62	7.04	0.0325	6.89	0.6814	2.06	0.0243	0.1108	88.7542	63.56868		0.1108	3	5.848368	0.041456	6.476975	0.934525	0.00437	1.630644	0.115888	0.634002	0.004921
ML168A-5-2c	37.43	0.1478	36.25	5.88	0.0185	6.35	0.3167	1.61	0.0404	0	88.0434	65.81649		0	3	5.897779	0.017516	6.731422	0.774728	0.002469	1.491651	0.053461	0.491816	0.00812
ML168A-5-2r	36.93	0.4379	34.58	6.91	0.0354	6.85	0.6343	2.02	0.0493	0.1288	88.642	63.86497		0.1288	3	5.862407	0.052283	6.469217	0.917229	0.004759	1.621109	0.107873	0.621665	0.009983
ML168A-5-3	37.44	0.2075	35.21	6.37	0.0155	6.32	0.4464	1.72	0.0362	0.1004	87.8978	63.88437		0.1004	3	5.942284	0.02477	6.585878	0.845396	0.002083	1.495407	0.075904	0.529242	0.007329
ML168A-6-1c	37.8	0.1916	36.32	5.96	0.0259	6.14	0.2359	1.7	0.0253	0.1192	88.518	64.74807		0.1192	3	5.930116	0.022608	6.71502	0.781845	0.003441	1.436034	0.039648	0.517045	0.005063
ML168A-6-1m	37.04	0.362	35.09	6.73	0.0155	6.49	0.4525	1.97	0.0349	0.0268	88.2407	63.22581		0.0268	3	5.87793	0.043207	6.562464	0.893042	0.002083	1.535405	0.07693	0.606077	0.007065
ML168A-6-1r	36.99	0.3102	35.24	5.56	0.1472	7.3	0.4969	2.08	0.0278	0.4045	88.5567	70.06731		0.4045	3	5.848114	0.036886	6.565948	0.735037	0.01971	1.720597	0.084163	0.637534	0.005606
6B1-1-1	36.55	0.2651	34.61	8.07	0.0641	5.44	0.9956	1.198	0.0325		87.2485	54.58346			3	5.897426	0.032172	6.581226	1.088809	0.008759	1.308576	0.1721	0.374749	0.006689
6B1-1-2	35.22	0.5219	33.03	8.8	0.0378	6.08	1.53	1.39	0.0612		86.671	20.05437			3	5.914644	0.025957	6.775467	1.705991	0.027539	0.427948	0.014126	0.550224	0.009764
164-3-1	36.47	0.2128	35.45	12.58	0.2005	1.77	0.0813	1.75	0.0472		88.5619	54.42441			3	6.005034	0.145783	5.946464	1.300722	0.006093	1.553266	0.108235	0.615708	0.005002
164-3-2	37.06	1.1962	31.14	9.6	0.0444	6.43	0.6235	1.96	0.0242		88.0783	54.42441			3	6.005034	0.145783	5.946464	1.300722	0.006093	1.553266	0.108235	0.615708	0.005002
164-2-1	37.21	0.2324	31.9	8.79	0	6.33	0.1396	2.39	0.0305		87.0226	56.21555			3	6.060116	0.028467	6.122687	1.197053	0	1.536915	0.024357	0.754619	0.006336
ML164-1	36.89	0.7274	35.23	6.08	0.0139	6.16	0.6622	1.97	0.02		87.7536	64.36637			3	5.866459	0.087003	6.602526	0.808489	0.001872	1.460404	0.112818	0.607354	0.004057
ML164-2	38.43	0.1319	32.49	7.91	0.0102	6	0.0387	2.22	0.0335		87.2788	57.48973			3	6.183113	0.015961	6.160509	1.064183	0.00139	1.439173	0.006671	0.692465	0.006875
ML164-3	37.2	0.3898	32.87	6.49	0.0534	7.02	0.8803	1.91	0.0286		86.8422	65.85254			3	6.002261	0.047305	6.250313	0.875628	0.007297	1.688628	0.152168	0.597467	0.005886
ML164-4	36.48	0.7211	35.3	6.02	0.0146	6.11	0.7855	2.03	0.0486		87.5389	64.40689			3	5.82475	0.086598	6.642434	0.803752	0.001974	1.454416	0.134366	0.628387	0.009898
ML164-5	37.5	0.4464	32.66	7.18	0.0358	6.43	0.4617	1.7	0.0415		86.4555	61.48876			3	6.076575	0.054406	6.236973	0.972871	0.004913	1.553329	0.080151	0.534054	0.008578
ML164-6	49.43	0.347	23.87	5.74	0.036	5.29	0.5166	1.48	0.0412		86.7509	62.16572			3	7.747688	0.040907	4.409243	0.75231	0.004779	1.236124	0.086748	0.44973	0.008237
ML164-7	36.57	0.9325	35.01	6.63	0.0753	5.42	0.4333	1.83	0.0326		86.9615	59.30818			3	5.879863	0.112767	6.633832	0.891372	0.010254	1.299171	0.074637	0.570429	0.006686
ML164-8	36.72	0.5771	31.56	8.85	0.0605	6.57	0.3791	2.02	0.0455		86.788	56.9626			3	6.008104	0.07102	6.085578	1.210824	0.008384	1.602599	0.066452	0.640759	0.009496
ML164-9	36.66	0.7926	32.15	6.22	0.0095	7.62	0.8092	2.15	0.0165		86.4492	68.59464			3	5.953026	0.096804	6.152568	0.844576	0.001306	1.844698	0.140774	0.67685	0.003418
ML164-10	36.66	0.314	31.27	8.91	0.032	6.34	0.1139	2.69	0.0398		86.3698	55.92044			3	6.037947	0.038897	6.069526	1.227094	0.004464	1.556722	0.020098	0.858929	0.008362
ML6-B2-Z1-1	35.19	0.08	32.74	8.90	0.04	5.87	1.65	1.24	0.07		85.78	54.04197			3	5.840432	0.010074	6.403752	1.235148	0.006199	1.452408	0.293381	0.398244	0.014206
ML6-B2-Z1-2	35.62	0.49	33.10	8.44	0.09	5.65	1.22	1.36	0.04		86.05	54.41106			3	5.868531	0.060818	6.426782	1.162736	0.013116	1.387742	0.215672	0.434393	0.009331
ML6-B2-Z5-1	34.69	0.59	32.41	8.83	0.02	5.81	1.69	1.27	0.07		85.38	53.98291			3	5.793045	0.07423	6.378399	1.23301	0.002701	1.446451	0.302351	0.411682	0.014996
ML6-B2-Z5-2	34.92	0.50	32.64	8.83	0.11	5.78	1.65	1.35	0.06		85.85	53.85428			3	5.800353	0.061941	6.389406	1.226434	0.015784	1.431307	0.29362	0.434733	0.013581
ML6-B2-Z4-1	35.18	0.59	32.51	8.59	0.01	5.82	1.49	1.37	0.05		85.63	54.70927			3	5.841401	0.074195	6.361627	1.192662	0.001969	1.440685	0.265051	0.441012	0.010993
ML6-B2-Z4-3	35.35	0.59	32.56	8.65	0.03	5.99	1.51	1.25	0.04		85.97	55.24961			3	5.844624	0.072797	6.34427	1.195877	0.004621	1.476451	0.267464	0.400348	0.008331
ML6-B2-Z3-1	35.63	0.46	32.52	8.87	0.07	5.81	1.39	1.27	0.06		86.17	0.38883			3	3.432574	4.841433	0.098875	4.912697	1.357152	0.019177	1.124513	0.487369	0.292901
ML6-B2-Z3-2	35.53	0.71	32.53	8.84	0.09	5.71	1.41	1.30	0.06		86.19	53.52318			3	5.864986	0.08815	6.328283	1.220189	0.013127	1.405182	0.249352	0.414589	0.012318
ML11-Z1-1	35.52	0.48	32.56	8.53	0.02	5.73	1.12	1.24	0.05		85.30	54.4967			3	5.901469	0.060394	6.375315	1.185057	0.003405	1.419275	0.200192	0.39928	0.011466
ML11-Z2-1	35.32	0.46	33.49	8.04	0.08	5.88	1.65	1.09	0.09		86.31	56.59527			3	5.808644	0.057357	6.490816	1.105639	0.011658	1.441638	0.29071	0.346156	0.018104
ML11-Z3-1	34.46	0.61	33.10	8.42	0.05	5.55	1.67	0.97	0.07		85.15	54.02669			3	5.7634	0.077073	6.524114	1.177548	0.007167	1.383825	0.299228	0.31536	0.01487
ML11-Z3-2	36.55	0.81	32.89	6.66	0.03	5.86	0.76	1.62	0.05		85.28	61.07009			3	6.001804	0.099422	6.364853	0.914475	0.003588	1.434554	0.134227	0.515725	0.011122
ML11-Z3-3	35.34	0.57	33.01	8.02	0.00	5.77	1.57	1.05	0.08		85.68	56.19212			3	5.852135	0.071005	6.44204	1.110517	0.000519	1.424454	0.278528	0.336383	0.016898
ML11-Z3-4	37.39	0.67	32.05	6.34	0.02	7.33	0.68	2.07	0.03		86.64	67.3339			3	6.048874	0.081244	6.110507	0.857653	0.00322	1.76786	0.117509	0.649229	0.006294
ML11-Z5-1	34.66	0.68	33.17	8.18	0.07	5.68	1.82	1.00	0.09		85.48	55.31703			3	5.763997	0.084654	6.500859	1.137501	0.010338	1.408213	0.324256	0.32347	0.018731
ML11-Z5-2	36.45	1.06	33.83	6.80	0.05	5.60	0.60	1.62	0.05		86.08	59.48551			3	5.929476	0.129118	6.485611	0.924977	0.006282	1.3581	0.104758	0.510907	0.009649
ML11-Z5-3	34.90	0.65	33.58	7.89	0.08	5.67	1.64	1.06	0.07		85.57	56.16404			3	5.774149	0.080711	6.547467	1.091548	0.011112	1.398526	0.290689	0.340191	0.014224
ML11-Z5-4	36.50	0.71	33.31	6.83	0.05	5.79	0.40	1.74	0.02		85.44	60.18158			3	5.983167	0.087314	6.434918	0.936186	0.006331	1.414952	0.07065	0.552963	0.004119
ML11-Z5-7	34.91	0.67	33.14	8.36	0.05	5.80	1.88	1.11	0.07		86.06	55.29578			3	5.770091	0.083614	6.455285	1.155426	0.006887	1.429176	0.332899	0.356165	0.014379
ML11-6	34.9	0.6314	33.91	8.4	0.0073	6.01	2.07	1.0293	0.0754		87.1488	56.05568			3	5.702321	0.077593	6.529563	1.147648	0.00101	1.463948	0.362342	0.326044	0.015715
ML11-7	36.42	0.612	34.11	5.6	0.0615	7.12	1.44	1.2159	0.0931		86.7227	69.38903			3	5.86305	0.074101	6.471359	0.753832	0.008385	1.708789	0.248352	0.379481	0.019118
ML11-8	35.66	0.7049	32.97	7.97	0.0927	6.22	1.47	1.43	0.0762		86.5967	58.18359			3	5.836585	0.086775	6.359552	1.090784	0.01285	1.517724	0.257761	0.453755	0.015909
V4-17	35.98	0.8486	35.13	7.82	0.019	4.99	0.6425	1.86	0.0553		87.3455	53.22005			3	5.804813	0.102973	6.679367	1.054962	0.002596	1.200197	0.111051	0.581766	0.01138
V4-18	35.85	0.8133	34.98	7.78	0.0263	4.88	0.6115	1.74	0.0414		86.7226	52.79254			3	5.819398	0.099296	6.691736	1.056019	0.003616	1.180956	0.106343	0.547579	0.008572
V4-19	36.6	0.3036	29.08	11.62	0.0298	6.19	0.1412	2.67	0.0717		86.7064	48.7112			3	6.107563	0.038105	5.718885	1.621422	0.004212	1.539935	0.025243	0.863787	0.015262

Analysis	SiO2	TiO2	Al2O3	FeO	MnO	MgO	CaO	Na2O	K2O	F	Total	Mg#		F	B	Si	Ti	Al	Fe	Mn	Mg	Ca	Na	K
V4-20	37.23	0.6489	27.73	12.9	0.0275	6.11	0.1831	2.68	0.1044		87.614	45.78326			3	6.195077	0.081213	5.43793	1.794926	0.003875	1.515723	0.032641	0.864563	0.02216
ML6A2-23	34.01	0.6571	33.78	8.81	0.0425	5.9	1.91	1.195	0.0949		86.4039	54.42078			3	5.622934	0.081711	6.581822	1.217967	0.005951	1.454231	0.338308	0.38303	0.020014
ML6A2-24	34.27	0.7007	33.84	8.61	0.0395	5.68	1.8	1.2858	0.0871		86.3132	54.04753			3	5.659844	0.087039	6.586441	1.189041	0.005525	1.398504	0.318482	0.411692	0.018349
ML6A2-27	36.26	0.8497	33.93	6.93	0.1276	6.08	0.5673	1.99	0.0329		86.8023	61.00147			3	5.871473	0.103485	6.474902	0.93833	0.017499	1.467735	0.098413	0.624713	0.006796
ML6A2-28	34.95	0.5299	32.7	8.92	0.1141	6	1.95	1.1413	0.0733		86.3787	54.52986			3	5.776077	0.065868	6.368889	1.23269	0.01597	1.478298	0.345257	0.365674	0.015453
ML6A2-29	33.66	0.5547	32.59	9.09	0.0102	5.86	1.83	1.1076	0.105		84.8518	53.47449			3	5.679062	0.07039	6.480029	1.282418	0.001457	1.473958	0.330777	0.362288	0.022598
ML6A2-30	34.48	0.5884	33.34	9.03	0.0461	6	1.86	1.1433	0.0968		86.6039	54.2258			3	5.689411	0.073024	6.483295	1.245922	0.006442	1.475965	0.328802	0.365737	0.020374
F1-1	37.4	0.0253	37.22	0.6916	2.31	0.0027	0.235	2.06	0.0189	0.7423	80.7542	0.691223		0.7423	3	6.300489	0.003206	7.389399	0.097423	0.329574	0.000678	0.042412	0.672788	0.004061
F1-2	37.14	0.0268	36.99	0.643	2.26	0.0108	0.2386	2.04	0.0166	0.5828	79.9487	2.907503		0.5828	3	6.300541	0.00342	7.395208	0.091212	0.324701	0.002731	0.043364	0.670926	0.003592
F1-4	36.78	0.0518	35.31	1.2594	3.5	0	0.3585	2.29	0.0414	0.8886	80.4798	0		0.8886	3	6.314503	0.006689	7.144228	0.180798	0.508902	0	0.065938	0.762204	0.009066
F1-5	37.09	0.0517	35.9	1.69	3.71	0.0046	0.2113	2.32	0.0086	0.9912	81.9775	0.482937		0.9912	3	6.277197	0.006581	7.160337	0.239166	0.531767	0.001161	0.038312	0.761211	0.001857
F1-6	34.48	0.0274	30.13	13.48	1.45	0.1962	0.0889	1.72	0.0395	0	81.6121	2.529326		0	3	6.173178	0.00369	6.357272	2.018062	0.219861	0.052368	0.017052	0.597006	0.009021
F1-7	33.91	0.0014	29.36	12.25	1.74	0.1835	0.075	1.97	0.0327	0	79.545	2.601209		0	3	6.212731	0.000193	6.339294	1.876696	0.269987	0.050121	0.014721	0.699728	0.007642
F2-1	37.5	0	36.98	0.9869	3	0.0182	1.2755	1.83	0.0255	1.57	83.1861	3.183248		1.57	3	6.253351	0	7.267392	0.137612	0.423684	0.004525	0.227868	0.591617	0.005424
F2-2	37.4	0.0474	36.21	0.9284	3.02	0.0046	1.2977	2.03	0.0176	1.5	82.4943	0.875638		1.5	3	6.293628	0.005999	7.181052	0.130637	0.430403	0.001154	0.233951	0.662268	0.003778
F2-3	38.33	0.0162	36.38	2.07	4.45	0.0167	0.1682	2.28	0.0351	0.5256	84.3071	1.417965		0.5256	3	6.305443	0.002004	7.05293	0.284741	0.619977	0.004096	0.029643	0.727143	0.007365
F2-4	37.28	0.0118	35.58	0.9924	3.2	0.0018	1.2667	1.87	0.0158	1.57	81.7886	0.322333		1.57	3	6.334121	0.001508	7.12437	0.140994	0.460468	0.000456	0.230572	0.615971	0.003424
F2-5	37.72	0	35.95	0.9092	3.06	0	1.3267	2.08	0.0105	1.42	82.4862	0		1.42	3	6.338984	0	7.119951	0.127765	0.43552	0	0.23886	0.677672	0.002251
F2-6	38.21	0.0059	36.15	1.91	4.21	0	0.1568	2.32	0.0056	0.5275	83.4959	0		0.5275	3	6.328889	0.000735	7.056492	0.264537	0.59057	0	0.027824	0.744984	0.001183
F2-7	38.4	0.0103	36.12	1.84	3.98	0	0.1798	2.14	0.018	0.5825	83.2707	0		0.5825	3	6.363012	0.001284	7.053576	0.254949	0.558539	0	0.031919	0.68747	0.003805
F2-8	33.55	0	25.18	18.06	1.2037	0.674	0.1551	2.41	0.0474	0	81.2803	6.238611		0	3	6.261699	0	5.538415	2.818516	0.190264	0.187536	0.031012	0.872017	0.011285
F2-9	33.82	0	25.19	17.17	1.34	0.3434	0.1084	2.29	0.0599	0	80.3344	3.442988		0	3	6.347017	0	5.571271	2.694446	0.21298	0.096077	0.021795	0.833182	0.014339
F3-1	36.88	0	37.52	0.7301	2.89	0.0163	1.0642	1.94	0.0231	1.44	82.5038	3.828031		1.44	3	6.18014	0	7.409695	0.102304	0.410151	0.004072	0.191052	0.630257	0.004938
F3-2	38.08	0.0491	38.34	0.6595	2.1	0.0153	0.7518	1.86	0.0023	1.1	83.0032	3.971886		1.1	3	6.262648	0.006073	7.430931	0.090694	0.292495	0.003751	0.13246	0.593038	0.000483
F3-3	38.1	0	39.05	0.4836	1.64	0	0.68	1.88	0.0015	0.9749	82.8101	0		0.9749	3	6.240646	0	7.537992	0.066236	0.227503	0	0.119326	0.596995	0.000313
F3-4	38.2	0	40.03	0	0.403	0.0096	0.5129	1.65	0.0224	0.8128	81.6957	100		0.8128	3	6.252592	0	7.721691	0	0.055865	0.002343	0.08994	0.523587	0.004677
F3-5	39.04	0	41.77	0	0.0475	0.0078	0.0764	1.59	0.0141	0.1759	82.7218	100		0.1759	3	6.226963	0	7.851652	0	0.006417	0.001855	0.013055	0.491668	0.002869
F3-6	38.3	0	41.53	0	0.1127	0	0.1209	1.61	0.0125	0	81.6861	0		0	3	6.18115	0	7.898825	0	0.015404	0	0.020903	0.503738	0.002573
F3-7	38.81	0	41.15	0.0098	0.0834	0	0.0713	1.62	0.0169	0.0896	81.8737	0		0.0896	3	6.251474	0	7.811577	0.00132	0.011377	0	0.012304	0.505897	0.003472
F3-8	37.73	0	37.03	0.2854	1.72	0.0089	0.4867	1.91	0.0147	0.748	79.982	5.266951		0.748	3	6.374598	0	7.373095	0.04032	0.246112	0.002242	0.088095	0.625616	0.003168
F4-1	37.35	0.0104	36.15	0.8798	3.19	0.0064	1.211	1.95	0.0289	1.62	82.3966	1.280329		1.62	3	6.299012	0.001319	7.184892	0.124071	0.455629	0.001609	0.2188	0.637565	0.006217
F4-2	37.19	0.0429	35.61	0.9653	3.11	0	1.178	2.01	0.0129	1.36	81.5112	0		1.36	3	6.325098	0.005488	7.137451	0.13728	0.447961	0	0.214639	0.662744	0.002799
F4-3	37.41	0.034	36.11	0.9287	3.16	0.0018	1.281	2.03	0.0041	1.48	82.4397	0.344366		1.48	3	6.299152	0.004306	7.16559	0.130759	0.45063	0.000452	0.231082	0.662672	0.000881
F4-4	37.63	0.0163	37.14	0.7803	2.93	0	1.2307	1.92	0.0219	1.22	82.966	0		1.22	3	6.260323	0.00204	7.28173	0.108549	0.412828	0	0.21935	0.619259	0.004647
E2-1	37.81	0.1032	36.24	1.33	3.75	0.0293	0.9919	2.24	0.0196	1.37	83.8841	3.779257		1.37	3	6.28385	0.0129	7.098023	0.184831	0.527824	0.00726	0.176607	0.721731	0.004155
E2-2	38.07	0.1035	36.37	1.2179	3.45	0.0055	1.352	2.04	0.0231	1.54	84.1721	0.798712		1.54	3	6.303069	0.012888	7.096474	0.16861	0.483757	0.001358	0.23981	0.654799	0.004879
E2-3	38.17	0.0516	36.01	1.43	3.82	0.0138	1.2416	2.24	0.023	1.58	84.5801	1.691438		1.58	3	6.316887	0.006423	7.023186	0.197888	0.535406	0.003405	0.220133	0.718683	0.004855
E3-1	37.51	0.0206	35.27	1.71	3.89	0.0037	0.8483	2.37	0.0307	1.46	83.1133	0.384287		1.46	3	6.322408	0.002612	7.006014	0.24101	0.555295	0.00093	0.153182	0.774448	0.006601
E3-2	37.92	0.0472	35.71	1.42	3.65	0	1.45	2.05	0.0262	1.44	83.7167	0		1.44	3	6.32545	0.005922	7.020096	0.198068	0.51565	0	0.259127	0.662957	0.005575
E8-1	37.52	0.056	36.19	2.07	3.24	0	1.1397	2.25	0.0232	1.44	84.0598	0		1.44	3	6.25372	0.00702	7.108767	0.288502	0.457361	0	0.203511	0.727054	0.004933
E8-2	37.85	0.0929	35.95	1.37	3.85	0.0248	1.1601	2.19	0.0004	1.72	84.2083	3.126496		1.72	3	6.299781	0.01163	7.051614	0.19067	0.542699	0.006154	0.20686	0.706662	8.49E-05
E10-1	37.82	0.0487	35.51	1.3	3.69	0.0193	1.2006	2.18	0.0251	1.53	83.3238	2.578635		1.53	3	6.34032	0.006141	7.01569	0.182237	0.523908	0.004824	0.21563	0.708524	0.005368
E10-2	37.12	0.1417	35.45	1.276	3.41	0.0027	1.2852	2.02	0.0185	1.44	82.1706	0.375837		1.44	3	6.296941	0.018079	7.087091	0.180999	0.489908	0.000683	0.233569	0.664326	0.004003
E1-1	36.78	0.0827	36.77	1.0428	3.34	0.0146	0.8686	2.06	0.0129	1.38	82.3868	2.435376		1.38	3	6.199898	0.010485	7.304602	0.146986	0.476824	0.003669	0.156861	0.673207	0.002774
E1-2	37.97	0.0549	37.44	0.697	2.46	0.017	0.496	1.92	0.0105	0.8234	81.8889	4.167271		0.8234	3	6.31553	0.006868	7.33897	0.09694	0.346532	0.004215	0.088384	0.619126	0.002228
E1-3	36.86	0.1078	36.47	1.031	3.4	0	1.1147	1.97	0.0199	1.28	82.2535	0		1.28	3	6.219054	0.01368	7.251616	0.145456	0.485833	0	0.201488	0.644382	0.004283

Table D1) Tourmaline major elements composition

Table D2

Table D2) Whole rock analyses o pelites and metapelites composition.

		Low grade metapelite		High grade metapelite		Crd-absent migmatites				Crd-bearing migmatites				Unmetamorphosed			
		ML161	**SD**	**ML153**	**SD**	**ML6**	**SD**	**ML6B**	**SD**	**ML118**	**SD**	**ML119**	**SD**	**V1**	**SD**	**V4**	**SD**
SiO2	wt%	66.1	0.2	63.8	0.3	56.0	0.4	54.5	0.4	63.7	0.4	60.2	0.2	68.9	0.26	68.7	0.33
TiO2	wt%	0.8	0.0	0.9	0.0	0.7	0.0	0.7	0.0	0.7	0.0	0.8	0.0	0.7	0.02	0.7	0.01
Al2O3	wt%	16.9	0.1	20.2	0.3	25.5	0.3	25.8	0.2	19.1	0.3	21.3	0.2	16.4	0.19	16.6	0.24
Fe2O3t	wt%	4.7	0.1	3.5	0.1	4.1	0.1	4.2	0.0	4.9	0.1	4.9	0.1	3.8	0.07	3.2	0.06
MnO	wt%	0.0	0.0	0.0	0.0	0.1	0.0	0.1	0.0	0.1	0.0	0.1	0.0	0.0	0.00	0.0	0.00
MgO	wt%	1.3	0.0	2.0	0.0	1.8	0.1	1.7	0.0	3.0	0.0	3.0	0.0	0.9	0.01	1.0	0.01
CaO	wt%	0.5	0.0	0.4	0.0	0.8	0.0	0.7	0.0	0.6	0.0	0.4	0.0	0.1	0.01	0.1	0.02
Na2O	wt%	1.5	0.0	2.1	0.0	0.8	0.0	0.9	0.2	1.4	0.0	1.2	0.0	0.4	0.01	0.8	0.01
K2O	wt%	6.1	0.1	5.4	0.0	8.6	0.1	10.2	0.0	5.4	0.1	6.3	0.0	5.2	0.05	5.5	0.05
P2O5	wt%	0.1	0.0	0.0	0.0	0.1	0.0	0.1	0.0	0.1	0.0	0.1	0.0	0.0	0.00	0.0	0.00
Li7	ppm	63.9	1.7	109.4	1.1	96.5	2.3	97.0	2.0	110.8	1.4	107.3	1.7	29.8	0.5	43.7	0.6
Be9	ppm	4.7	0.1	6.2	0.3	2.7	0.1	2.9	0.1	7.7	0.4	6.7	0.2	6.1	0.3	5.7	0.2
B11	ppm	183.8	8.3	50.6	1.3	89.4	1.4	90.2	1.4	60.5	1.3	99.0	2.8	206.4	4.5	157.0	3.8
Sc45	ppm	18.4	0.3	15.9	0.5	20.6	0.2	18.1	0.4	18.7	0.5	22.9	0.5	16.8	0.3	15.7	0.2
V51	ppm	82.8	1.4	76.2	3.7	89.4	0.7	79.5	0.5	58.4	1.6	69.0	1.9	85.0	1.1	53.7	0.8
Cr53	ppm	55.0	1.5	37.1	1.5	43.6	0.7	48.0	1.3	50.5	1.3	55.6	3.3	42.7	0.7	35.6	1.0
Co59	ppm	6.8	0.2	8.7	0.1	10.5	0.3	75.8	1.2	6.7	0.2	6.7	0.2	5.6	0.2	5.4	0.1
Ni60	ppm	19.8	0.6	15.0	0.4	18.3	0.5	23.9	0.1	15.4	0.4	17.9	1.3	18.1	0.5	16.6	0.3
Cu65	ppm	1.2	0.1	1.3	0.1	1.1	0.1	5.6	0.1	1.0	0.1	1.0	0.1	1.5	0.1	1.7	0.2
Zn66	ppm	38.3	1.9	28.5	1.7	40.0	1.6	39.8	0.2	33.5	1.7	33.4	2.1	44.8	1.5	31.4	0.9
Ga71	ppm	18.6	0.7	16.6	0.3	25.5	0.5	24.2	0.6	21.7	0.5	21.6	0.3	15.0	0.4	15.4	0.4
Ge73	ppm	2.0	0.1	2.4	0.1	2.8	0.1	2.1	0.2	2.0	0.1	2.1	0.1	1.9	0.1	2.2	0.0
Rb85	ppm	245.8	4.4	187.0	1.9	384.7	8.8	368.0	7.6	262.2	7.8	281.0	4.5	235.3	3.4	239.3	5.5
Sr88	ppm	64.8	1.7	149.5	4.5	200.8	4.8	210.0	3.2	114.0	3.9	131.5	2.8	31.4	0.4	45.0	1.3
Y89	ppm	33.7	5.8	61.9	4.6	58.7	4.4	54.7	1.7	39.2	5.6	41.8	8.2	38.9	3.4	45.0	3.8
Zr90	ppm	312.8	26.2	431.8	32.4	767.5	13.5	667.6	7.7	199.1	14.3	191.6	12.9	263.4	10.1	456.1	15.1
Nb93	ppm	19.4	0.5	26.0	0.5	18.9	0.3	17.1	0.7	20.8	0.8	21.8	0.6	13.4	0.4	17.5	0.4
Mo95	ppm	0.2	0.0	0.1	0.0	0.2	0.0	0.4	0.1	0.1	0.0	0.1	0.0	0.1	0.0	0.1	0.0
Cd111	ppm	0.0	0.0	BDL	BDL	0.1	0.0	BDL	BDL	0.0	0.0	BDL		BDL		0.0	0.0
In115	ppm	0.1	0.0	0.1	0.0	0.1	0.0	BDL	BDL	0.1	0.0	0.1	0.0	0.1	0.0	0.1	0.0
Sn118	ppm	5.3	0.2	5.4	0.3	5.3	0.1	BDL	BDL	5.9	0.2	6.7	0.2	3.6	0.1	4.6	0.1
Sb121	ppm																
Cs133	ppm	19.8	0.6	23.9	0.3	55.0	1.2	47.6	1.1	27.3	0.7	26.6	0.5	19.8	0.3	18.2	0.4
Ba137	ppm	400.8	10.7	565.0	10.4	1510.9	18.8	1669.5	4.9	938.8	18.8	1026.5	19.0	300.8	7.6	354.9	10.2
La139	ppm	37.3	3.3	50.1	2.9	66.3	5.7	64.5	0.8	47.1	3.2	43.3	1.4	27.8	2.3	46.8	2.6
Ce140	ppm	75.8	6.4	106.8	5.3	137.0	12.0	125.7	1.1	101.8	6.4	89.5	2.3	54.8	5.4	92.6	4.6
Pr141	ppm	9.0	1.0	12.1	0.7	16.8	1.5	14.9	0.5	10.9	0.7	9.8	0.2	6.8	0.7	11.3	0.5
Nd146	ppm	31.6	3.0	46.6	2.6	60.1	5.0	60.8	1.5	39.4	3.0	35.8	1.0	25.0	3.2	41.7	2.0
Sm149	ppm	6.3	0.5	10.2	0.5	12.3	0.9	12.2	0.3	7.9	0.6	7.3	0.2	5.4	0.6	8.6	0.4
Eu151	ppm	1.0	0.1	1.7	0.1	1.9	0.1	1.8	0.1	1.1	0.1	1.2	0.0	1.0	0.1	1.1	0.1
Gd157	ppm	5.7	0.5	9.8	0.5	10.9	1.3	10.3	0.5	7.1	0.7	6.9	0.3	6.2	0.6	7.5	0.2
Tb159	ppm	0.9	0.1	1.6	0.1	1.7	0.2	1.5	0.0	1.1	0.1	1.1	0.1	1.0	0.1	1.2	0.1
Dy163	ppm	6.0	0.9	10.2	0.6	10.9	1.0	10.3	0.2	7.1	0.9	7.2	1.0	6.4	0.6	7.4	0.4
Ho165	ppm	1.2	0.2	2.1	0.1	2.2	0.2	2.0	0.0	1.4	0.2	1.5	0.2	1.3	0.1	1.5	0.1
Er167	ppm	3.7	0.6	6.2	0.5	6.4	0.5	6.0	0.3	4.3	0.7	4.3	0.8	3.8	0.3	4.5	0.4
Tm169	ppm	0.6	0.1	0.9	0.1	1.0	0.1	0.9	0.0	0.6	0.1	0.7	0.1	0.6	0.0	0.7	0.0
Yb173	ppm	3.6	0.5	5.7	0.4	6.5	0.6	6.4	0.3	3.7	0.4	4.1	1.0	3.6	0.3	4.2	0.3
Lu175	ppm	0.5	0.1	0.8	0.1	0.9	0.1	1.0	0.0	0.5	0.1	0.6	0.1	0.5	0.0	0.7	0.0
Hf177	ppm	8.7	0.6	11.3	0.8	20.2	0.7	17.8	0.0	6.1	0.4	5.8	0.4	7.0	0.2	12.2	0.8
Ta181	ppm	1.5	0.0	2.6	0.1	2.1	0.0	1.8	0.0	1.4	0.1	1.5	0.1	1.1	0.0	1.4	0.0
W182	ppm	9.5	0.7	3.9	0.2	1.7	0.1	3.0	0.1	2.6	0.2	2.2	0.2	3.6	0.2	3.8	0.2
Pb208	ppm	15.8	0.5	11.9	0.2	14.2	0.4	15.1	0.2	11.4	0.3	13.4	0.3	10.1	0.3	8.6	0.4
Th232	ppm	13.4	0.9	18.8	1.2	27.0	3.6	25.9	0.5	18.1	1.3	17.5	0.4	13.8	1.6	17.4	0.4
U238	ppm	3.4	0.3	3.0	0.3	5.8	0.9	5.9	0.2	3.3	0.3	3.4	0.4	3.0	0.1	4.4	0.1

Table D3

Element	LCT pegmatites zone A												LCT pegmatites zone B		
Li7	1066.83	1157.75	1195.71	950.43	968.18	1121.64	938.4	1167.81	1201.76	1009.09	1027.89	952.83	1296.56	BDL	1479.88
Be9	1.71	0.96	1.97	2.18	2.07	1.24	1.94	2.13	1.22	1.3	1.11	2.49	2.81	BDL	3.26
B11	37.43	35.03	44.08	123.64	52.8	41.09	44.45	35.64	38.61	69.83	73.7	53.81	46.54	BDL	46.26
Sc45	19.66	24.38	29.53	6.33	12.47	12.23	9.71	15.54	17.32	25.8	24.18	7.47	16.64	BDL	16.53
Ti49	3071.71	2668.51	4011.02	657.83	1038.32	1468.34	685.08	11488.92	5453.95	2284.94	2126.19	1489.44	4141.85	BDL	2794.17
V51	71.55	89.91	139.5	15.25	65.08	67.37	32.67	222.56	168.16	7.12	5.38	25.14	60.79	BDL	45.44
Cr53	3.85	5.34	41	BDL	34.27	19.26	15.7	33.96	2.99	BDL	BDL	BDL	BDL	BDL	BDL
Mn55	951.41	904.62	953.58	1052.33	843.98	948.49	1003.51	1236.48	1150.62	1019.14	1234.55	1362.52	1231.58	BDL	1323.61
Co59	1.88	1.89	1.63	1.25	1.67	1.57	0.86	1.18	1.165	0.698	0.507	0.69	1.67	BDL	1.9
Ni60	4.62	5.82	9.19	7.36	5.95	7.59	3.41	4.52	4.21	BDL	BDL	1.19	0.98	BDL	0.78
Cu65	BDL	BDL	BDL	BDL	BDL	BDL	BDL	BDL	BDL	BDL	BDL	BDL	BDL	BDL	BDL
Zn66	40.69	39.42	38.43	40.49	29.3	36.89	40.02	45.58	45.17	46.3	51.54	53.55	34.81	BDL	37.02
As75	BDL	BDL	BDL	BDL	BDL	BDL	BDL	BDL	BDL	BDL	BDL	BDL	BDL	BDL	BDL
Rb85	695.18	611.6	649.37	1446.52	774.46	712.05	569.88	714.28	627.35	801.89	823.08	596.65	549.69	BDL	597.84
Sr88	4.52	7.76	6.6	2.38	3.76	4.02	3.56	3.64	6.05	2.12	2.03	3.77	7.44	BDL	4.66
Y89	0.028	0.042	BDL	0.0228	0.032	BDL	BDL	0.0248	0.0199	0.0143	0.0252	0.0162	0.0216	BDL	BDL
Zr90	2.23	1.87	2.29	0.551	6.94	1.276	1.095	2.69	2.35	1.77	1.93	2	3.72	BDL	2.86
Nb93	33.55	29.04	42.02	11.21	18.31	24.9	9.16	15	29.36	135.51	135.45	50.87	95.59	BDL	65.06
Cd111	BDL	BDL	BDL	BDL	BDL	BDL	BDL	BDL	BDL	BDL	BDL	BDL	BDL	BDL	BDL
Sb121	BDL	BDL	BDL	BDL	BDL	BDL	BDL	BDL	BDL	BDL	BDL	BDL	0.102	BDL	BDL
Cs133	41.64	37.28	38.8	224.46	54.5	44.05	24.73	47.92	45.16	52.86	55.12	35.56	30.05	BDL	32.23
Ba137	171.13	283.54	190.13	158.68	143.08	126.64	123.31	102.99	187.6	21.45	19.22	32.59	61.96	9.7	48.91
La139	0.0091	BDL	BDL	0.0089	BDL	BDL	0.0043	0.0018	BDL	BDL	BDL	BDL	BDL	1.39	0.0045
Ce140	0.002	BDL	BDL	0.0019	BDL	BDL	BDL	BDL	BDL	0.0018	BDL	BDL	BDL	BDL	BDL
Pr141	BDL	0.0015	0.0014	BDL	BDL	BDL	BDL	BDL	BDL	0.0014	BDL	BDL	BDL	0.93	0.0015
Nd146	BDL	0.009	BDL	BDL	BDL	BDL	0.0087	BDL	0.0076	BDL	0.0085	BDL	0.0092	5.63	BDL
Sm149	0.011	BDL	BDL	0.011	BDL	0.011	BDL	0.009	BDL	BDL	BDL	BDL	BDL	BDL	BDL
Eu151	0.035	0.044	0.05	0.0126	0.021	0.023	0.0242	0.0327	0.0345	0.0223	BDL	0.0191	0.038	BDL	0.0257
Gd157	BDL	BDL	BDL	BDL	BDL	BDL	0.019	BDL	0.0084	BDL	BDL	BDL	BDL	BDL	BDL
Tb159	BDL	0.0031	BDL	BDL	BDL	BDL	BDL	BDL	BDL	BDL	BDL	0.0014	0.0016	BDL	BDL
Dy163	0.0061	BDL	BDL	0.006	0.039	BDL	BDL	0.0048	BDL	BDL	BDL	BDL	BDL	BDL	BDL
Ho165	BDL	BDL	BDL	BDL	BDL	BDL	BDL	BDL	BDL	0.0014	BDL	BDL	0.0016	BDL	0.0016
Er167	BDL	0.0126	BDL	BDL	BDL	BDL	BDL	0.01	0.0053	0.0058	0.0118	BDL	0.0064	BDL	BDL
Tm169	0.0029	0.0028	BDL	BDL	BDL	BDL	BDL	0.0011	0.0036	BDL	BDL	0.0013	0.0043	0.88	0.0058
Yb173	BDL	0.037	0.044	0.064	0.03	0.053	0.026	0.056	0.054	0.056	0.017	0.076	0.047	BDL	0.028
Lu175	0.0193	0.0097	BDL	0.0088	0.0096	0.0127	0.0084	0.0089	0.0185	0.0095	0.0082	0.0081	0.0104	BDL	0.0194
Hf177	0.16	0.107	0.196	0.059	0.316	0.139	0.083	0.191	0.185	0.266	0.224	0.126	0.39	BDL	0.3
Ta181	2.89	2.68	4.64	1.871	2.24	3.51	0.929	0.961	2.31	5.57	6.23	2.53	7.24	BDL	4.74
W182	32.73	2.88	8.95	18.7	12.86	32.81	8.52	37.66	22.1	53.01	51.83	48.64	78.58	BDL	67.08
Pb208	0.938	1.226	1.129	0.486	0.643	0.825	0.687	0.667	0.996	0.639	0.584	0.664	1.105	BDL	0.847
Th232	BDL	BDL	BDL	BDL	BDL	BDL	BDL	BDL	BDL	BDL	BDL	BDL	0.0017	BDL	BDL
U238	0.0128	0.0126	0.012	0.0028	0.032	0.0108	BDL	0.009	0.0095	0.0039	0.0026	0.009	0.0114	BDL	0.0057

Table D3) Muscovite trace elements composition

Element	ML167_A_3.1							ML168_A_1.1								
Li7	103.51	96.83	85.22	86.28	82.49	78.24	87.39	68.58	78.59	74.59	70.38	55.62	62.93	72.46	56.28	74.85
Be9	1.06	0.99	2.08	1.33	2.7	2.48	2.66	0.54	1.12	0.77	0.9	0.106	0.21	1.18	1.31	1.02
B11	38.9	33.76	26.79	28.34	30.85	36.87	24.16	30.08	26.08	33.94	26.82	37.71	36.14	31.05	30.55	27.88
Sc45	12.33	22.45	55.72	9.48	6.76	28.6	20.43	30.28	65.46	78.19	49.18	77.85	86	36.04	13.01	16.58
Ti49	2278.45	3476.25	5460.95	4000.79	4075.07	3532.29	4274.36	3122.56	5293.74	5178.85	3882.62	5025.27	5007.11	4724.16	2524.21	2560.9
V51	21.51	47.19	108.34	54.01	52.31	65.5	74.62	75.04	122.5	112.4	105.56	69.3	84.7	99.58	38.37	68.49
Cr53	5.35	18.7	33.18	12.97	21.89	1.7	7.91	20.46	34.08	9.47	31.59	BDL	BDL	10.01	7.32	10.43
Mn55	137.18	144.94	92.83	134.73	127.58	92.24	113.24	103.59	110.76	113.66	109	96.76	108.44	120.87	117.61	135.54
Co59	3.23	3.25	2.26	3.31	2.76	2.06	2.42	1.44	1.41	1.25	1.33	1.51	1.6	1.39	1.43	1.64
Ni60	7.99	9.68	6.78	7.1	6.19	3.52	5.36	1.82	1.38	1.95	2.01	1.53	2.52	2.42	1.78	2.22
Cu65	BDL	BDL	BDL	BDL	BDL	BDL	BDL	BDL	BDL	BDL	BDL	BDL	BDL	BDL	BDL	BDL
Zn66	16.51	17.33	9.87	15.12	14.17	10.32	12.41	11.47	10.64	11.26	10.25	13.36	13.24	11.3	10.29	11.31
As75	BDL	BDL	BDL	BDL	BDL	BDL	BDL	BDL	BDL	BDL	BDL	BDL	BDL	BDL	BDL	BDL
Rb85	455.77	438.93	410.78	444	397.41	410.31	384.62	494.89	534.77	535.71	552.39	519.54	506.76	667.78	453	499.9
Sr88	5.33	7.02	8.24	4.71	6.75	5.59	6.85	7.19	7.03	7.07	6.25	7.5	8.94	7.64	7.81	8.02
Y89	BDL	0.0157	BDL	0.008	BDL	0.0127	BDL	BDL	BDL	0.0131	0.0261	0.0295	0.0365	0.0102	0.0267	0.0221
Zr90	2.94	2.77	2.59	1.76	1.256	2.01	1.75	1.351	1.97	2.4	1.92	2.92	3.17	1.84	0.898	1.51
Nb93	7.72	9.48	11.91	14.35	13.86	9.42	12.02	56.68	139.72	88.27	79.04	57.46	52.81	134.14	31.35	51.26
Cd111	BDL	BDL	BDL	BDL	BDL	BDL	BDL	0.26	BDL	BDL	BDL	BDL	BDL	0.245	BDL	BDL
Sb121	BDL	BDL	0.145	BDL	BDL	BDL	BDL	BDL	BDL	BDL	BDL	BDL	BDL	BDL	BDL	BDL
Cs133	56.56	36.32	26.55	88.25	49.13	48.03	57.39	43.66	50.88	41.53	70.33	30.25	28.11	162.51	33.67	44.25
Ba137	77.58	161.9	234.88	158.49	316.43	113.82	218.77	526.5	391.1	341.57	428.47	274.81	309.2	470.67	565.44	521.68
La139	BDL	0.0036	0.0018	0.0018	BDL	BDL	BDL	0.0022	0.0194	0.0064	BDL	0.0143	BDL	BDL	0.004	0.0041
Ce140	BDL	BDL	BDL	BDL	0.0016	BDL	BDL	BDL	0.0224	0.0056	BDL	0.0089	0.0018	0.0018	0.0035	BDL
Pr141	BDL	BDL	BDL	BDL	0.0012	0.0012	0.0012	BDL	0.0073	0.0029	BDL	0.0028	0.0055	BDL	0.0041	0.0014
Nd146	BDL	BDL	BDL	0.0075	BDL	BDL	BDL	BDL	0.026	BDL	BDL	0.017	0.0082	BDL	BDL	0.017
Sm149	BDL	BDL	BDL	BDL	BDL	0.018	0.0087	BDL	BDL	0.011	BDL	BDL	0.01	BDL	BDL	BDL
Eu151	0.0235	0.0274	0.0356	0.0199	0.036	0.042	0.0318	0.0216	0.0214	0.0213	0.0194	0.0164	0.0172	0.0133	0.0114	0.043
Gd157	BDL	BDL	0.0081	BDL	BDL	BDL	0.0078	BDL	BDL	0.0097	0.019	0.0092	BDL	0.0092	BDL	BDL
Tb159	BDL	BDL	BDL	BDL	BDL	0.0012	0.0024	BDL	BDL	BDL	BDL	BDL	0.0014	BDL	BDL	BDL
Dy163	BDL	0.0049	BDL	0.005	0.005	0.0048	BDL	0.0118	BDL	0.0116	BDL	0.028	BDL	BDL	0.0109	BDL
Ho165	0.0014	0.0013	0.0012	BDL	BDL	0.0012	0.0012	0.0015	0.0045	BDL	BDL	0.0014	0.0014	BDL	0.0014	0.0028
Er167	BDL	0.0051	0.0102	BDL	BDL	BDL	BDL	BDL	0.0122	BDL	BDL	0.017	0.0114	BDL	BDL	BDL
Tm169	BDL	BDL	BDL	BDL	0.0012	BDL	0.0022	BDL	BDL	0.0014	BDL	BDL	BDL	BDL	0.0013	BDL
Yb173	0.017	0.015	0.015	0.023	0.0076	0.029	0.014	0.009	0.027	BDL	0.0086	0.025	0.034	BDL	0.025	0.017
Lu175	0.0083	0.0132	0.0055	0.0024	0.0049	0.0081	0.0102	0.0072	0.0099	0.0028	0.0014	0.0081	0.0093	0.0075	0.004	0.004
Hf177	0.179	0.251	0.121	0.209	0.055	0.211	0.164	0.073	0.177	0.145	0.112	0.239	0.23	0.181	0.068	0.056
Ta181	0.263	0.284	0.294	0.861	0.973	0.368	0.615	9.08	17.92	8.56	12.44	2.49	2.15	10.95	5.58	7.13
W182	12.3	11.73	11.66	17.63	11.39	13.93	14.32	22.66	38.26	50.92	22.3	71.11	65.9	44.44	9.11	19.05
Pb208	0.967	1.046	1.162	1.037	1.125	0.993	1.217	1.016	1.051	1.094	1.059	0.799	0.913	0.966	1.113	1.166
Th232	BDL	BDL	BDL	BDL	BDL	BDL	BDL	BDL	0.0033	BDL	BDL	BDL	BDL	0.0016	BDL	BDL
U238	0.0329	0.0103	0.017	0.0058	0.007	0.0133	0.0044	0.0055	0.0299	0.0095	0.017	0.0142	0.0115	0.0141	0.0127	0.0064

Table D4

Type 0-I Diagenesis		
Analisi	**$\delta^{11}B$ (‰)**	**2SE (‰)**
V4_1c	-10.79	0.2525
V4_1r	4.67	0.2308
V4_2	-13.58	0.2270
V4_3c	-9.67	0.2277
V4_3r	3.96	0.2426
V4_4c	-10.50	0.2367

Type 0-I-II Greenschist		
Analisi	**$\delta^{11}B$ (‰)**	**2SE (‰)**
ML164_2	3.73	0.72
ML164_3v	6.83	0.71
ML164_4	6.91	0.71
ML164_6ca	-8.19	0.71
ML164_6ra	-7.22	0.71
ML164_6fb	-5.30	0.72
ML164_6g	-8.78	0.70
ML164_8	3.32	1.00
ML164_9	0.56	1.02
ML164_10	-9.77	0.99
ML164_12	-9.73	0.99
ML164_14	5.66	1.00
ML164_1	-7.62	0.13

Type 0-II Greenschist		
Analisi	**$\delta^{11}B$ (‰)**	**2SE (‰)**
ML161_1	-3.09	0.85
ML161_2	-3.35	0.82
ML161_4	-3.72	0.84
ML161_5	-4.02	0.82
ML161_7c	-13.62	0.82
ML161_8	-6.00	0.84

Type 0 Greenschist		
Analisi	**$\delta^{11}B$ (‰)**	**2SE (‰)**
ML163_1	-11.49	0.56
ML163_2	-10.32	0.56
ML163_3	-11.08	0.56
ML163_4	-8.54	0.57
ML163_5	-8.52	0.57

Type VI Barren pegmatites		
Analisi	**$\delta^{11}B$ (‰)**	**2SE (‰)**
PA_2c	-0.45	0.77
PA_3chiara	-0.61	0.77
PA_3scura	-1.00	0.76
PA_4sc	-0.51	0.76
PA_4sr	-0.82	0.76

Type III Crd-bearing		
Analisi	**$\delta^{11}B$ (‰)**	**2SE (‰)**
ML118_1	0.58	0.99
ML118_2	0.41	0.99
ML118_3	1.43	0.99
ML118_4	0.87	0.99
ML118_5	0.93	0.99
ML118_6TSX	0.74	0.99
ML118_6GZE	0.77	0.99
ML118_6GZI	1.00	0.60
ML118_7	0.99	0.60
ML118_8	1.17	0.60
ML118_9c	1.18	0.60
ML118_9r	1.06	0.60
ML118_10cc	1.41	0.60

Type IV Crd-absent		
Analisi	**$\delta^{11}B$ (‰)**	**2SE (‰)**
ML6B2_1	-2.93	0.57
ML6B2_2c	-3.53	0.57
ML6B2_2r	-3.53	0.57
ML6B2_3c	-3.03	0.57
ML6B2_3r	-3.12	0.49
ML6B2_4r	-2.69	0.49
ML6B2_4c	-2.89	0.49
ML6B2_5r	-2.70	0.49
ML6B2_5c	-2.95	0.49
ML6B2_6c	-2.90	0.49
ML6B2_6r	-2.86	0.50
ML6B2_7c	-2.78	0.49
ML6B2_7r	-2.72	0.50
ML6B2_8	-3.88	0.49
ML6B1_1c	-3.41	0.49
ML6B1-1r	-2.82	0.76
ML6B1-2c	-2.35	0.76
ML6B1-2r	-2.65	0.76
ML6B1-3	-3.05	0.76

Type V Leucosomes		
Analisi	**$\delta^{11}B$ (‰)**	**2SE (‰)**
ML167A-1	-2.37	0.19
ML167A-2	-2.37	0.19
ML167A-3	-2.55	0.19
ML167A-4	-2.24	0.19
ML167A-5	-2.15	0.20
ML167A-6	-1.78	0.20
ML167A-7	-2.18	0.20
ML167A-8	-1.96	0.20
ML167A-9	-1.15	0.21
ML167A-10	-2.56	0.19
ML167A-11	-2.50	0.20

LCT pegs zone A		
Analisi	**$\delta^{11}B$ (‰)**	**2SE (‰)**
ML121A-1	-2.34	0.69
ML121A-1	-2.11	0.69
ML121A-2	-1.96	0.69
ML121A-3	-2.34	0.68
ML121A-3	-1.76	0.69
ML121A-3	-1.49	0.69
ML121A-3	-1.06	0.69
ML121A-4	-0.89	0.69
ML121A-4	-1.18	0.69
ML121A-4	-1.64	0.69
ML121A-4	-1.36	0.69
ML121A-4	-0.85	0.69
ML121A-5	-1.22	0.69
ML121A-5	-1.29	0.69
ML121A-5	-1.10	0.69
ML121A-5	-1.09	0.69
ML121A-5	-1.19	0.69
ML121A-6	-1.53	0.69
ML121A-6	-1.57	0.69
ML121A-6	-1.45	0.69
ML121A-6	-1.54	0.69
ML121A-6	-1.63	0.68
ML121A-6	-1.68	0.69
ML121A-6	-1.53	0.69
ML121A-6	-1.54	0.69
ML121A-6	-1.50	0.69
ML121A-6	-1.62	0.69
ML121A-6	-1.74	0.69
ML121A-6	-2.05	0.69
ML121A-6	-2.01	0.69
ML121A-7	-2.01	0.69
ML121A-7	-2.17	0.69
ML121A-7	-1.80	0.69
ML121A-7	-1.57	0.69
ML121A-7	-1.49	0.69

LCT pegs zone D		
Analisi	**$\delta^{11}B$ (‰)**	**2SE (‰)**
DA-1-1r	-0.49	0.76
DA-1-1ri	-0.57	0.76
DA-1-1c	-0.03	0.76
DA-1-2pu	-0.07	0.76
DA-2-1c	0.05	0.76
DA-2-1r	-0.02	0.76
DA-2-2c	0.06	0.76
DA-2-2r	-0.16	0.76
DA-2-3cc	-0.83	0.76
DA-2-3cs	-0.23	0.76

LCT pegs zone C		
Analisi	**$\delta^{11}B$ (‰)**	**2SE (‰)**
ML121CA-	-1.25	1.78
ML121CA-	-0.74	1.78
ML121CA-	-0.54	1.78
ML121CA-	-0.39	1.78
ML121CA-	-0.73	1.78
ML121CA-	-1.28	1.78
ML121CA-	-0.91	1.78
ML121CA-	-0.86	1.78
ML121CA-	0.15	1.78
ML121CA-	-0.64	1.78
ML121CA-	0.08	1.78
ML121CA-	0.57	1.78
ML121CA-	0.97	1.78
ML121CA-	-0.27	1.78
ML121CA-	0.29	1.78
ML121CA-	0.05	1.78
ML121CA-	-0.32	1.78

LCT pegs zone C		
Analisi	**$\delta^{11}B$ (‰)**	**2SE (‰)**
ML121CB-	-0.65	1.78
ML121CB-	-0.72	1.78
ML121CB-	0.57	1.78
ML121CB-	0.85	1.78
ML121CB-	0.87	1.79
ML121CB-	1.10	1.78
ML121CB-	0.67	1.78
ML121CB-	0.50	1.78
ML121CB-	-0.50	1.78
ML121CB-	-1.09	1.78
ML121CB-	-1.72	1.78
ML121CB-	-1.62	1.78
ML121CB-	-1.38	1.78
ML121CB-	-1.10	1.78
ML121CB-	-1.03	1.78

LCT pegs zone D		
Analisi	**$\delta^{11}B$ (‰)**	**2SE (‰)**
DA-2-3r	-0.02	0.36
DA-3-1c	0.54	0.39
DA-3-1rm	-0.21	0.37
DA-3-1rv	-0.40	0.37
DA-3-2c	-0.04	0.37
DA-3-2r	-0.22	0.37
DA-3-3cc	-0.51	0.37
DA-3-3ce	-1.18	0.37
DA-3-3r	-0.91	0.37
DA-4-1c	-1.11	0.37
DA-4-1r	-0.63	0.24

LCT pegs zone D		
Analisi	**$\delta^{11}B$ (‰)**	**2SE (‰)**
DB-1-1c	-0.30	0.23
DB-1-1r	-0.18	0.23
DB-1-2c	-0.22	0.24
DB-1-2r	-0.81	0.22
DB-2-1cb	-0.77	0.24
DB-2-1rb	-0.59	0.24
DB-2-1cm	-0.82	0.22
DB-2-1rm	-0.61	0.23
DB-2-1ca	-1.08	0.23
DB-2-1ra	0.27	0.78
DB-2-2cb	-0.06	0.79
DB-2-2rb	-0.29	0.79
DB-2-2ca	-0.69	0.79
DB-2-2rb2	-0.33	0.79
DB-2-3c	-0.69	0.79
DB-2-3r	-0.38	0.79
DB-3-1c	-0.67	0.79
DB-3-1cs	-0.86	0.78
DB-3-1r	-1.09	0.78
DB-6-1cc	0.59	0.70
DB-6-1css	0.58	0.70
DB-6-1r	0.19	0.70
DB-6-2c	0.18	0.70
DB-6-2r	-0.02	0.70
DB-4-1r	-0.19	0.69
DB-4-1r	-0.19	0.69
DB-5-1cg	-0.42	0.70
DB-5-1cgs	-0.53	0.69
DB-5-1cp	-0.74	0.69
DB-5-1r	0.11	0.22

LCT pegs zone E		
Analisi	**$\delta^{11}B$ (‰)**	**2SE (‰)**
EB-1-1c	-0.68	0.22
EB-1-1r	-0.45	0.22
EB-2-1cc	-0.73	0.22
EB-2-1csx	-0.60	0.22
EB-2-1r	-0.92	0.22
EB-3-1c	-1.36	0.24
EB-3-1r	-1.03	0.25
EB-4-1c	-0.99	0.24
EB-5-1b	-1.40	0.22
EB-5-1asx	-0.55	0.17
EB-6-1sb	-0.71	0.20
EB-6-1sm	-1.16	0.17
EB-6-1sa	-1.40	0.18
EB-6-1cbs	-1.28	0.26
EB-7-1s	-0.40	0.18

LCT pegs zone F		
Analisi	**$\delta^{11}B$ (‰)**	**2SE (‰)**
FB-1-1b	-1.16	0.19
FB-1-1a	-0.75	0.57
FB-1-2b	-0.79	0.57
FB-1-2mb	-0.91	0.57
FB-1-2ma	-1.48	0.57
FB-1-2a	-0.95	0.57
FB-1-3mu	-1.18	0.57
FB-1-3mu	-1.15	0.56
FB-1-3mu	-0.99	0.56
FB-1-3mu	-1.07	0.57
FB-1-4tg	-0.12	0.57
FB-2-1c	-0.27	0.71
FB-2-1r	-0.88	0.73
FB-2-2	-1.01	0.71
FB-2-3c	-2.14	0.71
FB-2-3r	-1.49	0.71
FB-3-1	-1.65	0.71
FB-3-2	-1.40	0.74

LCT pegs zone B		
Analisi	**$\delta^{11}B$ (‰)**	**2SE (‰)**
ML121B-1	-1.70	1.78
ML121B-1	-1.56	1.78
ML121B-1	-2.41	1.78
ML121B-1	-3.10	1.78
ML121B-1	-3.67	1.78
ML121B-1	-4.25	1.77
ML121B-1	-3.83	1.78
ML121B-1	-3.97	1.78
ML121B-1	-3.67	1.78
ML121B-1	-3.82	1.78
ML121B-1	-2.72	1.78
ML121B-2	-2.32	1.78
ML121B-2	-1.99	1.78
ML121B-2	-2.54	1.78
ML121B-2	-2.35	1.78
ML121B-2	-3.07	1.78
ML121B-2	-2.86	1.78
ML121B-3	-2.59	1.78
ML121B-3	-2.72	1.78
ML121B-3	-2.39	1.78
ML121B-3	-2.35	1.78
ML121B-3	-1.27	1.78
ML121B-4	-2.07	1.78
ML121B-4	-1.94	1.78
ML121B-4	-2.10	1.78
ML121B-4	-2.35	1.78
ML121B-4	-2.11	1.78
ML121B-4	-1.55	1.78
ML121B-4	-1.49	1.78

LCT pegs zone F pockets		
Analisi	**$\delta^{11}B$ (‰)**	**2SE (‰)**
F1-1	-1.19	0.16
F1-2	-1.03	0.17
F1-3	-1.03	0.16
F1-4	-0.73	0.16
F1-5	-0.35	0.16
F2-1	-2.25	0.17
F2-2	-2.42	0.16
F2-3	-0.12	0.16
F2-4	-2.19	0.17
F2-5	-2.07	0.17
F2-6	0.18	0.16
F2-7	0.06	0.16
F3-1	-1.49	0.18
F3-2	-1.94	0.18
F3-3	-2.08	0.18
F3-4	-2.10	0.19
F3-5	-2.07	0.18
F3-6	-1.96	0.19
F3-7	-2.13	0.22
F4-1	-1.83	0.19
F4-2	-1.79	0.18
F4-3	-1.72	0.18
F4-4	-1.54	0.18

LCT pegs zone E pockets		
Analisi	**$\delta^{11}B$ (‰)**	**2SE (‰)**
E1-1	-1.54	0.19
E1-2	-1.10	0.13
E1-3	-1.21	0.14
E2-1	-0.61	0.13
E2-2	-0.83	0.13
E2-3	-0.81	0.12
E3-1	-0.48	0.12
E3-2	-0.45	0.12
E8-1	-0.66	0.12
E8-2	-0.89	0.14
E10-1	-0.22	0.13
E10-2	-0.67	0.13

Table D4) Tourmaline in-situ boron isotopic data